DISSERTATION | DOCTORAL THESIS

Titel | Title

Drought-influenced greenhouse gas fluxes and their emission pathways of the subsaline reed ecosystem of Lake Neusiedl

verfasst von | submitted by
Pamela Alessandra Baur B.Sc. M.Sc. (TUM)

angestrebter akademischer Grad | in partial fulfilment of the requirements for the degree of
Doktorin der Naturwissenschaften (Dr.rer.nat.)

Wien | Vienna, 2025

Studienkennzahl lt. Studienblatt | Degree programme code as it appears on the student record sheet:	UA 796 605 299
Dissertationsgebiet lt. Studienblatt | Field of study as it appears on the student record sheet:	Environmental Sciences
Betreut von | Supervisor:	Univ.-Prof. Dipl.-Geogr. Dr. Stephan Glatzel

Abstract

Wetlands are often spatially dynamic ecosystems and provide various ecosystem services, such as biodiversity, purification, livelihood, and storage of carbon and water. Wetlands dominated by the reed plant (*Phragmites australis*) can store carbon through photosynthetic assimilation of carbon dioxide (CO_2) and sequestration of organic matter in sediments. For this reason, they are often known as strong CO_2 sinks. However, these wetlands naturally release methane (CH_4) produced in the waterlogged sediments. In the context of climate change, more frequent or severe droughts increase the likelihood of periods in which wetland ecosystems act as CO_2 sources. Little is known about the contribution of central European reed wetlands as a source of greenhouse gases (GHG) due to drought.

The main objective of this thesis is to enhance our comprehension of the influence of drought on the spatial and temporal dynamics of reed wetlands, particularly with regards to GHG fluxes, emission pathways, sediment microbial communities, and land cover. The studies were conducted in a wetland of international importance, the reed belt of Lake Neusiedl on the Austrian-Hungarian border, which is characterized by exceptional properties such as subsalinity and high sulfate content. In order to deepen and improve our understanding of subsaline reed ecosystems, their processes, and their interactions, a combination of methodologies was applied. These included techniques for measuring GHGs, such as eddy covariance, chambers, and bubble traps; stable carbon isotope measurements; laboratory analyses of water and sediment properties; remote sensing using drone and satellite imagery; and image and data analyses, including deep learning and vegetation indices.

Since mid-2015, Lake Neusiedl's catchment area has experienced drought, with mostly negative SPEI (standardized precipitation evapotranspiration index) values, leading to a decrease in water levels. Under these conditions, the GHG exchange between this reed ecosystem and the atmosphere was continuously measured with an eddy covariance tower over 4.5 years (mid-2018 to 2022). From 2019 to 2022, annual CH_4 emissions decreased by 76% from 9.2 to 2.2 g CH_4-C m^{-2} a^{-1}. Initially, annual CO_2 emissions decreased by 85% from 181 to 27 g CO_2-C m^{-2} a^{-1} due to reed growth from 2019 to 2021. However, by 2022, they had risen to twice the 2019 level (391 g CO_2-C m^{-2} a^{-1}). This was the result of a sharp drop in sediment water content (SWC) from about 65 to 32 Vol-% in mid-2022, suggesting that SWC is a good proxy of the magnitude of CO_2 emissions from wetlands. In general, this study challenges the assumption that all reed wetlands are CO_2 sinks.

Another study in this thesis explored the intra-annual dynamics of the land cover mosaic of reed, water, and sediment patches within the reed ecosystem and its phenology within one year. The results showed that within the reed ecosystem in 2021, the reed area increased by 10%, the open sediment areas increased by 27%, and water areas decreased by

23% from May to November. Nevertheless, the reed area remained dominant throughout, accounting for 61–71%.

At lakes, and especially shallow lakes like Lake Neusiedl, it is often assumed that ebullition is the dominant CH_4 emission pathway, although ebullition is difficult to study and is therefore often not measured. Thus, one study in this thesis investigated whether ebullition or diffusion is the more important CH_4 emission pathway in three subsystems of the Lake Neusiedl ecosystem: the *Reed belt*, the *Channel*, and the *Open water/Lake*. The results show that at the *Reed belt* ebullition accounted for 48% of the sum of the two CH_4 emission pathways on a cumulative basis, while at the other two subsystems it was responsible for only about 1%. The *Reed belt* with 17 ± 28 mg CH_4 m^{-2} d^{-1} showed 340 times higher mean CH_4 ebullition rates than the other two subsystems.

In this reed wetland, all assessable emission pathways of CH_4 from the ecosystem to the atmosphere were investigated individually with chamber and ebullition trap measurements, in particular the contribution and isotopic signature of ebullition, but also the contribution of the plant-mediated transport and diffusion pathways at the water–air and sediment–air interfaces in each season for one year. In addition, the research aimed to investigate whether the reed ecosystem exhibits a diel cycle (24 h) of CH_4 emissions depending on the season and emission pathway. To improve system understanding of subsaline reed wetlands, the physicochemical properties and the microbial communities such as methanogens, methanotrophs, and sulfate reducers in the sediments were investigated and how they changed due to desiccation in one year. The plant-mediated transport showed the highest median CH_4 emission rates in all seasons, not only in summer but also in winter. A pronounced diel pattern of the CH_4 was found only for the plant-mediated transport in summer. Both approaches, the stable carbon isotope values of the ebullition gases from March to July 2021 and the seasonal source signatures of the Keeling plots, demonstrated that at Lake Neusiedl the dominant methanogenic pathway in the sediment is acetoclastic methanogenesis yearlong.

Overall, this thesis provides insights into the interplay of various dynamics in reed wetlands in relation to land cover, GHG fluxes, emission pathways, microbial diversity, and sediment properties, both within and between years, especially under the influence of drought.

Zusammenfassung

Feuchtgebiete sind häufig dynamische Ökosysteme, die verschiedene Ökosystemleistungen wie Biodiversität, Reinigung, Lebensgrundlage sowie Kohlenstoff- und Wasserspeicherung bieten. Von Schilfpflanzen (*Phragmites australis*) dominierte Feuchtgebiete können durch photosynthetische Assimilation von Kohlenstoffdioxid (CO_2) und Fixierung organischer Substanzen im Sediment Kohlenstoff speichern. Aus diesem Grund werden sie oft als starke CO_2-Senken bezeichnet. Allerdings setzen diese Feuchtgebiete auch auf natürliche Weise Methan (CH_4) frei, das in wassergesättigten Sedimenten gebildet wird. Im Zusammenhang mit dem Klimawandel erhöhen häufigere oder schwerere Trockenperioden die Wahrscheinlichkeit, dass Feuchtgebiete als CO_2-Quellen fungieren. Über den Beitrag mitteleuropäischer Schilfökosysteme als Quelle von Treibhausgasen infolge von Trockenheit ist nur wenig bekannt.

Das Hauptziel dieser Dissertation ist es, unser Verständnis über den Einfluss von Trockenheit auf die räumliche und zeitliche Dynamik Schilf-dominierter Feuchtgebiete zu erweitern, insbesondere im Hinblick auf Treibhausgasflüsse, Emissionspfade, mikrobielle Gemeinschaften im Sediment und die Landbedeckung. Die Studien wurden in einem Feuchtgebiet von internationaler Bedeutung durchgeführt: dem Schilfgürtel des Neusiedler Sees an der österreichisch-ungarischen Grenze. Dieser zeichnet sich durch außergewöhnliche Eigenschaften wie Subsalinität und einen hohen Sulfatgehalt aus. Um unser Verständnis von subsalinen Schilfökosystemen, ihren Prozessen und Wechselwirkungen zu vertiefen, wurde eine Kombination verschiedener Methoden angewendet. Dazu gehörten Techniken zur Messung von Treibhausgasen wie Eddy-Kovarianz, Hauben oder Gasblasenfallen, die Messung stabiler Kohlenstoffisotope, Laboranalysen der Wasser- und Sedimenteigenschaften, die Fernerkundung mittels Drohnen- und Satellitenbilder sowie Bild- und Datenanalysen einschließlich Deep Learning und Vegetationsindizes.

Seit Mitte 2015 herrscht im Einzugsgebiet des Neusiedler Sees Trockenheit, was zu überwiegend negativen SPEI-Werten (standardized precipitation evapotranspiration index) und zu sinkenden Wasserständen geführt hat. Unter diesen Bedingungen wurde der Austausch von Treibhausgasen zwischen dem Schilfökosystem und der Atmosphäre über einen Zeitraum von 4.5 Jahren (Mitte 2018 bis Ende 2022) kontinuierlich mit einem Eddy-Kovarianz Messturm gemessen. Von 2019 bis 2022 sanken die jährlichen CH_4-Emissionen um 76% von 9.2 auf 2.2 g CH_4-C m^{-2} a^{-1}. Anfangs sanken die jährlichen CO_2-Emissionen aufgrund des Schilfwachstums von 2019 bis 2021 zunächst um 85% von 181 auf 27 g CO_2-C m^{-2} a^{-1}. Im Jahr 2022 stiegen sie jedoch auf das Doppelte des Wertes von 2019 (391 g CO_2-C m^{-2} a^{-1}). Dies war das Ergebnis eines starken Rückgangs des Sedimentwassergehalts von etwa 65 auf 32 Vol-% Mitte 2022, was darauf hindeutet, dass der Sedimentwassergehalt ein guter Indikator für das Ausmaß der CO_2-Emissionen von Feuchtgebieten ist. Insgesamt stellt diese Studie die Annahme infrage, dass alle von

Schilf-dominierten Feuchtgebiete CO_2-Senken sind.

Eine weitere Studie dieser Dissertation untersuchte die innerjährliche Dynamik des Landbedeckungsmosaiks aus Schilf-, Wasser- und Sedimentflächen innerhalb des Schilfökosystems und dessen Phänologie im Jahresverlauf. Die Ergebnisse zeigen, dass die Schilfflächen innerhalb des Schilfökosystems im Jahr 2021 von Mai bis November um 10% und die offenen Sedimentflächen um 27% zunahmen, während die Wasserflächen um 23% abnahmen. Die Schilffläche ist mit einem Anteil von 61–71% stets der dominierende Teil.

Insbesondere bei flachen Seen wie dem Neusiedler See wird häufig angenommen, dass die Ebullition der dominierende CH_4-Emissionspfad ist, obwohl dieser Emissionspfad schwierig zu untersuchen ist und daher oft nicht gemessen wird. Im Rahmen dieser Arbeit wurde daher untersucht, ob die Ebullition oder die Diffusion als CH_4-Emissionspfad in drei Subsystemen des Neusiedler See-Ökosystems wichtiger ist: im Schilfgürtel, im Kanal und im Freiwasser/See. Die Ergebnisse zeigen, dass die Ebullition innerhalb des Schilfgürtels kumuliert 48% der Summe der beiden CH_4-Emissionspfade ausmachte, während sie an den beiden anderen Subsystemen nur für etwa 1% verantwortlich war. Mit 17 ± 28 mg CH_4 m^{-2} d^{-1} wies das Subsystem innerhalb des Schilfgürtels 340-mal höhere mittlere CH_4-Ebullitionsraten als die beiden anderen Subsysteme auf.

In dem untersuchten, von Schilf dominierten Feuchtgebiet wurden alle erfassbaren Emissionspfade von CH_4 aus dem Ökosystem in die Atmosphäre mittels Hauben- und Gasblasenmessungen einzeln untersucht. Dabei wurde insbesondere der Beitrag und die Isotopensignatur der Ebullition, aber auch der Beitrag des Gastransports durch die Schilfpflanzen sowie der Diffusionspfade an den Wasser–Luft- und Sediment–Luft-Grenzflächen in jeder Jahreszeit über einen Zeitraum von einem Jahr untersucht. Darüber hinaus wurde analysiert, ob die CH_4-Emissionen im Schilfökosystem einen Tagesgang (24 Stunden) in Abhängigkeit von der Jahreszeit und dem Emissionspfad aufweisen. Zur Vertiefung des Systemverständnisses wurden die physikalisch-chemischen Eigenschaften sowie die mikrobiellen Gemeinschaften — darunter Methanogene, Methanotrophe und Sulfatreduzierer — in den Sedimenten analysiert und die Veränderungen durch Austrocknung innerhalb eines Jahres untersucht. Der Gastransport durch die Schilfpflanzen wies in allen Jahreszeiten die höchsten mittleren CH_4-Emissionsraten auf, und zwar nicht nur im Sommer, sondern auch im Winter. Ein ausgeprägter Tagesgang der CH_4-Emissionen wurde nur für den Gastransport durch die Schilfpflanzen im Sommer festgestellt. Sowohl die stabilen Kohlenstoffisotopenverhältnisse der Ebullitionsgase von März bis Juli 2021 als auch die saisonalen Quellsignaturen der Keeling-Plots zeigten, dass am Neusiedler See ganzjährig die acetoklastische Methanogenese der dominante methanogene Stoffwechselweg im Sediment ist.

Insgesamt liefert diese Dissertation Einblicke in das Zusammenspiel verschiedener Dynamiken in Schilf-dominierten Feuchtgebieten in Bezug auf Landbedeckung, Treibhausgasflüsse, Emissionspfade, mikrobielle Diversität und Sedimenteigenschaften — sowohl innerhalb eines Jahres als auch zwischen verschiedenen Jahren — insbesondere unter dem Einfluss von Trockenheit.

Table of contents

Abstract i

Zusammenfassung iii

1 General introduction 1
- 1.1 Wetlands in a global perspective 1
- 1.2 Dynamics of wetlands and their GHG fluxes 4
  - 1.2.1 Land cover dynamics of wetlands 4
  - 1.2.2 GHG fluxes and related processes in wetlands 4
  - 1.2.3 Emission pathways of GHG fluxes 7
  - 1.2.4 Flux measurement techniques 9
- 1.3 Wetlands with reed 13
  - 1.3.1 Wetland plant: *Phragmites australis* 13
  - 1.3.2 Lake Neusiedl — a subsaline wetland with reed 15
- 1.4 Objectives and outline of the thesis 19
- 1.5 Contribution to publications 20
  - 1.5.1 Study I 20
  - 1.5.2 Study II 20
  - 1.5.3 Study III 21
  - 1.5.4 Study IV 21

2 Study I:
Is ebullition or diffusion more important as methane emission pathway in a shallow subsaline lake? 23
- Graphical Abstract 23
- Highlights 24
- Abstract 24
- 2.1 Introduction 24
- 2.2 Methods 28
  - 2.2.1 Study site and setup 28
  - 2.2.2 Methane measurements 29
  - 2.2.3 Flux calculations and isotope ratios 31
  - 2.2.4 Water sampling and in situ measurements 32
  - 2.2.5 Water analysis 33
  - 2.2.6 Additional data 33
  - 2.2.7 Data processing and statistical analysis 34

2.3 Results 35
2.3.1 Ebullition heterogeneity in space and time 35
2.3.2 Isotope ratios and fractionation factor of ebullition gas 36
2.3.3 Drivers of methane ebullition 38
2.3.4 Diffusion of methane in space and time 39
2.3.5 Ebullition vs. Diffusion pathways 40
2.4 Discussion 43
2.4.1 Ebullition heterogeneity in space and time 43
2.4.2 Isotope ratios and fractionation factors of ebullition gas 46
2.4.3 Drivers of ebullition 48
2.4.4 Diffusion of methane in space and time 49
2.4.5 Ebullition vs. diffusion pathway 51
2.5 Conclusions 52
Data availability 52

3 Study II: Consequences of intense drought on CO_2 and CH_4 fluxes of the reed ecosystem at Lake Neusiedl 53
Graphical Abstract 53
Highlights 54
Abstract 54
3.1 Introduction 54
3.2 Material and methods 56
3.2.1 Study site 56
3.2.2 Eddy covariance and biometeorological measurements 58
3.2.3 Eddy covariance data processing 58
3.2.4 Vegetation indices and reed growth data 60
3.2.5 Data and statistical analysis 61
3.3 Results 61
3.3.1 Environmental parameters of a subsaline reed ecosystem 61
3.3.2 Drought influence on temporal variations (diurnal, seasonal, annual) of C fluxes of a subsaline reed ecosystem 65
3.3.3 Drivers of C fluxes of a subsaline reed ecosystem 69
3.4 Discussion 72
3.4.1 Drought influence on environmental parameters of reed ecosystems 72
3.4.2 Drought influence on temporal variations (diurnal, seasonal, annual) of C fluxes of reed ecosystems 74
3.4.3 Drivers of C fluxes of reed ecosystems 77
3.5 Conclusions 78
Data availability 79

4 Study III:
Temporal dynamics of CH_4 emission pathways in the subsaline reed wetland of Lake Neusiedl 81
Abstract . . . 81
4.1 Introduction . . . 82
4.2 Material and Methods . . . 85
  4.2.1 Study site . . . 85
  4.2.2 Measurement setup . . . 85
  4.2.3 Water sampling and analysis . . . 91
  4.2.4 Sediment sampling and analysis . . . 91
  4.2.5 Data and statistical analysis . . . 93
4.3 Results . . . 94
  4.3.1 Seasonal and diel differences in CH_4 emissions of a subsaline reed wetland . . . 94
  4.3.2 Seasonal $\delta^{13}C$ source signatures of a subsaline reed wetland . . . 96
  4.3.3 Sediment properties of the reed belt . . . 97
  4.3.4 Change in the microbial community in the sediments within one year 98
4.4 Discussion . . . 102
  4.4.1 Seasonal and diel differences in CH_4 fluxes for each emission pathway in a subsaline reed wetland . . . 102
  4.4.2 Seasonal methanogenic characterization with $\delta^{13}C$ source signatures of a subsaline reed wetland . . . 103
  4.4.3 Sediment properties of a subsaline reed wetland . . . 104
  4.4.4 Change of the sediment microbial community in a subsaline reed ecosystem within one year . . . 105
4.5 Conclusions . . . 107
Data availability . . . 107

5 Study IV:
Spatial analysis of intra-annual reed ecosystem dynamics at Lake Neusiedl using RGB drone imagery and deep learning 109
Graphical Abstract . . . 109
Abstract . . . 110
5.1 Introduction . . . 110
5.2 Materials and methods . . . 112
  5.2.1 Study area . . . 112
  5.2.2 Data preparation . . . 113
  5.2.3 Semantic segmentation . . . 115
  5.2.4 Phenological analysis . . . 119
5.3 Results . . . 121
  5.3.1 Performance metrics . . . 121
  5.3.2 Land cover classification . . . 121
  5.3.3 Vegetation index . . . 122

5.4 Discussion . . . 124
5.4.1 Model prediction . . . 126
5.4.2 Spatio-temporal variability . . . 127
5.4.3 Vegetation phenology . . . 128
5.5 Conclusions . . . 129
Data availability . . . 130

6 General conclusions 131
6.1 Main findings . . . 131
6.2 Outlook and challenges . . . 135

References 137

List of Figures 177

List of Tables 187

List of Abbreviations 197

Acknowledgments 199

Supplementary material 201
S.1 Supplementary material to Study I . . . 201
S.1.1 Bubble fluxes . . . 201
S.1.2 Isotope ratios and fractionation factors . . . 202
S.1.3 Temperature dependency of ebullition rates . . . 204
S.1.4 Correlation analysis of all locations together . . . 205
S.1.5 Correlation analysis per location . . . 206
S.1.6 Surface water analysis . . . 209
S.1.7 Statistics of CH_4 ebullition and diffusion rates at Lake Neusiedl . . 214
S.2 Supplementary material to Study II . . . 215
S.2.1 U* threshold estimation . . . 215
S.2.2 Coordinates of the reed biomass harvesting . . . 216
S.2.3 Energy balance closure of the reed belt of Lake Neusiedl . . . 216
S.2.4 Diurnal variations of carbon and energy fluxes of the reed belt of Lake Neusiedl . . . 218
S.2.5 Seasonal and annual variability of the carbon fluxes of the reed belt of Lake Neusiedl . . . 220
S.2.6 Inter-annual variability of the growing season length . . . 220
S.2.7 Change of reed, water and open sediment areas in the reed belt of Lake Neusiedl . . . 221
S.2.8 Water level differences depending on wind speeds . . . 222
S.2.9 Drivers of carbon fluxes . . . 223
S.2.10 Temporal variability of environmental parameters and fluxes . . . 224

S.3 Supplementary material to Study III 230
  S.3.1 Diel and seasonal differences in biometeorological and water parameters of the reed belt of Lake Neusiedl 230
  S.3.2 Seasonal and layer specific differences in sediment properties of the reed belt of Lake Neusiedl 232
  S.3.3 Inter-annual differences in properties and microbial characteristics of sediments of the reed belt of Lake Neusiedl 233
S.4 Supplementary material to Study IV 234
  S.4.1 GCC maps and histograms 234
  S.4.2 Deep learning parameters and performance metrics of the CNN models 237

1 General introduction

1.1 Wetlands in a global perspective

Wetlands are diverse and valuable ecosystems that provide numerous ecosystem services and goods. These include flood and coastal protection, habitat for animals, plants, and microorganisms (biodiversity), improved water quality (purification), provision of food (e.g., fish) and raw material (e.g., fodder), stabilization of watershed, cultural identity, storage of carbon and water, and much more (de Groot et al., 2018, Millennium Ecosystem Assessment, 2005, Mitsch et al., 2015). The significance of wetlands for both human welfare and ecological integrity underscores the imperative for their conservation, rehabilitation, sustainable use, and careful maintenance (Ramsar, 1971). However, it also underscores the necessity for further research in wetlands to enhance our understanding of the processes, their ecological functions, and their value.

There is no universally accepted definition of wetlands due to the diverse purposes and interests of wetland users (Mitsch and Gosselink, 2015). However, there are factors that distinguish wetlands from other ecosystems, according to Mitsch and Gosselink (2015): Wetlands are in contact with water for at least part of the year, are often in transition between aquatic and terrestrial ecosystems, often have specialized wetland species of plants, animals, or microbes, can vary greatly in area size within seasons and years, occur in all climate zones and on all continents, and vary greatly in condition due to anthropogenic influences. Ecologist Keddy (2024) defines a wetland as an "ecosystem that arises when inundation by water produces soils dominated by anaerobic processes, which, in turn, forces the biota, particularly rooted plants, to adapt to flooding". However, the Convention of Wetlands (Ramsar, 1971), defines wetlands much more broadly as "areas of marsh, fen, peatland or water, whether natural or artificial, permanent or temporary, with water that is static or flowing, fresh, brackish or salt, including areas of marine water the depth of which at low tide does not exceed six metres" and "riparian and coastal zones adjacent to the wetlands, and islands or bodies of marine water deeper than six metres at low tide lying within the wetlands".

Wetlands are often categorized according to their location as inland, marine, or coastal wetlands, and according to their origin as natural or human-made (artificial) wetlands. According to Davidson et al. (2018a), the majority of wetlands are inland wetlands (92.8%). Wetland ecosystems can also be categorized into five major complex systems, all under the influence of similar hydrological, geomorphic, chemical, or biological factors (Cowardin et al., 1979): marine (exposed to the open ocean), estuarine (mix of fresh and salt water), riverine (running water), lacustrine (associated with lake or pond), and palustrine (non-tidal, vegetated, low salinity). In addition, wetlands are often categorized by climate zone (tropical, temperate, boreal, arctic), by water status (regularly or seasonally flooded, seasonally saturated), or by whether or not they are forested (as in Lehner et al. (2025) in Figure 1.2).

Keddy (2024) classifies wetlands into six types:

1. swamp: dominated by trees rooted in waterlogged soils (not peat), e.g., floodplain or mangrove swamps

2. marsh: dominated by emergent herbaceous plants (e.g., sedges or reeds) rooted in waterlogged soils (not peat), e.g., salt or riverine marshes

3. bog: dominated by peat moss, sedges, dwarf shrubs, or evergreen trees rooted in deep peat with a pH < 5, e.g., blanket or raised bogs

4. fen: dominated by sedges and grasses rooted in shallow peat, often with groundwater flow and a pH > 6, e.g., calcareous fens

5. wet meadow: dominated by herbaceous plants rooted in soils that are occasionally flooded (natural water level fluctuations), e.g., along rivers or lakes

6. aquatic: dominated by aquatic plants growing in or covered by at least 25 cm of water, e.g., water lily pond

Globally, wetlands cover an area of 6.8–18.2 $\times$ 10^6 km^2 (Davidson et al., 2018a, Fluet-Chouinard et al., 2015, Lehner et al., 2025, Mitsch and Gosselink, 2015), with a long-term (1993–2004) maximum inundation extent of 17.3 $\times$ 10^6 km^2 (Fluet-Chouinard et al., 2015). This means that wetlands cover about 5–14% of the earth's land surface, depending on the study approach (e.g., top-down or bottom-up), spatial and temporal resolution, and the wetland definition. Figure 1.1 shows the global coverage of wetlands (including lakes) per grid cell, as estimated by Lehner et al. (2025). The predominant wetland class per grid cell of the global wetland cover is displayed in Figure 1.2. However, in the time period between 1700 and 2020, approximately 16–23% of inland wetlands were lost worldwide, mainly through drainage or conversion for human use (Fluet-Chouinard et al., 2023). According to Fluet-Chouinard et al. (2023), the largest land use conversion was to cropland, followed by conversion to rice paddies, urban areas, forestry, wetland cultivation, pasture land, and peat extraction. This loss has primarily occurred in Europe, the United States, and China, and has intensified since the mid-20th century.

Large lakes worldwide, such as Lake Neusiedl, have lost 53% of their water volume in just 30 years (1992–2020). This decline is mainly attributed to elevated evaporation and greater anthropogenic water usage (Yao et al., 2023). In light of the ongoing climate change, there is a high potential for increased frequency and severity of droughts in wetlands (IPCC, 2023). This phenomenon will consequentially impact the distribution and functionality of these ecosystems (Middleton and Kleinebecker, 2012). Droughts have been identified as a substantial threat to wetland soils, leading to their degradation and subsequent impact on biogeochemistry and greenhouse gas (GHG) emissions (Stirling et al., 2020).

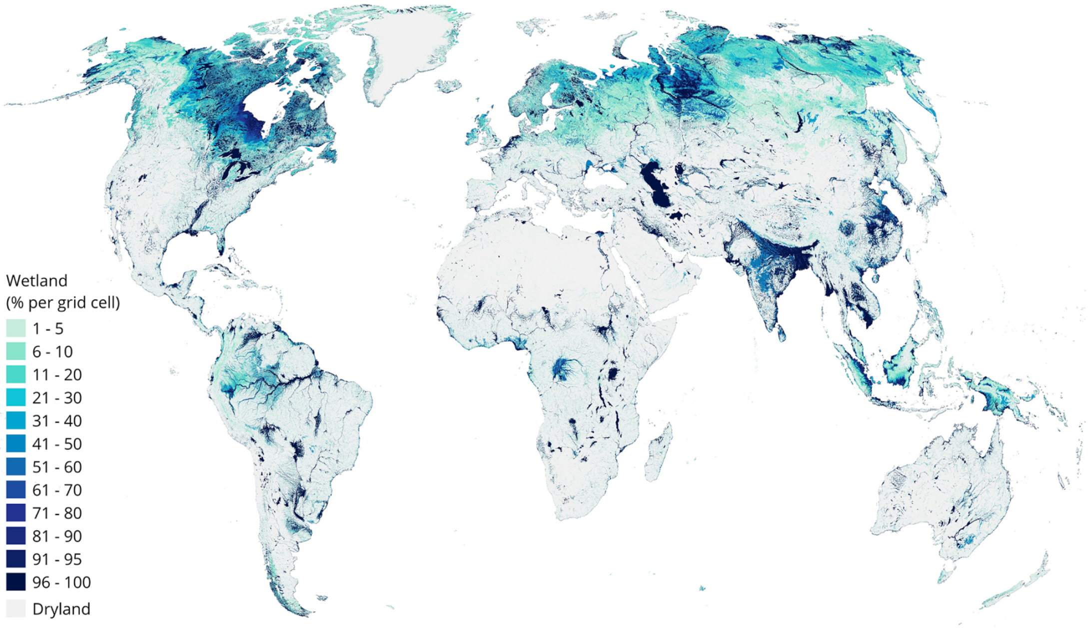

Figure 1.1: The global coverage of wetlands (including lakes) per grid cell (map source: Lehner et al. (2025)).

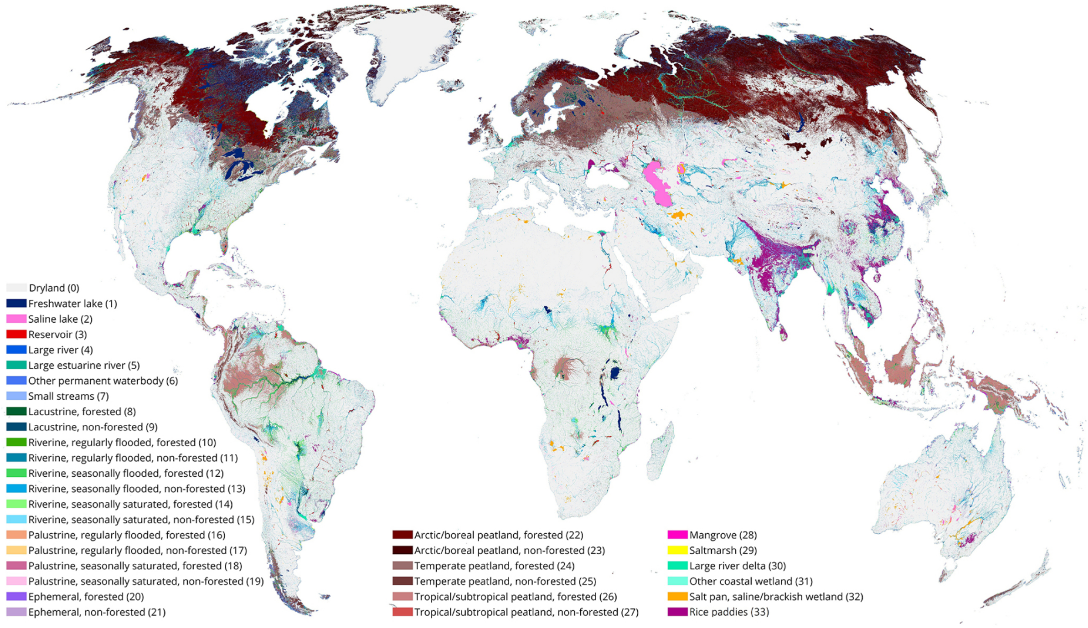

Figure 1.2: The predominant wetland class per grid cell of the global wetland cover (map source: Lehner et al. (2025)).

1.2 Dynamics of wetlands and their GHG fluxes

1.2.1 Land cover dynamics of wetlands

Wetlands can be highly dynamic in land cover and area due to the seasonal or inter-annual variability in precipitation and evapotranspiration, extreme events (e.g., drought, storm, or flood), tides, or anthropogenic factors (e.g., water withdrawals). Therefore, wetland ecosystems are vulnerable to climate change, especially those that are mainly dependent on precipitation (Winter, 2000), but can also be a key to mitigating or adapting to climate change (Hayal et al., 2012).

Globally, 46% of the wetland area are intermittently (seasonally or infrequently) inundated (Davidson et al., 2018a), illustrating the temporal and spatial dynamics of water cover in wetlands, but also making it more challenging to determine their general extent. These water dynamics have a particular influence on the mosaic of different land covers in wetlands, but also on whether an area is classified as wetland. In addition to water area dynamics, wetlands often exhibit vegetation dynamics, such as temporal changes at the community or species level (e.g., phenology) and spatial distribution changes (e.g., spread), both changes can be influenced by water levels or drought (Koebsch et al., 2020).

1.2.2 GHG fluxes and related processes in wetlands

Wetlands play an important role in the global biogeochemical cycle. They can store and release carbon (C) simultaneously, serving as sinks or sources of (atmospheric) C (Wantzen et al., 2022). Since wetlands are often coupled to their surroundings, they can import or export particulate or dissolved C laterally (Wantzen et al., 2022). These lateral hydrological C fluxes often occur through rivers flowing in and out of wetlands (or lakes) or through the influence of tides along coasts. Despite the dynamics of wetlands and the influences from the surrounding environment, wetlands (with reeds and mostly others) are often known as net carbon dioxide (CO_2) sinks (Brix et al., 2001). This is because organic matter accumulates in the soil over time due to reduced decomposition in waterlogged and often anaerobic conditions. Although wetlands cover only about 8–10% of the earth's land surface (Davidson et al., 2018a), they can store about 455–700 Pg C a^{-1}, or about 20–30% of the global C pool (Lal, 2008, Mitsch et al., 2013), depending on the definition and area estimates.

Wetlands remove CO_2 from the atmosphere (or the hydrosphere) through the primary production of autotrophs (e.g., vascular plant or algae). Some C is released directly to the atmosphere as a CO_2 flux due to autotrophic respiration (see Figure 1.3). Another part is accumulated as plant biomass or is incorporated into soil organic matter, where it can be remineralized (decomposed) by heterotrophs (e.g., microorganisms) and finally released to the atmosphere as a CO_2 (or methane) flux. Decomposition increases with higher temperature and oxygen (O_2) levels, whereas it is reduced under anaerobic conditions, e.g., under water or in deeper soil layers. Reduced (anaerobic) decomposition, can lead to C accumulation (as organic matter) in the soil and peat formation. Brouns et al. (2014) showed for peat that aerobic decomposition can be halved after salinization, while anaerobic decomposition remains stable. Primary production relies on plant species, nutrients, temperature, light, water availability, and relative humidity (Wantzen et al., 2022).

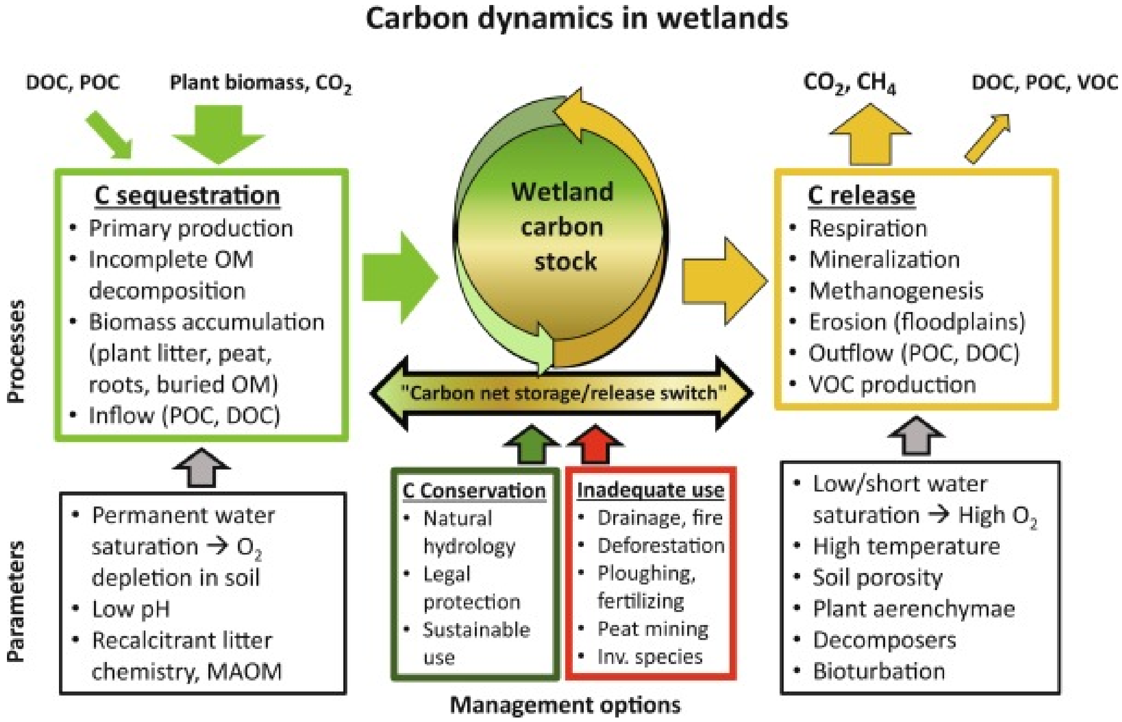

Figure 1.3: The processes, parameters, and management options that favor carbon (C) sequestration or C release in wetlands (figure source: Wantzen et al. (2022)).

Wetlands are the largest natural methane (CH_4) source with 102–200 Tg CH_4 a^{-1} (2008–2017), which is about 17–34% of the total global CH_4 emissions, and also represent the highest uncertainty in the global CH_4 budget (Saunois et al., 2020). In addition, Zhang et al. (2025) point out that climate change, primarily temperature increase, is driving the increased wetland CH_4 emissions in the last decade (2010–2019), for example, the emissions from wetland at latitudes 30–60° N increased by 1.8–2.4 Tg CH_4 a^{-1} compared to the decade before (2000–2009). CH_4 is a GHG with a 45 times higher sustained-flux global warming potential (SGWP) than CO_2 over a period of 100 years (Neubauer and Megonigal, 2015). Therefore, direct and long-term measurements are necessary to monitor the trends (Zhang et al., 2025). Networks such as FLUXNET (a global network of micrometeorological tower sites that use eddy covariance methods to measure the exchanges of CO_2, water vapor (H_2O), and energy between the biosphere and the atmosphere) and LTER (long-term ecological research) and their contributors and sites are indispensable (Baldocchi et al., 2001, Mirtl et al., 2015).

In wetlands, the CH_4 production (methanogenesis) occurs mainly in anoxic soils or sediments and is carried out by methanogenic archaea (methanogens). Methanogenesis represents the last step in the degradation of organic matter when the thermodynamically more favorable electron acceptors (oxygen, nitrate, manganese(III, IV) oxides, iron(II) oxides, sulfate) have already been depleted (Conrad, 1996). The process of methanogenesis is contingent on the type and amount of substrate, the oxidation–reduction potential (ORP), and the temperature (Conrad, 2023). For example, methanogenesis occur usually at an ORP < -200 mV (Mitsch and Gosselink, 2015). In addition, other variables such as salinity (and thus sulfate, especially in seawater) may be relevant, as the presence of sulfate-reducing prokaryotes may outcompete methanogens (Conrad, 1996, Lovley and Klug, 1983, Poffenbarger et al., 2011). Depending on the substrate, methanogenesis can be categorized into three different methanogenic pathways, which can be ranked according to their relative importance (Conrad, 2020a): acetoclastic (acetate, Equation 1.1), hydrogenotrophic (H_2/CO_2, Equation 1.2), and methylotrophic (methylated compounds like methanol, Equation 1.3). The latter substrate is not produced in the same quantities as the others, but methylotrophic methanogens are still widespread (Conrad, 2020a). Notably, methylotrophic methanogenesis is important in saline environments, where methylated compounds serve as non-competitive substrates, while acetate and hydrogen (H_2) are degraded by non-methanogenic processes such as sulfate reduction (Conrad, 2020a). Some methanogens, e.g., *Methanosarcinales*, use only one methanogenic pathway, the acetoclastic methanogenesis (Stams et al., 2019), while others, such as *Methanomicrobiales*, are not as specific (Garcia et al., 2006).

$$CH_3COOH \rightarrow CH_4 + CO_2 \tag{1.1}$$

$$4H_2 + CO_2 \rightarrow CH_4 + 2H_2O \tag{1.2}$$

$$4CH_3OH \rightarrow CO_2 + CH_4 + 2H_2O \tag{1.3}$$

In wetlands, the CH_4 oxidation (methanotrophy) typically occurs at the anoxic–oxic interface, such as the soil/sediment surface or water column, and is carried out by aerobic methanotrophic bacteria (methanotrophs) (Equation 1.4). However, there are also some anaerobic environments, such as in marine sediments of gas hydrates, where CH_4 can be oxidized anaerobically and are done together by methanotrophic archaea and sulfate-reducing bacteria (Valentine and Reeburgh, 2000). In addition, vascular wetland plants like *Phragmites*, *Typha*, or *Eleocharis* sp. can transport O_2 through aerenchyma to their roots and oxidize CH_4 in the rhizosphere Armstrong and Armstrong (1988), Armstrong et al. (1996), Brix et al. (1992). Consequently, the CH_4 exchange between the wetland ecosystem and the atmosphere is the net outcome of the simultaneously occurring production and consumption processes in the ecosystem (Conrad, 1996).

$$CH_4 + 2O_2 \rightarrow CO_2 + 2H_2O \tag{1.4}$$

In sulfate-rich wetlands, mainly marine but also brackish ecosystems, sulfate-reducing prokaryotes, which include mainly bacteria but also archaea, reduce sulfate ($SO_4{}^{2-}$) with

H_2 to hydrogen sulfide (H_2S) (Equation 1.5). This process is dependent on the availability of H_2 (Muyzer and Stams, 2008) and usually occurs as an electron acceptor reduction step prior to CH_4 production (ORP usually between −100 and −200 mV, Mitsch and Gosselink (2015)) due to the more favorable thermodynamics. However, there is a methane–sulfate transition zone where both processes can occur simultaneously (Kleint et al., 2021).

$$SO_4^{2-} + 4H_2 + 2H^+ \rightarrow H_2S + 4H_2O \tag{1.5}$$

Another GHG of concern is nitrous oxide (N_2O), which has a SGWP 270 times greater than CO_2 over a 100 year time frame (Neubauer and Megonigal, 2015). N_2O may play a role, especially in nutrient- and oxygen-rich wetlands. However, N_2O fluxes from wetland (waterlogged) soils are low in comparison to aerated soils, most likely because much of the produced N_2O is further reduced to nitrogen (N_2) by denitrifiers (Conrad, 1996). The primary focus of this thesis, however, is on carbon fluxes.

1.2.3 Emission pathways of GHG fluxes

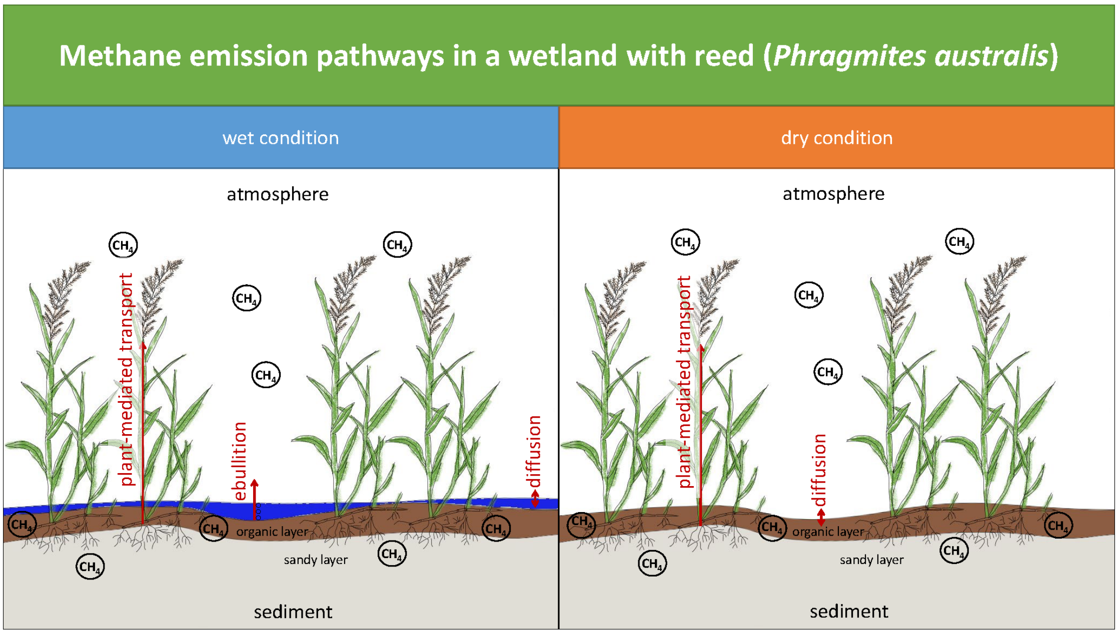

Figure 1.4: The methane emission pathways of a wetland with reed (*Phragmites australis*) under wet and dry conditions (dry means no water level above the surface).

Wetlands have several emission pathways or interfaces for the GHG fluxes. The following description outlines the emission pathways mainly for CH_4, although it should be noted that these pathways often are also valid for other GHGs such as CO_2. In Figure 1.4, the CH_4 emission pathways for a wetland with reed (*Phragmites australis*) is illustrated for two conditions, wet and dry, but of course there are also conditions in between.

First, there is the molecular diffusion pathway of GHGs at the water–air and soil–air interfaces of wetlands, which is driven by the GHG concentration gradient between the atmosphere and the other media (water or soil) (Butterbach-Bahl et al., 2011). Due to the dynamics of wetlands, the area of these interfaces can vary greatly within a year or between years.

Second, there is the plant-mediated transport pathway of GHGs in wetland plants, which transports O_2 from the atmosphere (via leaves) to the rhizosphere (via roots) and in turn releases soil gases into the atmosphere (Sebacher et al., 1985). However, the mechanism of the plant-mediated transport differs between the plant species. For instance, the gas transport in *Juncus effusus* is exclusively driven by diffusion, whose functionality is determined by the anatomical structure of the root system (Vroom et al., 2022) and is most strongly restricted by the area of the permeable root surface (Henneberg et al., 2012). Other wetland plants, such as *Phragmites australis* or *Typha latifolia*, exhibit a pressurized gas flow. This mechanism can be humidity-induced convection and/or thermal transpiration (Vroom et al., 2022). Pressurized flow is a gas transport mechanism that is over 5-fold more efficient than diffusion (Brix et al., 2001) due to its high flow rates and better aeration (Vroom et al., 2022). In particular, *Phragmites australis* is characterized by the absence of any meristematic tissue that closes the pith cavity, resulting in low resistance in rhizome and stem (Brix et al., 1992). This reduced resistance to gas flow, coupled with the optimal pore (stomata) size of 0.2 μm, enables *P. australis* to attain a remarkably elevated flow rate compared to other wetland plants (Armstrong et al., 1996), which gives the plant the capacity to thrive in water areas with higher water levels (Brix et al., 1992). However, this does not automatically imply that CH_4 fluxes are generally higher for pressurized flow species, as ecosystem characteristics such as lake characteristics, dry/wet conditions, and soil types may play a more important role in flux rates than the gas transport mechanism itself (Bergström et al., 2007, Kankaala et al., 2005, 2004, Vroom et al., 2022). In wetland trees such as *Salix fluviatilis* or *Betula pubescens*, the long distance CH_4 gas transport is driven by transpiration, where the roots take up the CH_4 from the pore water of the soil, transport it upwards through the sap flow in the tree, and release it via the leaf surface and stem (Pangala et al., 2015). Other wetland trees exhibit a combination of gas transport mechanism such as *Alnus* sp., which are driven by diffusion and transpiration (Vroom et al., 2022).

Third, ebullition is another emission pathway in wetlands, in which highly concentrated CH_4 bubbles are suddenly and rapidly released from oversaturated soil through the water column into the atmosphere. This pathway is very difficult to measure due to its sporadic nature, its high temporal-spatial variability (Saunois et al., 2020) and is therefore often neglected or rarely measured (Wik et al., 2016, Zheng et al., 2022b).

According to Chanton (2005), the relative importance of these three emission pathways is highly variable depending on seasonal temperature variations, the organic matter content, and the wetland plant type and density. Other ecosystem characteristics also play a role. For example, limnobathymetry and lake morphology are important factors in lakes (Li et al., 2020).

1.2.4 Flux measurement techniques

Several flux measurement approaches exist for estimating the exchange of GHGs between wetlands and the atmosphere. These approaches vary widely in terms of their temporal or spatial resolution, scale, purpose, and the personal, financial, and logistical effort required. The following two approaches — chamber measurement and the eddy covariance technique — are introduced because they are applied in this thesis.

One approach is the chamber measurement, which is using mainly static (non-steady-state) chambers for measuring the GHG fluxes on small-scale (plots, usually less than 1 m^2, Hutchinson and Livingston (1993)). The principle of the chamber measurements is the (non)linear temporal change (increase or decrease) of gas concentration (dry mole fraction) in the chamber headspace during closure (Butterbach-Bahl et al., 2011). With that the slope of the (non)linear regression is calculated. Together with the known (headspace) air temperature, molar mass of the gas, atmospheric pressure, the chamber volume, and the chamber area, the vertical net flux rate of the gas can be calculated using the Equation 1.6 adapted from Rochette et al. (1997).

$$F_{chamber} = \frac{chamber\ volume \cdot molar\ mass \cdot slope \cdot atmospheric\ pressure}{chamber\ area \cdot ideal\ gas\ constant \cdot headspace\ temperature} \tag{1.6}$$

For the validation of the linear regression the coefficient of determination (R^2) can be used (Butterbach-Bahl et al., 2011). If concentration changes over timer differ from assumed linearity, nonlinear regressions are advised (Kroon et al., 2008). This chamber approach is commonly employed to study spatial heterogeneity of ecosystems, experimental modified (treatment) and control plots, individual part of ecosystems (from leaf to plants, from soil to water surfaces), or individual process (e.g., respiration with opaque chambers) (Butterbach-Bahl et al., 2011). There are different types of chambers, such as vegetation, floating, and soil/sediment chambers, which are used to measure GHG fluxes. There are also bubble traps, which collect bubbles from ebullition. All of these are used in this thesis and are shown in Figure 1.5. In addition to chamber types, there are different chamber techniques, such as closed or dynamic (flow-through) (Butterbach-Bahl et al., 2011). The dynamic technique is applied in the studies in this thesis. The great advantages of chambers are their low cost and easy handling (Hutchinson and Livingston, 1993), and, in contrast to other flux measurements (like eddy covariance), the source (area) of the measured flux is exactly know. Despite the long history of chamber flux measurements, there is no widely accepted, standardized methodology for these measurements. However, there are strategies how to minimize sources of errors (Hutchinson and Livingston, 1993) due to the chamber design (Hutchinson and Livingston, 2001), the sampling procedure, and the data analysis (Butterbach-Bahl et al., 2011, Hoffmann et al., 2017, Maier et al., 2022, Rochette and Eriksen-Hamel, 2008).

Another approach is the eddy covariance (EC) technique, a micrometeorological method that is commonly used to continuously quantify the net vertical (turbulent) exchange of energy, water, and other GHGs between the land surface (ecosystem) and the atmosphere at the landscape scale (typically 100–1000 m^2, Hutchinson and Livingston (1993)).

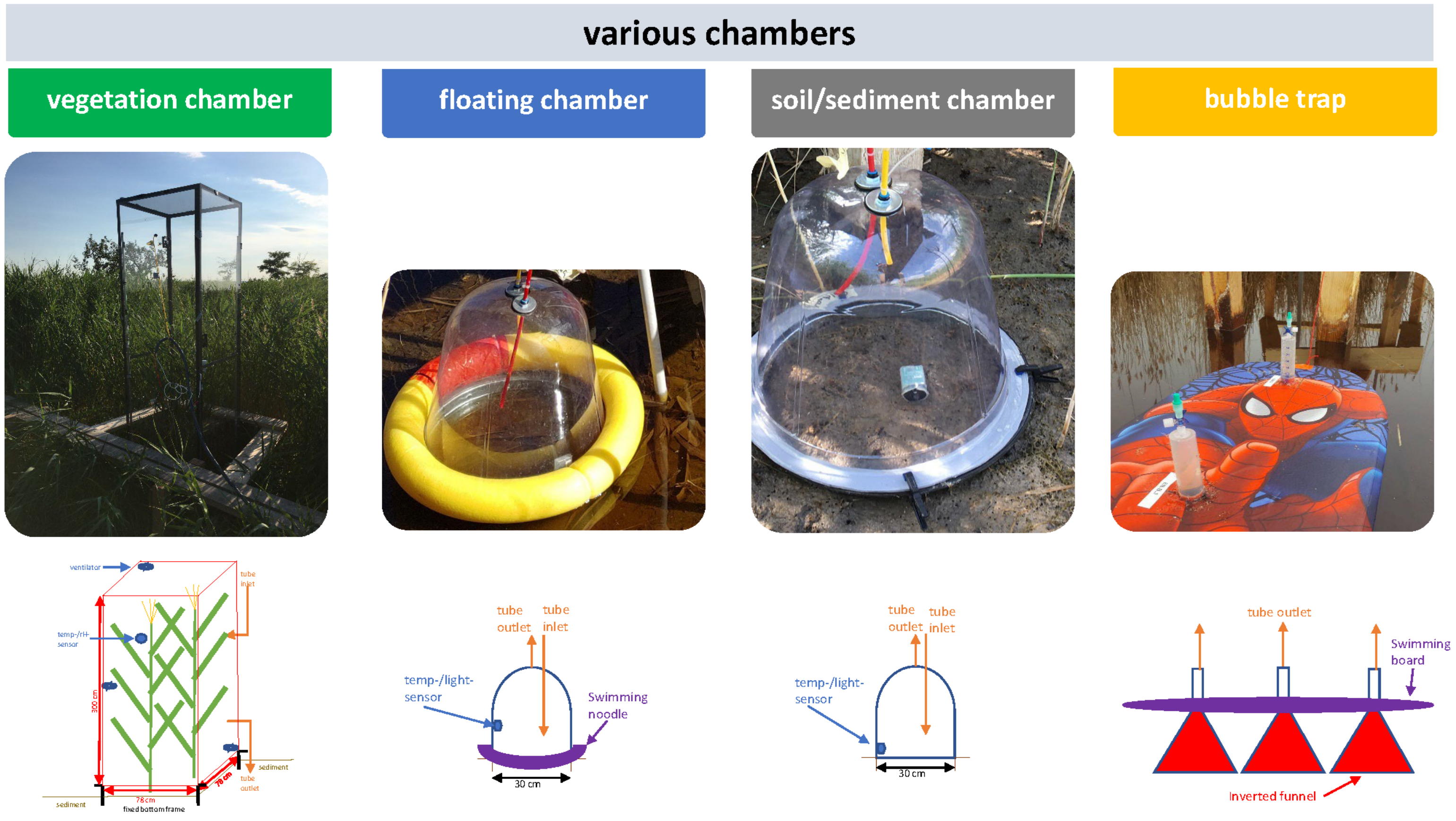

Figure 1.5: Various types of chambers such as vegetation, floating, or soil/sediment chambers for measuring greenhouse gas fluxes, but also bubble traps for collecting bubbles (from ebullition), all of which are used in this thesis.

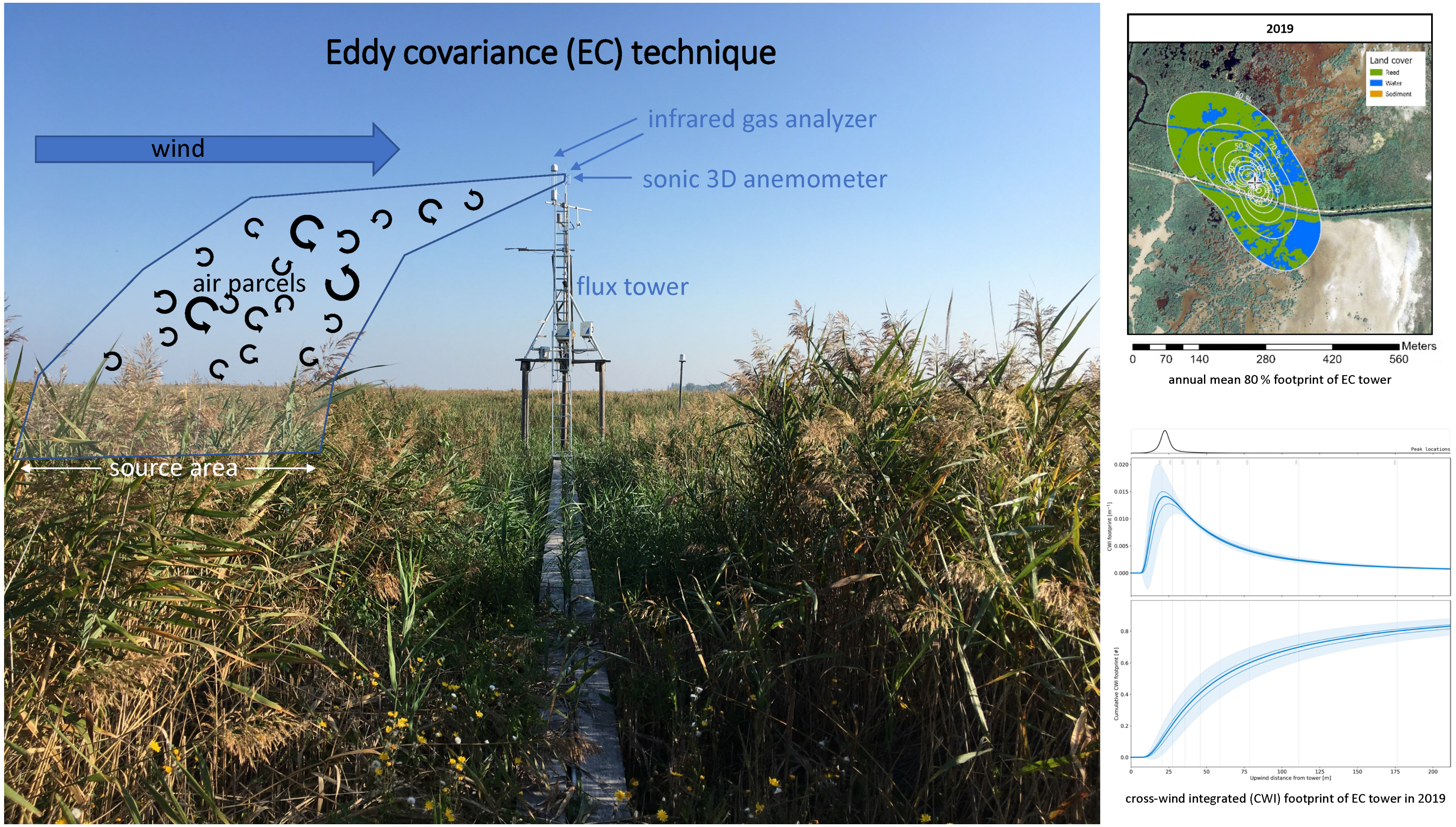

Figure 1.6: The principle of the eddy covariance (EC) technique including the flux tower and source area (drawing partly based on Schmid and Oke (1990)), the annual mean 80% footprint, and the cross-wind integrated (CWI) footprint (according to Kljun et al. (2015)), shown here for the EC tower at the reed belt of Lake Neusiedl.

The energy and GHGs are transported by upward and downward moving air parcels in turbulent motions (eddies) in the atmosphere (see drawing of the principle of the EC technique in Figure 1.6, partly based on Schmid and Oke (1990)). At one sampling point above the canopy at the EC tower, the fluctuations of the density/concentration of the gas and the vertical wind speed are measured simultaneously with high temporal resolution (10–20 Hz) (Butterbach-Bahl et al., 2011). There are important (micrometeorological) assumptions for the EC technique, such as the one point measurement represents an upwind area, the flux is fully turbulent, the measurements are within the boundary layer of interest, the terrain is flat and homogeneous, and the flux footprint is only within the area of interest (Aubinet et al., 2012, Lee et al., 2004). In simple terms (after a number of mathematical operations and assumptions, including Reynolds decomposition), the eddy (turbulent) flux can be expressed as the covariance of the instantaneous deviation of the dry mole fraction of the gas (c) from its mean value and the instantaneous deviation of the vertical wind speed (w) from its mean value, multiplied by the mean air density (ρ_a), usually averaged over 30 min, see Equation 1.7 (Baldocchi, 2003).

$$F_{eddy} = \overline{\rho_a} \cdot \overline{w'c'} \tag{1.7}$$

The flux footprint enlarges as the measurement height at the EC tower increases, as atmospheric conditions switch from unstable to stable, and as the roughness of the land surface diminishes (Burba, 2013). The annual mean 80% footprint and the cross-wind integrated (CWI) flux footprint (according to Kljun et al. (2015)) is shown here for the EC tower at the reed belt of Lake Neusiedl in Figure 1.6.

For the quality of the EC flux measurements and for the fulfillment of the micrometeorological assumptions many corrections, conversions and compensations are applied in the post-field data processing (Foken et al., 2004). For details about the applied corrections in the EC data processing see Subchapter 3.2.3. A quality criterion of the EC fluxes is the closure of the energy balance, as it is excepted that the total available energy (net radiation ($\mathrm{R_n}$) minus ground heat flux (G)) is equal to the turbulent heat fluxes (sensible heat flux (H) plus latent heat flux (LE)), see Equation S.13. However, in most studies, there is an imbalance with an underestimation of the turbulent fluxes, showing a energy balance closure of approximately 80% (Foken et al., 2012). This imbalance is a well-known source of uncertainty of the EC measurements and a not fully solved problem yet (Mauder et al., 2020).

$$R_n + G = H + LE \tag{1.8}$$

The greatest advantages of the EC method are that is one of the most direct flux methods and that it is measuring without disturbing the underlying landscape (e.g., vegetation or soil) (Burba, 2013). However, the instrumentation is much more expensive than that of the chambers. In micrometeorology, a positive flux indicates a net gas transport from the land surface (ecosystem) to the atmosphere, and a negative flux indicates a net gas transport from the atmosphere to the ecosystem (Baldocchi, 2003). This sign convention is also used in this entire thesis.

1.3 Wetlands with reed

1.3.1 Wetland plant: *Phragmites australis*

The common reed *Phragmites australis* (Cav.) Trin. ex Steud. is a wetland plant with a global distribution from boreal to tropical regions. It has a wide ecological amplitude and occurs in coastal salt marshes, fens (groundwater-fed, nutrient-rich peatlands), and along inland water bodies such as lakes, ponds, or rivers. In addition, this vascular plant is also often used in constructed wetlands to improve water quality (Moshiri, 1993). *P. australis* grows on all five continents and at almost all altitudes from sea level to Tibet, but is most abundant and most diverse in Europe (Haslam, 2010). This dominance in Europe is clearly seen in the distribution map of *P. australis* in Figure 1.7. *P. australis* is a single plant species, but contains three phylogeographic groups (North American, European, and East Asian/Australian) with multiple separate lineages within the groups (Eller et al., 2017). While *P. australis* is known to be invasive in coastal marshes of North America, it belongs to two introduced lineages from Europe and has an increased invasive potential with higher temperatures and coastal saltwater intrusion in the future (Eller et al., 2014). In the following, 'reed' always refers to the plant species *P. australis*.

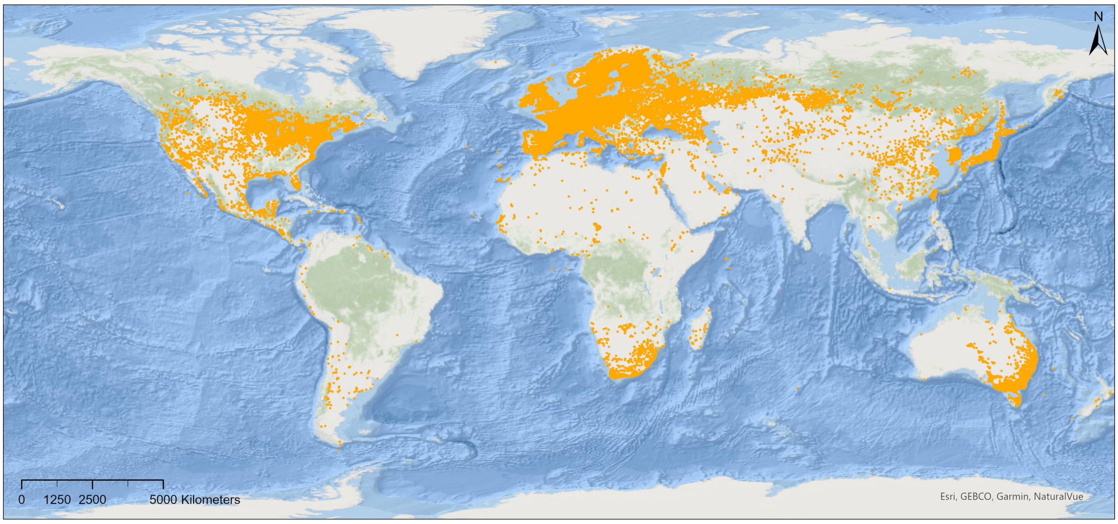

Figure 1.7: The global distribution map of *Phragmites australis* (Cav.) Trin. ex Steud. (data source: GBIF.org (2025)).

Reed has been used by humans since prehistoric times (Köbbing et al., 2013): In most regions and for most uses, the aboveground reed biomass is harvested in winter for nature conservation, cost, or harvesting equipment reasons. Reed biomass is used for energy (combustion, biogas, biofuel), agriculture (fodder and litter, fertilizer/compost, water treatment), and industrial materials (roofing, walls, panels, insulation, paper, etc.).

Another benefit of reed is that it stabilizes the shoreline of lakes, rivers, reservoirs, and coastlines (Ostendorp, 1989).

Phragmites australis is a helophyte (swamp plant), belongs to the grass family of *Poaceae*, and often forms dense, almost monodominant reed ecosystems (reed beds or reed belts) (Haslam, 2010). The plant has further characteristics:

- salt-tolerant: natural salinity ranges from 0 to 28 ppt (Eller et al., 2017)
- a tall grass with up to 8 m (or 10 m) high with large inflorescence (Haslam, 2010)
- seed and vegetative (rhizome) reproduction
- can grow in deep, shallow, and nearly stagnant water (Afreen et al., 2007)
- metal and nutrient removal from aquatic environment (phytoremediation) (Rezania et al., 2019)
- unresolved photosynthetic pathway: potential for variation within *P. australis* (Eller et al., 2017)
  - features of C_3 plants: elevated ratio of Rubisco to PEP carboxylase ratio, elevated rates of photorespiration, elevated CO_2 compensation point (Antonielli et al., 2002, Eller and Brix, 2012, Eller et al., 2017, Hansen et al., 2007)
  - C_4-like strategies (Eller et al., 2017)
- in optimal condition, very productive plant with an aboveground biomass of up to 3 kg m^{-2} a^{-1} (Köbbing et al., 2013)
- very effective plant-mediated transport of oxygen, CO_2, and CH_4 between the soil and the atmosphere with a pressurized gas-flow mechanism (Armstrong and Armstrong, 1990, Brix et al., 1996)
- capacity to form peat under water (Haslam, 2010).

Reed plays an important role in food webs, as it is the dietary foundation for numerous primary producers, secondary decomposer, and parasites, but is also important for mammals, fish, and birds (Ostendorp, 1989). Different species of birds and their different purposes for nesting, breeding, sheltering, living, and feeding depend on reeds. Bird species prefer different reed conditions, reed ages, and habitat structures (Nemeth and Dvorak, 2022): For instance, the great reed warbler (*Acrocephalus arundinaceus*) favors young and productive reed areas on the edge to mainly deep water (Leisler, 1981). Meanwhile, the moustached warbler (*Acrocephalus melanopogon*) favors older and less productive reed areas containing more open water areas (Leisler and Schulze-Hagen, 2011).

1.3.2 Lake Neusiedl — a subsaline wetland with reed

The study area of this thesis is an internationally significant wetland characterized by reed and an inland water body with distinctive water properties: Lake Neusiedl (in German: Neusiedler See; in Hungarian: Fertő tó). This large, shallow lake is situated on the Hungarian-Austrian border (see Figure 1.8) with a maximum water level of 1.8 m (Wolfram and Herzig, 2013) and a total lake area of around 312 km^2 in 2007/2008 (Csaplovics, 2019). Notably, the lake lacks a natural outlet, but it does have an artificial one (in German: Einserkanal; in Hungarian: Hanság-főcsatorna) that has been closed since spring 2015 (HD Bgld, 2023d) due to persistent low water levels. For this reason, the lake is often referred to as endorheic and the westernmost steppe lake in Europe (Löffler, 1974, Sauerzopf, 1959). Over half of the lake is covered by a reed belt (181 km^2, 2007/2008, Csaplovics (2019)), which is dominated by the plant species *Phragmites australis* and is the largest connected reed ecosystem in Europe after the Danube Delta.

The lake and its reed ecosystem hold international significance, as evidenced by various trans-border protected areas such as the Ramsar site, the UNESCO World Heritage Site, the Neusiedler See – Seewinkel / Fertő – Hanság National Park, and the Natura 2000 sites, including the special area of conservation (SAC) and the special protection area for birds (SPA). These areas are all shown in Figure 1.8. Beside the unique landscape and natural importance, most of these areas have been designated for the conservation of birds, given their reliance on the reed ecosystem for breeding, roosting, shelter, and food (Nemeth and Dvorak, 2022). Some bird species inhabit the reed ecosystem (or the nearby) permanently, others visit this ecosystem occasionally, and a third group are migratory birds. Numerous species of reed birds have large populations in the reed belt of Lake Neusiedl, for example the eurasian reed warbler (*Acrocephalus scirpaceus*), the water rail (*Rallus aquaticus*), or the reed bunting (*Emberiza schoeniclus*) (Dvorak et al., 2024).

The lake water's characteristics are summarized in Table 1.1. The lake has distinctive water properties, such as subsalinity (Hammer, 1986) with the primary salt component being sodium bicarbonate ($NaHCO_3$) (Wolfram and Herzig, 2013), an electrical conductivity of 2.4 ± 0.2 mS cm^{-1}, an alkalinity of 11.8 ± 0.7 mMol L^{-1}, a pH of 8.9 ± 0.1, and a sulfate concentration of 130 ± 13 mg SO_4-S L^{-1}. All these mean values ± SD (standard deviation) were measured in the open lake area near Illmitz in 2017–2019 by Zoboli et al. (2023).

The study site of this thesis is located in the eastern reed belt of Lake Neusiedl near the Biological Station Illmitz in Austria and in the core (nature) zone of the national park (see Figure 1.8).

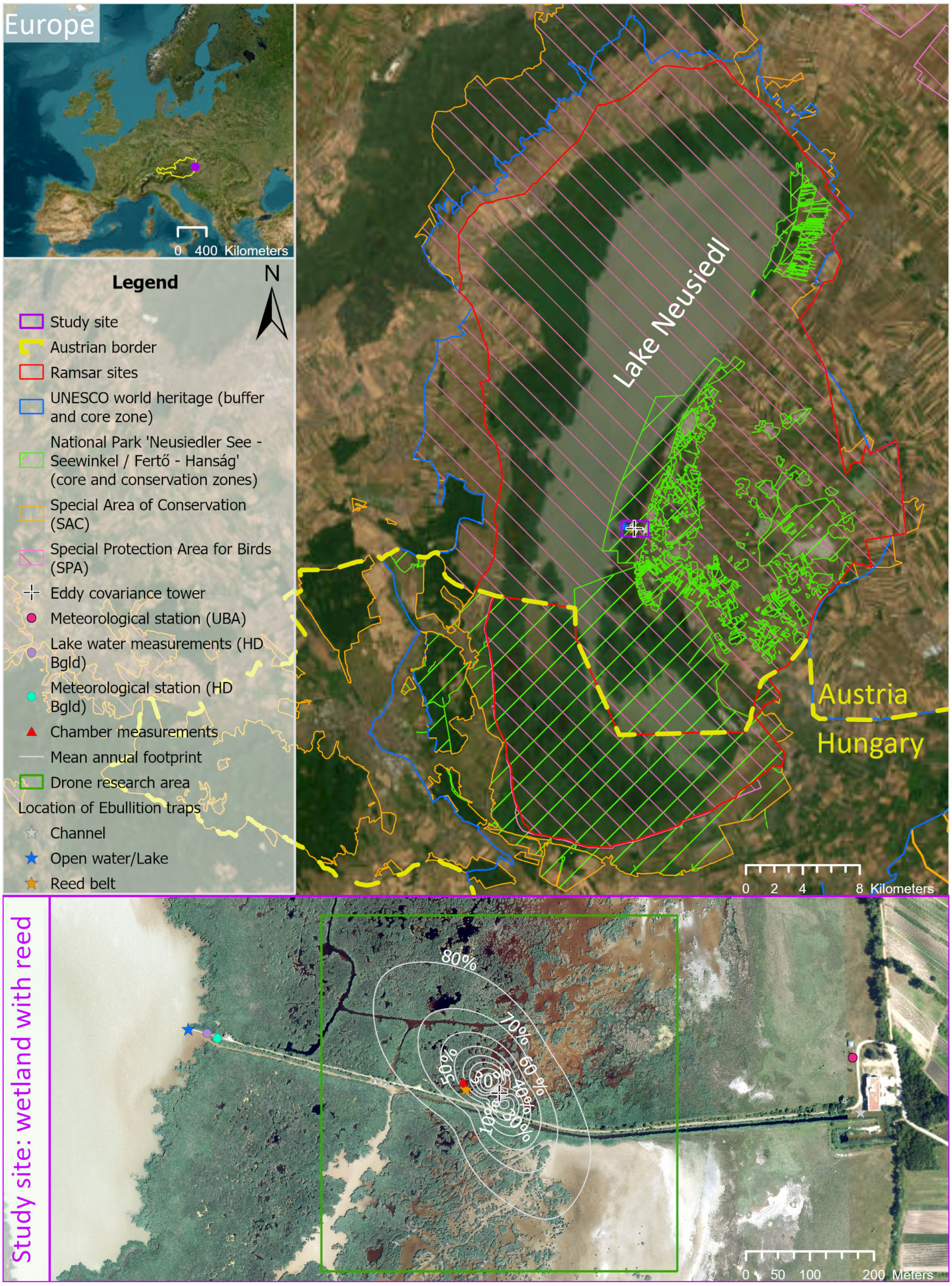

Figure 1.8: Lake Neusiedl and its reed belt are located on the Austrian-Hungarian border and demonstrate their international importance through various cross-border protected areas such as Ramsar, UNESCO Wold Heritage Site, national park, SAC, and SPA (data sources: ESRI World Imagery sources Land Burgenland, Land NÖ, Maxar, Microsoft, Earthstar Geographics; orthophoto from BEV (2019); boundaries of Austrian protected areas from Land Burgenland (2017, 2022a,b,c), Nationalparks Austria (2017); boundaries of Hungarian protected areas based on the database of the Fertő-Hanság National Park Directorate).

The lake and its reed belt are part of the network for long-term ecological research (LTER). The LTER site has a mean annual precipitation of 500.2 mm and an annual mean air temperature of 11.3°C (1993–2022, Baur et al. (2024b)). The region of Lake Neusiedl is assigned to the (continental) Pannonian climate and has no major relief differences (Löffler, 1979), with altitudes of about 115–125 m above sea level. The lake has only one major tributary (Wulka) and some minor tributaries (e.g., Golser Kanal, Rákos patak (in German: Kroisbach), Parndorfer Bach), but the majority of the lake's water input comes from precipitation (76–79%, (Kubu et al., 2014, Soja et al., 2013)). However, prior to spring 2015 (closure of the weir), on average about 10–11% of the lake's water output (water balance periods: 1961–2010 and 1965–2012) was discharged via the artificial outlet, while 89–90% was lost through evapotranspiration (Kubu et al., 2014, Soja et al., 2013). Due to its hydrological characteristics, the lake is very vulnerable to precipitation changes and climate change (Soja et al., 2013).

Lake Neusiedl has an interesting historical background. The lake was most likely formed by a tectonic depression outside the formerly glaciated area, however the age of the lake is still unclear, but estimated between 12 000 and 14 000 years (Draganits et al., 2022, Löffler, 1979). It is believed that the lake has undergone several periods of drying, with the most recent one occurring between 1865 and 1870 (Sauerzopf, 1959). The contemporary hydrological character of the lake differs significantly from its historical state, which is described as follows in the study of Draganits et al. (2022): Historically, the lake encompassed three additional tributaries, particularly in the southern region, and it possessed a natural outlet in the Hanság area (southeastern region). The disparity in water level between periods of drying and the highest flooding was approximately 4.2 m. The recorded modifications from 1568, the following increased drainage, and the construction of a dam road (completed in 1780) that severed the lake from its main tributaries have fundamentally altered its hydrological characteristics, suggesting that it was not endorheic for the majority of the time prior to 1780. Two further anthropogenic alterations have also impacted the hydrological conditions. Firstly, the construction of an artificial outlet in 1909, which diverted water from the lake. Secondly, an agreement between Hungary and Austria in 1965 regulated the artificial outflow with a weir based on a water level threshold of the lake, leading to an increase in the lake's average water level.

In addition, the lake and its surroundings are heavily used by humans, for example for agriculture (viticulture, grain, and vegetable growing), fishery, tourism, recreation, and water sports (sailing, kite, and windsurfing). In the past, reed biomass was harvested over a larger area, but now it is only harvested in part of the western reed belt of the lake during the winter for energy, fodder, roofing, or insulation purposes. The decrease in harvesting and the concentration of harvesting on the landside of the reed belt (Nemeth and Dvorak, 2022) is due to the decrease in ice cover (Soja et al., 2014a), which makes harvesting more difficult or less desirable, and to the general decrease in demand for reed biomass as building material since the 1970s (Nemeth et al., 2022). This decline in harvest also has consequences for the age of the reed stands and thus for the bird population (Nemeth et al., 2014).

Overall, Lake Neusiedl, a reed wetland with unique inland water characteristics (shallow, subsaline, and sulfate-rich), is of European and international importance. This wetland is rarely investigated with respect to its carbon cycle, related processes, and temporal and spatial dynamics, especially in the context of low water levels (e.g., since the closure of the artificial outlet). Therefore, more research is needed.

Table 1.1: The characteristics of the Lake Neusiedl and its reed belt in numbers, mainly measured near Illmitz and its Biological Station (SD = standard deviation; CON = electrical conductivity; DOC = dissolved organic carbon; POC = particulate organic carbon; Pt = total phosphorus; NO_3-N = nitrate-nitrogen; NH_4-N = ammonium-nitrogen; SO_4-S = sulfate-sulfur).

Parameter	**Value**	**Unit**	**Time period**	**Reference**
Lake Neusiedl				
mean water level	1.2	m		Wolfram and Herzig (2013)
maximum water level	1.8	m		Wolfram and Herzig (2013)
maximum lake surface (at a water level of 160 m above the Adriatic)	315	km^2		Wolfram and Herzig (2013)
reed belt area	181	km^2	2007/2008	Csaplovics (2019)
open lake area	131	km^2	2007/2008	Csaplovics (2019)
catchment area	1120	km^2		Wolfram and Herzig (2013)
mean annual precipitation	556	mm	1971–2020	Hackl and Ledolter (2023)
annual mean air temperature	11.1	°C	1971–2020	Hackl and Ledolter (2023)
main salt composition	sodium bicarbonate ($NaHCO_3$)			Wolfram and Herzig (2013)
salinity category	subsaline (0.5–3 ‰)			Hammer (1986)
water of the open lake area				
mean ± SD of CON	2.4 ± 0.2	mS cm^{-1}	2017–2019	Zoboli et al. (2023)
mean ± SD of pH	8.9 ± 0.1		2017–2019	Zoboli et al. (2023)
mean ± SD of alkalinity	11.8 ± 0.7	mMol L^{-1}	2017–2019	Zoboli et al. (2023)
mean ± SD of water temperature	13.7 ± 5.4	°C	2017–2019	Zoboli et al. (2023)
mean ± SD of DOC	16 ± 1	mg L^{-1}	2017–2019	Zoboli et al. (2023)
mean ± SD of POC	4 ± 2	mg L^{-1}	2017–2019	Zoboli et al. (2023)
mean ± SD of Pt	67 ± 34	μg L^{-1}	2017–2019	Zoboli et al. (2023)
mean ± SD of NO_3-N	21 ± 39	μg L^{-1}	2017–2019	Zoboli et al. (2023)
mean ± SD of NH_4-N	17 ± 6	μg L^{-1}	2017–2019	Zoboli et al. (2023)
mean ± SD of SO_4-S	130 ± 13	mg L^{-1}	2017–2019	Zoboli et al. (2023)
water of the reed belt				
mean ± SD of CON	2.8 ± 0.5	mS cm^{-1}	2017–2019	Zoboli et al. (2023)
mean ± SD of pH	8.8 ± 0.2		2017–2019	Zoboli et al. (2023)
mean ± SD of water temperature	14.4 ± 5.3	°C	2017–2019	Zoboli et al. (2023)
mean ± SD of DOC	27 ± 8	mg L^{-1}	2017–2019	Zoboli et al. (2023)
mean ± SD of POC	3 ± 2	mg L^{-1}	2017–2019	Zoboli et al. (2023)
mean ± SD of Pt	53 ± 17	μg L^{-1}	2017–2019	Zoboli et al. (2023)
mean ± SD of NO_3-N	5 ± 13	μg L^{-1}	2017–2019	Zoboli et al. (2023)
mean ± SD of NH_4-N	44 ± 44	μg L^{-1}	2017–2019	Zoboli et al. (2023)
mean ± SD of SO_4-S	143 ± 25	mg L^{-1}	2017–2019	Zoboli et al. (2023)

1.4 Objectives and outline of the thesis

The overall goal of this doctoral thesis is to improve our understanding of the influence of drought on the spatial and temporal dynamics of reed wetlands, in particular on greenhouse gas fluxes, emission pathways, microbial community, and land cover. The following specific objectives are formulated in the four studies (Chapter 2–5):

1. the assessment whether ebullition or diffusion is more important as CH_4 emission pathway in shallow subsaline lakes, using Lake Neusiedl, a site of international importance, as an example (**study I**, Chapter 2)
    - investigating the spatial and temporal heterogeneity of CH_4 ebullition at the shallow and subsaline Lake Neusiedl
    - determining the carbon source for methanogenesis based on isotopic ratios of CH_4 from ebullition
    - exploring the drivers of CH_4 ebullition
    - comparing the ebullition and diffusion pathways in this lake ecosystem
2. the analysis of the influence of intense drought on the CO_2 and CH_4 fluxes of reed ecosystems, conducted at Lake Neusiedl (**study II**, Chapter 3)
    - What are the effects of drought on carbon (C) fluxes in a reed ecosystem over several years?
    - How does the decreasing water level (WL) affect the temporal (diurnal, seasonal, annual) variations of the C fluxes in a reed wetland ecosystem?
    - What are the drivers of the C fluxes in a subsaline reed ecosystem?
3. the evaluation of the temporal dynamics of CH_4 emission pathways in the subsaline reed wetland of Lake Neusiedl (**study III**, Chapter 4)
    - Does the CH_4 flux show a distinct diel cycle in different emission pathways or seasons?
    - Which emission pathway dominates the diel CH_4 fluxes in which season, and what is its contribution?
    - To what extent can the microbial community or $\delta^{13}C$ source signatures explain the CH_4 formation or emission dynamics?
4. the spatial analysis of intra-annual reed ecosystem dynamics at Lake Neusiedl using RGB drone imagery and deep learning (**study IV**, Chapter 5)
    - providing a detailed workflow for land cover classification of high-resolution orthoimagery using deep learning image segmentation
    - revealing the spatial and temporal variability of a reed ecosystem under intensive drought conditions
    - disclosing the phenological stages of *Phragmites australis* in the reed stands of Lake Neusiedl over the 2021 vegetation period

1.5 Contribution to publications

This doctoral thesis consists of three independently published, peer-reviewed journal articles and one accepted manuscript for publication (published as a preprint). In order to distinguish my personal contributions from those of co-authors, the following statement is provided:

1.5.1 Study I

Title: Is ebullition or diffusion more important as methane emission pathway in a shallow subsaline lake?

Baur, P.A.*, Henry Pinilla, D., Glatzel, S.

* Corresponding author

This article is published in *Science of the Total Environment*, 2024, 912, 169112.
`https://doi.org/10.1016/j.scitotenv.2023.169112`

My contribution to the publication of **study I**: Data curation (with DHP), methodology, formal analysis (with DHP), visualization, conceptualization (with SG), investigation (with DHP), software, validation, project administration (with SG), writing - original draft, writing - review & editing (with DHP, SG).

1.5.2 Study II

Title: Consequences of intense drought on CO_2 and CH_4 fluxes of the reed ecosystem at Lake Neusiedl.

Baur, P.A.*, Maier, A., Buchsteiner, C., Zechmeister, T., Glatzel, S.

* Corresponding author

This article is published in *Environmental Research*, 2024, 262 (2), 119907.
`https://doi.org/10.1016/j.envres.2024.119907`

My contribution to the publication of **study II**: Data curation (with CB, AM), methodology, formal analysis (with CB), visualization, conceptualization (with SG), investigation, software, validation, project administration, writing - original, draft writing - review & editing (with AM, SG).

1.5.3 Study III

Title: Temporal dynamics of CH_4 emission pathways in the subsaline reed wetland of Lake Neusiedl

Baur, P.A.*, Rodrigues-Oliveira, T., Hager, K., Luo, Z.-H., Schleper, C., Glatzel, S.

* Corresponding author

This manuscript is accepted for publication in *Biogeosciences* (27 June 2025) and published as a preprint on *EGUsphere* since 6 February 2025. `https://doi.org/10.5194/egusphere-2025-443`

My contribution to the publication of **study III**: Data curation (with TRO, KH, ZHL), methodology (with TRO, KH), formal analysis (with TRO, KH, ZHL), visualization (with ZHL), conceptualization (with TRO), investigation, software, validation, project administration, writing - original draft (with TRO), writing - review & editing (with TRO, ZHL, SG).

1.5.4 Study IV

Title: Spatial analysis of intra-annual reed ecosystem dynamics at Lake Neusiedl using RGB drone imagery and deep learning.

Buchsteiner, C.*, **Baur, P.A.**, Glatzel, S.

* Corresponding author

This article is published in *Remote Sensing*, 2023, 15 (16), 3961.
`https://doi.org/10.3390/rs15163961`

My contribution to the publication of **study IV**: Data curation (with CB), methodology (with CB), formal analysis (with CB), visualization (with CB), conceptualization (with CB, SG), validation (with CB), writing - original draft (with CB), writing - review & editing (with SG), supervision (with SG).

2 Study I:
Is ebullition or diffusion more important as methane emission pathway in a shallow subsaline lake?

Baur, P.A., Henry Pinilla, D., Glatzel, S.
Science of the Total Environment, 2024, 912, 169112.
`https://doi.org/10.1016/j.scitotenv.2023.169112`

Graphical Abstract

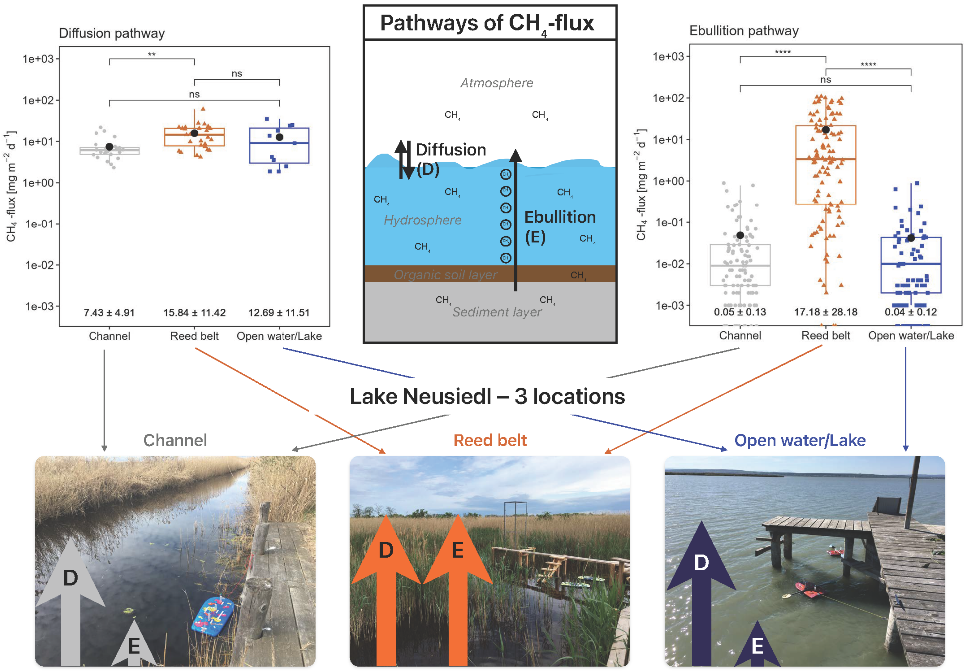

Figure 2.1: The contribution and dominance of CH_4 emissions from the ebullition and the diffusion pathway of a shallow subsaline lake was investigated at three representative locations (*Channel*, *Reed belt*, *Open water/Lake*) at Lake Neusiedl.

Highlights

- Higher median CH_4 fluxes via diffusion compared to ebullition at Lake Neusiedl.
- Acetoclastic methanogenesis is the dominant CH_4 production type at Lake Neusiedl.
- Highest (mean) CH_4 fluxes occur at the *Reed belt* site, irrespective of the pathway.
- In the *Reed belt*, ebullition contributes 48% to the total cumulative CH_4 emission.
- In the *Channel* and *Open water/Lake* locations, ebullition accounts for only about 1%.

Abstract

Methane (CH_4) emissions via ebullition contribute significantly to greenhouse gas emissions from freshwater bodies. According to the literature, the ebullition pathway may even be the most important pathway in some cases, particularly in shallow lakes. Ebullition rates are not often estimated because of the high uncertainty associated with episodic releases, leading to difficulties in their determination. This study provides an estimate of such emissions in a large, shallow, subsaline lake in eastern Austria, Lake Neusiedl, and compares them to the diffusion pathway. Ebullition gas sampling was conducted every 5–10 days over a period of 107 days from late March to mid-July 2021, using ebullition traps placed in three distinct locations: *Reed belt*, *Channel*, and *Open water/Lake*. The aim was to study the temporal and spatial heterogeneity of ebullition and its contribution to total emissions. At the same time, several water quality and other environmental parameters were measured and then tested against the CH_4 ebullition rates to explore them as potential drivers for this pathway. The carbon isotope fractionation factor (α_C) of the measured CH_4 ebullition gas, ranging from 1.03 to 1.06, indicates a dominance of the acetoclastic methanogenesis in the sediments of Lake Neusiedl, regardless of the location. The *Reed belt* location showed the highest mean CH_4 ebullition rate (17 ± 28 mg CH_4 m^{-2} d^{-1}), which is $>$ 340-fold higher than the mean of the other two locations, and demonstrated also a strong temperature dependency. In all locations at Lake Neusiedl, the median CH_4 fluxes via diffusion are significantly higher than via ebullition. Our analyses do not confirm the dominance of the ebullition pathway in any of the studied locations. Whereas at the *Reed belt*, ebullition accounts for 48% of the CH_4 emissions, in the other two locations, is responsible only for about 1%.

2.1 Introduction

Lakes cover only around 1.8–2.2% of the earth's land surface (Messager et al., 2016, Pi et al., 2022), nevertheless, they emit yearly on average 151 ± 73 Tg (mean ± 95% confidence interval) of methane (CH_4), accounting for about 35% of the total aquatic and about 19% of the global CH_4 emissions (Rosentreter et al., 2021). Lakes are natural sources of CH_4, where its production (methanogenesis) occurs mainly in anoxic sediments by methanogenic archaea (methanogens). Globally, more than half of all large lakes (53%, including Lake Neusiedl) have decreased in water volume over the last three decades (1992–2020) due to anthropogenic and climatic drivers such as higher water consumption or higher evaporation rates (Yao et al., 2023). Saline lakes, which represent a significant portion of all lakes in terms of both volume (44%) and area (23%) (Messager et al., 2016), also showed a strong decline (Wurtsbaugh et al., 2017). This is particularly concerning since several biogeochemical processes that occur within lakes play a fundamental role in the global carbon (C) cycle, such as primary production, sedimentation and burial, lateral transport, and exchange with the atmosphere (Alin and Johnson, 2007).

CH_4 is a powerful greenhouse gas (GHG), with a 96 times higher sustained-flux global warming potential (SGWP) than carbon dioxide (CO_2) over a 20-year time horizon on a mass basis (Neubauer and Megonigal, 2015). Therefore, it is of major significance to study in detail the quantity, frequency, and distribution of CH_4 fluxes in lake ecosystems.

Methanogenesis can be classified into three different types (also referred in the literature as methanogenic pathway) according to the main substrate that methanogens consume for CH_4 production. These types are: acetoclastic (acetate), hydrogenotrophic (hydrogen plus CO_2), or methylotrophic (methyl-compounds). According to Whiticar (1999), the hydrogenotrophic methanogenesis is the dominant metabolism of CH_4 production in marine ecosystems and the acetoclastic methanogenesis is more relevant in freshwater ecosystems. Methylotrophic methanogenesis is widespread in saline environments, but its proportion is considered to be lower than the other two methanogenesis types because of the smaller amount of substrate available for consumption (Conrad, 2020a). In consequence, the methylotrophic methanogenesis is often neglected in many environmental studies.

Stable carbon isotopes are used to trace the sources of CH_4 production and its transformation through CH_4 oxidation and transportation (Conrad, 2005). The carbon isotope fractionation factor (α_C, Equation 2.4 in Section 2.2.3) determines the degree of isotopic discrimination between the reactant (CH_4) and product (CO_2) molecules (Whiticar et al., 1986) and is used to characterize environments based on their dominant methanogenesis type and the transformation due to CH_4 oxidation. Whiticar et al. (1986) showed that α_C differs between freshwater and marine ecosystems, and that it is related to the major methanogenic mechanism. For example, if α_C fluctuates between 1.055 and 1.09, hydrogenotrophic methanogenesis is considered to be the dominant methanogenic mechanism, while α_C values between 1.04 and 1.055 indicate that acetoclastic methanogenesis is the dominant source of CH_4 production. Stable carbon isotopes are further used to detect CH_4 oxidation in lakes (Bastviken et al., 2002, Miller et al., 2022), because CH_4 oxidation enriches the $\delta^{13}C\text{-}CH_4$ value (Chanton, 2005). CH_4 oxidation occurs mainly at the anoxic–oxic interface (e.g., water–sediment interface) and is carried out by methanotrophic bacteria (Conrad, 2009).

Once produced, CH_4 can be transported from the anoxic sediment layers to the atmosphere through different pathways, including ebullition (bubble flux released directly and rapidly from sediments), molecular diffusion at the water–air or sediment–air interface, and plant-mediated transport of vascular plants such as *Phragmites australis* (Butterbach-Bahl et al., 2011). The relative importance of each transport pathway varies according to the organic content, the seasonal variation of temperature, and the type and density of vascular plants (Chanton, 2005), as well as the limnobathymetry and the lake morphology (Li et al., 2020).

Ebullition can become the preferential pathway in certain lakes (Aben et al., 2017, Bastviken et al., 2011, Peeters et al., 2019, Sø et al., 2023, Wang et al., 2021a,b), but its dominance is still uncertain due to its high temporal and spatial heterogeneity, and the consequent difficulty to quantify it accurately (Saunois et al., 2020, Wik et al., 2016, Zheng et al., 2022b). In global data sets, ebullition was found to be the dominant pathway in (freshwater) lakes, ranging from 56 to 80% of CH_4 emissions, depending on the approach (Bastviken et al., 2011, DelSontro et al., 2018, Johnson et al., 2022, Zheng et al., 2022b). Especially subsaline lakes (salinity 0.5–3 ‰; Hammer (1986)) have often been excluded from global CH_4 estimates due to a lack of observations. Hence, there is a need for more accurate and continuous CH_4 ebullition measurements across different lake ecosystems to reduce the uncertainty in lake methane budgets (Saunois et al., 2020).

Bubble formation occurs because CH_4 is only slightly soluble in water (Yamamoto et al., 1976). Since no reaction with the oxygenated water column takes place during ebullition, at least in shallow waters, and the methanotrophic region in the sediments is bypassed (Happell et al., 1994), no isotopic fractionation takes place during ebullition. This implies that by measuring the δ^{13}C-CH_4 value of the bubbles, conclusions can also be drawn about the main CH_4 production type in the sediments (Chanton, 2005). The bubbles are mainly built up by CH_4 and nitrogen (N_2), whereas other gases like CO_2 account for $< 1\%$, and thus, they can be considered negligible (Langenegger et al., 2019).

Diffusion is one of the other pathways of the CH_4 flux occurring at the sediment–water, water–air, or sediment–air interfaces. Diffusion rates are regulated by the concentration gradient, the diffusion coefficient, and the porosity of soil/sediments (Chanton, 2005). Besides CH_4 production, variations in the extent of CH_4 oxidation appear to be the main factor controlling the δ^{13}C-CH_4 value of CH_4 emitted via diffusion (Happell et al., 1994). Peeters et al. (2019) found that in shallow waters, the diffusive CH_4 fluxes from the upper sediments are the main source of dissolved CH_4 in lakes and reservoirs, and of diffusive CH_4 emissions from the water to the atmosphere, rather than CH_4 derived from oxic methanogenesis in the water column as hypothesized by Bogard et al. (2014). Lateral transport can be a possible process causing CH_4 relocation from shallow water zones (site of CH_4 production) to deeper water zones of a lake and, thus, is a main source of diffusive CH_4 emissions from open water of lakes (Encinas Fernández et al., 2016). Globally, the diffusion pathway can account for about 21–25% of total CH_4 emissions from (freshwater) lakes (DelSontro et al., 2018, Zheng et al., 2022b), from which $> 84\%$ would be contributed by lakes with an average depth of < 5 m (Li et al., 2020).

Until now, ebullition has primarily been studied in freshwater lakes, such as thermokarst (Wang et al., 2021b), boreal and subarctic (Schenk et al., 2021, Wik et al., 2013, 2014, 2020), northern temperate (Thottathil and Prairie, 2021), tropical (Linkhorst et al., 2020, Miller et al., 2022), and small lakes or reservoirs (Langenegger et al., 2019, McClure et al., 2020, Sø et al., 2023), as well as in urban inland waters (Wang et al., 2021a). However, it has not been comprehensively studied in large shallow and subsaline lakes like Lake Neusiedl. Understanding ebullition in subsaline lakes is crucial. These ecosystems are often shallow (ebullition is restricted to < 3 m depth, according to DelSontro et al. (2016))

and if they have a salinity between 0.5 and 5 ‰, they can have the highest (and most variable) CH_4 emissions as known from marshes (Poffenbarger et al., 2011). Subsaline lakes are found across the globe (from Argentina to Greenland) and are often highly sensitive to hydrological and climatic changes (Soja et al., 2013).

Large lakes (> 100 km^2) account only for 0.05% of the total numbers of lakes, but cover 59% of the total lake area (Pi et al., 2022). Therefore, it is highly important to improve accuracy in the quantification of CH_4 ebullition rates in such large lake ecosystems for more accurate global up-scaling CH_4 emission estimates. Lake Neusiedl, the site of our study, is one of these lakes.

Lake Neusiedl has a surface area of around 315 km^2 and more than half of it is covered by a reed belt dominated by *Phragmites australis* (Wolfram and Herzig, 2013). Due to its unique landscape, it is a cross-border UNESCO World Heritage Site, a national park, and a wetland of international importance (Ramsar site) on the Austrian-Hungarian border. Lake Neusiedl is characterized by its subsalinity (Hammer (1986); dominating salt: soda), alkalinty (pH > 8, Reif et al. (2022)), high inorganic turbidity (Zoboli et al., 2023), moderate eutrophication (Tolotti et al., 2021), shallowness (maximum water level of 1.8 m, Wolfram and Herzig (2013)), and by no natural outlet. Due to its shallowness, the high evapotranspiration rates — caused by strong winds and high temperatures — and its dependency on 79% water input from direct precipitation, Lake Neusiedl is highly sensitive to any climatic change (Soja et al., 2013).

First attempts to investigate the CH_4 fluxes at Lake Neusiedl were conducted by Soja et al. (2014b). They measured diffusive CH_4 fluxes using floating chambers during six sampling days in 2011/2012, and did not use a separate methodology for measuring CH_4 ebullition. Furthermore, they did not include the ebullition pathway in the estimated lake's CH_4 budget because of the sporadic release of ebullition. With this approach, they found that 2/3 of the up-scaled lake's diffusive CH_4 fluxes were originated in the reed belt and 1/3 in the pelagic zone. To complement these findings, our study focuses on CH_4 ebullition rates and their significance in comparison to the diffusive CH_4 fluxes in three representative lake ecosystem types of Lake Neusiedl.

To enhance comprehension of the spatial and temporal distribution of CH_4 ebullition, it is essential to identify the sources of CH_4 production and the factors driving ebullition in various lake ecosystems. This is crucial for improving estimates of the CH_4 budget, and exceptionally important given the particular vulnerability of shallow lakes to the impacts of climate variations (Aben et al., 2017, Soja et al., 2013). The objectives of this study are to (**1**) investigate the spatial and temporal heterogeneity of CH_4 ebullition at the shallow and subsaline Lake Neusiedl, (**2**) determine the carbon source for methanogenesis based on isotopic ratios of CH_4 from ebullition, (**3**) explore the drivers of CH_4 ebullition, and (**4**) compare the ebullition and diffusion pathways in this lake ecosystem. Clarification of these points will help answering the question whether ebullition or diffusion is more important as CH_4 emission pathway in shallow subsaline lakes, using Lake Neusiedl, a site of international importance, as an example.

2.2 Methods

2.2.1 Study site and setup

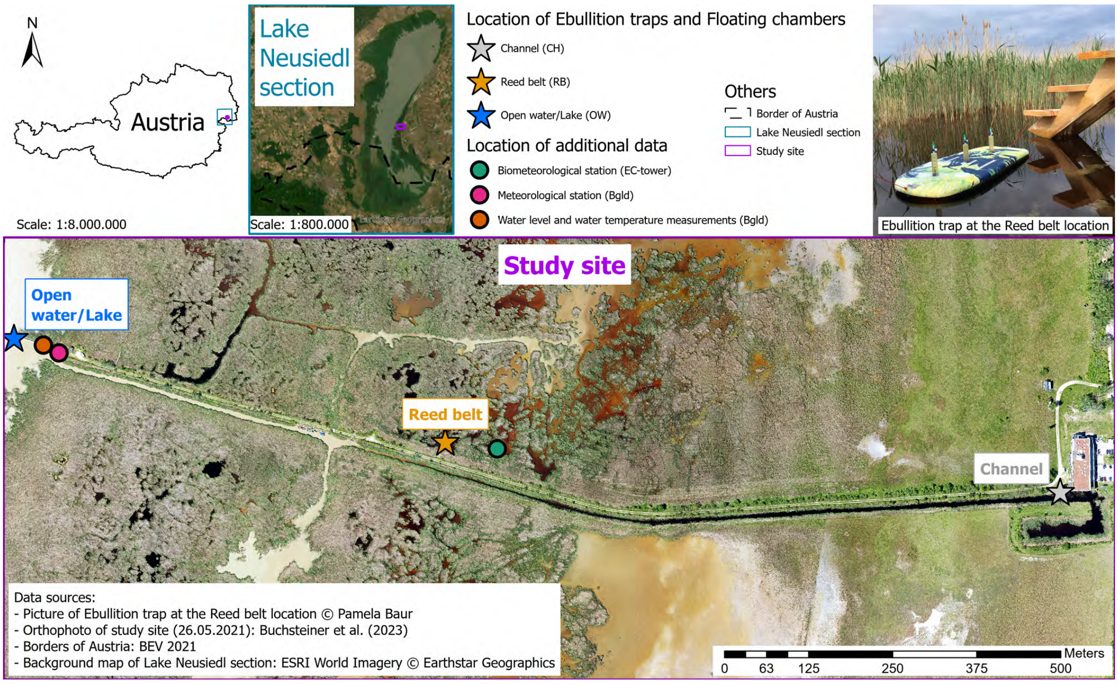

Figure 2.2: Geographic location of the study site and monitoring locations of ebullition traps and floating chambers at the reed belt of Lake Neusiedl, near Illmitz, Austria (map data source: Buchsteiner et al. (2023)).

Lake Neusiedl (Fertő, in Hungarian) is the largest "steppe" lake in central Europe without natural outlets, and the only existing artificial outlet has been closed since April 2015 due to low water levels of the lake. The region of Lake Neusiedl holds the status of a transnational UNESCO World Heritage Site due to its diverse and unique (cultural) landscape. Lake Neusiedl, located on the Austrian-Hungarian border, is a subsaline shallow lake with more than half of its surface covered by a reed belt (181 km^2, Csaplovics (2019)). The reed belt is a dynamically changing mosaic of reed (*Phragmites australis*), water, and sediment patches (Buchsteiner et al., 2023), and it is the second largest coherent reed ecosystem in Europe, following the Danube Delta. Especially in 2021, when our ebullition study also took place, intra-annual changes in the mosaic of the reed belt were evident due to the sharp decrease in water areas and the associated overgrowth of the former water pool areas with reeds (Buchsteiner et al., 2023). Our study was conducted on the eastern reed belt of Lake Neusiedl, near the Biological Station Illmitz in Austria (116 m above sea level, Lat. 47.769° N, Long. 16.758° E, see Figure 2.2) in the "nature (core) zone" of the Neusiedler See – Seewinkel National Park. The region has a mean annual air temperature of 11.1°C and an annual precipitation of 556 mm (1971–2020) (Hackl and Ledolter, 2023).

Three distinct locations were carefully chosen within the study site, which represent the typical lake ecosystem types of Lake Neusiedl: *Channel* (CH), *Reed belt* (RB), and *Open water/Lake* (OW). These specific locations were selected to represent the spatial variability over the study area and because of their significant differences in water quality (see Table 2.1) and environmental conditions, such as vegetation cover and wind influence. CH represents the man-made channels in the reed belt, extending from open water to the landward side, often serving as waterways from the open lake to harbors and are, therefore, often maintained. Their lateral exchange with open lake water varies depending on the lake water level, wind direction and wind speed. Location RB represents the water pool areas within the reed belt, characterized by humic-rich, clear, very shallow water and are (almost) not in exchange with open lake water. OW represents the open lake water area, which, although it is not far from the edge of the reed belt, shares similar water levels and water characteristics and experiences high turbidity as in the middle of the lake. This area is significantly influenced by strong winds and waves and is particularly exposed to the main wind direction northwest as well as open to the south, which means that OW does not receive shade or wind protection from reeds.

Table 2.1: Spatial variability of water characteristics at Lake Neusiedl, illustrated using selected water parameters of three representative locations (CH = *Channel*; RB = *Reed belt*; OW = *Open water/Lake*) prior to the start of the measurement campaign in mid-March 2021 (WL = water level; T_{water} = water temperature; DO = dissolved oxygen; CON = electrical conductivity; TDN = total dissolved nitrogen; NPOC = dissolved non-purgeable organic carbon).

Location	**WL** [m]	**pH**	**T_{water}** [°C]	**DO** [%]	**CON** [mS cm^{-1}]	**NO_3^-** [mg L^{-1}]	**NH_4^+** [mg L^{-1}]	**TDN** [mg L^{-1}]	**NPOC** [mg L^{-1}]
CH	1.5	8.45	12.1	91.4	2.71	0.91	0.12	2.51	37.04
RB	0.2	8.38	10.7	95.8	2.86	0.15	0.23	2.67	40.14
OW	1.5	8.69	5.7	103.5	1.62	0.82	0.28	1.38	16.26

2.2.2 Methane measurements

Field measurements of the study started in spring (30 March 2021) and ended in early summer (14 July 2021). This study period was chosen to enhance our understanding of CH_4-related processes in a reed-influenced and subsaline lake ecosystem, during a period of rising temperature when reeds start to grow (from dormancy to maturity, see Buchsteiner et al. (2023)) and reach their maximum growth (and subsequent increment in rhizodeposition). The focus of this study is on the ebullition pathway of CH_4, but for comparison purposes the diffusion pathway was also measured. Two different methodologies were applied for measuring the two CH_4 emission pathways and are described in the following subsections.

Ebullition pathway with ebullition traps

The measurement period for ebullition covered a total of 107 days, during which ebullition gas collection frequency ranged between 5 and 10 days (closure time for the ebullition traps) depending on transport and equipment availability. A total of 14 ebullition gas collection days were registered over the entire study period (15 weeks in total).

At each location (CH, RB, OW), three ebullition traps were permanently installed for gas collection. These traps were built using a floating body-board (approx. 91 cm × 44 cm, Hot Tuna, SportsDirect.com Retail Ltd., UK) equipped with three inverted 23.5 cm diameter HDPE funnels (Emil Lux GmbH & Co. KG, Wermelskirchen, Germany) pierced through. Thus, each location had 9 simultaneous ebullition measurements (funnels). Each funnel was topped with a 50 mL PP syringe featuring a luer lock connector (Omnifix, B. Braun SE, Melsungen, Germany) and regulated by a three-way stopcock (Discofix, B. Braun SE, Melsungen, Germany) to extract emerging gases (as shown in the top-right picture in Figure 2.2). To install the ebullition traps, ambient air was extracted from the funnels and syringes until they were completely filled with water, allowing the board to float with the submerged funnels. A temperature data logger (HOBO Pendant, Model UA-002-08, Onset Computer Corporation, USA) was fixed beneath the board of one trap at each location to record water temperature every 30 min.

To quantify CH_4 ebullition rates during closure period, the gas was extracted from the funnels of the ebullition traps only when there was > 1 mL accumulated in the syringe on the collection day. The extracted gas was injected in 20 mL vacuumed glass vials (Agilent Technologies, Inc., Santa Clara, USA), sealed with gray butyl septa (Machery-Nagel GmbH & Co. KG, Düren, Germany) and aluminum crimp caps (Machery-Nagel GmbH & Co. KG, Düren, Germany). The filled vials were stored in a dry and dark compartment at room temperature until analysis, and the storage time was kept as short as possible (from days to a few weeks).

Dry mole fractions of CH_4 and the isotopic signature (δ^{13}C-CH_4 and δ^{13}C-CO_2) of gas samples from the ebullition traps were determined in the lab using a gas and isotope analyzer G2201-i, which uses cavity ring-down spectroscopy (CRDS; a highly sensitive laser absorption technology), connected to a small sample isotope module (SSIM2) (Picarro, Inc., Santa Clara, USA), which enables syringe injection of small gas sample volumes with measurement repetitions. The instrument was calibrated using two certified stable isotope standard gases: one gas cylinder of 2 ppm CH_4 with δ^{13}C-CH_4 of -45 ± 0.5 ‰ VPDB (Vienna Pee Dee Belemnite) and 350 ppm CO_2 with δ^{13}C-CO_2 of -10 ± 0.3 ‰ VPDB, and a second gas cylinder of 10 ppm CH_4 with δ^{13}C-CH_4 of -69 ± 0.5 ‰ VPDB and 1000 ppm CO_2 with δ^{13}C-CO_2 of -20 ± 0.3 ‰ VPDB (Alphagaz, Air Liquide S.A., Paris, France).

Dilution of the gas samples from the ebullition traps was necessary in cases where CH_4 concentrations exceeded the measurement range of the instrument or when the volume of sampled gas was not sufficient for conducting duplicate measurements of each sample. The latter was possible only if the CH_4 concentration in the sample was high enough to conduct dilution and still be in the measurement range of the instrument. For each measurement, a minimum of 15 mL of the (diluted) gas sample was injected into the SSIM2 using a syringe. The measuring protocol was separated into two groups: samples taken in the RB location, and samples taken in the OW and CH locations. This was necessary because, in most cases, the samples from the RB had much higher CH_4 concentrations than those from the other two locations. When a sufficient amount of collected gas ($\geq$ 12 mL) was available and the concentrations fell within the measurement specification range guaranteed by the Picarro G2201-i instrument (1.8 ppm $\leq CH_4 \leq$ 500 ppm, for simultaneous measurement mode of CO_2 and CH_4, high precision or high dynamic range mode), the sample was directly measured. Otherwise, dilution with N_2 gas (6.0, Messer Austria GmbH, Gumpoldskirchen, Austria) was required. Dilutions were performed in 1 L multi-layer foil gas bags (Restek Corporation, Bellefonte, USA) using 0.5 L and 1 mL acrylic syringes with PTFE luer lock connectors (Hamilton Company, Reno, USA) and needles (26G Agani, Terumo Corporation, Japan).

Diffusion pathway with floating chambers

To quantify CH_4 diffusion rates at each location, in situ chamber measurements were carried out using a floating chamber connected to a mobile gas analyzer (Ultra-portable Greenhouse Gas Analyzer (UGGA) for CH_4, CO_2, and H_2O (water), model 915-0011, Los Gatos Research Inc., Mountain View, USA) on 9 out of the 14 monitoring days. In the remaining weeks, the equipment was not available. The floating chamber was made of transparent PVC in a bird-cage-shape with a diameter of 30 cm. It was supported by an aluminum collar at its base, which was immersed 3 cm into the water. To ensure buoyancy, the collar was girded with a foam tube. During measurements, the chamber was directly connected to the gas analyzer through two 4 mm inner diameter polyurethane tubes (Festo GmbH, Esslingen a.N., Germany), one as inlet and the other as outlet, which circulated the air between the closed chamber and the instrument (through-flow system). CH_4 concentrations were registered constantly for 4 min and corrected by the H_2O concentrations. Three replicate chamber measurements were taken at each location on each monitoring day. The water-corrected dry mole fractions of CH_4 were used for further analyses.

2.2.3 Flux calculations and isotope ratios

Gas concentrations were transformed into fluxes by converting them from ppm to mass per unit volume according to Boguski (2006), and by considering collection time and funnel area. The equation used to estimate CH_4 ebullition fluxes [mg CH_4 m^{-2} d^{-1}] was the following, adapted from Davidson et al. (2018b):

$$F_{Eb\text{-}CH_4} = \frac{c_{CH_4} \cdot V_{occ} \cdot M_m \cdot p_a}{R \cdot T_c \cdot A_{fun} \cdot \Delta t} \cdot 10^6 \cdot 1000 \tag{2.1}$$

Where F_{Eb-CH_4} is the ebullition flux of CH_4, and c_{CH_4} is the analyzed CH_4 concentration expressed in ppm. V_{occ} corresponds to the total volume (in L) of occurred gas in the respective syringe from where the gas was collected. A_{fun} is the funnel area (0.0434 m^2) and Δt is the elapsed time in days. M_m is the molar mass of CH_4 (16.04 g mol^{-1}). T_c is the mean air temperature inside the chamber during closure time [K], p_a is the atmospheric pressure [Pa], and R is the ideal gas constant [kg m^2 s^{-2} mol^{-1} K^{-1}].

Without considering the gas composition in the bubbles captured within the ebullition traps, the bubble flux F_{Bubble} [mL m^{-2} d^{-1}] can be a better proxy, as suggested by DelSontro et al. (2016), to estimate the actual production rate of CH_4 bubbles in sediments and is, therefore, more appropriate for quantifying their control by environmental parameters:

$$F_{Bubble} = \frac{V_{occ}}{A_{fun} \cdot \Delta t} \tag{2.2}$$

F_{Eb-CH_4} may differ from F_{Bubble} due to the possibility of diffusion (at the gas–water interface) and CH_4 oxidation occurring during ebullition trap closure time (DelSontro et al., 2016), which cannot be excluded, or due to measurement errors during gas collection, dilution, or measurement with the gas analyzer.

From the diffusion measurements, the initial 25% of the floating chamber closure time (death band) was excluded from the linear regression fit of the temporal change of CH_4 concentration inside the chamber. This was done to account for the potential artifacts that may have occurred during chamber closure at deployment, as described by Hoffmann et al. (2017). The diffusion fluxes of CH_4 [mg CH_4 m^{-2} d^{-1}] were calculated with the following equation, adapted from Rochette et al. (1997):

$$F_{Diff\text{-}CH_4} = \frac{S}{10^6} \cdot \frac{V_c \cdot M_m \cdot p_a}{A_c \cdot R \cdot T_c} \cdot 3600 \cdot 24 \cdot 1000 \tag{2.3}$$

Where $F_{Diff-CH_4}$ is the diffusion flux of CH_4, S is the calculated slope of the linear regression of CH_4 concentration change inside the chamber over closure time [ppm(v) s^{-1}], V_c corresponds to the volume of the floating chamber (0.0165 m^3), and A_c is the chamber area where the gas exchange between air and water occurs (0.0707 m^2). Only flux data that had a coefficient of determination $R^2 \geq 0.7$ for linear regression were used. Therefore, about 23% of all CH_4 diffusion fluxes could not be used due to lack of linearity, especially in the OW location.

The cumulative sums of the diffusion and ebullition rates of CH_4 at each location were calculated for the entire measurement period of 107 days to compare the total amount of diffusion and ebullition.

To estimate the contribution of the major methanogenic type and CH_4 transformation through oxidation, the carbon isotope fractionation factor (α_C, unitless) between δ^{13}C-CO_2 [‰ VPDB] and δ^{13}C-CH_4 [‰ VPDB] was calculated using the following equation (Whiticar and Faber, 1986):

$$\alpha_C = \frac{(\delta^{13}C\text{-}CO_2 + 1000)}{(\delta^{13}C\text{-}CH_4 + 1000)} \tag{2.4}$$

2.2.4 Water sampling and in situ measurements

To monitor water quality, in situ parameters were routinely measured at the water surface of each location, and water samples were collected every 5–10 day throughout the study period (a total of 15 sampling and measurement dates). The in situ measurements were carried out with a portable multi-parameter meter (WTW, Xylem Analytics Germany Sales GmbH & Co. KG, Weilheim, Germany) connected with water temperature (T_{water}), pH (both Sentix, WTW), electrical conductivity (CON) (TetraCon, WTW), dissolved oxygen (DO), and oxidation–reduction potential (ORP) sensors. For the lab analysis, water was collected from right next to each trap, filtered, and then stored in three 20 mL plastic bottles for each sample. This approach ensured that separate lab analyses could be conducted for each bottle, minimizing the need to thaw the sample multiple times. Filtration of the water samples was done in the field, first with a MN 619 G 1/4 ⌀ 125 mm phosphate-free filter paper (Machery & Nagel GmbH & Co. KG, Düren, Germany) due to the high turbidity of the samples at OW and CH, and second, with a 0.45 μm nylon syringe filter to get the dissolved part of the compounds. The plastic bottles with the filtered water samples were transported to the lab in a cooling box containing ice packs. At the end of the sampling day, the samples were stored in a freezer at −20°C until analysis (Gardolinski et al., 2001, Worsfold et al., 2005).

2.2.5 Water analysis

The water samples were analyzed in the Geoecology lab of the University of Vienna. Triplicate measurements were taken from each sample in order to analyze the following parameters: nitrate (NO_3^-), nitrite (NO_2^-), ammonium (NH_4^+), and orthophosphate (PO_4^{3-}). Concentrations were determined by colorimetry using a UV-vis spectrometer (Infinite 200 Pro NanoQuant, Tecan Group Ltd., Männedorf, Switzerland) at 540 nm for NO_3^- and NO_2^-, and at 660 and 880 nm for NH_4^+ and PO_4^{3-}, respectively. Sulfate (SO_4^{2-}) was determined by turbidity using the same UV-vis spectrometer at 420 nm. Absorbance values (%) from the UV-vis spectrometer analysis were transformed to concentration units using a standard curve to create a linear regression. The intercept of the regression line was fixed to the average of the blanks, and the R^2 of the linear regression was always higher than 0.98. The procedures used to determine NO_3^- by VCl_3 (vanadium(III) chloride) reduction, NO_2^-, and NH_4^+, are a modification of the methods described by Miranda et al. (2001) and Kandeler and Gerber (1988), respectively. The procedure used for PO_4^{3-} determination is based on the method described by Murphy and Riley (1962), although modified for analysis using microtiter plates. The procedure used for SO_4^{2-} determination is based on the method described by U.S.EPA (1999). The dissolved part of the non-purgeable organic carbon (NPOC), inorganic carbon (DIC), and total nitrogen (TDN) were determined from the filtered samples by combustion catalytic oxidation using a TOC-L analyzer (with ASI-L and TNM-L, Shimadzu Scientific Instruments, Inc., Japan).

2.2.6 Additional data

Biometeorological (Biomet) data were collected from the nearby eddy covariance flux tower (EC tower) (47.769150° N, 16.758482° E), at about 50 m from the RB location (see Figure 2.2). Variables such as photosynthetically active photon flux density (PPFD), incoming and outgoing shortwave radiation (SW_{in}, SW_{out}), incoming and outgoing longwave radiation (LW_{in}, LW_{out}), relative humidity (rH), air temperature (T_{air}), air pressure (PA), water vapor pressure deficit (VPD), precipitation (P), wind speed (WS), wind direction (WD), sediment water content at 5, 10, and 15 cm depth (SWC), sediment temperature at 5, 10, and 15 cm depth (T_{sed}), and sediment heat flux at 5, 10, and 15 cm depth (SHF) are permanently measured in 1 min time interval. Additionally, T_{air}, P, rH, SW_{in}, WD, T_{water}, and WL data of Lake Neusiedl were taken from the meteorological station of Hydrographischer Dienst Burgenland (HD Bgld). This station is located 50 m away from the OW location (47.769996° N, 16.752730° E; see Figure 2.2) and has a measurement time interval of 30 min. For each closure period of the ebullition traps and the floating chambers, the mean and the standard deviation (SD) of the environmental variables were calculated to study their potential impact on CH_4 ebullition and diffusion fluxes. In certain cases, variables like temperature were also analyzed for their median, minimum, and maximum values.

2.2.7 Data processing and statistical analysis

Data processing and statistical analysis were conducted using R (Version 4.2.2, R Core Team (2022)). The R package *data.table* was employed for faster data processing (Dowle and Srinivasan, 2023). For visualization of the results, the R packages *ggplot2*, *ggpubr*, *ggh4x*, and *gridExtra* were utilized (Auguie, 2017, Kassambara, 2023a, van den Brand, 2023, Wickham, 2016). Furthermore, the R packages *tidyverse* and *stringi* were applied for data manipulation (Gagolewski, 2022, Wickham et al., 2019).

The non-parametric Kruskal-Wallis test was used to assess whether the medians of the measured fluxes, emission rates and isotopic values of the three location significantly differ. The two-sided Dunn's post-hoc test was applied with the R package *rstatix* (Kassambara, 2023b) to statistically evaluate which locations exhibited significant differences from the others ($p < 0.01$, Adjustment Holm). The effect size of the Dunn's test (r) was calculated by dividing the absolute z-value by the square root of the sample size (N). Following Cohen (1988), an r value > 0.5 indicates a large effect.

The temperature dependency of the CH_4 ebullition rates at the study site was analyzed using the modified Arrhenius equation, according to Aben et al. (2017). This equation was fitted through non-linear least square regressions (using the R package *nlstools* by Baty et al. (2015)), and all models showed to be statistically significant ($p < 0.01$). The fitted equation includes the modeled CH_4 ebullition rate at 20°C (E_{20}) and the overall system temperature coefficient (θ_s, dimensionless). A θ_s value of, for example, 1.11, indicates that a 1°C increase in temperature would lead to an 11% higher ebullition (Wang et al., 2021a). The non-linear models were compared with the Kling–Gupta Efficiency (KGE, Gupta et al. (2009)) metric to assess the overall agreement with the best-fitting model. An ideal match between simulated and observed values correspond to a KGE value of 1. To facilitate this analysis, the R package *hydroGOF* by Zambrano-Bigiarini, Mauricio (2020) was employed. Additionally, for comparability with other studies, the θ_s values were converted to activation energy (EA) in electron volts (eV) using the conversion equations of Wilkinson et al. (2019). Moreover, for calculating the confidence intervals for the parameters of the Arrhenius models the R package *Rmisc* (Hope, 2022) was used.

Potential relationships between CH_4 ebullition rates or bubble fluxes and environmental parameters (for all locations together, but also separately), were tested using Spearman's rank correlation. This analysis aims to evaluate the strength and direction of monotonic relationships between these variables. Correlations were indicated by the Spearman rank correlation coefficient ρ, with significance determined at $p < 0.01$ (Holm's adjustment). For conducting and visualizing the correlation analysis, the R package *ggstatsplot* (Patil, 2021) was used.

2.3 Results

2.3.1 Ebullition heterogeneity in space and time

In this study, 311 quality-checked CH_4 ebullition rates were measured along the three locations, from which 88% had ebullition rates higher than zero. Zero values were included in the ebullitive CH_4 flux estimates because they represent periods during which no ebullition events occurred. Their inclusion ensure that the contribution of the ebullition pathway is not overestimated. Ebullition data were only excluded, when the CH_4 gas measurement with the Picarro instrument did not work well or the ebullition trap broke due to harsh conditions (too strong winds and waves) and needed repairing.

CH_4 ebullition rates showed temporal and spatial variations. They notably increased at the *Channel* (CH) and *Reed belt* (RB) locations from March to July 2021 (calendar week from 13 to 27; see Figure 2.3B). At the *Open water/Lake* (OW) location, variations were observed, although no distinct temporal trend was evident. Also, all three locations showed high variance of CH_4 ebullition rates within each location per week. The highest CH_4 ebullition rate (109.20 mg CH_4 m^{-2} d^{-1}) and the strongest increase were, by far, at RB. The median CH_4 ebullition rate at RB is significantly higher than the median of the CH and OW locations (Dunn's post-hoc test, $p < 0.0001$ (Holm's adjustment), effect size $r = 0.7$; see Figure 2.3A). The mean CH_4 ebullition rate of the RB location (17.18 ± 28.18 mg CH_4 m^{-2} d^{-1} (± SD)) is more than 340-fold higher than the mean of the other two locations, 0.05 ± 0.13 and 0.04 ± 0.12 mg CH_4 m^{-2} d^{-1} at the CH and OW locations, respectively.

The temporal variation of the bubble fluxes at the CH and RB locations showed the same increasing trend from March to July 2021 as the CH_4 ebullition rates (compare Figure S.1B to 2.3B), but unlike the CH_4 ebullition rates, the bubble fluxes at those two locations were nearly in the same range.

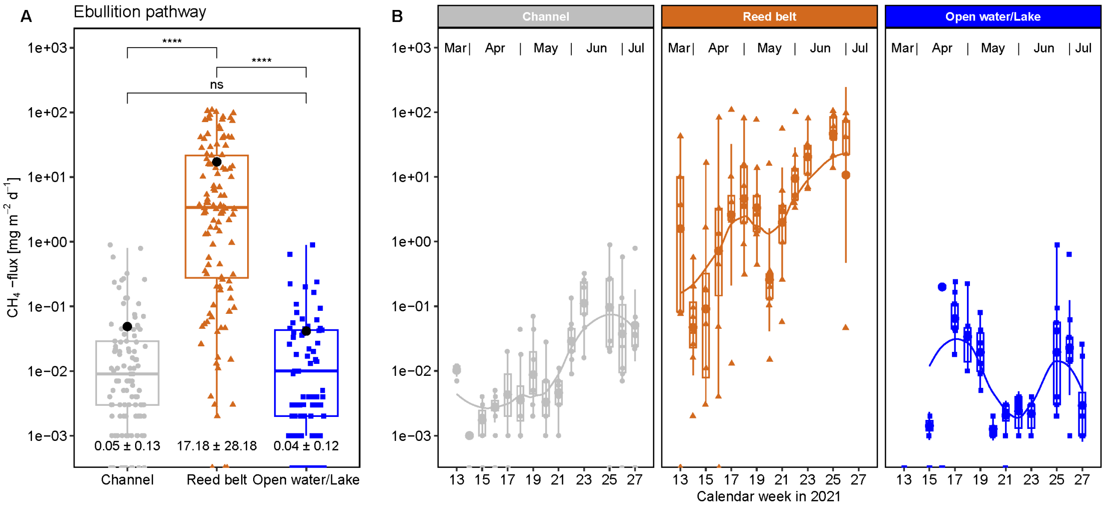

Figure 2.3: Methane ebullition rates and their spatial (**A**) and temporal (**B**) variability at Lake Neusiedl during the measurement period from March to July 2021 (locations: *Channel* (CH, gray), *Reed belt* (RB, brown), and *Open water/Lake* (OW, blue); black dots (●) showing mean value per location; number under boxplot per location in the left graph is mean ± standard deviation; Dunn's post-hoc test with non-significant (ns, $p > 0.05$) or very significant (****, $p < 0.0001$) differences (Holm's adjustment); the fitted lines show the local polynomial regressions (loess)).

2.3.2 Isotope ratios and fractionation factor of ebullition gas

The stable carbon isotope ratio of CH_4 (δ^{13}C-CH_4) was analyzed in the lab for all the gas samples collected using the ebullition traps. After data quality checking, a total of 274 mean and SD values of δ^{13}C-CH_4 were used for subsequent analysis (see Figure 2.4A). The stable carbon isotope ratio of CO_2 (δ^{13}C-CO_2) was also analyzed for all the collected ebullition gas samples but could only be measured for the CH and OW locations. Due to the high CH_4 concentration in the ebullition gas samples from the RB location, high dilution ratios were required (refer to Section 2.2.2). As a result, the diluted gas samples fell below the CO_2 measurement range of the instrument, resulting in (almost) no δ^{13}C-CO_2 values available for RB. Both stable carbon isotope ratios of the measured ebullition gas samples showed some variances within each location per week, and no temporal trend could be observed (see Figure S.2A and B).

The CH location showed a significantly enriched median δ^{13}C-CH_4 compared to the median of the two other locations, RB and OW (Dunn's post-hoc test, $p < 0.0001$ (Holm's adjustment), effect sizes r = 0.35 and r = 0.45; see Figure 2.4A). The median δ^{13}C-CH_4 of the OW was slightly more depleted than the RB but not significantly (ns, $p > 0.05$). The median δ^{13}C-CO_2 of the CH was significantly more depleted compared to that of the OW ($p < 0.01$, effect size r = 0.36; see Figure 2.4B).

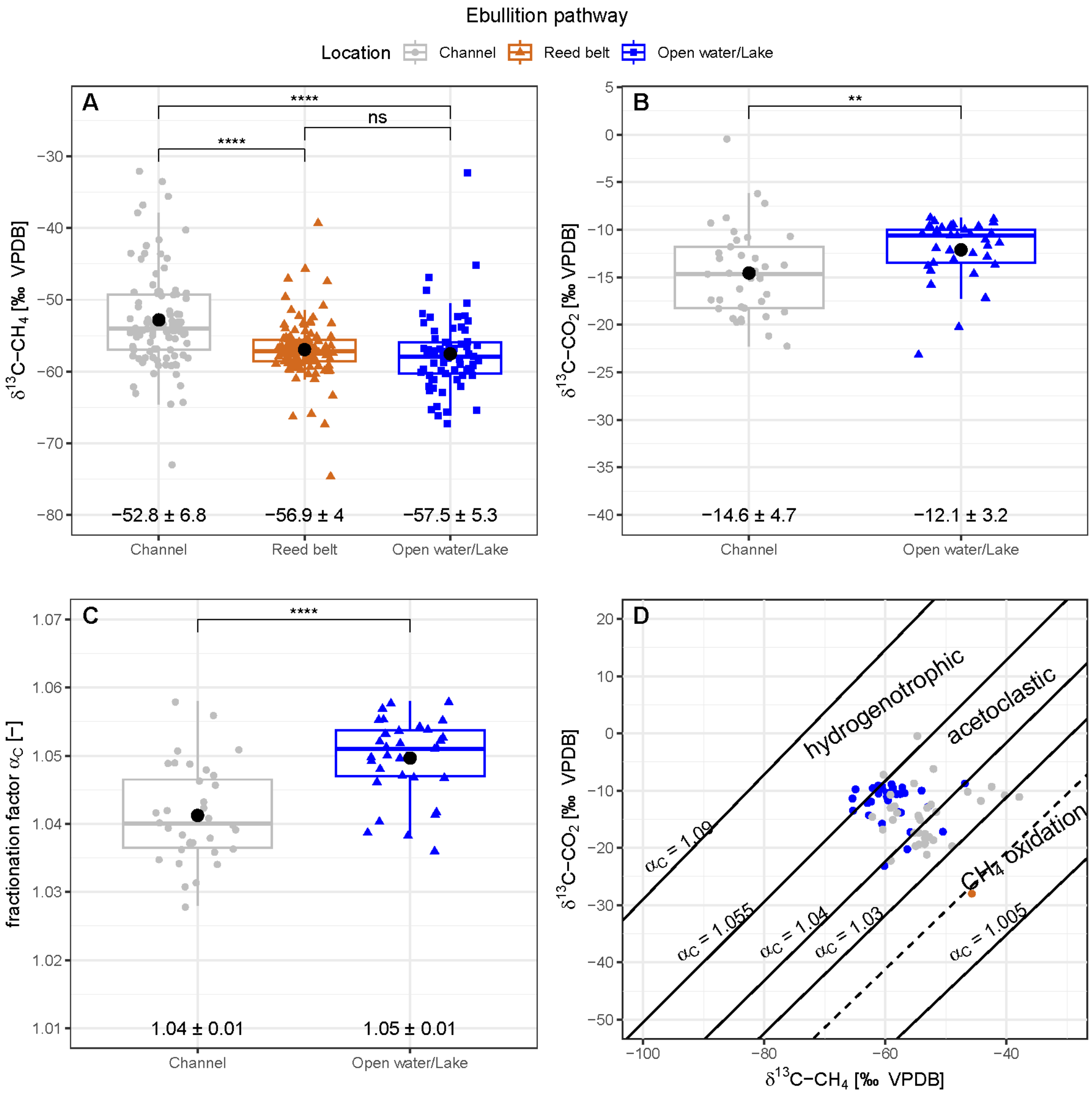

Figure 2.4: Stable carbon isotopes δ^{13}C-CH_4 (**A**) and δ^{13}C-CO_2 (**B**) and their fractionation factor α_C (**C**) measured from the ebullition gas samples in the different locations: *Channel* (CH, gray), *Reed belt* (RB, brown), and *Open water/Lake* (OW, blue) at Lake Neusiedl (black dots (•) showing mean value per location; number under boxplot indicating the mean ± standard deviation per location; Dunn's post-hoc test with non-significant (ns, $p > 0.05$), significant (**, $p < 0.01$), or very significant (****, $p < 0.0001$) differences (Holm's adjustment)). **D**: Methanogenic characterization after Whiticar and Faber (1986) using the measured δ^{13}C-CH_4 - and δ^{13}C-CO_2 - pairs.

Combining the two stable carbon isotopes (δ^{13}C-CH_4 and δ^{13}C-CO_2) for estimating the carbon fractionation factor, α_C, the OW location showed a median α_C of 1.05, which is significantly higher than the median α_C of 1.04 of the CH location ($p < 0.0001$, effect size r = 0.55; see Figure 2.4C). The α_C values of the ebullition pathway ranged from 1.03 to 1.06 at the CH and OW locations, respectively. Following the methanogenic characterization of the measured stable carbon isotope ratios according to Whiticar and Faber (1986) (see Figure 2.4D), the measured stable carbon isotope ratios indicate that the dominant methanogenic type for the studied environment, and for our study period, is probably the acetoclastic methanogenesis. This plot also suggests that CH_4 oxidation likely occurred more extensively at the CH location compared to the OW.

2.3.3 Drivers of methane ebullition

In this study, the drivers of ebullition were addressed in order to better understand the temporal variability (due to temperature dependency) and the spatial heterogeneity (across different locations) in ebullition rates.

A strong temperature dependency of CH_4 ebullition rates was observed at the CH and RB locations, and also with any temperature parameter such as water, air, and sediment temperature (see Section S.1.3). Meanwhile, at OW, it is likely that factors other than temperature exerted a more pronounced influence on CH_4 ebullition rates. This is indicated by the fact that all non-linear Arrhenius models of the OW location had negative KGE values, which show that these models do not sufficiently fit the data. For the RB, the best non-linear fitting Arrhenius model, with a KGE of 0.35, was with the manually measured mean T_{water} and the CH_4 ebullition rate (see Figure S.3B). In contrast, for the CH, the best fitting model, with a KGE of 0.285, was with T_{water} (HOBO) and the CH_4 ebullition rate (see Figure S.3D). The ebullition rate at 20°C (E_{20}) at RB, was in all models > 400-fold higher than at CH (see Table S.1). At the RB location, depending on which temperature was used for the estimation, E_{20} ranged from 12.47 (T_{water}) to 24.82 mg CH_4 m^{-2} d^{-1} (T_{air}). The E_{20} rates of the other two locations, CH and OW, were considerably lower than RB and ranged between 0.03 and 0.06 mg CH_4 m^{-2} d^{-1}, with the highest E_{20} values obtained using T_{air}. The highest θ_s (1.33) and EA (2.21 eV) were found at CH, using T_{water} (HOBO). Whereas the location with the highest ebullition rates (RB), showed lower EA as CH, except for its highest EA (1.47 eV) using T_{sed}.

The Spearman correlation analysis revealed a significant negative correlation between the CH_4 ebullition rate and both the mean WL of the lake ($\rho = -0.68$, $p < 0.01$ (Holm's adjustment)) and the mean NO_3^- concentration at surface water ($\rho = -0.48$, $p < 0.01$; see Figure S.4). In contrast, CH_4 flux via ebullition is positively correlated with other factors: the SD of T_{water} ($\rho = 0.6$, $p < 0.01$), the mean CON of the surface water ($\rho = 0.72$, $p < 0.01$), and the mean NPOC, TDN, and SO_4^{2-} concentration of the surface water ($\rho = 0.65, 0.49, 0.5$, respectively; all $p < 0.01$). The influence of the environmental parameters at the three locations at Lake Neusiedl, characterized by distinct water properties, on the CH_4 ebullition rate is studied in detail by individual correlation analysis (see Figures S.5 to S.7).

At the CH location, CH_4 ebullition rates exhibited a significant positive correlation with temperature parameters, such as maximum T_{air} and median T_{water} ($\rho = 0.5, 0.53$, respectively; all $p < 0.01$), as well as with mean PPFD, VPD, and DIC concentration of the surface water ($\rho = 0.55, 0.56, 0.43$, respectively; all $p < 0.01$) (see Figure S.5). The ebullition rates of the CH were negatively correlated with the mean WL (HD Bgld) of the open water area of Lake Neusiedl ($\rho = -0.39$, $p < 0.01$), which is connected to the CH location through a channel.

At the OW location, the CH_4 ebullition rates showed a significant negative correlation with physical environmental parameters, such as, median and maximum PA, mean WD, and mean WL of Lake Neusiedl ($\rho = -0.66, -0.61, -0.54, -0.46$, respectively; all $p < 0.01$) (see Figure S.7). Furthermore, CH_4 ebullition rates also demonstrated a significant positive correlation with the mean DIC concentration of the surface water ($\rho = 0.53$, $p < 0.01$).

In contrast to the other two locations, the RB has the largest number of significantly correlated environmental parameters with the CH_4 ebullition rate (see Figure S.6). The CH_4 ebullition rates at the RB location showed, besides the influence of temperature, a significant negative correlation with mean WL, ORP, and maximum p_a ($\rho = -0.61, -0.5, -0.44$, respectively; all $p < 0.01$).

Temporal changes in water parameters were observed at CH, RB, and OW from late March 2021 to mid-July 2021 and are described in detail in Section S.1.6. From calendar week 27 (mid-July), no water level above the surface was observed at the RB location, therefore, there are no measurements available for this date and the campaign was concluded. Surface T_{water} increased over the measurement period from approx. 9°C to around 28°C at CH and OW, and from approx. 10°C to over 30°C at RB (see Figure S.10C). In contrast, ORP and WL decreased over the measurement period in all three locations (see Figure S.12A and B).

2.3.4 Diffusion of methane in space and time

After data quality checking, a total of 62 CH_4-diffusion rates (with $R^2 \geq 0.7$) of the three locations were used for subsequent analysis, accounting for about 77% of the total measured diffusion rates. The median CH_4 diffusion rate at RB was significantly higher compared to the median at the CH location (Dunn's post-hoc test, $p < 0.01$ (Holm's adjustment), effect size r = 0.5; see Figure 2.5A). Whereas the other locations were not significantly different from each other's median. Especially at RB and OW, CH_4 diffusion rates varied strongly within each location per week, and no clear temporal trend of the diffusion rates for the entire study period was evident at any location (see Figure 2.5B). Moreover, for the CH_4 diffusion flux, no significant correlation with any available environmental parameter was found.

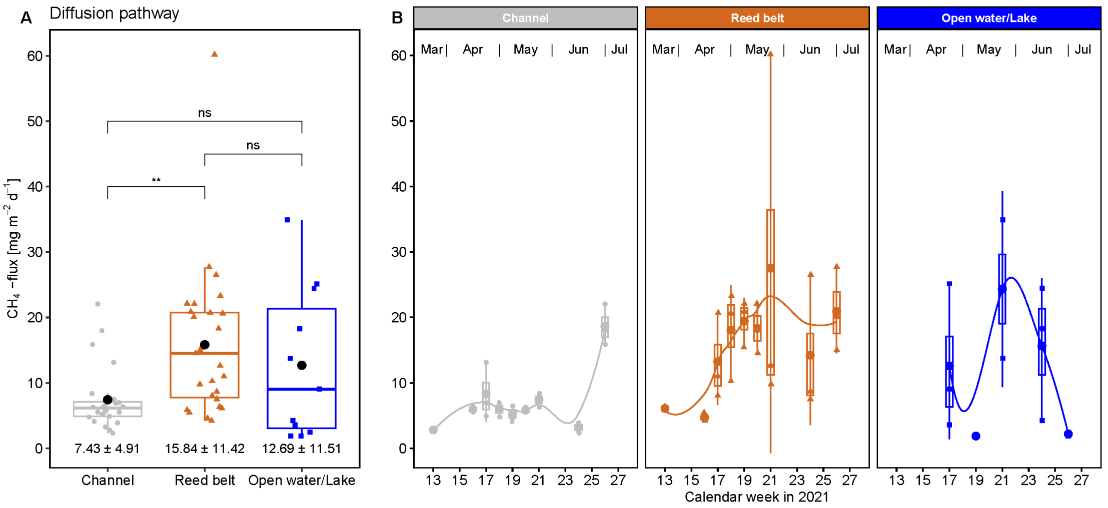

Figure 2.5: Methane diffusion rates and their spatial (**A**) and temporal (**B**) variability at Lake Neusiedl during the measurement period from March to July 2021 (locations: *Channel* (CH, gray), *Reed belt* (RB, brown), and *Open water/Lake* (OW, blue); black dots (●) showing mean value per location; number under boxplot per location in the left graph is mean ± standard deviation; Dunn's post-hoc test with non-significant (ns, $p > 0.05$) or significant (**, $p < 0.01$) differences (Holm's adjustment); the fitted lines show the local polynomial regressions (loess)).

2.3.5 Ebullition vs. Diffusion pathways

The aim of this part of the study was to explore the dominance or preference of these pathways within the ecosystem on a daily temporal scale and over a certain season (March to July 2021). The ebullition pathway of the CH_4 fluxes showed, at least at CH and RB, an increasing trend from March to July 2021 (see Figure 2.5B). In contrast, the diffusion rates displayed no distinct trend, regardless of the location (see Figure 2.5B). Independent of the location, the CH_4 ebullition rates had larger variance within each location per week than the CH_4 diffusion rates.

The median CH_4 diffusion rates were significantly higher than the median CH_4 ebullition rates in all three locations at Lake Neusiedl, especially at CH and OW (Dunn's post-hoc test, $p < 0.0001$ (Holm's adjustment), effect size $r = 0.66$ and 0.55; see Figure 2.6). Nevertheless, at the RB location, the mean CH_4 ebullition rate (17.18 mg CH_4 m^{-2} d^{-1}) was higher than the mean CH_4 diffusion rate (15.84 mg CH_4 m^{-2} d^{-1}). For both pathways, the RB location showed the highest CH_4 fluxes and the widest range (see Table S.2).

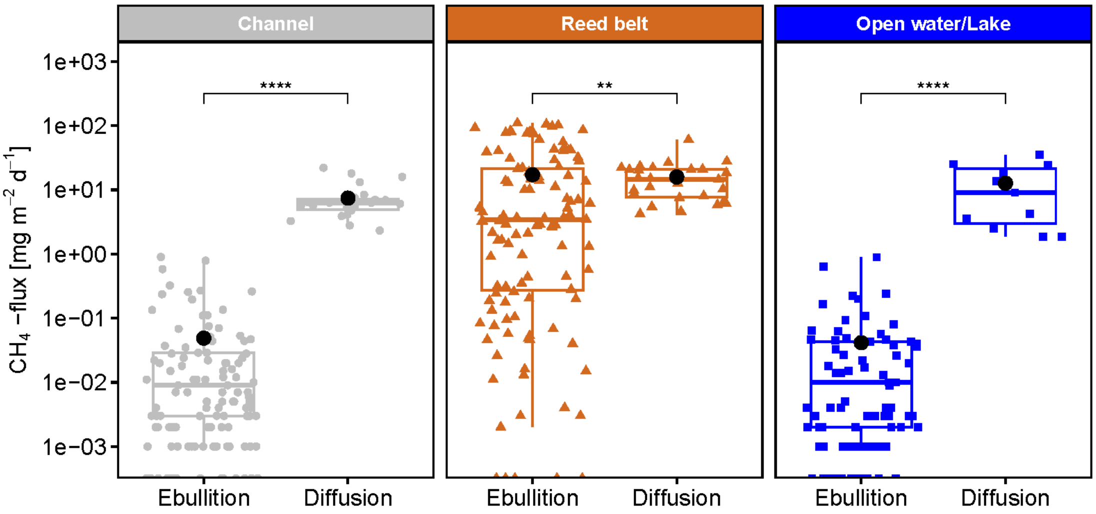

Figure 2.6: Methane ebullition and diffusion rates and their spatial variability at Lake Neusiedl during the measurement period from March to July 2021 (locations: *Channel* (CH, gray), *Reed belt* (RB, brown), and *Open water/Lake* (OW, blue); black dots (●) showing mean value per location; Dunn's post-hoc test with significant (**, $p < 0.01$) or very significant (****, $p < 0.0001$) differences (Holm's adjustment)).

For a better comparison between the two pathways, ebullition and diffusion, the cumulative sums of CH_4 fluxes were calculated for each ebullition trap or floating chamber at every location. This calculation spanned the entire study period. At CH and OW, the median cumulative CH_4 diffusion rates were significantly higher than the cumulative CH_4 ebullition rates ($p < 0.05$, effect size r = 0.80), whereas at RB, no significant difference was observed in the cumulative CH_4 rates between the ebullition and diffusion pathways (see Figure 2.7A). The median cumulative CH_4 diffusion rates were not significantly different between the locations, neither the cumulative ebullition rates between the CH and OW locations. Nevertheless, the cumulative CH_4 ebullition rates at RB were significantly higher compared to the CH and OW locations ($p < 0.001$, effect size r = 0.83 and 0.87, respectively). For both pathways, the highest mean cumulative CH_4 fluxes were found at RB, and, as a result, also the highest sum of the cumulative CH_4 ebullition and diffusion rates (see Figure 2.7B). The mean (± SD) share of the ebullition pathway on the total cumulative CH_4 emissions was 47.8 ± 17.0% for the RB location, whereas for the CH and OW locations, it was 1.2 ± 1.9% and 0.7 ± 0.7%, respectively.

By far, the highest cumulative sum of the bubble fluxes was found at OW (see Figure 2.7C), and not at RB location like for the cumulative CH_4 ebullition rates. The median cumulative bubble flux at the OW location was significantly higher compared to CH ($p < 0.001$, effect size r = 0.95) and to RB ($p < 0.01$, effect size r = 0.66). Meanwhile, the lowest mean cumulative sum of bubble fluxes was found at CH.

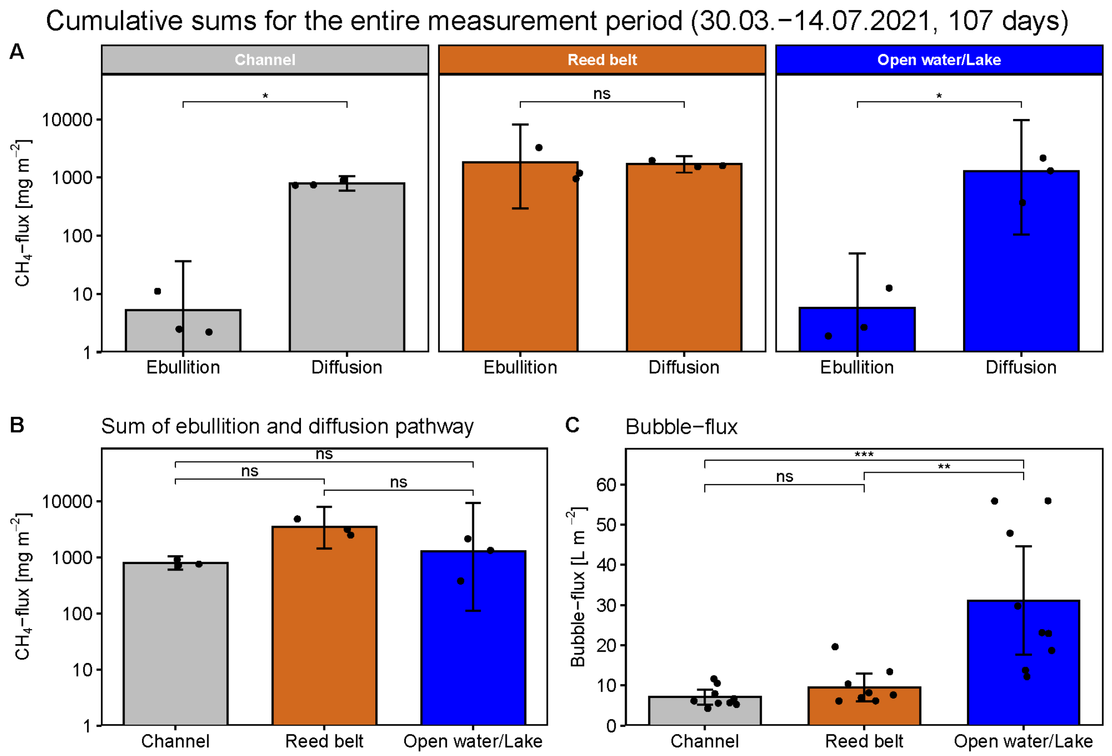

Figure 2.7: Cumulative sums of CH$_4$ ebullition and diffusion rates (**A**), total CH$_4$ emission rates (**B**), and bubble fluxes (**C**) for the entire measurement period of 107 days, separated by the three locations: *Channel* (CH, gray), *Reed belt* (RB, brown), and *Open water/Lake* (OW, blue). Black dots (●) showing the replicated measurements per location; colored bar indicates the mean value of the replicates per location; error bar presents the 95% confidence interval of the replicates per location; Wilcoxon signed-rank test with non-significant (ns, $p > 0.05$), significant (*, $p < 0.05$), (**, $p < 0.01$), or very significant (***, $p < 0.001$) differences (Holm's adjustment).

2.4 Discussion

2.4.1 Ebullition heterogeneity in space and time

This study explored the occurrences and CH_4 ebullition rates across three representative locations of Lake Neusiedl, continuously from late March to mid-July 2021. The location within the reed belt of Lake Neusiedl (RB) exhibited, by far, the highest CH_4 ebullition rates over the entire measurement period. One explanation for the elevated CH_4 ebullition rates at RB in comparison to the other two locations, may be the greater availability of organic matter, including both fresh and old reed biomass, along with higher NPOC concentrations in the RB area. This can be assumed by the fact that RB, in contrast to the other two locations, shows a significant positive correlation between NPOC and ebullition rate (see Figure S.6 in contrast to Figures S.5 and S.7). Another contributing factor might be the lower water levels at the RB site, leading to enhanced methanogenesis within the sediments due to elevated sediment temperatures compared to the other locations. This relationship can be confirmed by a significant negative correlation between water level and T_{sed} at the RB location (see Figure S.6).

The increasing trend in CH_4 emission rates, particularly at the RB site (but also at the CH site) from March to July 2021 (see Figure 2.3B), can be attributed to the seasonal pattern of influencing factors such as temperature and is therefore discussed in more detail in Section 2.4.3.

Although the mean and median CH_4 ebullition rates at CH and OW were not significantly different from each other, their temporal pattern over the measurement period varied. This disparity could be potentially attributed to distinct factors driving the release of bubbles, and perhaps with lesser influence, due to the different CH_4 production rates. This is shown by the fact that in OW the ebullition rate is influenced more by physical parameters (wind direction and air pressure), whereas in CH the temperature plays a major role (compare Figure S.7 with S.5). The differences between the locations could also be explained by considering that the produced CH_4 has been oxidized more strongly. Although ebullition is characterized for rapid release from the sediments to the atmosphere, allowing little to no reaction within the water column to occur, it cannot be completely ruled out. In addition, it should be noted that both CH and OW locations have consistently higher water levels than RB, and thus, a larger water column for interaction opportunities. Nevertheless, if CH_4 oxidation occurs, it is more likely to happen in the upper sediments rather than in the water column, if it occurs at all. We assumed this because in our study we did not find any correlation between the ebullition rate and the DO values in the water column.

Whereas the CH_4 ebullition rates showed strong differences between RB and the other two locations, the mean bubble flux showed no significant differences among any of the locations. This might be due to the reduction of CH_4 concentration in the trapped bubbles during the closure time due to diffusion (at the gas–water interface) or CH_4 oxidation. If this factor indeed had an impact, its magnitude would likely differ between the locations, resulting in different rates. Nonetheless, it is more likely that varying levels of CH_4 production in the sediments between the three locations explain the strong differences in ebullition rates. The OW location, which showed the highest bubble fluxes, experiences the strongest wind and wave influences, potentially triggering more frequent bubble release with distinct volumes and possibly lower concentrations compared to the other locations. This assumption can be confirmed by the fact that in OW, the bubble flux shows a significant positive correlation with the wind speed in contrast to the ebullition rate (see Figure S.7). Perhaps these wind and wave conditions also explain why the OW location showed an almost 3-fold higher mean and 5-fold higher maximum bubble flux compared to Canadian lakes (DelSontro et al., 2016), which share similar shallow conditions to Lake Neusiedl, but may not experience such strong winds and waves. However, the extent of this effect requires further investigation.

Soja et al. (2014b) estimated ebullitive CH_4 emissions at Lake Neusiedl using the same measurements they utilized for estimating CH_4 diffusion flux on six distinct days between 2011 and 2012. They did not employ a separate methodology such as ebullition traps. The authors used the CH_4 concentration leaps (if they occurred) during the 30-min closure time of the floating chambers as a basis to calculate the ebullitive flux. Using this method, Soja et al. (2014b) observed ebullition only in 40% of the chamber measurements. In contrast, our study conducted at Lake Neusiedl involves continuous measurements of ebullition rates, documenting ebullition occurrences in 88% of all observations. This suggests that measurements with ebullition traps offers a more comprehensive coverage of the spatial and temporal heterogeneity of ebullition compared to non-separate measurements using floating chambers. Furthermore, Soja et al. (2014b) do not provide average ebullition rates, though most of their reported ebullition rates seem to be higher than our values.

Among the very few studies related to ebullition in subsaline lakes, Aguirrezabala-Campano et al. (2019) did not detected ebullition in subsaline ponds in Spain during a total of 40 hours of continuous CH_4 measurement. The reason for this is not entirely clear, but one possibility could be that the short measurement period did not capture the sporadic release of ebullition bubbles. To avoid this possibility, we used longer closure time of ebullition traps (5–10 days) in our study. A study by Wang et al. (2021b) with potentially two subsaline lake sites (thermokarst lakes with conductivity values $>$ 1 mS cm^{-1}) found a negative correlation of the ebullition rate with salinity and therefore the lake site with lower conductivity showed the highest mean ebullition rate (27 mg CH_4 m^{-2} d^{-1}). In our study, however, it was the other way around, we found a positive correlation between ebullition rate and conductivity (see Figure S.4), because the location with the highest conductivity in the water (RB) showed the highest ebullition rates. At Lake Neusiedl, the rising conductivity values in the water of all three locations can be probably explained by the increasing concentration of salt due to the decline in water levels from March to July 2021 and the general differences of the water levels between the locations (see Figures S.10B and S.12B). The increasing concentration of salt may occur less in sediments than in the water column and therefore might not significantly contribute to the different CH_4 production rates between locations. Furthermore, Poffenbarger et al. (2011) confirmed that CH_4 emissions (from tidal marshes) decrease with increasing salinity, but only polyhaline systems (salinity $>$ 18 ‰) showed significantly lower CH_4 emissions. However, oligohaline marshes (salinity 0.5–5 ‰), which are comparable to subsaline lakes due to their salinity, have the most variable and significantly higher CH_4 emissions than other saline or freshwater systems (Poffenbarger et al., 2011). The high variability of CH_4 emissions from a subsaline lake can be confirmed with this study (see Table S.2).

Because there is hardly any published CH_4 ebullition study of subsaline lakes, a comparison with other (shallow) lakes is made. On average, CH and OW had very low CH_4 ebullition rates compared to RB (see Table S.2), to the global mean ebullition rate of freshwater lakes (40.1 mg CH_4 m^{-2} d^{-1}; Zheng et al. (2022b)), and to other related studies (Aben et al., 2017, Bastviken et al., 2008, Bogard et al., 2014, DelSontro et al., 2016). For example, the mean ebullition rates observed in OW or CH are 100-fold smaller than the mean ebullition rate from the small shallow lake Hummingbird, which is the lake with the lowest mean ebullition rate in the study of Bastviken et al. (2008). In contrast, the mean CH_4 ebullition rate at RB in our study is around 1.8-fold higher than the average ebullition flux recorded in the small shallow Lake Jacques during the dry summer of 2012, as reported by Bartosiewicz et al. (2015). Whereas the mean ebullition rate at RB is almost in the same range as the average ebullition rate of three Canadian lakes (17.6 mg CH_4 m^{-2} d^{-1}), where ebullition only occurred in water levels < 3 m (DelSontro et al., 2016). A possible explanation for this discrepancy could be that the salinity and sulfate concentration at Lake Neusiedl might have reduced or somewhat suppressed CH_4 production, consequently leading to lower CH_4 emission rates in comparison to Lake Hummingbird, the global mean ebullition rate of Zheng et al. (2022b), and other studies. Although most of these studies are from northern and small shallow lakes, which have different climatic and lake characteristics compared to our studied temperate, large, shallow and subsaline Lake Neusiedl, the RB location still has similar ebullition rates to some lakes. Presumably, the lower ebullition rate, especially in the OW location, can be better explained by the lower availability of substrate for CH_4 production.

In subsaline lakes, such as Lake Neusiedl, where salinity of 10–15 ‰ (Wang et al., 2017) are not reached, sulfate reduction and CH_4 production are processes that most likely occur at the same time and next to each other, allowing sulfate-reducing bacteria and methanogens to coexist and compete (Rosentreter et al., 2021). The ability of sulfate-reducing bacteria to outcompete methanogenic bacteria is well known. Lovley and Klug (1983) reported this process to occur even at freshwater sulfate concentrations. More recently, Kleint et al. (2021) reported CH_4 to be consumed via sulfate in sulfate–methane transition zones that have been observed for a few specific freshwater environments only. We did not examine these transition zones in the spatial resolution required to clearly detect them. Nevertheless, it appears reasonable that a gradient in the redoxcline found in a freshwater lake (Lake Willersinnweiher) by Kleint et al. (2021), can be also found in a subsaline environment such as Lake Neusiedl. Although, the $\delta^{13}C$-CH_4 values that we encountered are more depleted than the ones determined in Lake Willersinnweiher around the redoxcline.

Ebullition rates are rarely determined continuously, they are rather estimated as a side product of diffusion measurements using floating chambers on specific sampling days during daytime (Käki et al., 2001, Linkhorst et al., 2020, Soja et al., 2014b, Wang et al., 2021b). These short-term ebullition measurements probably miss most ebullition events, leading to an underestimation of the ebullition pathway (Bastviken et al., 2011, Wik et al., 2016). Some studies stir the sediments to artificially release the bubbles (Männistö et al., 2019, Schenk et al., 2021, Thottathil and Prairie, 2021), which can be used to estimate the original CH_4 concentration or the isotopic signature of the bubbles within the sediments (DelSontro et al., 2016). However, we needed an approach that could capture the temporal patterns of ebullition with the naturally released bubble size. Therefore, we desist from manually triggering ebullition events (unlike Thottathil and Prairie (2021)), as our aim was to investigate the natural ebullition occurrences and their underlying drivers, while preserving the integrity of the sediment surface by avoiding stirring. Furthermore, we chose to use bubble traps with longer closing times (5–10 days as e.g., in Aben et al. (2017), McClure et al. (2020)), which proved to be optimal for our study site, ensuring the accumulation of the minimum gas volume for extraction at all locations. It is important to note that this approach holds its own drawbacks, including plausible errors such as the underestimation of ebullition rates due to potential exchange between the trapped CH_4 and the underlying water column or the possible oxidation of the trapped CH_4 (DelSontro et al., 2016), or potential diffusion from the syringe to the atmosphere through the plastic and the stopcock during the closure period of the ebullition traps.

2.4.2 Isotope ratios and fractionation factors of ebullition gas

The measured $\delta^{13}C$-CH_4 values from this study confirmed the biogenic (also called 'bacterial' or 'microbial') origin of CH_4 at Lake Neusiedl, according to Whiticar (1999). Both, the $\delta^{13}C$-CH_4 and α_C values obtained in this study can be isotopically classified as indicative of CH_4 originating from freshwater sediments, in line with the classification provided by Whiticar and Faber (1986), and discarding a marine origin. Only a few α_C values were lower than 1.04, probably due to CH_4 oxidation. While Lake Neusiedl is not a marine ecosystem, it should be noted that due to its high salinity (2.1–5.2 g L^{-1}, transformed from CON values with the regional constant correction of Boros et al. (2014) due to the special salt composition, see Figure S.10B), the lake cannot be longer defined as a freshwater system (salinity < 1 g L^{-1}), but is rather classified as a subsaline lake according to Hammer (1986). Furthermore, both the water column of Lake Neusiedl and the pore water in the upper sediments have high sulfate concentrations, ranging from 250 to 1250 mg SO_4^{2-} L^{-1} (see Figure S.9A). These levels are typically found in brackish waters or even seawater, which would likely suppress CH_4 production.

Ebullition is recognized for lacking C fractionation, opposed to other processes such as diffusion or CH_4 oxidation. Therefore, the isotopic signature of the ebullition gases could be used as an indicator of the CH_4 source in the sediments. For Lake Neusiedl, this estimate would average -55.6 ± 5.9 ‰ VPDB $\delta^{13}C$-CH_4.

The α_C values derived from this study suggest the prevalence of the acetoclastic methanogenesis type at CH and OW according to Whiticar and Faber (1986) and Thottathil and Prairie (2021). Unfortunately, we are unable to provide a statement regarding the α_C values at RB, as the $\delta^{13}C$-CO_2 measurements were not feasible at that location. Nevertheless, considering that the $\delta^{13}C$-CH_4 values at RB are in the same range as at OW, it is likely that they share the same predominant methanogenesis type. Also, the fact that most organic material is found within the reed belt, which serves as main substrate for the dominant acetoclastic CH_4 production, could explain, among other reasons, the significantly higher CH_4 ebullition rates at the RB location in comparison to the other locations.

Furthermore, our study did not show a shift in methanogenic types with depth from acetoclastic (shallow water) to hydrogenotrophic methanogenesis (deep water) as in Thottathil and Prairie (2021), Wik et al. (2020). One reason could be that Lake Neusiedl is generally too shallow and therefore has no deep water zones. A second reason could be that the root exudates of the reed influence the entire lake, which is why acetoclastic methanogenesis dominates. A third reason could be that Lake Neusiedl and its microbial community are different from the studies of the northern lakes by Thottathil and Prairie (2021), Wik et al. (2020) due to the different climatic (and environmental) conditions.

At Lake Neusiedl, the acetoclastic methanogenesis was likely dominant throughout the entire study period, because δ^{13}C-CH_4 and δ^{13}C-CO_2 showed minor temporal variability (see Figure S.2A and B). This result is in contrast to the temporal pattern of the isotopic signature found in the study of Thottathil and Prairie (2021), which included a seasonal shift from hydrogenotrophic to acetoclastic methanogenesis over the season due to the change in substrate supply. The absence of a temporal pattern of the isotopic signature in our study could be due to the fact that the seasonal shift of methanogenesis types has not yet occurred, as there may not have been any relevant change in substrate availability. However, our study at Lake Neusiedl already showed a dominance of acetoclastic methanogenesis in spring and early summer, which is why a shift from hydrogenotrophic to acetoclastic cannot actually occur anymore. Nevertheless, acetoclastic methanogenesis seems to be more dominant in shallow than deep waters (Thottathil and Prairie, 2021, Wik et al., 2020), which we could confirm with this study for at least two locations in the shallow Lake Neusiedl.

Although the two locations, CH and OW, showed both a dominance in the diffusion compared to ebullition pathway (see Figure 2.6), they showed a significant difference in their median δ^{13}C-CH_4 values (see Figure 2.4A). This could be explained by the fact that in diffusion dominated systems, the variations in the extent of the CH_4 oxidation, besides the methanogenesis types, determine the isotopic signature of the emitted CH_4 (Happell et al., 1994). Whereas in ebullition dominated systems, variations in CH_4 production mechanisms mainly control $\delta^{13}C$-values of emitted CH_4 (Happell et al., 1994).

On average, CH exhibits more enriched δ^{13}C-CH_4 values compared to the other two locations. This could be attributed to higher CH_4 oxidation rates at CH, which tend to favor the lighter stable carbon isotope (^{12}C), resulting in an enrichment in δ^{13}C-CH_4 at this site in comparison to the other locations. δ^{13}C-CO_2 values were notably more depleted at CH (mean δ^{13}C-CO_2 of -14.6 ± 4.7 ‰ VPDB) compared to OW (see Figure 2.4B). This observation suggests that CH_4 oxidation likely occurred more intensively at CH compared to OW. Nevertheless, CH_4 oxidation at CH seems to be noticeably lower than, for instance, in a tropical lake that showed δ^{13}C-CO_2 values < -35 ‰ VPDB (Miller et al., 2022). At OW, CH_4 oxidation probably played a minor role, since the δ^{13}C-CO_2 values only showed slight depletion compared to atmospheric values.

The reed plant *Phragmites australis* is known to enhance aeration in certain parts of the rhizosphere through aerenchymatic oxygen (O_2) transport (Armstrong and Armstrong, 1990), facilitating CH_4 oxidation in the sediments. Moreover, in wetlands, the acetate production is commonly higher within the rhizosphere of vascular plants such as *P. australis* because of organic matter decay and root exudates, which favors the acetoclastic type of methanogenesis (Ström et al., 2003, 2005). The reed not only dominates the vegetation cover in the RB location but also surrounds the channels at the CH location. Therefore, our results corroborate this notion of Ström et al. (2003, 2005), as α_C in the CH location is lower than in the OW location (see Figure 2.4C and D), indicating a higher contribution of acetoclastic methanogenesis. However, a few α_C values from the RB location are even lower, beyond this range, indicating the occurrence of CH_4 oxidation.

2.4.3 Drivers of ebullition

The identified drivers of CH_4 ebullition fluxes differ among studies. Some studies found a temperature dependency of CH_4 ebullition rates, resulting indeed in seasonal patterns (Aben et al., 2017, Thottathil and Prairie, 2021, Wang et al., 2021a). The CH_4 ebullition rate may even rise by 6–20% per 1°C global temperature increase (if organic matter is not limited), thereby contributing to further global warming (Aben et al., 2017). Whereas Wang et al. (2021b) found no clear seasonal pattern of CH_4 ebullition rates related to temperature changes at thermokarst lakes on the Tibetan Plateau. In our study, we can confirm a seasonal pattern of ebullition (increasing trend from March to July 2021) at two of three sites on Lake Neusiedl, showing that even within a lake (and not only between lakes) the drivers of ebullition can be different.

According to DelSontro et al. (2016), this temperature dependency of ebullition is regulated by the ecosystem's trophic status (in their case, determined by total phosphorus) and weakens in oligotrophic lakes due to limitations in organic substrate availability. In addition, the study states that a strong positive interaction between phosphorus and temperature controls the predominant emission pathway where ebullition is disproportionately boosted. As CH_4 production is a function of temperature and Lake Neusiedl is eutrophic, we anticipated that ebullition rates would increase in all locations due to the persistent increase in water temperature, added to the fact of shallow water levels. This phenomenon was observed at RB and CH but not at OW. In the RB and CH locations, we could observe a temperature dependency of the ebullition rates, consistent with the findings of Aben et al. (2017), although they excluded saline and brackish waters in their study. However, our highest modeled E_{20} value at RB (24.82 mg CH_4 m^{-2} d^{-1}), which represents CH_4 ebullition at 20°C, was 10-times lower than the E_{20} values for the most comparable ecosystem (temperate ponds) in the study by Aben et al. (2017). These substantial differences could be attributed to variations in ecosystem types, nutrient status, organic matter availability, salinity, pH, or differences in the measurement intervals of the ebullition traps (24 h vs. 1 week) and associated effects (as mentioned in Section 2.4.1). Nevertheless, the overall system temperature coefficient, θ_s, at RB falls within the same range (1.11–1.22) as that of temperate ponds studied by Aben et al. (2017), with only the values at CH being higher (1.22–1.33). Especially the range of EA from the CH location (1.47–2.21) is higher than the mean ecosystem-level EA estimate of 0.96 eV in Yvon-Durocher et al. (2014) but still within the upper range of ecosystem-level EA estimates ($<$ 2.5 eV, Yvon-Durocher et al. (2014)) as well as in the range of ponds

(1.75 eV, DelSontro et al. (2016)) and temperate shallow lakes (1.85 eV, Schmiedeskamp et al. (2021)). Some differences could also result from differences in the used equations for conversion of θ_s to EA from Wilkinson et al. (2019). Nevertheless, both, the EA and the θ_s, indicated a high temperature-sensitivity of the ebullition pathway and its higher contribution with increasing temperature at the CH and RB locations at the shallow subsaline Lake Neusiedl. However, the values vary greatly depending on whether one takes sediment-, water-, or air-temperature (see Table S.1), which is why comparability may only be possible with the same temperature parameter.

As outlined by DelSontro et al. (2016), the processes influencing CH_4 emissions are more complex than originally thought. CH_4 ebullition rates not only depend on temperature but are rather regulated by an interaction between trophic status (e.g., total phosphorus) and temperature. In our study at Lake Neusiedl, we did not identify a correlation between the CH_4 ebullition rate and PO_4^{3-} concentration in the surface water. However, we did observe a positive and significant correlation of the ebullition rate with the TDN concentration in the surface water (see Figure S.4). In contrast, the nitrate concentration correlated negatively with the ebullition rate. This negative relationship, as discussed in Flury et al. (2010), can be explained by the possible coupling between CH_4 oxidation in the water column with denitrification. Similar to the effect of temperature increase, enhanced nitrogen availability (through e.g., deposition) can also stimulate methanogenesis through higher production of organic matter, consequently leading to an increase of CH_4 emissions (Flury et al., 2010).

In their study, Bogard et al. (2014) linked acetoclastic CH_4 production in the oxic water column to algal dynamics, indicated by chlorophyll-a concentration in water. Particularly within the reed belt of Lake Neusiedl (CH and RB locations), along the reed stands, we observed some algal growth during the study period. On 29 March 2021, the average chlorophyll-a concentration was < 1 µg L^{-1} in the RB and CH locations, and about 17 µg L^{-1} in the OW location. By 28 June 2021, the chlorophyll-a concentration in the water had increased to about 40 µg L^{-1} at OW, 56 µg L^{-1} at RB, and 80 µg L^{-1} at CH. OW exhibited the highest increase in chlorophyll-a, even though it did not have the highest CH_4 emission rates at Lake Neusiedl, unlike RB. Unfortunately, we have not continuously measured chlorophyll-a in the water throughout the entire study period. Thus, the statement of Bogard et al. (2014) cannot be confirmed at Lake Neusiedl with the current knowledge.

In northern temperate lakes, higher CH_4 ebullition rates were connected with an enrichment in $\delta^{13}C$-CH_4 values by supporting the prevalence of acetoclastic methanogenesis (Thottathil and Prairie, 2021). In contrast to Thottathil and Prairie (2021), we found no significant correlation between the ebullition rates and the $\delta^{13}C$-CH_4 values, despite the dominance of acetoclastic methanogenesis. This discrepancy could be due to the different lake characteristics and the occurrence of *P. australis.*

2.4.4 Diffusion of methane in space and time

CH_4 diffusion is a function of the gradient of CH_4 concentrations at the water–air interface. This gradient can be influenced by various factors, including wind (and waves), mixing of the water column and the solubility of CH_4 gas in the water, with the latter being influenced by temperature, salinity and pressure. Nevertheless, the primary influencing factor for diffusion flux is methanogenesis and its production rates.

In this study, the diffusion pathway was primarily measured for the purpose of comparison with the ebullition pathway. In all three locations at Lake Neusiedl, the water temperature increased over time (see Figure S.10C), which should have also increased the solubility of CH_4 gas in water. The salinity of the surface water, which can be estimated with the CON value (see Figure S.10B), increased slowly over time at the CH and OW locations, but very strongly at the RB location due to the more pronounced decrease of the water level. This decrease in water level would likely have decreased the solubility of CH_4 gas in water. Pressure fluctuations at all locations occurred during the study period, which could have also altered the solubility of CH_4 gas in water, but it would likely influence all three locations in a similar matter. Moreover, both the maximum and highest mean CH_4 diffusion rates were observed at the RB location. This could be attributed to several factors, including the higher salinity of the surface water, lower water levels, and the influence of wind on the water pools inside the reed belt.

In the OW location, the mean CH_4 diffusion rate was approximately 40% higher than at CH. These two locations had similar water levels, but the DO content in the water was higher at the OW location most of the time (see Figure S.11B). Taking into account the strong wind that exists at Lake Neusiedl, particularly in open water areas not protected by the reed, wind might be regarded as a crucial physical driver for diffusion emissions at OW due to its role in water mixing and the transport of new air parcels.

At Lake Neusiedl, Soja et al. (2014b) conducted measurements of diffusive CH_4 fluxes during 2011/2012 with six-month intervals and employed long closure periods for the floating chambers (30 min). The authors found that high CH_4 diffusion rates were observed at water channels within the reed belt only in early spring (April 2012), which may be attributed to delayed ice melt that resulted in the winter-delayed methane diffusion peak. Otherwise, the water channels exhibited CH_4 fluxes approximately two-thirds lower than the rest of the reed belt (Soja et al., 2014b). In contrast, our study demonstrates that there were no high diffusion rates observed during spring 2021, since there was no ice cover present at any location. However, the CH_4 diffusion rates we obtained in the CH location were, on average, up to half lower than those in the other two locations (RB and OW). This discrepancy could potentially be attributed to the more wind- and wave-protected nature of the CH location. In 2011/2012, the diffusion rates at Lake Neusiedl ranged from 2 to 50 mg CH_4 m^{-2} d^{-1} (Soja et al., 2014b), which falls within the same range as our observations. However, it is worth noticing that in our case, the diffusion rate exceeded the 35 mg CH_4 m^{-2} d^{-1} only once.

The mean CH_4 diffusion rate at OW (12.7 mg CH_4 m^{-2} d^{-1}) falls within the same range as the global mean diffusion flux from freshwater lakes (Zheng et al., 2022b) and the average pelagic diffusive flux from lake Cromwell (Bogard et al., 2014). Depending on the amount of precipitation in summer, a small shallow lake (Bartosiewicz et al., 2015) showed a slightly higher mean diffusion flux (dry summer) than our study or a lower flux (rainy summer) than two locations in our study. Whereas the average diffusion flux of three Canadian lakes (DelSontro et al., 2016) is more than twice as large as the highest mean diffusion flux (15.8 mg CH_4 m^{-2} d^{-1}, RB location) in our study. These differences could be explained by the different measurement periods between the respective studies (March-July vs. May-Oct) or to the differences in lake characteristics.

In comparison to subsaline ponds in Spain (ranging from 0.12 to 0.98 mg CH_4 m^{-2} d^{-1}; Aguirrezabala-Campano et al. (2019)), the diffusive CH_4 rates of our study were clearly higher. However, these ponds have significantly higher concentrations of sulfate in the water (> 1.2 g L^{-1}) than the subsaline Lake Neusiedl, which likely resulted in lower CH_4 production.

2.4.5 Ebullition vs. diffusion pathway

The ebullition pathway is rarely estimated because of the sporadic nature of ebullition episodes and their significant spatial heterogeneity. This makes determining ebullition challenging, potentially leading to an underestimation of CH_4 emissions in shallow lakes. Often, CH_4 ebullition rates are compared with CH_4 diffusion rates only when bubbles occur, omitting the periods of zero ebullition when calculating ebullition rates, or even neglecting the CH_4 ebullition in the CH_4 budget, as in Soja et al. (2014b). In addition, ebullition rates are sometimes measured with very short closure period (minutes-hours) and not continuously. These short-term measurements are often up-scaled to estimate ebullition rates over longer time periods. However, for a more accurate assessment of the significance of CH_4 release via bubbles, longer closure periods and extended measurement periods are required, ideally covering an entire season or even a full year. Omitting instances of zero CH_4 ebullition rates from the calculation of CH_4 emissions might result in an overestimation of the contribution of the ebullition pathway. In our study, we identified instances of zero CH_4 ebullition rates in 12% of the observations (and included them in the ebullition flux estimates), whereas Soja et al. (2014b) did not observe ebullition in 60% of their measurements.

Some studies consider the ebullition pathway for CH_4 fluxes of lakes to be more dominant than the diffusion pathway (Aben et al., 2017, Bastviken et al., 2011), or at least to play a significant role (DelSontro et al., 2016, Soja et al., 2014b). Camacho et al. (2017) studied CH_4 emissions, included ebullition but not measuring it with distinct methodologies, of saline lakes in Spain, having conductivity values higher than 7.2 mS cm^{-1}, which are higher and, therefore, maybe not comparable to conductivity values of subsaline lakes such as Lake Neusiedl (see Figure S.10B). Nevertheless, their CH_4 emission increased by 30–50% when adding ebullition to diffusion. One potential subsaline lake site (conductivity 1–3 mS cm^{-1}) in the study of Wang et al. (2021b) showed on average slightly lower ebullition contribution (47%) compared to diffusion, whereas all other lake sites had on average a dominance of the ebullition pathway. This example confirms that not all lake ecosystems behave in the same way and highlights the need for more accurate ebullition measurements to better understand and assess these systems.

Our study demonstrates that, on average and cumulatively, from March to July 2021, the diffusion pathway of CH_4 flux dominates over the ebullition pathway in two out of three locations at Lake Neusiedl (OW and CH). In contrast, the RB location at Lake Neusiedl presents a more complex scenario: the median CH_4 flux of the ebullition pathway was smaller than that of the diffusion pathway, whereas the mean values showed the opposite trend. Nonetheless, at this location, the mean values of the two pathways showed non-significant differences from each other. Additionally, at this location, the highest and lowest CH_4 flux rates were measured through the ebullition pathway. Cumulatively over the measurement period, from March to July 2021, both transport pathways at RB showed no significant difference. Further unraveling this complexity at the RB location would require more extensive ebullition measurements in the future, as this matter cannot be definitively addressed solely with the current findings at Lake Neusiedl.

2.5 Conclusions

Our study demonstrated a clear heterogeneity in CH_4 ebullition rates over both time (from March to July 2021) and space (locations) at Lake Neusiedl. By studying just three locations within the lake, not too far away from each other, we were able to observe the substantial influence of lake characteristics on CH_4 emission rates, particularly affecting the ebullition pathway. Thereby, the ebullition rates of distinct ecosystems within a lake should not be considered homogeneous due to the spatial differences in the influencing factors such as temperature, water level, and organic carbon, which strongly impact ebullition rates. Even though ebullition rates vary significantly within the lake, the dominant type of methanogenesis (acetoclastic) remains consistent throughout the lake.

The prevalence of the ebullition pathway over diffusion pathway, or vice versa, can vary considerably across different sites within a lake. In two out of three locations at Lake Neusiedl, an example for a subsaline lake, ebullition is not more important as CH_4 emission pathway than diffusion, whereas at one location, the two emission pathways are almost equally important.

Data availability

The data generated during this study are available at the PHAIDRA repository of the University of Vienna under `https://doi.org/10.25365/phaidra.424`.

3 Study II:
Consequences of intense drought on CO_2 and CH_4 fluxes of the reed ecosystem at Lake Neusiedl

Baur, P.A., Maier, A., Buchsteiner, C., Zechmeister, T., Glatzel, S.
Environmental Research, 2024, 262 (2), 119907.
`https://doi.org/10.1016/j.envres.2024.119907`

Graphical Abstract

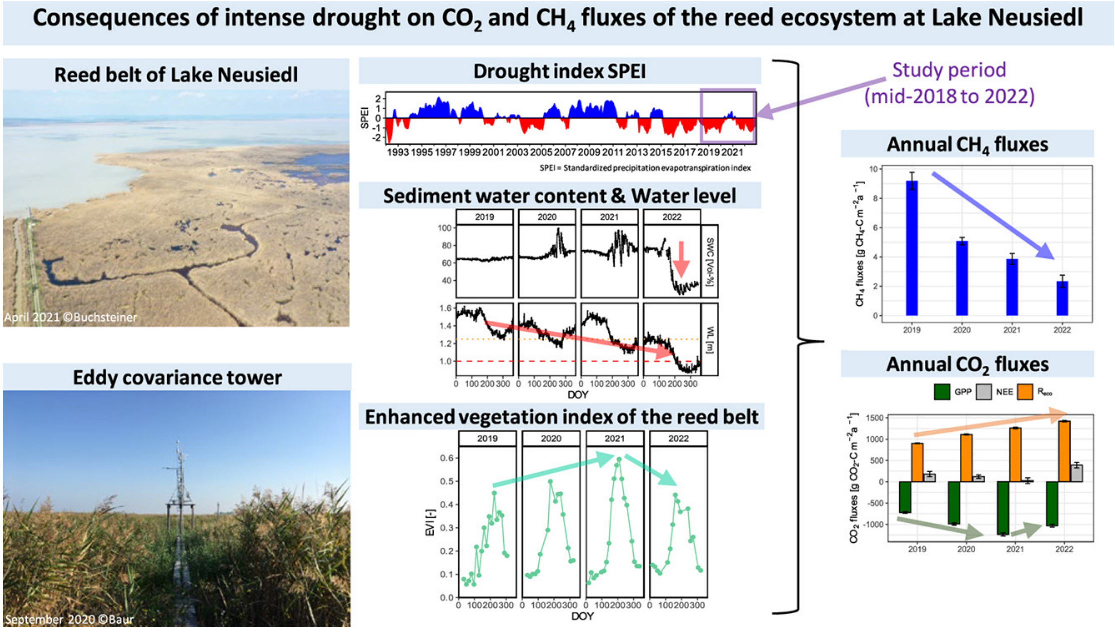

Highlights

- Falling lake water levels altered the mosaic in the reed belt and its carbon cycle.
- Initially, drought led to reed growth within the reed belt, reducing CO_2 emissions.
- With drop in sediment water content in 2022, CO_2 emissions doubled compared to 2019.
- Annual CH_4 emissions of the reed belt decreased strongly over 4 years (2019–2022).

Abstract

Reed (*Phragmites australis*) dominated wetlands are commonly known as strong carbon (C) sinks due to the high productivity of the reed plant and C fixation in the wetland soil. However, little is known about the effects of drought on reed-dominated wetlands and the possibility of Pannonian reed ecosystems being a source of greenhouse gases (GHG). The drought at Lake Neusiedl had a particular impact on the water level, but also had consequences for the reed belt. Therefore, we investigated the drought-influenced C fluxes and their drivers in the reed ecosystem of this subsaline lake over a period of 4.5 years (mid-2018 to 2022). We applied eddy covariance technique to continuously quantify the vertical turbulent GHG exchange between reed belt & atmosphere and used vegetation indices to account for reed growth.

Methane emissions decreased by 76% from 9.2 g CH_4-C $m^{-2}a^{-1}$ (2019) to 2.2 g CH_4-C m^{-2} a^{-1} (2022), which can be explained by the falling water level, the associated drying out of the reed belt and its consequences. Carbon dioxide emissions initially decreased by 85% from 181 g CO_2-C m^{-2} a^{-1} (2019) to 27 g CO_2-C m^{-2} a^{-1} (2021), but then increased to twice the 2019 level in 2022 (391 g CO_2-C m^{-2} a^{-1}). Due to the drying reed belt, the reed initially grew into formerly water-covered areas within the reed belt, especially in 2021, leading to higher photosynthesis through 2021. This development stopped and even reversed in 2022 as a consequence of the sharp decrease in sediment water content from about 65 to 32 Vol-% in mid-2022.

Overall, drought led to a decoupling of the reed ecosystem from the open lake area and developed the wetland into a strong C source.

3.1 Introduction

Although wetlands cover only about 5–8% of the world's land surface (Davidson et al., 2018a, Mitsch et al., 2013), they may be a net carbon (C) sink of about 685–830 Tg C a^{-1} (Li et al., 2023, Mitsch et al., 2013). Nevertheless, wetlands act as a natural source of methane (CH_4) due to CH_4 production mainly in their anoxic waterlogged sediments, emitting on mean 149–181 Tg CH_4 a^{-1} (2008–2017, Saunois et al. (2020)), which is about 35–42% of the natural aquatic CH_4 emissions (Rosentreter et al., 2021). Wetland ecosystems and other inland waters are the largest contributors to the uncertainty in the global CH_4 budget

(Saunois et al., 2020). Consequently, there is a pressing need for more CH_4 measurements in wetlands in order to reduce the uncertainty. In particular, wetlands dominated by wetland plants such as common reed (*Phragmites australis*) should be considered, as these are able to enhance the transport of gas (van den Berg et al., 2016). In reed ecosystems, plant-mediated transport is the dominant and highly effective transport pathway of CH_4 from soil to atmosphere (Brix et al., 2001).

Furthermore, these reed ecosystems are mainly known as strong carbon dioxide (CO_2) sinks due to their high photosynthetic assimilation and soil C sequestration (Brix et al., 2001, van den Berg et al., 2016, Zhang et al., 2016). Consequently, wetlands with reeds often show highly negative annual CO_2 fluxes (high CO_2 uptake), as measured by eddy covariance (EC) technique. However, the magnitude of this flux varies considerably, from -901 g CO_2-C m^{-2} a^{-1} in estuaries to -65 g CO_2-C m^{-2} a^{-1} in tidal wetlands (Gao et al., 2021, Huang et al., 2020, Sanders-DeMott et al., 2022, van den Berg et al., 2016, Zhang et al., 2016, Zhong et al., 2016, Zhou et al., 2009). Most of these studies are located in coastal wetlands, which Lu et al. (2017), found to be larger CO_2 sinks on average than inland wetlands. *P. australis* wetlands have a median annual CH_4 emission of about 12 g CH_4-C m^{-2} a^{-1} based on EC studies, but also offer a wide range from 3 g CH_4-C m^{-2} a^{-1} in tidal wetlands to 28.8 g CH_4-C m^{-2} a^{-1} in oasis-desert areas (Gao et al., 2021, Sanders-DeMott et al., 2022, Serrano-Ortiz et al., 2020, van den Berg et al., 2016, Zhang et al., 2016, Zhou et al., 2009). Whereas, lakes (Golub et al., 2023) and especially shallow lakes can act as sources of CO_2 (94.2–99.4 g CO_2-C m^{-2} a^{-1}) and CH_4 (3.7–4.3 g CH_4-C m^{-2} a^{-1}), especially when the organic C content of water and sediment is high (Heiskanen et al., 2023). None of the aforementioned examinations focused on the effects of drought conditions on reed-dominated wetlands and were located in a Pannonian ecosystem under a dry sub-humid climate. This emphasizes the need for further investigation into the possibility of central European reed belts of lakes acting as a source of greenhouse gases (GHG) due to drought (Čížková et al., 2013).

Globally, the water volume of more than half of all large lakes ($>$ 100 km^2), including Lake Neusiedl, has decreased over the last three decades (1992–2020) due to anthropogenic and climatic factors such as increased water consumption or evaporation (Yao et al., 2023). Lake Neusiedl, with an area of about 320 km^2, is a shallow and subsaline lake on the Austrian-Hungarian border with no natural outflow. More than half of Lake Neusiedl is covered by a reed ecosystem, which, depending on the water level and season, is a mosaic of reed patches with *P. australis*, water, and open sediment areas (Buchsteiner et al., 2023). It is the second largest coherent reed ecosystem in Europe. The importance of the lake is reflected in its status as a Ramsar site, a national park, and a UNESCO World Heritage Site. Due to its shallowness and its high dependence on water supply from direct precipitation (79%), the lake is very sensitive to climatic changes (Soja et al., 2013) such as droughts. Drought can reduce the annual gross primary production (GPP) and CH_4 emissions of wetlands (Chamberlain et al., 2020, Helfter et al., 2022) and shallow lakes (Heiskanen et al., 2023), but it can also promote rapid spread of vegetation in former water areas and enhance GPP (Koebsch et al., 2020). Drought can therefore not only influence the water levels and volumes of lakes, but also the C fluxes of their reed belts.

So far, only one GHG budget study of Lake Neusiedl has been conducted by Soja et al.

(2014b). However, the study was limited to five measurement days, exclusively consider the water–air interface as emission pathway and did not consider winter emissions in the upscaling process to the annual C budget of the lake. Nevertheless, the authors estimated that 2/3 of the lake's C emissions originated from the reed belt, although they did not consider the highly effective plant-mediated gas transport of *P. australis* (van den Berg et al., 2020). Rõõm et al. (2014) demonstrated the necessity to consider GHG emissions from helophytes such as *P. australis* in the lake's net GHG budget, even if the area coverage of helophytes is small. Consequently, the contribution of the reed belt to the GHG budget of Lake Neusiedl in Soja et al. (2014b) was most likely underestimated and requires further investigation. Other studies have investigated the transport pathways of CH_4 emissions at Lake Neusiedl individually: Brix et al. (2001) showed that the plant-mediated transport of *P. australis* was mainly a convective gas flow during time in July. While Baur et al. (2024a) found that the cumulative contribution of ebullition as CH_4 emission was not significantly different from the diffusion pathway. Therefore, the current study aims to fill the research gaps by continuously quantifying the total emissions of the reed belt, including the important plant-mediated transport of *P. australis*, over several years.

Thus, we conducted this study at the reed belt of the subsaline, shallow Lake Neusiedl with the following research questions: **A)** What are the effects of drought on C fluxes in a reed ecosystem over several years? **B)** How does the decreasing water level (WL) affect the temporal (diurnal, seasonal, annual) variations of the C fluxes in a reed wetland ecosystem? **C)** What are the drivers of the C fluxes in a subsaline reed ecosystem?

3.2 Material and methods

3.2.1 Study site

Lake Neusiedl (Fertő), the westernmost "steppe" lake in central Europe, is characterized by subsalinity (Hammer, 1986) with sodium bicarbonate as the main salt (Wolfram and Herzig, 2013), alkalinity (7–15 mmol L^{-1} and pH 8.5–9, Zoboli et al. (2023)), and shallowness (maximum WL 1.8 m, Wolfram and Herzig (2013)). The lake has an artificial outflow, which has been closed since mid-March 2015 (HD Bgld, 2023d) due to the low WL of the lake. The reed belt of Lake Neusiedl is dominated by *Phragmites australis* and covers more than half of the lake (181 km^2, aerial photographs of 2007/2008, Csaplovics (2019)).

The study site is located in the eastern reed belt of Lake Neusiedl near Illmitz in Austria (47.7692° N, 16.7585° E; 116 m above sea level; see Figure 3.1) and in the "nature (core) zone" of the transborder national park 'Neusiedler See – Seewinkel / Fertő – Hanság'. According to Nemeth and Dvorak (2022), the reed stands at the study site are older than 14 years since they were last cut or burned. The site has a mean annual air temperature of 11.3℃ and an annual precipitation of 500.2 mm (1993–2022, data from UBA (2023)).

The reed biomass, harvested at the study site in 10 randomly selected plots within the footprint of the EC tower in October/November 2022 (see Table S.4 for coordinates), stored 1.44 ± 0.66 kg C m^{-2} aboveground (mean ± standard deviation (SD))

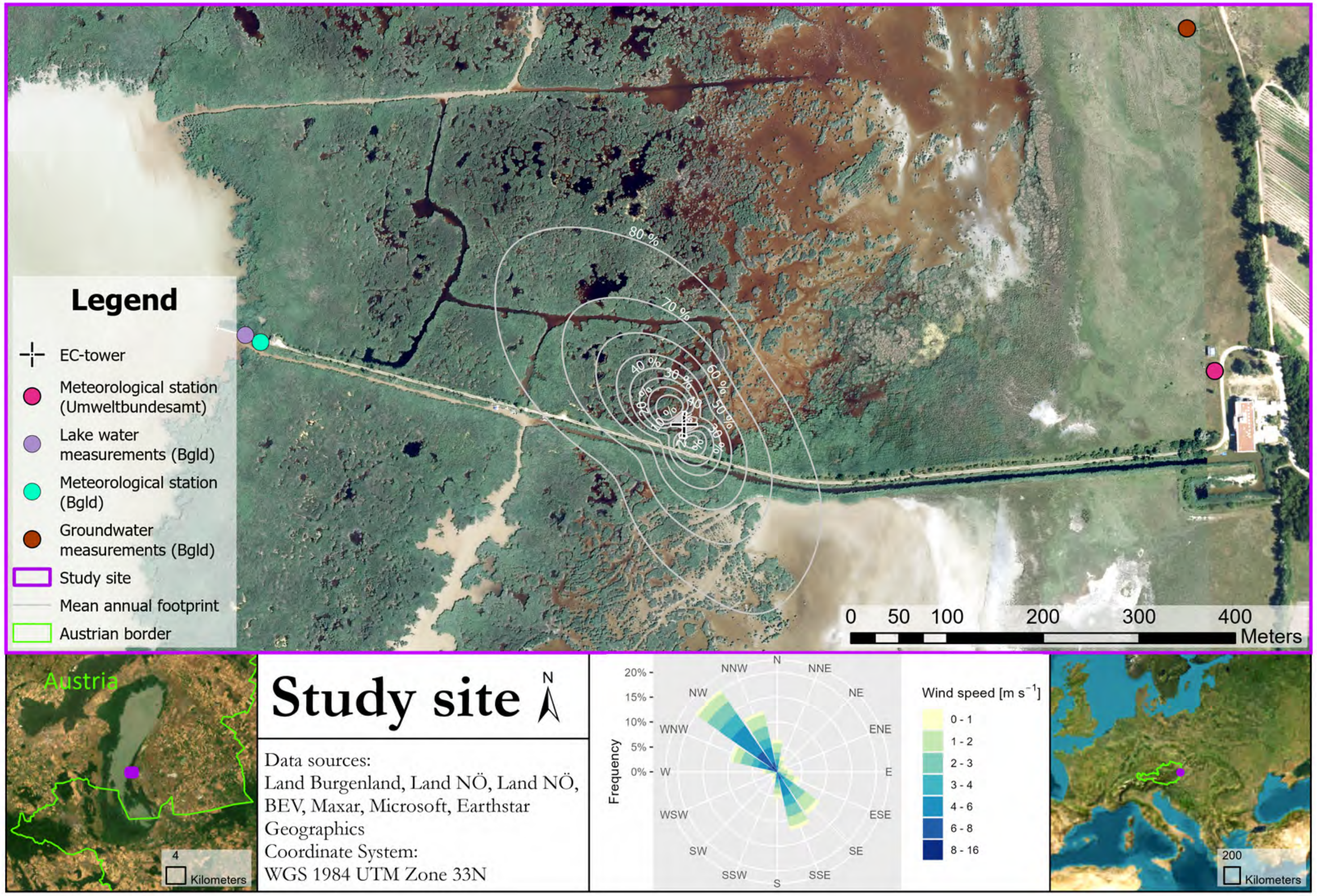

Figure 3.1: The study site is located in the eastern reed belt of Lake Neusiedl near Illmitz in Austria, showing the position of the eddy covariance (EC) tower, the 80% annual mean footprint of the EC tower from 2019, and a wind rose with the two main wind directions at this site.

and 2.33 ± 1.28 kg C m^{-2} belowground to a depth of 30 cm. About 99% of total C was organic, and on average about 50% of the aboveground biomass was litter. In fall 2022, the average shoot density was 159 ± 85 shoots m^{-2} (Holzer, 2024).

The reed belt had two visually distinct sediment layers: an organic (peaty) layer at the top — with a depth of 9.3 ± 1.8 cm and a C content of 15 ± 4.7 mass-% in 2021 — and a sandy layer below (C content of 3.2 ± 0.1 mass-% in 2021). The surface water in the reed belt had a pH of 8.9 ± 0.1 and an electrical conductivity of 4.6 ± 1.4 mS cm^{-1} in 2021 (Baur et al., 2024a). The average height of the vegetation (reeds) at the study site was 2 m.

3.2.2 Eddy covariance and biometeorological measurements

EC measurements at time intervals of 10 Hz have been conducted at the study site since July 2018. A 4.5-year data set (until end of December 2022) is used in this study. The 8.5 m high EC tower is equipped with an enclosed infrared CO_2/H_2O gas analyzer LI-7200RS, an open-path CH_4 gas analyzer LI-7700 (both from LI-COR Inc., Lincoln, USA), and a 3-D ultrasonic anemometer (WindMaster Pro, Gill instruments Limited, Lymington, UK). The following biometeorological measurements were performed on the EC tower at 1 min intervals. Air temperature (T_{air}) and relative humidity (rH) were measured (HMP155, Vaisala Oyj, Helsinki, Fl). Three self-calibrating sediment heat flux (SHF) plates (HFPO1SC, Hukseflux Thermal Sensors B.V., Delft, NL) were used at a depth of 5, 10, and 15 cm. The incoming and outgoing shortwave and longwave radiation (SW_{in}, SW_{out}, LW_{in}, LW_{out}) were measured (CNR4, Kipp & Zonen B.V., Delft, NL). Photosynthetically active photon flux density (PPFD) was measured with a quantum sensor (LI-190/R, LI-COR Inc, Lincoln, USA). Three sediment probes (Hydra Probe II, Stevens Inc., Portland, USA) measured sediment temperature (T_{sed}) and volumetric sediment water content (SWC) at 5, 10, and 15 cm depth. All sediment sensors were replaced on 9 October 2020 due to dry fall of the reed belt.

To fill the gaps in our meteorological data set, parameters such as T_{air}, rH, air pressure (PA), SW_{in}, and precipitation (P) were obtained from the meteorological station of UBA (2023), located about 550 m east of the EC tower (47.769553° N, 16.765865° E), and from the observation station of HD Bgld (2023a), located about 440 m west of the EC tower (47.769996° N, 16.752730° E). Surface water temperature (T_{water}) and WL of Lake Neusiedl near Illmitz from the latter station (HD Bgld, 2023a) were used as additional data. For our analyses, we used the mean P of these two stations, as our EC tower is located in the middle of both stations. Additionally, we used groundwater depth (GW) data from HD Bgld (2023b), measured at the landward edge of the reed belt (47.77274° N, 16.76568° E) and about 670 m northeast of the EC tower. The locations of all monitoring stations are shown in Figure 3.1.

3.2.3 Eddy covariance data processing

The EC data were processed into half-hourly CO_2 and CH_4 fluxes using EddyPro software, version 7.0.8 (LI-COR, Inc., Lincoln, USA). The anemometer's tilt correction was performed using the planar fit method without velocity bias and with fitting planes coefficients for eight wind sectors according to van Dijk et al. (2004). The angle-of-attack correction for wind components was performed according to Nakai and Shimoyama (2012) due to the known *w-boost* bug of the Gill ultrasonic anemometer WindMasterPro. Wherever possible, WPL (Webb–Pearman–Leuning) conversion from density to mixing ratios was applied (Burba et al., 2012, Ibrom et al., 2007, Webb et al., 1980). Time-lags between anemometer and other high-frequency measurements (CO_2 and CH_4) were compensated with the automatic time lag optimization in EddyPro. The estimation of the footprint of the EC measurements was carried out according to the method of Kljun et al. (2015). Despiking and statistical screening of the raw data and filtering of (co)spectra (removing low data quality, flag value = 2) were performed according to the test results of Vickers and Mahrt (1997) and Mauder et al. (2013). Analytic corrections of high-pass filtering effects (Moncrieff et al., 2005) and of low-pass filtering effects (Fratini et al., 2012) were applied. Corrections for spectral losses due to physical instrument separation (for cross-wind and vertical wind) were made according to Horst and Lenschow (2009). All data were checked for plausibility. Raw data coverage of flux measurements was 93% for CO_2 and 64% for CH_4. These data gaps were caused by instrument/sensor failures, precipitation, cobwebs or dust in the open-path measurement cell of the gas analyzer, implausible values, sensor/instrument repair times or lack of power.

The Mauder and Foken (2015) data quality control (QC) flagging system, which ranges from 0 (high-quality data) to 2 (low-quality data), was applied and only the highest quality data (filtered out QC flag ≥ 1) were used for threshold estimation of u* (friction velocity) and subsequent analysis. The high-quality data set (prior to u* filtering) had a coverage of 54% for CO_2 fluxes and 38% for CH_4 fluxes. Flux measurements taken under insufficient turbulence conditions were excluded below a seasonal site-specific threshold for u* (see Table S.3). This was done with the moving-point test of Papale et al. (2006) using the REddyProc tool (Wutzler et al., 2018) and with continuous seasons to avoid breaks at annual boundaries (Papale et al., 2006). If too few records per season were available (at least 700 for 7 temperature classes, Papale et al. (2006)), the maximum seasonal u* threshold of the entire data set was used (from winter to fall: 0.211, 0.183, 0.404, and 0.381 m s^{-1}) and marked with $^+$ in Table S.3. After u* filtering, the data set had a data coverage of 41% for CO_2 fluxes and 30% for CH_4 fluxes.

Gap-filling of the flux data was performed using various methods. Here we present the approach that yielded the best results for our wetland site. The marginal distribution sampling (MDS) approach of Reichstein et al. (2005) with the predictors T_{air}, SW_{in}, and VPD (water vapor pressure deficit) was chosen for gap-filling of net CO_2 fluxes (NEE = net ecosystem exchange) due to its good performance ($R^2 = 0.92$ and NMAE (normalized mean absolute error) = 0.27) and was performed with REddyProc (Wutzler et al., 2018). For the CH_4 fluxes, the machine learning algorithm xgBoost (xgb - extreme gradient boosting) showed the best gap-filling performance with all available predictors ($R^2 = 0.84$ and NMAE = 0.22), as did the EC CH_4 flux data sets from wetlands in Irvin et al. (2021a). For the latter, we used the Python toolkit *FluxGapfill* (version 0.2.1; Irvin et al. (2021b)) performing with the Python version 3.11.0 (Van Rossum and Drake, 2009). The random uncertainty estimation of the gap-filled (predicted) C fluxes was carried out by bootstrapping using a 95% confidence interval (CI) of 10 000 mean random samples (normal distributed). For the observed C fluxes, the random error estimation of Finkelstein and Sims (2001) was used. The total random uncertainty of the predicted and observed fluxes was combined by the quadratic error propagation as described in Richardson and Hollinger (2007).

The half-hourly MDS gap-filled NEE were partitioned into its two components, GPP and ecosystem respiration (R_{eco}), using the nighttime approach according to Reichstein et al. (2005) in REddyProc.

We used the micrometeorological sign convention for C and energy fluxes, which states that negative fluxes represent the uptake of the ecosystem from the atmosphere and positive fluxes represent the release from the ecosystem to the atmosphere. All C and energy fluxes include the storage term.

3.2.4 Vegetation indices and reed growth data

The land cover classification of water, open sediment, and vegetation (reed) areas of the study site is described in detail in Buchsteiner et al. (2023): The deep learning technique CNN (convolutional neural network) was applied to aerial imagery to identify the three classes. The land cover of 18 June 2021 was classified on high-resolution drone images (about 2.5 cm/pixel) and has been published in Buchsteiner and Baur (2023). The land cover analysis of 26 June 2019 and 3 July 2022 was performed on orthophotos obtained from BEV (2019) and GeoData Bgld (2024). Due to the lower resolution of the orthophotos (20 cm/pixel), small adjustments had to be made.

Since fall 2020, a Phenocam has been installed on the EC tower, facing the main wind direction northwest in order to study the phenological changes of *P. australis*. The image analysis of the Phenocam data is described in detail in Buchsteiner et al. (2023): Using the R package *phenopix* (Filippa et al., 2020, 2016), the green chromatic coordinates (GCC) were calculated as a vegetation index and the daily averaged GCC were filtered with the *max* approach following Sonnentag et al. (2012). In this study, the full GCC data set from 15 September 2020 to the end of 2022 was used, while the year 2021 has already been published in Buchsteiner and Baur (2023).

Vegetation indices calculated from satellite data can be a helpful and non-destructive tool to estimate the reed growth and biomass change over the season and between the years. The vegetation indices NDVI (normalized difference vegetation index), EVI (enhanced vegetation index), and LAI (leaf area index) from the MODIS (moderate-resolution imaging spectroradiometer) satellite data set were used. These indices have a spatial resolution grid of 250 or 500 m and a temporal resolution of 16 or 8 days (the latter always for LAI). The R package *MODISTools* (Hufkens, 2022, Tuck et al., 2014) was used to download and process the MODIS data products. We checked the quality and filtered the MODIS indices with the included QC flags: NDVI and EVI data were of good quality if the QC rank was present and < 3. LAI data were of good quality if the QC flag was < 19 and a SD value of the LAI value was present. The used coordinates are located in the 80% annual mean footprint of the EC tower (see Figure 3.1) and do not include a gravel road, shrubs, or trees along it: For the NDVI and the EVI, the mean values of the pixels of two coordinates were used: 125 m (47.769979° N, 16.757789° E) and 250 m (47.771118° N, 16.756866° E) northwest of the EC tower. For the LAI, only the pixel with the coordinate 125 m northwest of the EC tower was used due to the lower resolution of the spatial grid of this data product.

3.2.5 Data and statistical analysis

Most data and statistical analyses were performed in R version 4.2.2 (R Core Team, 2022) using the following R packages for data processing and visualization: *data.table, DTSg, ggpubr, ggplot2* (Dowle and Srinivasan, 2023, Hepp, 2022, Kassambara, 2023a, Wickham, 2016). The drought index SPEI (standardized precipitation evapotranspiration index) is capable of detecting drought at both shorter and longer time scales (Vicente-Serrano et al., 2010). It was calculated with a 12-month time scale for the reed belt of Lake Neusiedl from 1992 to 2022 using the R package *SPEI* (Beguería and Vicente-Serrano, 2023), the daily mean T_{air} & P sum from UBA (2023) and the potential evapotranspiration (PET) equation according to Thornthwaite (1948). Spearman correlation analyses between fluxes and environmental variables were performed using the R package *ggstatsplot* (Patil, 2021) and the correlation coefficients (ρ) shown are significant with $p < 0.01$ (Adjustment Holm). The R package *boot* (Canty and Ripley, 2021, Davison and Hinkley, 1997) was used for bootstrapping.

3.3 Results

3.3.1 Environmental parameters of a subsaline reed ecosystem

Since mid-2015, the frequency and duration of drought in the study site have increased considerably, as shown by the drought index SPEI in red periods with negative values in Figure 3.2A. As a result, the annual mean of the daily water level (WL) in Lake Neusiedl's open water (Biological Station Illmitz) decreased from 1.49 m in 2018 to 1.08 m in 2022 (see Figure 3.2B, bottom row). Additionally, the annual maximum and minimum of the daily WL also decreased from 1.66 m to 1.33 m and 1.27 m to 0.87 m, respectively, during the same period. The WL showed a seasonal pattern, with the highest WL in spring and the lowest in fall, which persisted over the years. However, in fall 2022, the WL was about 40 cm lower than in fall 2018. Additionally, the difference in WL between the beginning and end of each year ranged from 0 cm (2020) to -24 cm (2022).

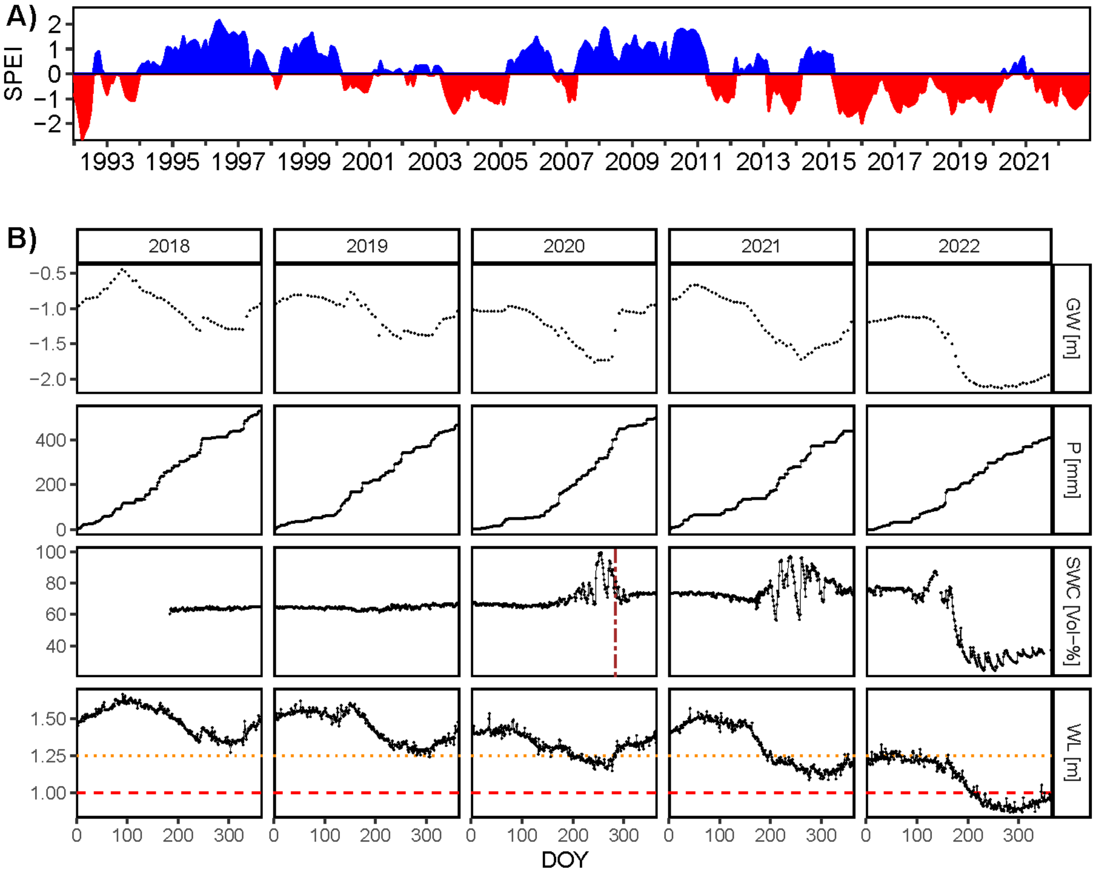

Figure 3.2: **A)** Temporal change of the drought index SPEI (standardized precipitation evapotranspiration index) with a 12-month time scale for the reed belt of Lake Neusiedl from 1992 to 2022 (data source for the calculation: UBA (2023); dry periods in red and as negative values). **B)** Temporal variation of groundwater depth (GW) at the landward edge of the reed belt, cumulative sum of precipitation (P), sediment water content (SWC) in 5 cm depth at the reed belt, and the daily mean water level (WL) of the open water of Lake Neusiedl (Biological Station Illmitz) per day of year (DOY) from 2018 to 2022 (Data source of WL and GW: HD Bgld (2023a,b)). Our estimated WL threshold for a (mostly) dry reed belt at 1.25 m WL of the open lake (orange dotted line) and a completely dry reed belt at 1 m WL of the open lake according to Wolfram et al. (2020) (red dashed line) without considering the water channel (with dredging) that runs across the reed belt from the Biological Station to the open lake area along the dam pathway. The brown dashed vertical line shows the date (9 October 2020) when the sediment sensors were replaced.

Not only the WL of the open lake water area showed a decreasing trend in the annual average from 2018 to 2022, but also the GW depth at the landward edge of the reed belt (see Figure 3.2B, first row). The SWC of the reed belt at a depth of 5 cm remained almost constant at about 65 Vol-% until mid-2020 (see Figure 3.2B, third row). In the second half of 2020 and 2021, the areas around the EC tower fell dry, causing the sediment to crack. This led to these large fluctuations in SWC caused by P events. However, the SWC in the upper (organic) layer of the sediment remained relatively high until it suddenly dropped to about 32 Vol-% in mid-2022.

Potential threshold for lateral flow

Due to the shallowness of the lake and strong winds from the two main wind directions (NW (northwest) and SE (southeast), see wind rose in Figure 3.1), the WL can differ greatly between the eastern and western sides of Lake Neusiedl. We found that the WL (measured in the open water area near the reed belt, see Figure 3.1) was different from the daily mean WL at wind speeds of ≥ 4 m s^{-1}, independent of the main wind directions (see Figure S.16A). Compared to the weekly mean WL, differences in the WL were already observed at wind speeds ≥ 2.5 m s^{-1} (see Figure S.16B). These two wind speeds could be potential thresholds for lateral currents. At the study site, wind speeds of ≥ 4 m s^{-1} ($\approx$ potential lateral flow times) from NW were recorded on 83 days and from SE on 31 days per year (median 2018–2022). 2022 showed the shortest duration of strong winds from SE (21 days). However, based on field observations, we estimated a threshold of 1.25 m of the WL of the open water area of Lake Neusiedl (Biological Station Illmitz) for a possible dry reed belt, where there was (almost) no water above surface at our study site (see Figure 3.2B). Considering the time periods when the WL exceeded our estimated WL threshold, the potential lateral flow times decreased since 2020, but especially in 2022 to 0.4 days from SE and 7 days from NW. Regardless of a WL threshold, the number of potential days of lateral flow from NW was always higher than from SE.

Land cover share

Furthermore, the water coverage share in the 80% annual mean footprints (source area) of the EC measurements decreased by 26.2% from June 2019 to July 2022 (see Figure 3.3 and Table S.7). In 2021, open sediment areas appeared and covered 1.9% of the 80% annual mean footprint in June and increased to 8.1% in July 2022. Additionally, the share of the reed land cover class in the 80% annual mean footprints increased by 18% from 2019 to 2021 and remained stable at 85% in 2022 (see Figure 3.3 and Table S.7). The change in the land cover of the reed belt resulted in a change in the albedo. This is demonstrated by the SW_{out}, which showed higher summer values in 2021 and 2022 compared to previous years (see Figure S.19).

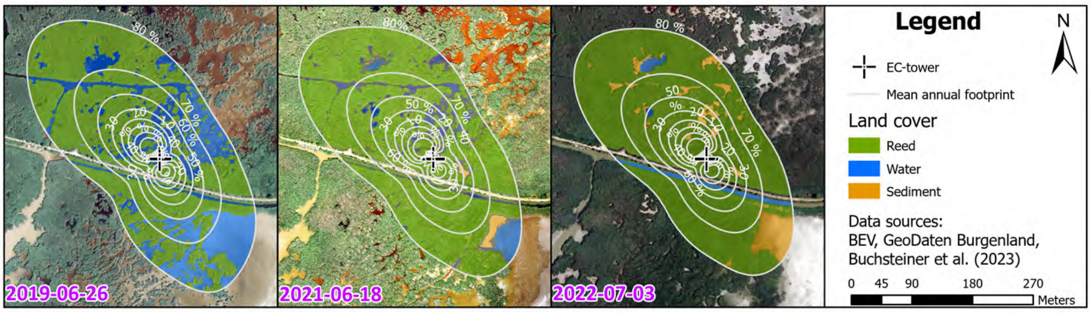

Figure 3.3: The change in the share of land cover classes (reed, water, and open sediment) in the 80% annual mean footprints of the eddy covariance (EC) tower in the reed belt of Lake Neusiedl from June 2019, 2021 to July 2022.

Growth of reeds

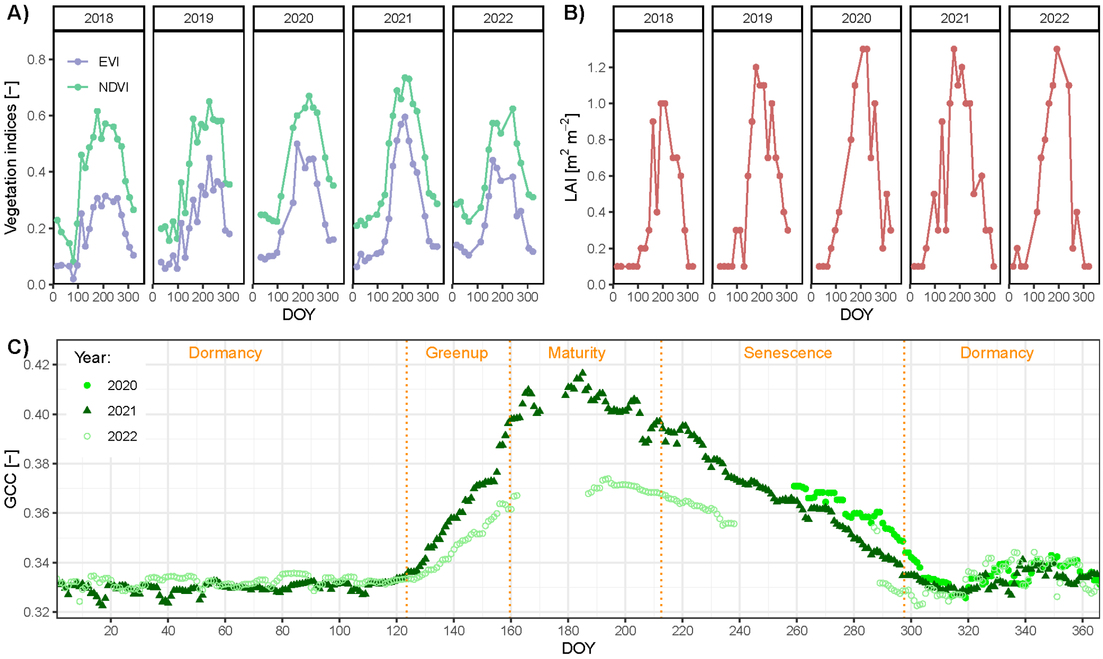

Figure 3.4: Temporal variability of vegetation and green indices of the reed belt of Lake Neusiedl per day of the year (DOY) from 2018 to 2022: **A)** the enhanced vegetation index (EVI) and the normalized difference vegetation index (NDVI) from MODIS, **B)** the leaf area index (LAI) from MODIS, and **C)** the *max*-filtered green chromatic coordinates (GCC) of the Phenocam at the eddy covariance tower. The GCC data set of 2021 has already been published in Buchsteiner et al. (2023).

The study site's reed development was analyzed using various vegetation indices. The maximum LAI per year showed an increasing trend from 2018 to 2020, but then remained stable at 1.3 until 2022 (see Figure 3.4B). However, the annual peak values of the EVI and NDVI increased until 2021 (0.59 and 0.73) before declining in 2022 (see Figure 3.4A). The maximum GCC per year of the Phenocam confirm this trend, with 0.42 in July 2021 and with 0.37 in 2022 (see Figure 3.4C), despite some data gaps in 2022.

3.3.2 Drought influence on temporal variations (diurnal, seasonal, annual) of C fluxes of a subsaline reed ecosystem

This multi-year GHG study focuses on the consequences of drought on the C fluxes of the subsaline reed ecosystem of Lake Neusiedl. The closure of the energy balance can serve as a quality criterion for EC measurements. The energy balance of the reed belt of Lake Neusiedl had a closure of 81.3% ($R^2 = 0.93$) considering daily mean energy fluxes from mid-2018 to 2022 (see Figure S.13A). When considering individual years separately, the energy balance closure increased from 76.7% (2019) to 86.1% (2021) and then fell again to 77.9% (2022) (see Figure S.13B). Taking the season into account, the energy balance closure increased substantially from winter (53.6%) to summer (85.5%) (see Figure S.13C).

CO_2 fluxes

The CO_2 fluxes of the reed belt showed a strong seasonality, as the highest monthly GPP and R_{eco} values (in absolute terms) occurred in the growing season from May to October (see Figure 3.5). Negative monthly NEE were observed at least once every year in June. The absolute value of GPP of the growing season more than doubled from 2018 to 2021, with the most negative seasonal GPP of -1225 ± 19 g CO_2-C m^{-2} in 2021, which, however, became slightly less negative by about 200 g CO_2-C m^{-2} in 2022 (see Table S.5). The R_{eco} of the entire growing season also doubled from 2018 to 2021, but increased even further in 2022. In particular, the monthly R_{eco} in May and October 2022 were higher than in previous years. By comparison to the previous years, the non-growing season (November-April) of 2022 had the highest R_{eco} with 218 g CO_2-C m^{-2}, which is almost equivalent to the amount by which the GPP of this year's growing season was reduced. As a result, the annual NEE decreased substantially by 85% from 181 ± 61 g CO_2-C m^{-2} a^{-1} (2019) to 27 ± 68 g CO_2-C m^{-2} a^{-1} (2021), but then rose to twice as high CO_2 emissions in 2022 (391 ± 65 g CO_2-C m^{-2} a^{-1}) than in 2019 (see Figure 3.6C). The inter-annual variability of the cumulative NEE started around DOY (day of the year) 125 (beginning of May), as shown in Figure 3.6A.

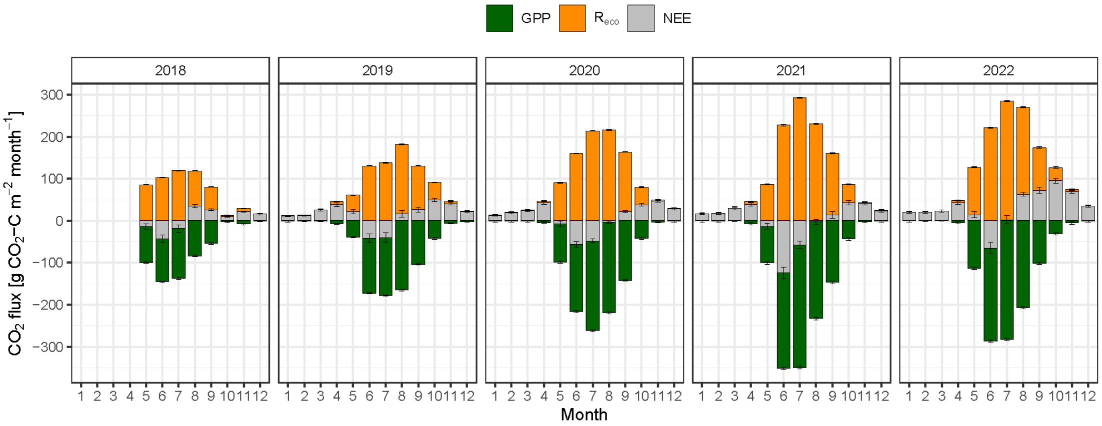

Figure 3.5: Monthly CO_2 fluxes ± uncertainty estimate (random error) of the reed belt of Lake Neusiedl from mid-2018 to 2022: net ecosystem exchange (NEE, gray), gross primary production (GPP, green) and ecosystem respiration (R_{eco}, orange).

In most years (2018, 2020, 2021), the reed belt was a CO_2 sink in the growing season with the most negative NEE of -141 ± 49 g CO_2-C m^{-2} in 2021 (see Table S.5). Despite the fact that on average only three out of the six months of the growing season had a negative NEE. R_{eco} of the non-growing season exhibited less inter-annual variability in all four years, ranging from 167 ± 5 g CO_2-C m^{-2} (2019) to 218 ± 9 g CO_2-C m^{-2} (2022). However, in 2020 and 2021, these contributions turned the reed belt into a CO_2 source on an annual basis.

The NEE showed a distinct diurnal cycle from May to October (growing season) with a negative peak just before noon (around 11 o'clock UTC+1), which corresponds to the local summer time (UTC+2) at noon (see Figure S.14C). The negative peak values of the summer months (June to August) became more negative from 2019 to 2021, but less negative in 2022. October 2018 no longer displayed a diurnal cycle of the NEE, unlike the subsequent years. The R_{eco} exhibited a distinct diurnal cycle during the growing season, but with a peak in the afternoon (around 15 o'clock UTC+1) and with an increase in the mean diurnal course in every month from 2018 to 2022 (see Figure S.14A). The GPP showed diurnal cycles that were analogous to the NEE (see Figure S.14B).

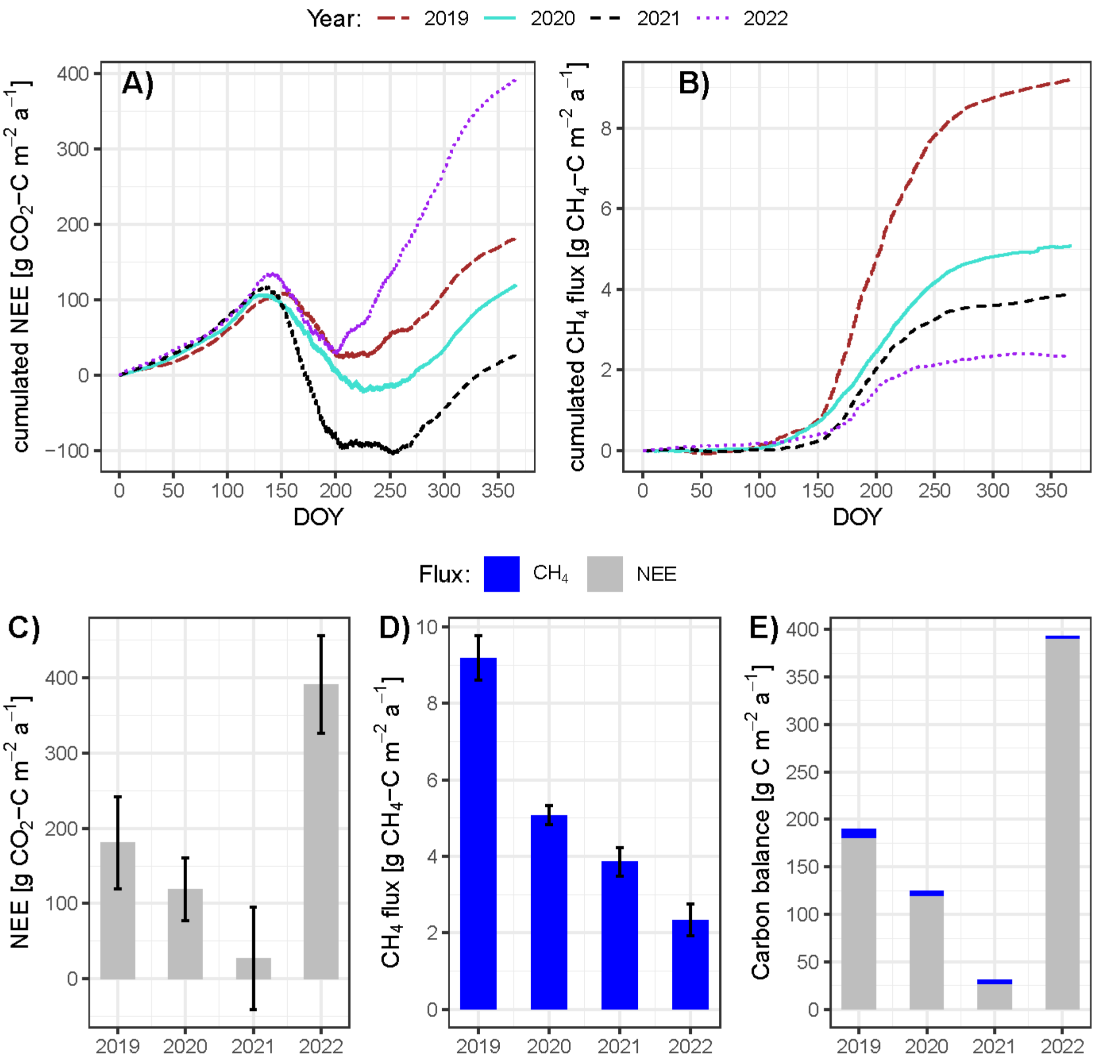

Figure 3.6: Inter-annual variability of the carbon fluxes of the reed belt of Lake Neusiedl from 2019 to 2022: **A)** cumulative sums of net ecosystem exchange (NEE) and **B)** CH_4 flux over the day of the year (DOY), **C)** annual NEE and **D)** CH_4 flux ± uncertainty estimation (random error) and **E)** carbon balance.

CH_4 fluxes

The CH_4 fluxes of the reed belt showed a strong seasonality, with the highest monthly emissions consistently occurring in July (see Figure 3.7). The CH_4 emissions of the growing season decreased from 2019 to 2022 (see Table S.5), resulting in a sharp decline of 75% in annual CH_4 emissions from 9.2 ± 0.6 g CH_4-C m^{-2} a^{-1} (2019) to 2.3 ± 0.4 g CH_4-C m^{-2} a^{-1} (2022) (see Figure 3.6B and D). Over 90% of the annual CH_4 emissions occurred during the growing season of the reed (May–October, see Table S.5).

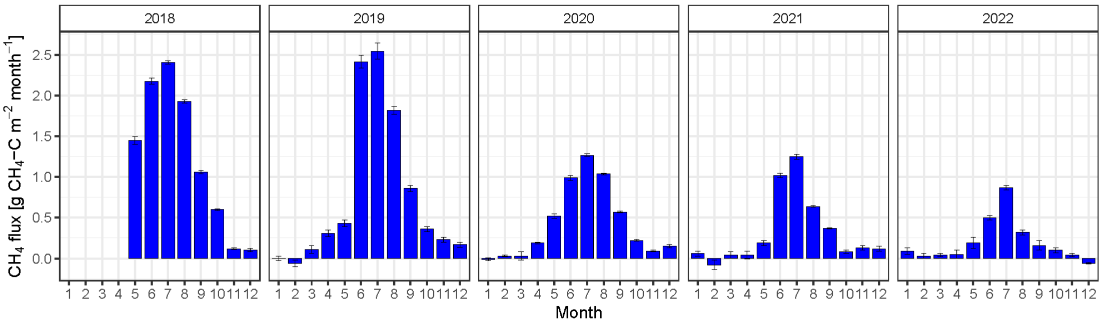

Figure 3.7: Monthly CH_4 emissions ± uncertainty estimate (random error) of the reed belt of Lake Neusiedl from mid-2018 to 2022.

The CH_4 flux showed a strong diurnal cycle from June to August, with a peak in the late afternoon (around 15 and 16 o'clock UTC+1) in 2018 and 2019, as shown in Figure 3.8. In 2020 and 2021, the CH_4 flux displayed two small peaks in June and July, with one peak in the morning and the other in the afternoon. In 2022, the CH_4 flux showed only minor daily fluctuations from June to October, with the lowest point occurring around midday. In the summer months (June–August) of 2018 and 2019, the median CH_4 emissions from the reed belt were significantly higher during the day than at night. However, in June–August 2022, the median night-time emissions were significantly higher (Dunn's test, $p < 0.001$).

When combining the CO_2 and CH_4 fluxes of the reed belt in annual C balances, they show the same trend as the annual NEE. However, there is a decreasing amount of CH_4 emissions in the annual C balances from 2019 to 2022 (see Figure 3.6E). So far, this study has assumed that the growing season lasts from May to October, mainly for reasons of comparison. However, the duration, start and end dates of the reed belt's growing season varied between years (2018–2022), depending on the definition used (see Section S.2.6 for details).

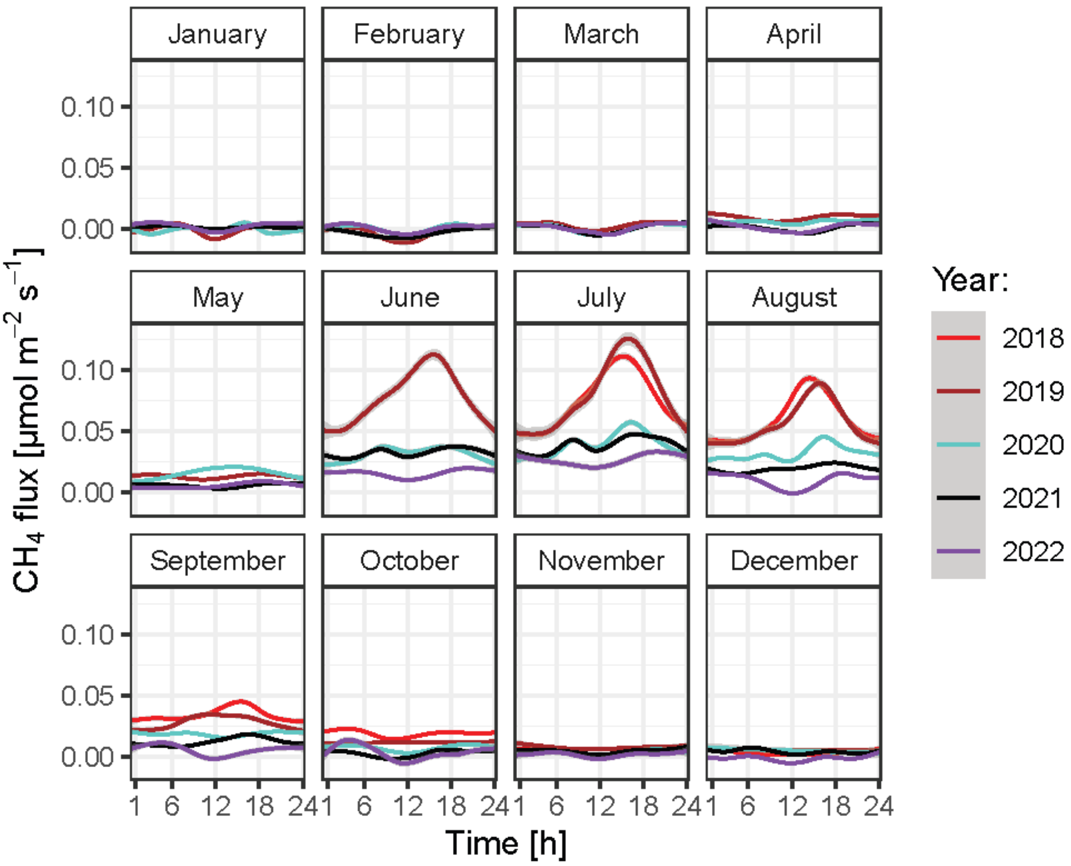

Figure 3.8: Diurnal variations of CH_4 flux of the reed belt of Lake Neusiedl for each month from mid-2018 until 2022 using the smoothing gam-function (gray area indicates 95% confidence interval). The displayed time is in UTC+1 (local time zone without daylight saving time).

3.3.3 Drivers of C fluxes of a subsaline reed ecosystem

The half-hourly (filtered) CH_4 flux exhibited a significant positive correlation with temperature variables, including T_{sed} at 5, 10, and 15 cm depth and T_{water} of the open water area of Lake Neusiedl (all $\rho = 0.58$, see Figure S.17). The correlation coefficient between CH_4 flux and LW_{in}, absolute water vapor pressure (e_a), R_{eco}, and NDVI was found to be $\rho = 0.58$, 0.57, 0.49, and 0.58, respectively. Upon examination of the data for each individual year, it was observed that the correlation coefficient between LAI and CH_4 flux exhibited a notable decline, from $\rho = 0.79$ (2019) to $\rho = 0.32$ (2022). A comparable pattern was observed between the temperature variables and CH_4 flux. Only the data from 2020 showed a significant negative correlation between CH_4 flux and the WL of the lake. In the case of the data from 2022, the CH_4 flux exhibited a paucity of high correlations, with the highest negative correlation observed with SPEI ($\rho = -0.31$) and the highest positive correlation with LAI ($\rho = 0.32$). On a monthly time scale, the mean CH_4 flux exhibited an exponential relationship with T_{sed} and e_a, with high significant positive correlations (see Figure 3.9A and B).

The half-hourly (filtered) NEE exhibited a significant negative correlation with radiation parameters such as SW_{in} and PPFD ($\rho = -0.63$ and -0.6) and with energy fluxes such as H and LE ($\rho = -0.6$ and -0.58, see Figure S.17). The CO_2 flux component R_{eco} demonstrated the strongest positive correlation coefficient with the EVI ($\rho = 0.89$) and a significant negative correlation with the WL of the open water area of Lake Neusiedl ($\rho = -0.44$, see Figure S.17). Upon examinations of the data for each year separately, the data of 2020 exhibited the most significant negative correlation between R_{eco} and WL ($\rho = -0.85$). While R_{eco} demonstrated a positive correlation with the vegetation indices for each year, with high coefficients. However, the other CO_2 flux component GPP demonstrated a significant negative correlation with WL ($\rho = -0.47$) only in the data of 2020. On a monthly timescale, both mean CO_2 flux components exhibited a high degree of correlation with EVI, as illustrated in Figures 3.9C and D.

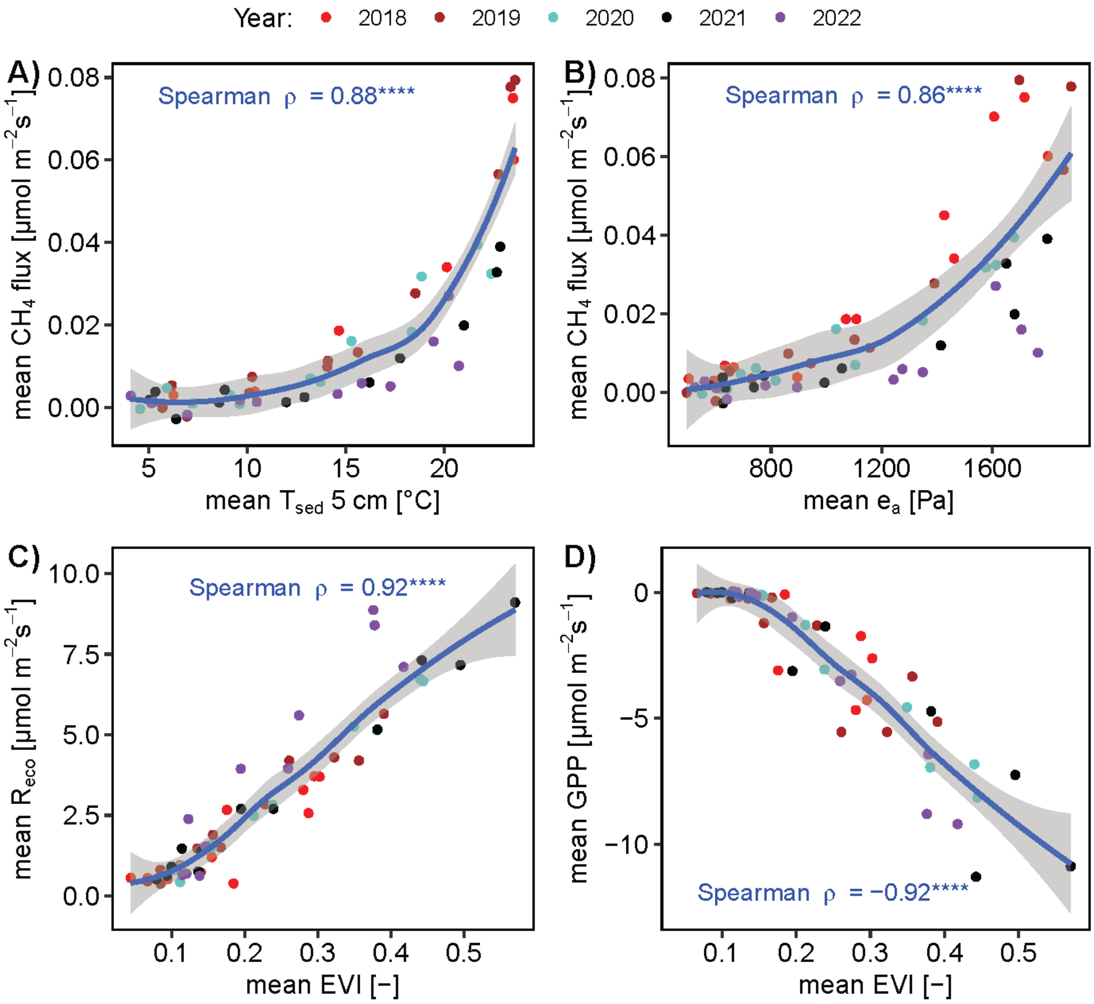

Figure 3.9: Relationships between environmental variables and carbon fluxes: Monthly **A)** mean sediment temperature (T_{sed}) at 5 cm depth vs. mean methane (CH_4) flux, **B)** mean absolute water vapor pressure (e_a) vs. mean CH_4 flux, **C)** mean enhanced vegetation index (EVI) of the reed belt vs. mean ecosystem respiration (R_{eco}), and **D)** mean EVI vs. gross primary production (GPP); Significant Spearman correlation coefficient (ρ) with $p < 0.0001$ (****, Adjustment Holm); The fitted lines (blue) show the local polynomial regressions (loess) with the 95% confidence interval (gray area).

3.4 Discussion

With 4.5 years (mid-2018 to 2022), this study is one of the few multi-year GHG studies of wetlands with reeds and the first one of a subsaline lake ecosystem with *Phragmites australis*. Compared to other EC studies in wetlands, our study achieved a closure of 81.3% for the energy balance, which is clearly above the mean of wetlands (76%) (Stoy et al., 2013) and thus showed an acceptable quality of the EC measurements. For further discussion on energy balance see Section S.2.3.

3.4.1 Drought influence on environmental parameters of reed ecosystems

Modified potential lateral exchange

The change in the WL of Lake Neusiedl from 2018 to 2022 could also have had an influence on the potential lateral exchange between the reed belt and the open lake area. Wolfram et al. (2019) identified that the water exchange is mainly via channels (linear flow) and they doubt that there is still diffuse flow into the reed belt of 1.3 km width as it was mentioned by Gunatilaka (1986) because it was very rare at that time and only limited for a certain area. Wolfram et al. (2019) found out that reed belt sites that are located directly on the shoreline to the open lake but separated from very dense reed stands show virtually no response to WL fluctuations in the open lake, which would suggest almost no direct/diffuse flow through the reed stands. Stalzer and Spatzierer (1987) found that only about 25% of WL changes in the open water area of Lake Neusiedl were also registered by a WL change inside the reed belt, and the lowering of the WLs in the reed belt rarely exceeded 3 cm per wind event.

Lateral C fluxes can be a C source and sink in a reed ecosystem but in most studies this flux is neglected because it is very difficult to measure. Some lateral fluxes depend on (high) WL and/or are wind driven such as hydrological C fluxes (dissolved organic C (DOC), particulate organic C (POC), and dissolved inorganic C (DIC)), lateral detrital C fluxes, migration of mobile species like fish, and other physical transfer from for example animal excretion and mortality. In contrast, herbivores such as wild game or horses may be a potential for lateral C loss due to reed biomass removal, but they probably only enter the reed belt at low or no WLs and then with a much lower rate than shown in Bakker et al. (2016). The estimation of the annual lateral net C detritus flux from an estuary wetland with *P. australis* into the ocean influenced by the tide can be quite high (1.13–1.96 kg C m^{-2} a^{-1}, Gao et al. (2021). In addition, tidal hydrological C export from marshes can be up to 50% of NEE (105 g C m^{-2} a^{-1}, Bogard et al. (2020)), being mainly inorganic C (Bogard et al., 2020, Wang et al., 2016). In contrast, the lateral hydrological C net flux from a marsh with reed influenced by agricultural runoff was much lower (23 ± 13 g C m^{-2} a^{-1}, Chu et al. (2015)). However, our site is not affected by tides or surface runoff due to its flat terrain.

There may be potential lateral water exchange between the reed belt and open lake area at Lake Neusiedl, depending on wind direction (NW or SE), wind speed ($\geq$ 4 m s^{-1}) and a WL of at least 1 m or even higher. Due to this temporary difference in WL, water can be laterally pushed almost exclusively via the channels (Wolfram et al., 2019) from the lake into the reed belt and vice versa, depending on the current wind direction, suction effect, channel efficiency/condition, lake edge wall and mean lake WL. This was particularly more likely in 2018 and 2019 when the WL was higher, the reed overgrowth of the channels had not yet occurred and the sedimentation in the channels was not yet so advanced. This lateral hydrological flux may transport DOC, POC, and DIC from the open lake area into the reed belt and vice versa. The water in the reed belt at our site exhibited higher DIC concentrations than the open lake water (reed belt: 265 ± 95 mg L^{-1} (mean ± SD), open lake: 160 ± 36 mg L^{-1}, measured in 2021, Baur et al. (2024a)) and higher DOC concentrations (reed belt: 27 ± 8 mg L^{-1}, open lake: 16 ± 1 mg L^{-1}, measured 2017–2019, Zoboli et al. (2023)). While the open lake water had higher POC values than the water in the reed belt (reed belt: 3 ± 2 mg L^{-1}, open lake: 4 ± 2 mg L^{-1}, measured 2017–2019, Zoboli et al. (2023)). However, as NW is the predominant wind direction at our site, it is possible that more water may have been pushed laterally into the reed belt over time than drawn out into the open lake water area. This may indicate a potential hydrological C input from the open lake area into the reed belt, rather than an export. This C input could then be released into the atmosphere as CO_2 from the water surfaces within the reed belt, as has been observed in other lakes without reeds (Weyhenmeyer et al., 2015, Wilkinson et al., 2016).

We assume that a lateral import of C may have occurred via the channels at our site in years with higher WL, such as 2018 and 2019. However, we assume that this import did not exceed the C source of 181 g C m^{-2} a^{-1} in 2019. As for 2022, it is almost certain that no relevant lateral exchange between the reed belt and the lake has taken place. To make more precise statements, research on the lateral exchange at Lake Neusiedl would be necessary.

Growth of reeds

The observed EVI values indicate lower photosynthetic activity at our site compared to other reed wetlands, except for 2021, as the EVI is a good proxy for this activity Serrano-Ortiz et al. (2020). At our site, the maximum annual EVI increased from 2018 to 2021, indicating the growth of the reed stands. In 2022, however, the EVI decreased compared to the previous year, indicating that this reed development has stopped and even been reduced. The EVI has the advantage over the LAI that, due to its sensitivity, it can still indicate an increase in reed growth in times of high biomass production, where the LAI already indicates saturation (Alexandridis et al., 2020). Our site showed lower maximum annual EVI values (0.31–0.60) than a Mediterranean reed wetland (0.62 ± 0.06), but the peak values also occurred in July or August (Serrano-Ortiz et al., 2020). The differences in living and old reed biomass compared to other wetlands with reeds may be one explanation for the lower productivity of our site. The aboveground biomass C storage at our site (fall 2022) showed more than 2-fold higher values compared to *Phragmites* stands in Gao et al. (2021). Furthermore, our study showed a higher mean dry weight of aboveground and belowground biomass compared to Brix et al. (2001), who studied the reed biomass in the Hungarian reed belt of Lake Neusiedl in the 1990s. The differences could be due to the fact that Brix et al. (1996) only examined living shoots and living rhizomes, while our aboveground biomass, for example, consisted on average about half litter. However, our biomass values also showed a much higher variability, which could be an indicator that our site offers a greater spatial heterogeneity of reed stands in 2022 with some young reeds in former water pools compared to Brix et al. (2001).

3.4.2 Drought influence on temporal variations (diurnal, seasonal, annual) of C fluxes of reed ecosystems

CO_2 fluxes

Our site was a CO_2 source, although these reed ecosystems are often shown as strong CO_2 sinks (Brix et al., 2001, Huang et al., 2020, Minke et al., 2016, Sanders-DeMott et al., 2022, Zhou et al., 2009). One possible explanation for this is the impact of drought and the corresponding decrease in WL, while the coastal reed wetland studied by Sanders-DeMott et al. (2022) was impounded and showed little variation in WL and salinity during the growing season.

Some wetland ecosystems are vulnerable to drought, as demonstrated by our study and by Helfter et al. (2022). In their study, the seasonal floodplain (with *P. australis*) in the Okavango Delta switched from a CO_2 sink to a source of 428 g CO_2-C m^{-2} a^{-1}, which is comparable to the annual CO_2 flux observed at our site in 2022. However, Helfter et al. (2022) explained the reason for the CO_2 source by a reduction in GPP rather than an increase in R_{eco}. In contrast, at our site, the drought initially increased GPP due to reed colonization in the dried-up former water areas (Buchsteiner et al., 2023, Koebsch et al., 2020). However, this was followed by a decrease in GPP in 2022. It is likely that the vegetation at our site experienced more drought stress in 2022 compared to the sites in Koebsch et al. (2020), as they recorded no decrease in GPP.

Furthermore, the drought had a substantial impact on R_{eco} at our site, especially after the drop in SWC (mid-2022), which transformed our site into a strong source of CO_2 beginning in July. As a result, 86% of the annual CO_2 emissions in 2022 were released during the second half of the year, but also 40% of the 4.5-year CO_2 emissions were emitted during this period. This underlines the importance of high SWC in wetlands with reed. The increase in annual R_{eco} from 2021 to 2022 is nearly equivalent to the typical amount emitted during the non-growing season. This may indicate an increase in heterotrophic respiration due to enhanced aerobic conditions in the sediments (Maes et al., 2024).

At our site, the two months (June and July) with the highest net CO_2 uptake were insufficient, except for 2021, to compensate for the net CO_2 release during the entire non-growing season. This is in contrast to the findings of Zhou et al. (2009), who demonstrated that the reed ecosystem was a CO_2 sink, primarily due to the notable CO_2 uptake during these two months, with a maximum of -115 g CO_2-C m^{-2} $month^{-1}$. In addition, our site was no CO_2 sink, as only a maximum of four out of the six months in the growing season (May–October) had a negative monthly NEE. In contrast to previous studies on temperate wetlands with reeds (Han et al., 2013, Huang et al., 2020, Minke et al., 2016), our study found that the ratio of monthly R_{eco} to GPP was already higher than 1 in September and

October, and often in other months of the growing season as well. This could be due that our site was only temporarily inundated and experienced drought. Additionally, the age might play a role, as the reed in the wetland in Han et al. (2013) is considerably younger than at our site (Nemeth and Dvorak, 2022). This could provide an explanation for the higher productivity of the young, fresh reed shoots at their site and could explain their ratio of 0.68 during the entire growing season.

Moreover, the CO_2 sink or source of a reed ecosystem may be determined by further environmental conditions such as peat formation, salinity, and reed condition: Our site is no peatland due to the thin organic layer in the sediments, and may therefore have not yet experienced conditions as peatlands with *P. australis* (Koebsch et al., 2020, Minke et al., 2016, van den Berg et al., 2016). Compared to most salt marshes, our site exhibited lower salinity values and the main salt in our site is sodium bicarbonate (Wolfram and Herzig, 2013) in contrast to sodium chloride on coastal wetlands. Therefore, it is possible that the salt stress for the reed belt is lower than that experienced on the coast, as shown in the study of Huang et al. (2020). However, a salt bloom was evident on the upper sediment at our site when it dried out, particularly during the summer 2022. According to Chamberlain et al. (2020), drought-induced salinization may have played a role in reducing wetland productivity. They showed that annual GPP decreased by 64% during peak salinization. However, at our site, the annual GPP only decreased by 16% from 2021 to 2022. Decomposition underwater is often reduced due to the decrease in oxygen concentration. This phenomenon would also be expected to occur in subsaline lakes. The extent to which salinity affects decomposition rates and whether this is a direct or indirect effect is still under debate (Luo et al., 2019, Stagg et al., 2017). It is likely that this depends not only on salt concentration (Stagg et al., 2018) but also on salt type (Li et al., 2019). As the majority of studies originate from coastal regions or employ sodium chloride as the salt type, the salt composition differs from that of Lake Neusiedl, making direct comparison challenging. However, it also highlights the necessity for further studies to investigate the impact of subsalinity on decomposition rates in reed ecosystems. Furthermore, the condition of the reed stands may explain why our site is not a CO_2 sink. As noted by Dinka et al. (2010), there were reed die-back sites on the Hungarian part of Lake Neusiedl that had a lower aboveground biomass and LAI than vigorous reed stands. According to Nemeth and Dvorak (2022), the reed stands at our site are older than 14 years and more than 50% of this age class is covered with matted reeds. Therefore, further research is needed to investigate the influence of reed mats on CO_2 fluxes.

Our study confirms the importance of the winter season, which is frequently neglected in the annual CO_2 budget, as in Soja et al. (2014b). We demonstrated that the winter (December-February) account for at least 30% of the CO_2 emissions during the non-growing season. Even in 2021, with the highest CO_2 sink in the growing season, the CO_2 emissions of the non-growing season exceeded this, highlighting its relevance for the annual CO_2 budget. Furthermore, the CO_2 emissions of the non-growing seasons in our study were already at least three times higher than the annual CO_2 emissions from Lake Neusiedl, as reported by Soja et al. (2014b) for 2011/2012. They only considered the diffusion pathway at the water–air and not at the sediment–air interface. This underscores the advantage of EC over chamber measurements, as it continuously considers all available emission pathways.

CH_4 fluxes

Our study shows that the annual CH_4 emissions of a subsaline wetland with reeds (2.3–9.2 g CH_4-C m^{-2} a^{-1}) are clearly lower than the median CH_4 emissions of temperate wetlands (27.4 ± 3.4 g CH_4-C m^{-2} a^{-1}) and higher than the median of salt marshes (0.8 ± 2.9 g CH_4-C m^{-2} a^{-1}), as reported by Knox et al. (2019).

CH_4 production in subsaline Lake Neusiedl is likely suppressed by the coexistence of methanogens with sulphate-reducing bacteria (Baur et al., 2024a), resulting in lower emissions than from freshwater wetlands. However, the salinity content in the sediments of our site can be classified as oligohaline (Anonymous, 1958), which represents the lower edge of the salinity gradient of coastal wetlands in Martin and Moseman-Valtierra (2015). In a coastal reed ecosystem, Martin and Moseman-Valtierra (2015) found that daytime CH_4 emissions decreased with increasing salinity in the sediments. Nevertheless, with higher WL as in 2019, the annual CH_4 emission from our site is comparable to those of an impounded saline and tidal restricted reed wetland (11.4 g CH_4-C m^{-2} a^{-1}) studied by Sanders-DeMott et al. (2022).

The relatively lower annual CH_4 emissions of our site compared to other temperate wetlands, as shown by Delwiche et al. (2021), may also be attributed to the rhizospheric CH_4 oxidation by reeds. As Kowalska et al. (2013) observed in a temperate wetland, CH_4 emissions are lower in areas with reeds compared to areas with sedges. They postulated that this was due to the more effective aeration of the rhizosphere by *P. australis*.

The inter-annual variability of CH_4 fluxes at our site can be attributed to a combination of decreasing WLs and increasing dryness of the reed belt from 2019 to 2022. However, a significant and strong negative correlation with the WL was only confirmed for 2020, the first year in the study period in which the reed belt felt temporally dry. In particular, during the fall of 2020-2022, there was a notable absence of surface water in the reed belt due to the drought. This allowed oxygen to infiltrate directly into the sediments through the cracks, which likely reduced methanogenesis and stimulated CH_4 oxidation. Furthermore, drought also reduced annual CH_4 emissions in other wetlands with reeds. For instance, in a seasonal floodplain within the Okavango Delta, emissions were reduced by a factor of four (Helfter et al., 2022). Nevertheless, even in the drought year, this ecosystem exhibited higher CH_4 emissions (6.5 g CH_4-C m^{-2} a^{-1}) than our site in three out of four years.

The annual CH_4 emission of the reed belt in 2019 was about 4 times higher than the up-scaled chamber data of Lake Neusiedl from Soja et al. (2014b) in 2011/2012, which were only measured at the water–air interface. This highlights the importance of plant-mediated transport in *P. australis* (van den Berg et al., 2020) and its inclusion in the GHG budget of lakes (Rõõm et al., 2014) such as Lake Neusiedl. Due to the inter-annual variability of CH_4 emissions, it is noteworthy that 2011 was a particularly dry year at Lake Neusiedl, with only about 410 mm of precipitation (Hackl and Ledolter, 2023). Despite this, the mean WL was still higher than in 2019, indicating potentially higher CH_4 emissions in 2010/2011.

At our site, CH_4 emission was highest in July of each year, which is consistent with the seasonality observed in temperate wetlands (Delwiche et al., 2021, Kim et al., 1998a). This indicates that CH_4 emissions in wetlands with reeds during the growing season are strongly dominated by the highly effective plant-mediated transport of *P. australis*. Whereas in the non-growing season diffusive transport pathways becomes more important, but with lower exchange rates.

At the reed belt of Lake Neusiedl, we observed pronounced diurnal cycles of CH_4 fluxes only in the summer months with higher WL (2018 and 2019): In this time period, the diurnal peak of CH_4 fluxes was observed in the late afternoon, corresponding to the potential peak of acetate availability in the rhizosphere, as acetoclastic methanogenesis is the dominant methanogenic pathway at Lake Neusiedl (Baur et al., 2024a). The afternoon peak of CH_4 fluxes is consistent with the diurnal peak of the VPD, which is one of the factors controlling the stomatal conductance (Philipp et al., 2017). This regulates the CH_4 release as the convective gas flow of *P. australis* is driven by humidity-induced pressure gradients between the atmosphere and the internal aerenchymatic tissues of reeds (van den Berg et al., 2020). The lowest diurnal CH_4 fluxes were observed between 3 and 6 am (UTC+1), preceding sunrise, as in other studies (Philipp et al., 2017, van den Berg et al., 2020). The observed diurnal pattern can be explained by the plant-mediated transport mechanism and its bypass function of the CH_4 oxidation zone (Brix et al., 2001), as well as by the change in transport mechanism from molecular diffusion to convective flow (Kim et al., 1998a). The diurnal pattern was observed only during summer months, thus confirming that there are no significant diurnal differences before reed emergence and that the differences decrease rapidly as the reeds senesce (Kim et al., 1998a). However, in the subsequent years (2020–2022), the diurnal pattern of CH_4 fluxes in our site changed: We observed two small peaks (in the morning and afternoon) and a depression at midday during the summer months when the WL in the reed belt was low or non-existent. This may be a result of enhanced rhizospheric CH_4 oxidation due to oxygen transport from *P. australis* into the rhizosphere via venturi- and humidity-induced convection flows (Armstrong et al., 1992, 1996). In general, however, this is also due to higher daytime CH_4 oxidation in the top sediments and via cracks.

3.4.3 Drivers of C fluxes of reed ecosystems

We found no significant relationship between net C fluxes and WL, as did Acosta et al. (2019) in a Mediterranean reed wetland, but interestingly the CO_2 flux component R_{eco} showed a significant negative correlation with WL, whereas GPP did so only in 2020. This underscores that the temporal development of the effects of drought on the CO_2 fluxes is not linear and in one direction, but rather anticyclic and with the SWC as marker.

Like Kim et al. (1998a), we found that CH_4 flux was significantly correlated with T_{sed}, but our study showed that this was independent of year (see Figure 3.9A). This correlation explains the general temperature dependency of the CH_4 production in sediments and explains the seasonal differences (Baur et al., 2024a) instead of inter-annual differences due to the WL. However, it does not explain the strong diurnal variations of the CH_4 flux in the summer months with higher WL (2018 and 2019), as in these months T_{sed} in 5 cm depth showed almost no diurnal fluctuations, while in the summer months with low or no WL T_{sed} peaked in the afternoon.

The effects of drought observed in our study on a wetland with reeds and their GHG fluxes due to the decrease in lake water levels can also be applied to other wetlands. We observed that a decreasing WL leads to plant colonization in former water areas (Buchsteiner et al., 2023), but dry sediments (SWC $<$ 40 Vol-%) lead to a substantial loss of C. These effects were also a demonstrated by a wetland simulation model scenario of Lake Erie for the 21st century showing a C loss of 370 g C m^{-2} a^{-1} (Morin et al., 2022), which is comparable to our site in 2022. In addition, our study confirms the results of the model scenario of Morin et al. (2022) that CH_4 emissions from a wetland were greatly reduced due to a strong decline in WL. However, what we could not yet observe is the change in vegetation composition (emergence of non-wetland vegetation and colonization of woody plants), as predicted in Morin et al. (2022).

3.5 Conclusions

This study, conducted over a period of 4.5 years (mid-2018 to 2022), was the first to demonstrate the impact of drought on reed belts in lakes and their consequences for the C fluxes. Additionally, the study revealed that a reed wetland can emit more CO_2 rather than it takes up on an annual basis, challenging the assumption that reed ecosystems are exclusively CO_2 sinks. The investigation of this wetland of international importance was fascinating due to Lake Neusiedl's special water characteristics for inland waters.

The study discovered that a reed ecosystem can initially benefit from falling water levels by growing reeds in previously water-covered areas. However, the water content of the sediment appears to be a good indicator of the point at which a reed ecosystem no longer benefits, but becomes a strong source of C, despite the reduction in CH_4 emissions. Further investigation is required to determine how the condition of the reed stands, specifically the ratio of old to fresh shoots, may affect productivity.

The drought had a particularly strong effect on the diurnal pattern of the CH_4 fluxes in the summer months, indicating an increase of CH_4 oxidation in the reed belt. Overall, the drought led to a decoupling of the reed ecosystem from the open water surface of Lake Neusiedl and transformed the wetland into a strong C source. This may have serious consequences for the food web and substantially alter the C cycle.

The effects of drought observed in this study may also be applicable to other large lakes worldwide, as over half of them have experienced a decrease in water volume and some of them have reed ecosystems. This is especially relevant for ecosystems in shallow lakes, which are more vulnerable to climatic changes.

If drought persists and occurs frequently, a reed ecosystem may transition from an aquatic to a terrestrial ecosystem, resulting in a loss of C storage in the wet soil and submerged under water. Therefore, from a C storage perspective, it can be concluded that the reed ecosystem would benefit from a higher WL of Lake Neusiedl. However, it remains to be seen whether Lake Neusiedl and its reed ecosystem will recover from the intense drought and its consequences. Further monitoring is necessary to determine this.

Data availability

The data generated during this study are available at the PHAIDRA repository of the University of Vienna under `https://doi.org/10.25365/phaidra.490`.

4 Study III:
Temporal dynamics of CH_4 emission pathways in the subsaline reed wetland of Lake Neusiedl

Baur, P.A., Rodrigues-Oliveira, T., Hager, K., Luo, Z.-H., Schleper, C., Glatzel, S.

accepted manuscript for publication in *Biogeosciences* (27 June 2025) and published as a preprint on *EGUsphere* since 6 February 2025.
`https://doi.org/10.5194/egusphere-2025-443`

Abstract

Wetlands are a natural source of methane (CH_4) emissions and represent a substantial uncertainty in the global CH_4 budget. Furthermore, wetlands dominated by reed (*Phragmites australis*) have various CH_4 emission pathways, some of which are challenging to quantify (e.g., ebullition) or require additional research (e.g., plant-mediated transport). Plant-mediated transport is often not considered in greenhouse gas balance models for wetlands, nor is the correct mode of gas transport in reeds (pressurized flow). Therefore, further field studies on CH_4 emissions in wetlands, especially reed wetlands, are needed to reduce uncertainties in the global CH_4 budget and to improve the parametrization and implementation of emission pathways in greenhouse gas balance models of wetlands. This field study investigates all assessable CH_4 emission pathways and interfaces (diffusion, ebullition, plant-mediated transport) with various chamber types over four seasons and over the entire diel cycle (24 h) in the subsaline and dynamic reed wetland of Lake Neusiedl in Austria. The pathways of CH_4 formation (methanogenesis) were examined in each season by determining $\delta^{13}C$ source signatures, and over the course of a year, by investigating specific microbial groups (methanogens, methanotrophs, and sulfate reducers) in the sediments. The highest CH_4 emissions were observed in summer, regardless of the emission pathway, with the highest emissions in all seasons occurring via the plant-mediated transport. Significant differences in CH_4 fluxes were observed between the plant-mediated transport and diffusion pathway in each season. However, a distinct diel cycle of CH_4 flux was exclusively observed via plant-mediated transport during summer. The source signatures $\delta^{13}C$-CH_4 exhibit seasonal variation, with the highest ^{13}C-depletion occurring in fall. Despite the different seasonal source signatures, the dominant methanogenic pathway remains acetoclastic throughout all seasons. Desiccation of the reed ecosystem resulted in a reduction in methanogenic microbial diversity in the

sediments over the course of one year. Concurrently, the drought resulted in an increase and dominance of oxygen-tolerant *Methanomicrobiales.*

4.1 Introduction

Methanogens are well known for being producers of methane (CH_4) in various environments, with wetlands constituting the main natural source of this gas on the planet (Wang et al., 1996). However, wetland CH_4 emissions (102–200 Tg CH_4 a^{-1}, 2008–2017) represent a significant source of uncertainty in the global CH_4 budget (Saunois et al., 2020). In wetlands, methanogenesis predominantly occurs in anoxic sediments and can be classified into three different methanogenic pathways based on the substrate utilized for microbial anaerobic CH_4 production (Conrad, 2020a): acetoclastic (acetate), hydrogenotrophic (H_2/CO_2), and methylotrophic (methyl compounds, e.g., methanol). The stable carbon isotope ratio of CH_4 ($\delta^{13}C$-CH_4) is useful for distinguishing between biogenic and thermogenic sources of CH_4 production, with thermogenic sources generally showing more enriched ^{13}C values between -20 and -50 ‰ (Whiticar, 1999). The ratio can be also used to ascertain the dominant methanogenic pathway and the influence of CH_4 oxidation in different environments (Conrad, 2005, Whiticar et al., 1986, Whiticar, 1999). Acetoclastic methanogenesis produces $\delta^{13}C$-CH_4 values between -50 and -65 ‰ in sediments, whereas CH_4 produced by hydrogenotrophic methanogenesis is more depleted in ^{13}C, with values ranging from -60 to -100 ‰ (Whiticar et al., 1986). The presence of specific methanogens in sediments can also provide valuable insights into wetlands. For example, only two genera, *Methanosaeta* and *Methanosarcina*, conduct acetoclastic methanogenesis, whereas hydrogenotrophic methanogenesis is more common across methanogens (Megonigal et al., 2003). Additionally, some methanogens specialize in growing on one, two, or multiple substrates (Megonigal et al., 2003).

Methanogenesis is particularly relevant when considering that it is the final step of organic matter degradation in anoxic ecosystems (Schlesinger and Bernhardt, 2013). However, due to its lower energy yield, methanogenesis occurs last, with other alternative electron acceptors (nitrate $>$ manganese $>$ iron $>$ sulfate) being used first as substrates for anaerobic respiration. Consequently, the concentrations of these substrates and the presence of specific microbial communities in sediments, aside from methanogens, such as sulfate reducers or methanotrophs, can serve as indicators of environmental conditions. These indicators offer insights into the intricate interactions, processes, and methanogenic pathways that occur within and beyond the sediments (Hilderbrand et al., 2020, Soman et al., 2024, Zhang et al., 2020a). Wetlands with sulfate-containing sediments usually occur along the coast or are influenced by seawater (brackish). Sulfate-reducing bacteria convert sulfate (SO_4^{2-}) into less oxidized sulfur compounds, such as hydrogen sulfide (H_2S), to derive energy. Due to their higher energy yield, sulfate-reducing bacteria often outcompete methanogens for substrate uptake (King, 1984, Lovley et al., 1982, Lovley and Goodwin, 1988, Lovley and Klug, 1983), resulting in reduced or suppressed CH_4 production. However, there is a sulfate-methane transition zone in some environments, where they co-occur (Egger et al., 2016, Sela-Adler et al., 2017). Sulfate reduction is driven by the availability of hydrogen (H_2) (Muyzer and Stams, 2008) and is often coupled to anaerobic CH_4 oxidation (Hoehler et al., 1994, Valentine, 2002). Anaerobic CH_4 oxidation occurs in anoxic environments, such as coastal wetland or freshwater lake sediments, and can use various alternative electron acceptors, such as sulfate, nitrate, nitrite, humic substances, or metal oxides, for the oxidation of CH_4 (Bai et al., 2019, Dang et al., 2021, Haroon et al., 2013, Scheller et al., 2016, Valentine and Reeburgh, 2000). Aerobic CH_4 oxidation occurs mainly near the sediment surface or in the water column at the oxic–anoxic interface (King, 1992), where methanotrophs oxidize CH_4 to CO_2. In wetlands, sediments are often flooded or water-saturated, creating anoxic environments where oxygen (O_2) is limited or absent (Schlesinger and Bernhardt, 2013). Vegetated wetlands, however, such as those with reed plants, exhibit rhizospheric CH_4 oxidation influenced by the gas transport of the wetland plant (Armstrong and Armstrong, 1990, Brix et al., 2001, van der Nat and Middelburg, 1998). Taken together, these factors make examining wetlands with reeds (and sulfate) of particular interest.

Wetlands dominated by reed (*Phragmites australis*) can be a highly dynamic mosaic of reed, water, and sediment patches that vary due to seasonal or environmental factors (Baur et al., 2024b, Buchsteiner et al., 2023). Consequently, these ecosystems exhibit different interfaces and emission pathways for CH_4 fluxes with the atmosphere, not all of which are present in every season (Baur et al., 2024b). The plant-mediated transport of CH_4 via *P. australis* predominately occurs as pressurized convective gas flow (Armstrong and Armstrong, 1991, Brix et al., 2001), while molecular diffusion at the water–air and sediment–air interfaces represents another emission pathway. Additionally, ebullition as direct release of CH_4 bubbles from sediments, is another notable emission pathway. To date, only a few field studies have been conducted on all assessable emission pathways of wetlands with reed. An experiment was conducted in a German fen lake with high water levels on three days in June 2013, which suggested that plant-mediated transport plays a more significant role as ebullition (van den Berg et al., 2020). Another study, conducted in a subtropical Australian wetland partially covered with *P. australis*, demonstrated that the plant-mediated transport had the highest CH_4 emissions in only one of the two field campaigns (Jeffrey et al., 2019). The few available studies on this subject and the inconclusive results illustrate the necessity for further field studies on reed wetlands. Such research should incorporate measurements of all assessable emission pathways of each season. This would facilitate the determination of the precise contribution of plant-mediated CH_4 transport in comparison to the other emission pathways. A more comprehensive understanding of the various emission pathways of wetlands is essential to reduce uncertainty and account for the high variability associated with the processes of CH_4 production, transformation, and consumption in various types of wetlands before it reaches the atmosphere (Rosentreter et al., 2021). This understanding is particularly crucial for vegetated wetlands, where plant-mediated CH_4 transport plays a significant role (Vroom et al., 2022).

The CH_4 emissions in process-based vegetation models, such as LPJ-GUESS in Kallingal et al. (2024) or CLM4Me model in Riley et al. (2011), only partially implement the plant-mediated transport by considering only the passive mechanism (concentration gradient). Furthermore, these models do not account for pressurized flow, which occurs in plant species such as *Phragmites*, *Typha* sp., and others. However, it is known that CH_4 emissions from plant-mediated transport by *Phragmites australis* can be more than five times higher than by diffusion (Brix et al., 2001). According to Vroom et al. (2022), most other wetland greenhouse gas balance models do not consider plant-mediated CH_4 fluxes and exclude them in the total flux due to high variability in their contribution and the lack of data about this variability. This underscores the necessity of field studies in reed wetlands. Such studies could improve the parametrization and the implementation of emission pathways, such as the plant-mediated transport and, in particular, the pressurized flow mechanism, in the models. This could help to accurately model wetlands' greenhouse gas balances and reduce the global wetland CH_4 emission uncertainties (Vroom et al., 2022).

The diel (24 h) pattern of CH_4 emissions from aquatic macrophytes such as *P. australis* is highly influenced by the mode of gas transport and emission pathway (Chanton et al., 2002) and depends on the growth stage of the plant (Kim et al., 1998b). In wetlands with reed, the diel variations in CH_4 emissions exhibited a wide range (2- to 5-fold) during the summer months (June–August/September), with the lowest emission occurring at night (Kim et al., 1998b, Sanders-DeMott et al., 2022, van den Berg et al., 2016). However, the studies revealed discrepancies in the timing of the diel peak of CH_4 emissions during summer. Some studies have observed that this peak occurs around 12 o'clock (Jeffrey et al., 2019, Kim et al., 1998b, Sanders-DeMott et al., 2022, van den Berg et al., 2016, Zhang et al., 2016), while others have reported that it occurs in the afternoon (Baur et al., 2024b, Philipp et al., 2017). Moreover, in a wetland with reed that is subject to drought, the diel variation of the total ecosystem CH_4 emissions is less pronounced and exhibits a different diel pattern with two peaks, which is likely due to CH_4 oxidation (Baur et al., 2024b). However, these studies have often focused on the total CH_4 emissions of the ecosystem, regardless of the emission pathways (van den Berg et al., 2016), or only on the summer season (Kim et al., 1998b, van den Berg et al., 2020). However, there is a paucity of research examining diel patterns of each assessable emission pathway during all seasons, particularly in subsaline reed wetlands and in winter.

An example of a reed-rich wetland environment that is also subject to drought (Baur et al., 2024b), is Lake Neusiedl in Austria/Hungary. The reed ecosystem, which covers 181 km^2 (Csaplovics, 2019), occupies more than half of the lake and is the largest contiguous reed area in Europe after the Danube Delta. The lake is subsaline (0.5–3 ‰, Hammer (1986)), rich in sulfate (250–1250 mg SO_4^{2-} L^{-1} in 2021, Baur et al. (2024a)), has no natural outflow, and is very shallow ($<$ 1.8 m, Wolfram and Herzig (2013)). Lake Neusiedl is an international important wetland that is recognized by its cross-border protected areas, including a UNESCO World Heritage Site, a Ramsar site, and the Neusiedler See – Seewinkel & Fertő – Hanság National Park. The presence of the main salt, sodium bicarbonate (Wolfram and Herzig, 2013), and sulfate creates specific environmental conditions for reed ecosystems in inland waters (Baur et al., 2024a). Subsaline wetlands, especially subsaline reed ecosystems, are rarely ever studied. Due to their salinity, these ecosystems are more comparable to brackish ecosystems than to freshwater ecosystems. However, Lake Neusiedl's salt composition differs from these ecosystems, because another main salt is present besides sodium chloride. Overall, this underscores the need for microbial investigations and makes this wetland type interesting for studying carbon-related processes in different wetland types and conditions.

The objective of this study is to address the following research questions in the subsaline reed wetland of Lake Neusiedl: **(a)** Does the CH_4 flux show a distinct diel cycle in different emission pathways or seasons? **(b)** Which emission pathway dominates the diel CH_4 fluxes in which season, and what is its contribution? **(c)** To what extent can the microbial community or $\delta^{13}C$ source signatures explain the CH_4 formation or emission dynamics? In order to answer these questions, we carried out various chamber measurements during all seasons, determined isotopic source signatures, analyzed sediment properties, and investigated the microbial community in the sediments.

4.2 Material and Methods

4.2.1 Study site

Lake Neusiedl (Fertő) on the Austrian-Hungarian border with an area of 315 km^2 (Wolfram and Herzig, 2013) is the westernmost steppe lake in Europe with no natural outflow, but with an artificial outlet, which is closed since mid-2015 due to low water levels (Baur et al., 2024b). The lake is very shallow, with declining annual maximum water levels from 1.66 m (2018) to 1.33 m (2022) due to drought (Baur et al., 2024b). The major salt of the subsaline lake is sodium bicarbonate (Wolfram and Herzig, 2013). More than half of the lake is covered by a reed ecosystem dominated by *Phragmites australis*. Due to drought, the mosaic of the reed belt has exhibited a notable increase in reed and open sediment areas, but also a corresponding loss of water areas during the years 2021 and 2022 (Baur et al., 2024b, Buchsteiner et al., 2023).

The study site (Lat: 47.7693°, Long: 16.7576°) is situated in the eastern reed belt of Lake Neusiedl near the Biological Station Lake Neusiedl (Illmitz, Austria) and in the nature zone of the national park (see Figure 4.1a). In order to prevent any disturbance during the measurements, a boardwalk was constructed in the reed belt in December 2020. The site has a mean annual air temperature of 11.3°C and an annual precipitation of 500.2 mm (1993–2022) (Baur et al., 2024b).

4.2.2 Measurement setup

We conducted intensive 24 h measurement campaigns in each season (spring, summer, fall, winter; see Figure 4.1b) to investigate the diel variability of CH_4 fluxes for each assessable emission pathway and their seasonal variability in the reed belt. As the reed belt is a dynamic mosaic of reed, water, and open sediment areas that vary according to season and condition, the reed belt has different exchange interfaces with the atmosphere, which are not always all available in every season (Baur et al., 2024b). For that reason, chamber and ebullition trap measurements were conducted for each emission pathway with the objective of investigating their respective contributions and dominance within the reed belt: plant-mediated transport of *P. australis*, diffusion at the water–air and sediment–air interfaces, and ebullition (see Figure 4.1c). The spring campaign took

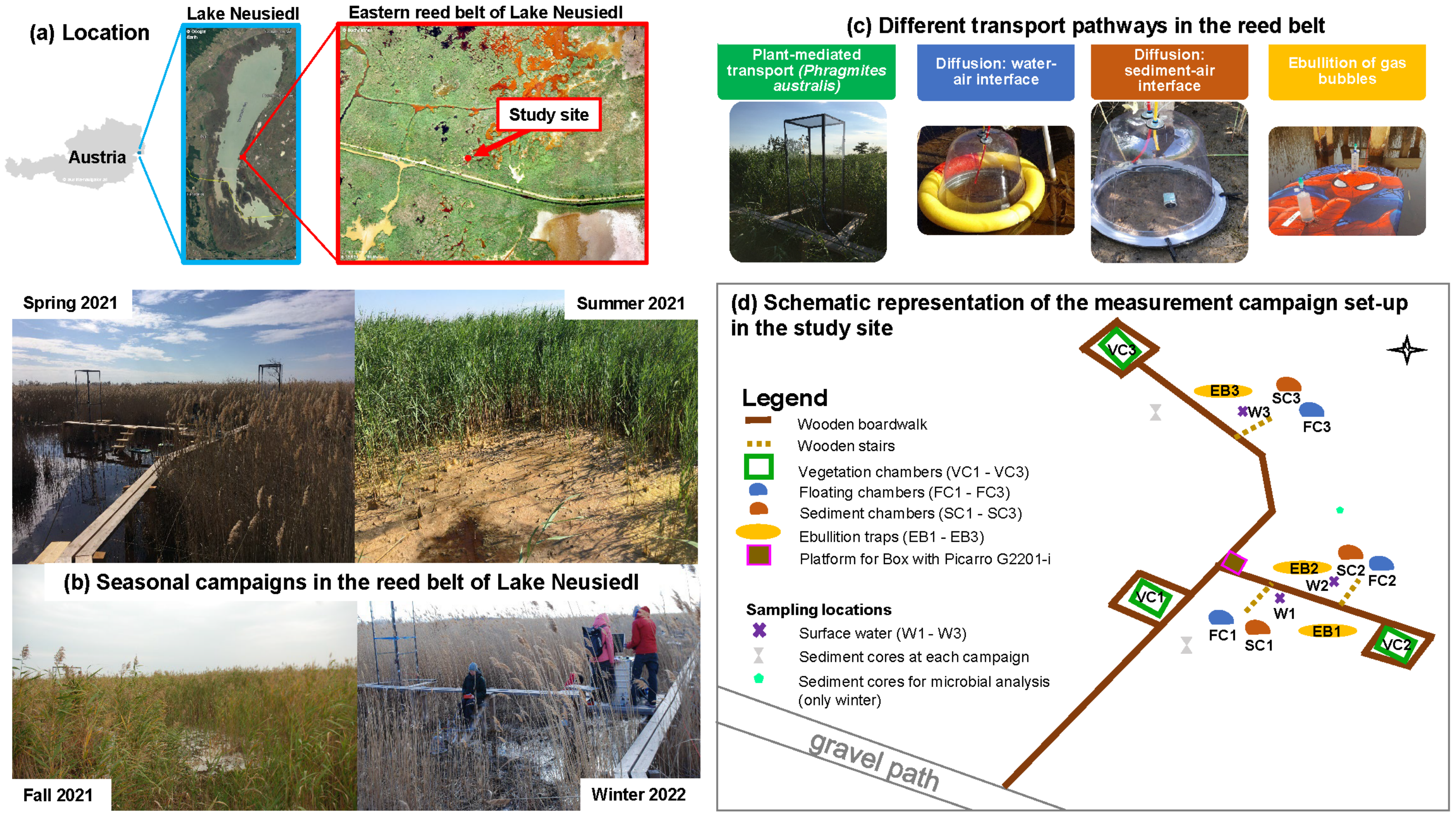

Figure 4.1: The study site is **(a)** located in the eastern reed belt of Lake Neusiedl in Austria (maps data: ©2020 austria-navigator.at, ©2020 Google Earth Image Landsat/Copernicus, Buchsteiner and Baur (2023)) and was used for **(b)** intensive 24 h measurement campaigns in each season. The different emission pathways of the CH_4 fluxes in the reed belt were measured with four chamber types illustrated in **(c)**. The setup of the measurement campaigns is shown in a schematic representation in **(d)**.

place on 29 and 30 March 2021, the summer campaign on 28 and 29 June 2021, the fall campaign on 28 and 29 September 2021, and the winter campaign on 22 and 23 February 2022. To avoid a subjective selection of measurement days/nights, there was exactly a three-month period between the individual campaigns. The winter campaign was the only one that had to be postponed due to channel sediment excavation work in the study area, including local sediment deposits, which would have affected the measurements too much. In addition to seasonal water level fluctuations, there was a sharp decline in water levels in the study area, particularly in 2021 (and 2022; see Baur et al. (2024b)), indicating that the reed belt had experienced a prolonged dry period following the summer campaign. The meteorological conditions, water, and reed properties of the studied reed belt during the campaigns are pictured in Figure 4.1b and summarized in Table 4.1. Table 4.1 summarizes the characteristics of each 24 h campaign and allows for comparison with other days/nights in the same season. During the study period, the surface water of the reed belt showed water levels ranging from 0 to 23 cm (see Table 4.1). If water was present, pH values ranged from 8.4 to 9 and electrical conductivity from 3.3 to 7 mS cm^{-1}.

The measurement intervals in a 24 h measurement campaign were every 3 h for each chamber type and every 6 h for gas bubbles in the ebullition traps. There were 3 replicates of each chamber type and 9 replicates of ebullition traps (funnels) spatially distributed around the constructed boardwalk at the study site (see Figure 4.1d). In situ measurements of surface water were conducted, and samples were collected every 6 h in each season when water was available above the surface (see Section 4.2.3 for details). Sediment cores were sampled in each campaign and analyzed in the laboratory for chemical and physical properties (see Section 4.2.4 for details). In order to determine the microbial status in the sediments and its changes over time, two sediment cores were taken before the first and after the last measurement campaign (one year apart) and are described in Section 4.2.4.

Pathways divided by different chamber measurements and ebullition traps

Different measurement types were used to capture the different emission pathways of CH_4 fluxes in the reed belt individually: plant-mediated transport of *P. australis* with vegetation chambers (VC), diffusion at the water–air interface with floating chambers (FC), diffusion at the sediment–air interface with sediment chambers (SC), and ebullition with ebullition traps (EB) (see Figure 4.1c). The setup of the campaigns with the location of the chambers and the sampling points is schematically represented in Figure 4.1d.

VCs were used to capture the plant-mediated transport of *P. australis.* For each VC, a steel frame (2.99 m × 0.78 m × 0.78 m) was welded with a ground frame (0.2 m × 0.78 m × 0.78 m), which was anchored permanently at the study site since early March 2021 and inserted at least 7 cm into the ground. At the beginning of each campaign, every VC was covered with transparent acryl glass plates (3 walls and 1 lid), which were all surrounded with highly strong magnetic stripes. A mobile acryl glass plate equipped with an inlet tube plug-in connector, an outlet tube plug-in connector, and a power cable was used to close the chamber during measurements. Each VC had three fans at three different heights to ensure good ventilation inside the chamber.

FCs were used to capture the transport of molecular diffusion at the water–air interface

Table 4.1: The mean ± standard deviation of meteorological, water, and reed properties of the reed belt at our study site during the seasonal 24 h measurement campaigns (T_{air} = air temperature, rH = relative humidity, LAI = leaf area index, T_{water} = water temperature, WL = water level, CON = electrical conductivity, DO = dissolved oxygen, ORP = oxygen–reduction potential, Chl-a = chlorophyll-a, SO_4^{2-} = sulfate, and TOC = total organic carbon concentration of the surface water, if water was present). For LAI and WL, pure spatial mean values per campaign were used. For the other water parameters, three spatial replicates were used (location see Figure 4.1d), which were sampled several times per campaign. For T_{air} and rH, pure temporal mean values of the 24 h campaigns were used. The number of data points per parameter is given in parentheses.

Season	**DOY**	**Year**	**T_{air}** [°C]	**rH** [%]	**LAI**	**T_{water}** [°C]	**WL** [cm]	**pH_{water}**	**CON_{water}** [mS cm^{-1}]	**DO_{water}** [%]	**ORP_{water}** [mV]	**Chl-a_{water}** [µg L^{-1}]	**$Sulfate_{water}$** [mg L^{-1}]	**TOC_{water}** [mg L^{-1}]
spring	88 & 89	2021	14.3 ± 3.1 (8640)	57.8 ± 19.0 (8640)	0.7 ± 0.4 (7)	13.8 ± 1.6 (12)	20 ± 3 (9)	8.40 ± 0.04 (12)	3.26 ± 0.02 (12)	96.8 ± 9.6 (9)	138.2 ± 45.4 (12)	1.4 ± 3.1 (12)	576.7 ± 12.6 (12)	48.6 ± 2.8 (12)
summer	179 & 180	2021	26.8 ± 6.5 (8640)	64.1 ± 19.8 (8640)	2.5 ± 1.1 (6)	26.4 ± 5.9 (12)	4 ± 3 (6)	8.98 ± 0.04 (12)	6.96 ± 0.42 (12)	46.7 ± 68.7 (12)	−184.8 ± 115.2 (12)	36 ± 33 (12)	1366.1 ± 103.7 (12)	132.1 ± 16.3 (12)
fall	271 & 272	2021	15.9 ± 4.7 (8640)	86.3 ± 12.5 (8640)	1.4 ± 0.6 (8)	-	0	-	-	-	-	-	-	-
winter	53 & 54	2022	5.4 ± 2.8 (8640)	71.9 ± 17.3 (8640)	-	6.1 ± 3.2 (12)	4 ± 1 (6)	8.91 ± 0.08 (12)	6.02 ± 0.60 (12)	97.2 ± 21.2 (12)	−34.2 ± 105.1 (12)	36 ± 47 (12)	1021.3 ± 160.1 (12)	120.9 ± 14.8 (12)

and are described in detail in Baur et al. (2024a). SCs were used to capture the molecular diffusion transport at the sediment–air interface. The SC top was made of transparent PVC in the form of a growing bell with a diameter of 30 cm and a hard plate with sealing rubber on the base. The bottom frame was an aluminum ring surrounded by a sealing rubber, which was inserted to the sediments 2–3 weeks in advance of each campaign. The upper chamber and the bottom frame were fixed and held together with at least 5 clamps during each measurement.

In VC, FC, and SC, the dry mole fraction of CH_4 (sum of $^{13}CH_4$ and $^{12}CH_4$) and the stable carbon isotope ratios (δ^{13}C-CH_4 and δ^{13}C-CO_2) of the chamber air were measured directly in the field during chamber closure with an isotopic gas analyzer (G2201-i, Picarro Inc., Santa Clara, USA) using cavity ring-down spectroscopy (CRDS; highly sensitive laser absorption technology) and with an external diaphragm vacuum pump (MD 1, Vaccuubrand GmbH, Wertheim, Germany) for the CRDS. During the field measurements, the simultaneous measurement mode for CO_2 and CH_4 as well as the high precision mode of the Picarro instrument were used, which has a measurement interval of about every 5 sec. During measurements, SC, VC, and FC were directly connected to the Picarro instrument through two 6 mm outer diameter polyurethane tubes (Festo GmbH, Esslingen a.N., Germany), one as inlet and another as outlet, which circulated the air between the closed chamber and the instrument. For air circulation, an additional KNF diaphragm gas pump (NMP830KNDC, KNF Micro AG, Reiden, Swiss) and an external air flow controller (2510A2A13BVBN, Brooks Instrument, LLC, Hatfield, USA) with a constant flow rate of 0.9 LPM were used. The closing time for FC and SC was 5 min each, the VC closing time was 10 min due to the larger chamber volume. All isotopic ratios measured in this study are expressed in ‰ relative to Vienna Pee Dee Belemnite (VPDB). Before each campaign, the instrument was calibrated using two certified stable isotope standard gases, which are described in Baur et al. (2024a). The standard deviation of δ^{13}C-CH_4 during the field measurements (uncertainty) was, on average, 3.5 ‰ VPDB, while the standard deviation of δ^{13}C-CO_2 was 0.6 ‰ VPDB.

EBs were used to capture the ebullition pathway of gas bubbles from supersaturated sediments and are described in detail in Baur et al. (2024a). This study of Baur et al. (2024a) examined the ebullition pathway continuously over a more extended period (from March to July 2021) at the same lake and not solely within the reed belt. The δ^{13}C-CH_4 values and the dry mole fraction of CH_4 of the collected gas from EB were measured with the same Picarro instrument, but with an additional small sample isotope module (SSIM2) (A0314, Picarro, Inc., Santa Clara, USA) including an additional external diaphragm vacuum pump (MD 1, Vaccuubrand GmbH, Wertheim, Germany) for the SSIM in the lab shortly after each campaign (for further details, please refer to Baur et al. (2024a)). The SSIM enables syringe injection of small gas sample volumes with measurement repetitions. With the SSIM, the fast method was used with two measurement repetition per gas sample and a pure measurement duration of 8 min for recording an average value per gas sample repetition. The standard deviation of δ^{13}C-CH_4 during the measurements (uncertainty) was, on average, 0.25 ‰ VPDB. Due to the high CH_4 concentration of ebullition gas bubbles, the high dynamic range mode of the Picarro had to be applied in the lab.

During the spring campaign, there were no open sediment areas at the study site due to higher water levels within the reed belt, which precluded the possibility of performing SC measurements. During the course of the year, due to the sharp drop in water levels not only in the open lake area of Lake Neusiedl, but also in the reed belt (Baur, 2024), EB and FC measurements were not possible in fall, as there was no water level above the surface. Furthermore, it was not feasible to conduct EB measurements during the winter campaign, as the exceedingly low water levels (and small water areas) precluded the installation of the inverted funnels, which would have entailed contact with and disturbance of the sediments. The EB measurements in summer were only possible despite the low water level and before the site ran dry, because the traps had already installed at the beginning of March 2021, when the water level was high.

Flux calculation

For the calculation of the fluxes of the chamber measurements (FC, SC, and VC), the initial 25% of the chamber closure time (death band) was removed from the linear regression fit of the temporal change of the dry mole fractions of CH_4 to exclude potential artifacts due to chamber closing (Hoffmann et al., 2017). Ebullition (a sudden exponential increase in the dry mole fraction) during chamber measurements was excluded for the calculation of diffusive fluxes. Due to the presence of a highly agile sediment layer (soft and waterlogged), ebullition was sometimes triggered by the closure of the SC during the summer campaign. However, since the aim was to measure diffusion rates at the sediment–air interface with the SC, a substantial proportion of the SC measurement data from summer had to be excluded. The equations utilized to estimate chamber fluxes and ebullition rates are thoroughly delineated in Baur et al. (2024a). Only flux data from FC, SC, and VC were utilized that exhibited a coefficient of determination R^2 of at least 0.6 for the linear regression of the temporal change of the dry mole fractions of CH_4, or in instances where the CH_4 flux was minimal (near zero), i.e. between -0.01 and 0.01 mg CH_4 m^{-2} h^{-1} and the R^2 was at least 0.6 for the temporal change of the dry mole fraction of CO_2. In total, 213 chamber CH_4 fluxes were used, with a mean R^2 of 0.9. Additionally, 72 ebullition rates were calculated across two season campaigns (spring and summer), of which 26 exhibited ebullition rates exceeding zero.

Stable carbon isotope ratios

The Keeling plot approach was applied to determine the seasonal source signatures of $\delta^{13}C$ (Keeling, 1958, Pataki et al., 2003) because transport and oxidation fractionate the stable carbon isotopes (Chanton, 2005, Conrad, 2005). The source signature of CH_4 is the intercept of the linear regression between the reciprocal of the dry mole CH_4 fraction and the values of $\delta^{13}C$-CH_4. The values used in the Keeling plot are the mean values of the chamber air (of VC, FC, or SC) during the chamber closure of each individual chamber measurement (5–10 min depending on the chamber type, see Section 4.2.2). The CO_2 source signature was determined in a similar manner, albeit with CO_2 values. Subsequently, with the $\delta^{13}C$ source signatures of CH_4 and CO_2 of each season, the methanogenic characterization according to Whiticar et al. (1986) was applied to determine the dominant methanogenic pathway of each season and the contribution of CH_4 oxidation. Since ebullition is known not to fractionate the δ^{13}C-CH_4 values and to bypass the CH_4 oxidation region (Chanton, 2005), the measured values of the collected ebullition gas can directly show the isotopic source signature of CH_4 within the sediments without applying the Keeling plot approach.

Environmental variables

Each SC and FC was equipped inside with an air temperature and a light sensor (HOBO Pendant Temperature/Light 8K Data Logger, Onset Computer Corporation, Bourne, USA) with a measurement time interval of 30 sec. Each VC was equipped inside with an air temperature and relative humidity sensor (HOBO U23 Pro v2 Temperature/Relative Humidity Data Logger, Onset Computer Corporation, Bourne, USA) with a measurement time interval of 10 sec. Under each floating board with three ebullition traps, a water temperature sensor (HOBO Pendant Temperature/Light 8K Data Logger, Onset Computer Corporation, Bourne, USA) was fixed with a measurement time interval of 30 min due to the smaller data memory. Additionally, ambient air temperature, water vapor pressure deficit (VPD), incoming shortwave radiation (SW_{in}), and sediment temperature (in 5 cm depth) were measured nearby (50 m distance) at an eddy covariance tower (detailed description in Baur et al. (2024b) and published data in Baur (2024)).

4.2.3 Water sampling and analysis

During the 24 h campaigns, the following parameters were measured in situ in three surface water areas (sampling location Figure 4.1d) every 6 h using a portable WTW multiparameter probe (Multi 3420, Xylem Analytics GmbH, Weilheim, Germany): pH, electrical conductivity (CON), water temperature (T_{water}), dissolved oxygen (DO), and oxygen–reduction potential (ORP). At the same time interval, three surface water samples were collected, stored in a cool box, and analyzed immediately after the campaign in the accredited laboratory of the nearby Biological Station Lake Neusiedl (Illmitz, Austria). In the laboratory, the sulfate concentration was analyzed according to DIN EN ISO 10304 − 1 (DIN, 2009) using ion chromatography (Dionex ICS 1100, Thermo Fisher Scientific Inc., Waltham, USA). The chlorophyll-a concentration (Chl-a) was determined by the LORENZEN method (Goltermann, 1969). Total organic carbon concentration (TOC) was determined according to DIN EN 1484 (DIN, 2019) by catalytic combustion oxidation using the TOC-L analyzer (Shimadzu Corp., Kyoto, Japan).

4.2.4 Sediment sampling and analysis

In each campaign, at least two sediment cores were sampled with polycarbonate push core tubes (diameter 7 cm, length 60 cm). Each sediment core was divided according to its two visibly distinct layers for physical and chemical analysis. Fresh samples of each layer were sieved with a 2 mm sieve to remove large rhizomes, large roots, or snail shells.

Additionally, two sediment cores for microbial analysis were sampled in the reed belt always in winter before the first (11 February 2021) and after the last campaign (23 February 2022) using push core tubes, which were sealed with Parafilm after sampling. The sediment cores were divided into 2 cm depth sections in an anaerobic tent filled with nitrogen (N_2), individually packed, sealed, and stored at 4℃ in a refrigerator until laboratory analysis. The microbial analysis was carried out in four specific depth sections of each sediment core, two of which belong to the same layer: 0–2 cm, 4–6 cm, 20–22 cm, and 24–26 cm.

Physical and chemical sediment characterization

The gravimetric water content (WC) of the sediments was determined by completely drying the accurately weighed field wet sample in a freeze dryer (Lio 5P, Kambic d.o.o., Semic, Slovenia) until constant dry weight was reached and calculated according to Gardener (1986). The completely dry sediment samples were finely ground (pulverized) and homogenized using a mixer mill (MM400, RETSCH GmbH, Haan, Germany). A multiphase carbon analyzer (RC612, LECO Europe B.V., AG Geleen, Netherlands) was used to determine the content of organic (TOC, $\leq$ 450℃), inorganic (TIC, $>$ 450℃ & $\leq$ 1000℃), and total carbon (TC, sum of TOC and TIC) of the finely ground samples (in percentage of dry mass) via temperature-dependent CO_2 measurement (dry combustion method).

The analysis of sulfate, ammonium, nitrate, nitrite, and orthophosphate in the sediments was conducted by preparing sediment extracts from 4 g field wet sediment samples and 30 mL extraction solution (0.01 M $CaCl_2{\cdot}2H_2O$ for sulfate; ultrapure distilled water for the other parameters). The sediments were extracted on a horizontal shaker at 300 rpm for 60 min at room temperature to obtain optimal suspension of the slurry. The extracts were filtered through 0.45 µm nylon syringe filters. The concentration of the extracts were determined by turbidity or colorimetry using a UV-vis spectrometer (Infinite 200 Pro NanoQuant, Tecan Group Ltd., Männedorf, Switzerland). The specific methods are described in detail in Baur et al. (2024a).

For the pH and CON, the field wet sediment samples were air dried at 40℃ until mass stability was achieved. The samples were then incubated overnight with ultrapure distilled water (1:10 w/v ratio), shaken in an overhead shaker for 1 h, and allowed to stand for 30 min before pH (pH meters 7110 and 720) and CON (Cond 7110) were measured (Xylem Analytics GmbH, Weilheim, Germany).

Microbial 16S rRNA gene amplification, sequencing and analysis

Each sediment depth section sample, weighing between 0.5 to 1.0 g, underwent DNA (deoxyribonucleic acid) extraction utilizing the DNeasy PowerSoil Pro Kit (Qiagen NV, Venlo, Netherlands), following the manufacturer's guidelines. Subsequently, DNA concentration was determined using a Qubit 2.0 Fluorometer (Invitrogen, Carlsbad, USA) equipped with the dsDNA HS kit. For amplification of prokaryotic 16S rRNA genes, we employed PCR (polymerase chain reaction) with the primer pair 515f (5'- GTG CCA

GCM GCC GCG GTA A) and 806r (5'- GGA CTA CHV GGG TWT CTA AT), as detailed previously (Caporaso et al., 2011). The PCR products were then barcoded and sequenced at the Vienna BioCenter Core Facilities (VBCF) on the Illumina Miseq platform (300 PE). The initial raw reads underwent preprocessing using cutadapt (Martin, 2011) to eliminate primer sequences, followed by sequence analysis via the QIIME2 pipeline (Bolyen et al., 2019). In summary, the data was denoised and filtered for low-quality reads and chimeras using the DADA2 algorithm. Subsequently, sequences exhibiting 100% identity were clustered into amplicon sequence variants (ASVs). Taxonomic classification of these ASVs was conducted utilizing the SILVA database (release 138) in conjunction with the 'q2-feature-classifier' plugin (Bokulich et al., 2018).

4.2.5 Data and statistical analysis

Most data and statistical analysis were performed in R, version 4.2.2 (R Core Team, 2022), using the following R packages for data processing, manipulation, and visualization: *data.table, ggplot2, ggpubr, scales, hms* (Barrett et al., 2024, Kassambara, 2023a, Müller, 2023, Wickham, 2016, Wickham et al., 2023). The two-sided Dunn's post-hoc test was applied using the R package *rstatix* (Kassambara, 2023b) to statistically assess which emission pathway or season had significant differences in median CH_4 fluxes compared to the others and in sediment properties between the two sediment layers ($p < 0.05$, Adjustment Holm). Linear ordinary least squares regression using the R package *lmodel2* (Legendre, 2018) was used to determine the $\delta^{13}C$ source signatures in Keeling plots.

Potential interactions between the methanogenic archaea and other microbes were investigated by employing SparCC (Sparse Correlations for Composition data) network (Friedman and Alm, 2012) analysis at the ASVs level. Only those with > 10 reads and detected in $> 20\%$ of the samples were used for network construction to prevent false associations caused by low abundant ASVs. 1000 bootstraps were used and those with $p < 0.05$ were retained. The positive relationships (correlation coefficient > 0) were summarized at the class level. Only the top 10 groups with highest number of potential interactions with methanogenic archaea were shown, with network visualization being conducted in Cytoscape (Shannon et al., 2003).

4.3 Results

4.3.1 Seasonal and diel differences in CH_4 emissions of a subsaline reed wetland

Plant-mediated transport exhibited significantly elevated CH_4 emissions compared to emissions through diffusion or ebullition pathways throughout all seasons, as illustrated in Table 4.2. Regardless of the emission pathway, the highest median CH_4 emission rate and fluctuation range occurred during the summer campaign. The highest CH_4 emission of 18.56 mg CH_4 m^{-2} h^{-1} was observed via plant-mediated transport at 15 o'clock during the summer campaign. In summer, the median CH_4 emissions at the two diffusion interfaces (water–air and sediment–air) and the ebullition pathway did not show significant differences. However, in winter, the water–air interface exhibited a median CH_4 flux of 0.05 mg CH_4 m^{-2} h^{-1}, which was more than 10-fold and significantly higher than that observed at the sediment–air interface. Almost all emission pathways exhibited a significantly different median CH_4 flux between the seasons. Only at the sediment–air interface, the median flux did not differ significantly between fall and winter. The ebullition pathway exhibited the most pronounced fluctuations in CH_4 emissions across the two seasons in which EB measurements were possible, and demonstrated the lowest emission rate in spring. In spring, bubbles were trapped in only 3% of the EB measurements, while in summer it happened in 69%. The measurement of all pathways was not possible in all seasons due to variations in water levels and the dryness of the reed belt (see Figure 4.1).

Only plant-mediated transport showed a clear visible diel cycle of CH_4 fluxes in summer with the highest emission rates during daytime and on average a peak in the late afternoon (see Figure 4.2). In contrast, the diffusion pathways showed only some small diel variations, but no distinct diel cycle. However, we were able to detect a decrease in diffusive CH_4 fluxes at the water–air interface around midday in summer. In spring and fall, only plant-mediated transport displayed some diel variations of CH_4 fluxes, but not the diffusion pathways. Significant differences in the median CH_4 flux between daytime and nighttime ($SW_{in} < 10$ W m^{-2}) were identified for only two emission pathways, occurring in one season each: water–air in spring and plant-mediated in summer (see Table 4.2). Given that the ebullition trap measurements were consistently obtained over a 6 h period, we have not plotted a fitted line of diel variations, as the precise timing of bubble release from the sediments remains uncertain. Instead, the observed CH_4 ebullition rate was placed in the middle of the 6 h bubble collecting time in Figure 4.2. During the spring campaign, only one ebullition rate of 5.98 mg CH_4 m^{-2} h^{-1} could be observed during daytime. In contrast, during the summer campaign, ebullition occurred at nighttime and during daytime, with the highest rate of 17.03 mg CH_4 m^{-2} h^{-1}.

Table 4.2: Differences in CH_4 fluxes for each emission pathway (plant-mediated, water–air interface, sediment–air interface, ebullition) and season are represented by their median ± standard deviation; significant differences ($p < 0.05$ with Holm's adjustment, Dunn's test) between the pathways in each season are indicated by different superscript letters, between the seasons in each pathway by different superscript symbols or between daytime and nighttime in each pathway and season by different superscript numbers; the number of quality checked measurement data is provided in brackets; due to the water level or dryness of the reed belt, not every pathway could be measured in each season; nighttime when incoming shortwave radiation was < 10 W m^{-2}.

		CH_4 flux [mg CH_4 m^{-2} h^{-1}]			
Time period	**Pathways**	**Spring 2021**	**Summer 2021**	**Fall 2021**	**Winter 2022**
diel (24 h)	plant-mediated	$1.36 \pm 0.23^{\mathrm{a},+}$(24)	$4.59 \pm 3.61^{\mathrm{d},*}$(24)	$0.35 \pm 0.30^{\mathrm{f},\otimes}$(24)	$0.12 \pm 0.06^{\mathrm{h},\wedge}$(24)
	water–air	$0.11 \pm 0.07^{\mathrm{b},\cap}$(23)	$1.12 \pm 0.51^{\mathrm{e},\pi}$(16)	-	$0.05 \pm 0.06^{\mathrm{i},\cup}$(23)
	sediment–air	-	$1.21 \pm 0.52^{\mathrm{e},\backslash}$(08)	$0.002 \pm 0.01^{\mathrm{g},\oplus}$(24)	$0.004 \pm 0.09^{\mathrm{k},\oplus}$(23)
	ebullition	$0.000 \pm 1.00^{\mathrm{c},\Omega}$(36)	$1.35 \pm 3.69^{\mathrm{e},\Phi}$(36)	-	-
daytime	plant-mediated	$1.54 \pm 0.23^{\mathrm{a},+,1}$(13)	$6.37 \pm 3.90^{\mathrm{d},*,2}$(15)	$0.52 \pm 0.38^{\mathrm{f},+\wedge,4}$(10)	$0.11 \pm 0.05^{\mathrm{h},\wedge,5}$(9)
	water–air	$0.14 \pm 0.08^{\mathrm{b},\cap,6}$(12)	$1.07 \pm 0.42^{\mathrm{e},\pi,8}$(12)	-	$0.06 \pm 0.02^{\mathrm{hk},\cup,9}$(9)
	sediment–air	-	$1.21 \pm 0.48^{\mathrm{e},\backslash,10}$(06)	$0.001 \pm 0.01^{\mathrm{g},\oplus,11}$(11)	$0.006 \pm 0.10^{\mathrm{k},\otimes,12}$(11)
	ebullition	$0.000 \pm 1.41^{\mathrm{c},\Omega,13}$(18)	$1.28 \pm 3.77^{\mathrm{e},\Phi,14}$(27)	-	-
nighttime	plant-mediated	$1.23 \pm 0.22^{\mathrm{a},+,1}$(11)	$3.19 \pm 1.60^{\mathrm{d},+,3}$(09)	$0.29 \pm 0.21^{\mathrm{f},\wedge,4}$(14)	$0.12 \pm 0.06^{\mathrm{h},\wedge,5}$(15)
	water–air	$0.09 \pm 0.04^{\mathrm{b},\pi\cup,7}$(11)	$1.59 \pm 0.60^{\mathrm{d},\pi,8}$(04)	-	$0.03 \pm 0.08^{\mathrm{hk},\cup,9}$(14)
	sediment–air	-	$1.48 \pm 0.84^{\mathrm{d},\oplus,10}$(02)	$0.002 \pm 0.01^{\mathrm{g},\oplus,11}$(13)	$0.001 \pm 0.08^{\mathrm{k},\oplus,12}$(12)
	ebullition	$0.000 \pm 0.00^{\mathrm{c},\Omega,13}$(18)	$2.31 \pm 3.59^{\mathrm{d},\Phi,14}$(09)	-	-

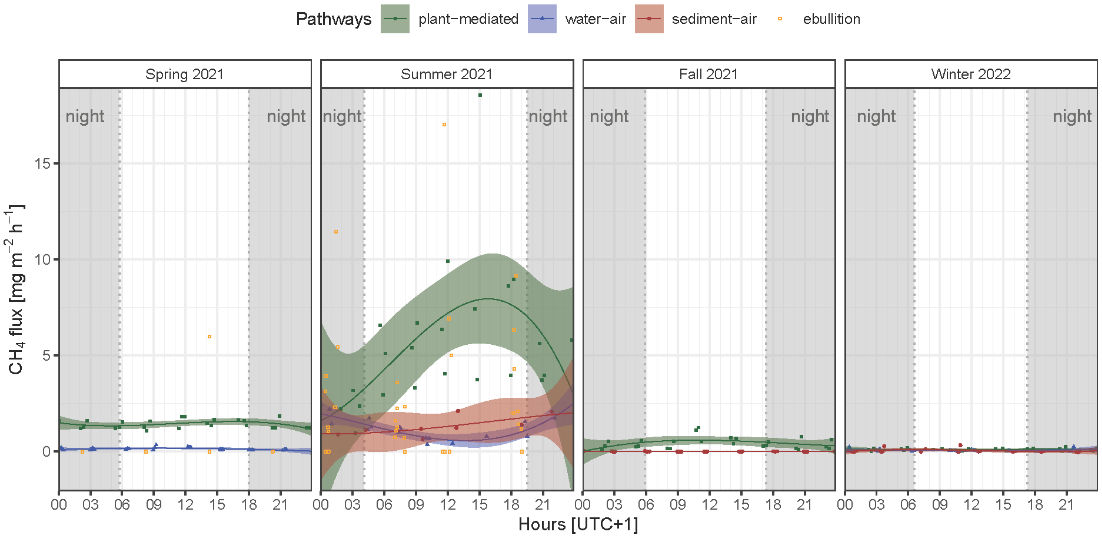

Figure 4.2: Diel variability of the CH_4 fluxes for each season and emission pathway (plant-mediated, water–air interface, sediment–air interface, ebullition); each point represents an individual measured flux rate; the fitted lines show the 3^{rd} order polynomial regressions with the 95% confidence interval; due to the water level or dryness of the reed belt, not every pathway was present or could be measured in each season; nighttime when incoming shortwave radiation was < 10 W m^{-2} (gray shading).

4.3.2 Seasonal δ^{13}C source signatures of a subsaline reed wetland

The Keeling plots' source signatures $\delta^{13}C\text{-}CH_4$ differ between seasons and are most ^{13}C-depleted in fall (-73.6 ± 2.4 ‰ VPDB; see Figure 4.3a). The Keeling plots' source signatures $\delta^{13}C\text{-}CO_2$ differ between seasons and are most ^{13}C-depleted in winter (-30 ± 1.6 ‰ VPDB; see Figure 4.3b). The methanogenic characterization after Whiticar et al. (1986) indicates the dominance of acetoclastic methanogenesis in the reed belt of Lake Neusiedl regardless of the seasons (see Figure 4.3c). However, the values of the source signatures including the standard error of the winter campaign are already partially within the range of CH_4 oxidation in this representation. For this subsaline reed wetland, the means of the seasonal isotopic source signatures are -63.6 ± 2.7 ‰ VPDB for CH_4 and -28.1 ± 1.2 ‰ VPDB for CO_2.

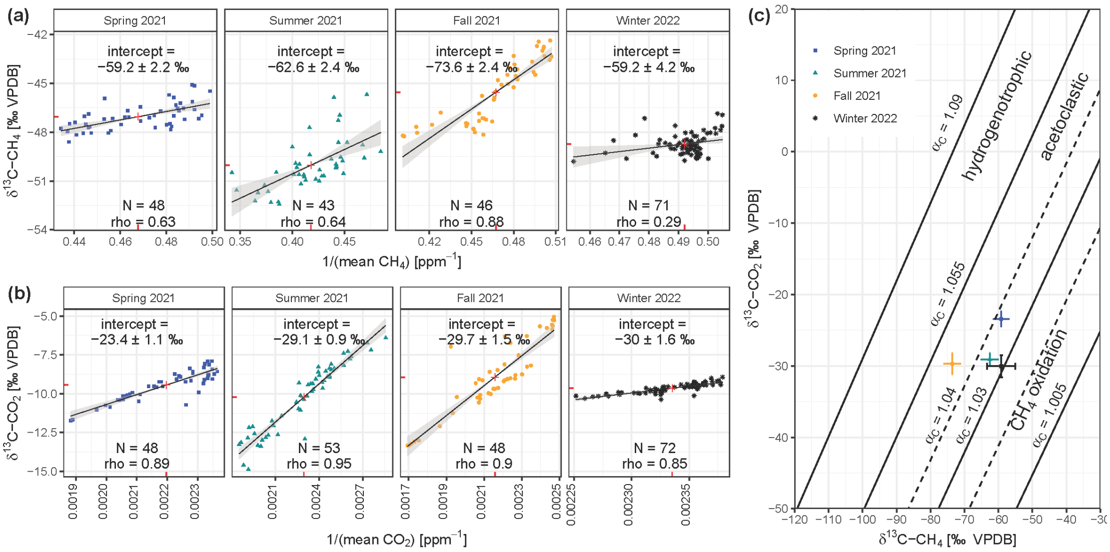

Figure 4.3: Keeling plots to determine the seasonal source signatures **(a)** δ^{13}C-CH_4 and **(b)** δ^{13}C-CO_2 of the reed belt as the y axis intercepts (shown as number in ‰ VPDB) of the fitted ordinary least square linear regression lines (black) with 95% confidence interval (shaded light gray) and their centroids (red cross) using the mean chamber air values during the chamber closure, and **(c)** the methanogenic characterization according to Whiticar et al. (1986) using the calculated source signature pairs of δ^{13}C-CH_4 and δ^{13}C-CO_2 and their standard errors from the plots **(a)** and **(b)**.

The δ^{13}C-CH_4 values of the collected ebullition gases were −54.2 ‰ VPDB ($N = 1$) in the spring campaign and −59.9 ± 1.9 ‰ VPDB ($N = 25$) in the summer campaign. In fall and winter, no ebullition trap measurements were possible due to the dryness of the reed belt.

4.3.3 Sediment properties of the reed belt

The sediments of the reed belt of Lake Neusiedl had two clear distinguishable layers with significant differences in most physical and chemical parameters (see Figure 4.4 and S.26). The upper layer (L1) was very wet (mean ± standard deviation of gravimetric WC: 82.3 ± 6.7 mass-%, see Figure 4.4b), brown, peaty (mean TOC: 18.2 ± 9.6 mass-%, see Figure 4.4a), and with a mean thickness of 9.7 ± 3.8 cm. The lower layer (L2) was gray, sandy, and low in organic carbon (mean TOC: 0.8 ± 0.6 mass-%). In spring, L1 was a fluffy layer, had the highest water level above it (20 ± 3 cm), and had occasionally a maximum thickness of 19 cm. However, there were no significant differences in L1 thickness between seasons. In contrast, the TOC and TIC values of L1 in particular differed between the seasons (see Figure 4.4a and S.26a). The mean TIC decreased from spring to winter, while the mean TOC increased during the same period, except for the mean value of the summer season. The SO_4^{2-} concentration in the sediments

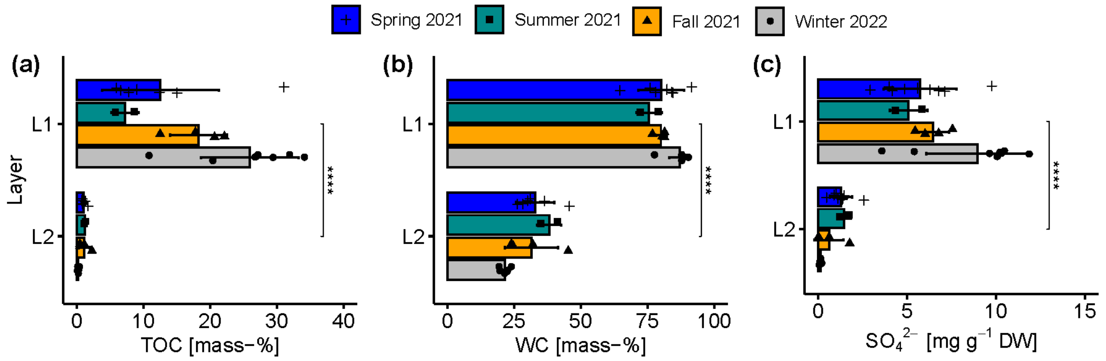

Figure 4.4: Seasonal and layer specific differences of **(a)** total organic carbon content (TOC), **(b)** gravimetric water content (WC), and **(c)** sulfate ($SO_4{}^{2-}$) concentration in the upper (L1) and lower layer (L2) of sediments in the reed belt of Lake Neusiedl. Very significant differences (****, $p < 0.0001$ with Holm's adjustment, Dunn's test) in the parameters between the two layers in the sediments independent of the season.

showed the same seasonal pattern as the TOC values (see Figure 4.4a and c). L1 showed the highest concentration of $NH_4{}^+$ in summer and the highest concentration of $NO_2{}^-$ in fall (see Figure S.26d and f). The upper sediment layer exhibited, on average, a significantly higher CON value and a significantly lower pH value compared to the lower layer (see Figure S.26g and h).

4.3.4 Change in the microbial community in the sediments within one year

Considering the findings regarding CH_4 fluxes throughout 2021, and acknowledging the central role the microorganisms play in CH_4 emission dynamics, our study investigated the microbial community composition within sediments from Lake Neusiedl at two different sampling dates: one in winter 2021 and another a year later in winter 2022. We conducted our analysis across various depths in two sediment cores each winter, employing prokaryotic 16S rRNA gene amplicon sequencing. It is worth pointing out that there was a marked decrease in total DNA yield in samples from the lower layers in comparison to those from the upper layers, with a decrease of almost 1000-fold in 2021 and almost 32-fold in 2022 (see Table S.8). Due to the significance of sulfate-reducing bacteria, methanogens, and methanotrophs in carbon cycling within anaerobic sediment environments (Conrad, 2007, Jones, 1985, Muyzer and Stams, 2008), we specifically targeted these three groups for further investigation (see Figure 4.5). The amplicon sequencing quality of core II at the depth of 4–6 cm from the 2022 sampling was insufficient for its inclusion in further analyses.

Examination of the distribution pattern of methanogens (see Figure 4.5a) reveals a noticeable trend: their relative abundance is higher in the lower depths (20–22 cm and

Figure 4.5: Relative abundance of **(a)** methanogens, **(b)** sulfate-reducing bacteria, and **(c)** methanotrophs in four depth sections of the two sediment cores (I and II) in winter 2021 and 2022. The two sediment sections, 0–2 cm and 4–6 cm, are part of the top organic layer (L1) of the sediment, while the sections 20–22 cm and 24–26 cm are located in the lower sandy layer (L2). Due to the insufficient amplicon sequencing quality of core II at the depth of 4–6 cm from the 2022 sampling, the sample was not used for further analyses.

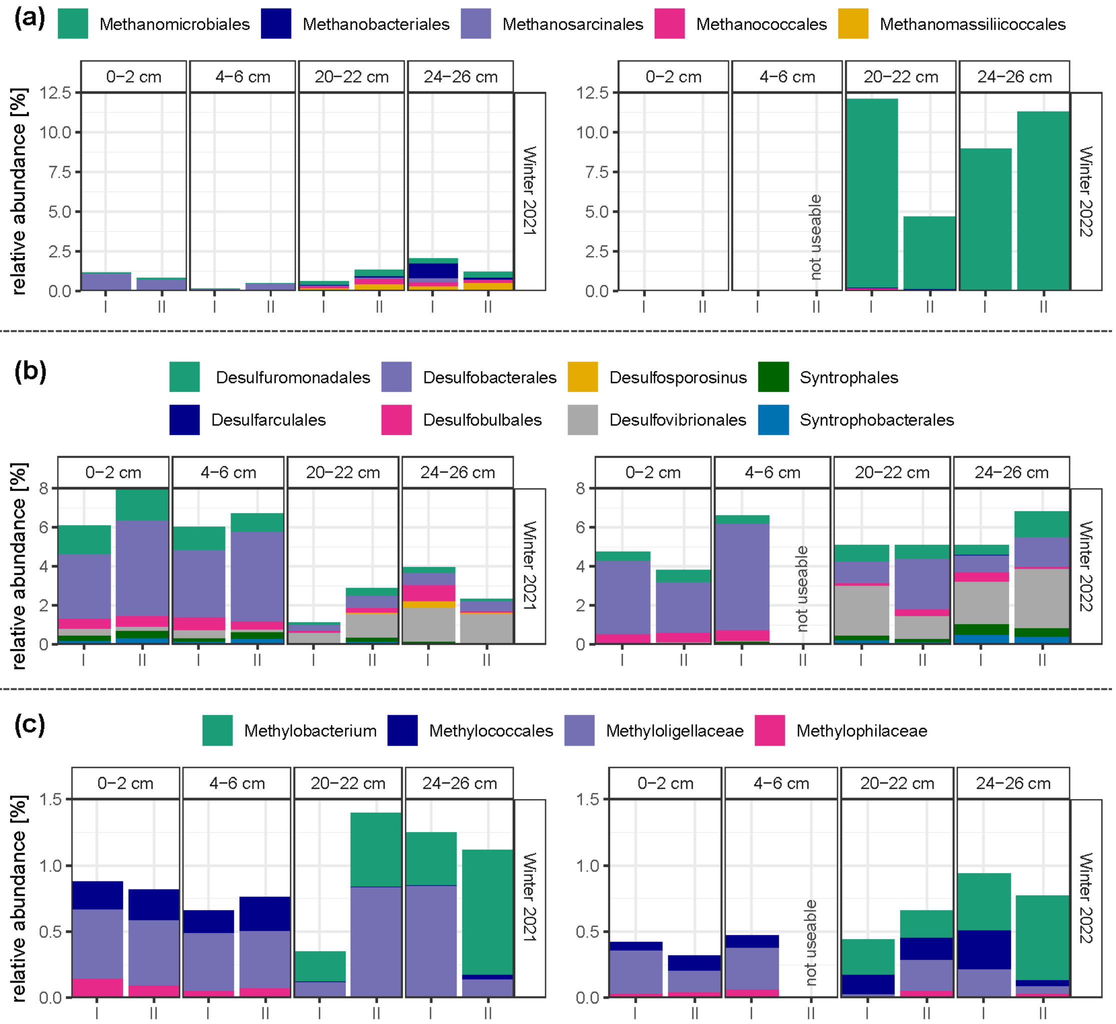

24–26 cm) samples compared to the upper layer in both years, although this difference is less pronounced in the 2021 sampling. When comparing their diversity across the two years, various observations emerge. First, in 2022, their relative abundance was substantially higher, reaching up to 12% compared to a maximum of around 2% in 2021. Second, the composition of methanogenic communities differed substantially. In 2021, sediments exhibited a broader array of detected methanogenic groups, encompassing orders such as *Methanobacteriales*, *Methanosarcinales*, *Methanococcales*, *Methanomicrobiales*, and *Methanomassiliicoccales.* Conversely, in 2022, the methanogenic community displayed greater homogeneity, predominantly dominated by organisms from the order *Methanomicrobiales.*

The relative abundances of sulfate-reducing bacteria (see Figure 4.5b) display a distinct trend in the year 2021. There is a marked discrepancy between the upper (0–2 cm and 4–6 cm) and the lower layer (20–22 cm and 24–26 cm). In the upper layer, the relative abundance of sulfate-reducing bacteria is higher, reaching levels of up to around 8%, in contrast to the deeper layer where it reaches numbers of around 4%. This difference in abundance is accompanied by a visible diversity pattern. The upper layer predominantly hosts taxa such as *Desulfobacterales*, *Desulfuromonadales*, and *Desulfobulbales.* While these groups persist in the lower layer, there is a shift towards an increased prevalence of organisms belonging to the order *Desulfovibrionales*, eventually becoming the most abundant sulfate-reducing bacterial group in the 24–26 cm depth. The sediments sampled in 2022 present a different pattern, with comparable sums of relative abundances of sulfate reducers across different depths in 2022 in contrast to 2021. However, the dominant taxa are similar to those observed in the previous year, where the same groups are also prevalent in the upper layer, and *Desulfovibrionales* becomes more abundant as depth increases.

Analysis of methanotroph distribution reveals similar patterns across samplings from both 2021 and 2022 (see Figure 4.5c). In both years, a clear distinction is observed between the upper and lower layer, with *Methylobacterium* being detected exclusively in depths $\geq$ 20 cm, while *Methyloligellaceae* and *Methylococcales* dominate the upper layer (0–2 cm and 4–6 cm). However, there is an overall lower relative abundance of methanotrophs across all depths in 2022 compared to 2021, with maximum values of approximately 0.9% compared to 1.4%.

A network interface of significant non-random relationships between the different hydrogenotrophic methanogenic groups and other microbes in the Lake Neusiedl sediment community was constructed (see Figure 4.6). We obtained 1,398 nodes (ASVs) and 132,305 edges, and after clustering and filtering, a co-occurrence network with 153 nodes and 325 edges were generated. In the network, the groups that displayed the highest number of relationships with methanogens included *Aminicenantales*, *Anaerolineales*, *Bacteroidales*, *Burkholderiales*, *Desulfatiglandales*, *Desulfobacterales*, *Pseudomonadales*, *Sedimentisphaerales*, and *Woesearchaeales.*

Figure 4.6: Co-occurrence network ($p < 0.05$) of hydrogenotrophic methanogens (yellow) with other microbes, with groups containing organisms with potential for acetate oxidation highlighted (pink). Only the top 10 microbes (blue) with links to methanogens were included. The size of each node is proportional to the relative abundance of the group and the thickness of each line is proportional to the number of links between the nodes.

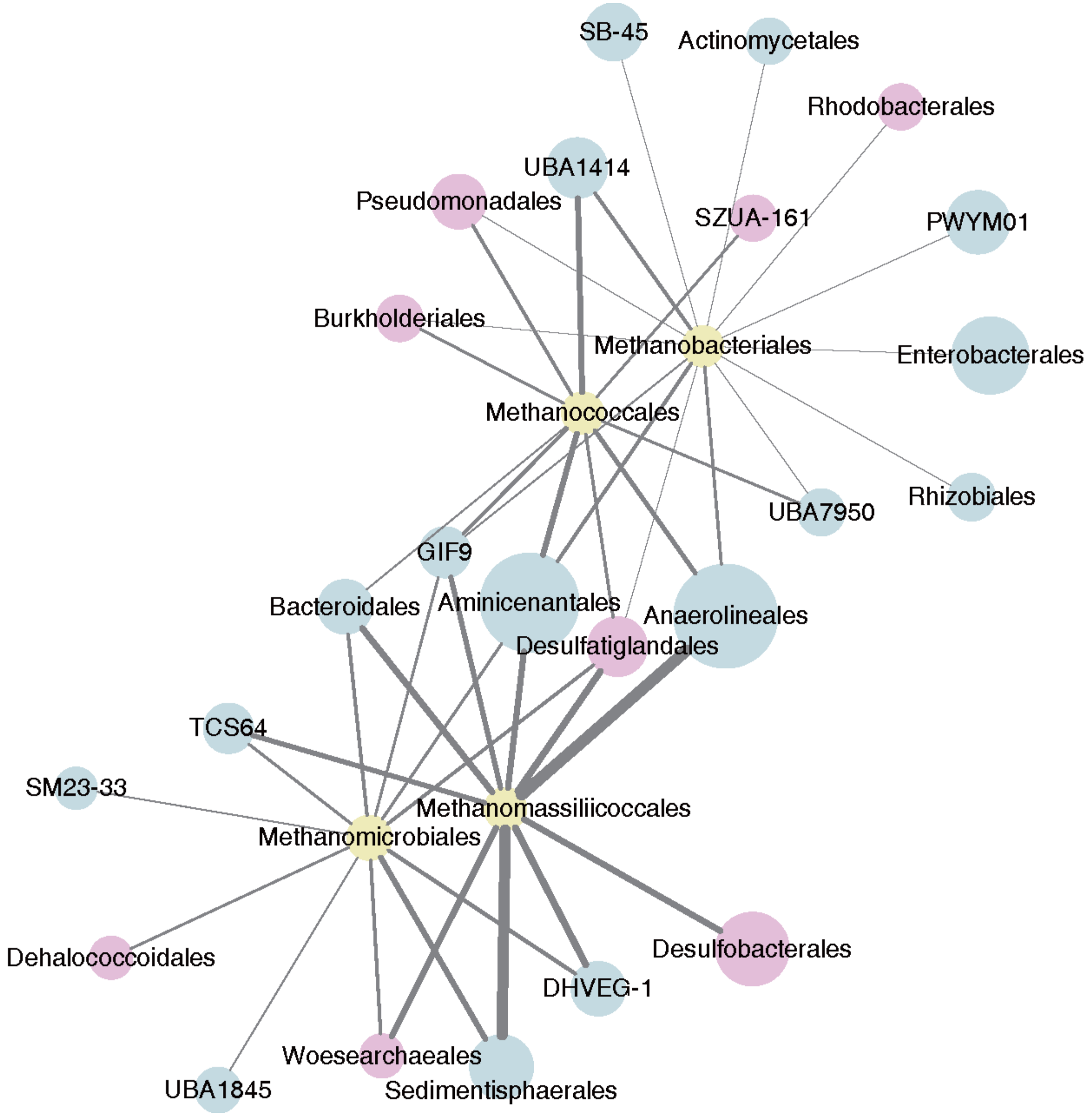

4.4 Discussion

4.4.1 Seasonal and diel differences in CH_4 fluxes for each emission pathway in a subsaline reed wetland

This is one of the first studies to date to investigate all assessable CH_4 emission pathways in a wetland with reed over the entire diel cycle (24 h) and in all seasons individually. In the studied subsaline reed wetland, plant-mediated transport was identified as the most significant emission pathway for CH_4, irrespective of the season.

The highest seasonal median plant-mediated CH_4 flux (summer) at our studied wetland with reed is approximately half that of the average plant fluxes from studies of littoral zones in lakes or wetlands (8.3 mg CH_4 m^{-2} h^{-1}), as reported by Bastviken et al. (2011). Moreover, our observed flux is 4 to 10 times lower than that reported in studies of other wetlands with reed (Duan et al., 2006, van den Berg et al., 2020) and twice as high as the flux observed in a subtropical *Phragmites* wetland subjected to drought (Jeffrey et al., 2019). One possible explanation for this discrepancy is the influence of lower water levels, given that Lake Neusiedl was experiencing drought (Baur et al., 2024b). A second possible explanation is that the subsaline reed ecosystem exhibited lower CH_4 production rates than the fen (van den Berg et al., 2020), which may be attributed to the coexistence and competition of sulfate reducers and methanogens.

The plant-mediated CH_4 fluxes at our site were consistently higher than diffusive CH_4 fluxes at the water–air and sediment–air interfaces, also in the non-growing season. One potential explanation is the chimney effect, which has been observed in the context of standing dead or non-intact reed culm between the sediment and the atmosphere (Brix, 1989, van den Berg et al., 2020). An additional potential explanation is Venturi-induced flow, as observed by Armstrong et al. (1992) in *P. australis*. This phenomenon is wind-induced and is likely to occur during the winter months when humidity-induced convection is absent.

In reed ecosystems, a clear diel cycle of CH_4 fluxes is only observed when pressurized flow is present, as opposed to diffusion. Pressurized flow is contingent upon the presence of living and intact reed culm (van den Berg et al., 2020, Vroom et al., 2022). Accordingly, at our site, a distinct diel cycle of CH_4 fluxes was discerned solely in summer and in instances of plant-mediated transport. However, when the reed ecosystem is considered as a whole and without partitioning in emission pathways, the reed belt exhibited a diel cycle with two peaks (with a slightly higher peak in the afternoon) during the summer months of 2021 (Baur et al., 2024b). This phenomenon is likely caused by CH_4 oxidation during daytime due to the low or absent water levels above the sediments (Baur et al., 2024b). The higher water level would also account for van den Berg et al. (2020)'s observation of a distinct diel cycle of CH_4 fluxes in June, both at the ecosystem level and in plant-mediated transport.

It can be reasonably assumed that the pressurized flow at our site is primarily driven by humidity and temperature. These findings are corroborated by observations that the plant-mediated CH_4 fluxes of *P. australis* exhibited a peak in the diel cycle in summer in the late afternoon, as did sediment temperature (in 5 cm depth) and VPD (see Figure S.24). In addition to light, these drivers were also identified by Vroom et al. (2022). In a reed wetland in an arid region of China, the diel cycle was explained by light-induced convection flow and the peak often occurred in the afternoon, coinciding with the time of the highest sediment temperature (Duan et al., 2006). In contrast, in a fen with reed, the peak of diel CH_4 fluxes were around midday (van den Berg et al., 2020), which could indicate the higher influence of light intensity and the lack of influence of soil temperature due to the high water levels. Another study conducted in the Hungarian part of Lake Neusiedl on 30 June 1993 revealed a daily maximum of pressure and flow in the efflux reed culms in the afternoon (Brix et al., 1996), indicating a potential contribution of old reed stubbles to the afternoon peak of diel CH_4 fluxes. At our site, there are enough standing dead and broken reed culm in summer to potentially exert an influence.

The ebullition rates at our site are, on average, lower than the plant-mediated CH_4 emissions, with a notable increase observed in summer compared to spring. The median summer ebullition rate of 1.35 mg CH_4 m^{-2} h^{-1} is comparable to the average ebullition rates observed in a subtropical wetland (partially covered with reed) across two seasons (Jeffrey et al., 2019). However, at our study site, the release of ebullition was found to be highly sporadic and less frequent in spring. Consequently, ebullition measurements require the use of longer periods than 24 h outside of summer. Baur et al. (2024a) employed a sampling frequency of one week at Lake Neusiedl to more effectively capture the natural sporadic release of ebullition gases from April to July 2021. Nevertheless, the two 24 h campaigns with ebullition measurements adequately captured ebullition when compared to the median (± standard deviation) of the continuously measured and weekly collected CH_4 ebullition rates within the reed belt, separated by seasons, in Baur et al. (2024a): In spring in Baur et al. (2024a), the median ebullition rate from March to May was 0.04 ± 0.86 mg CH_4 m^{-2} h^{-1}, while the median CH_4 flux of the ebullition pathway in the spring campaign was 0.00 ± 1.00 mg CH_4 m^{-2} h^{-1} (see Table 4.2). During the summer season, when the water level was above the surface (from June to mid-July), the median ebullition rate was 1.19 ± 1.35 mg CH_4 m^{-2} h^{-1}, while the median flux of the ebullition pathway in the summer campaign was 1.35 ± 3.69 mg CH_4 m^{-2} h^{-1}. In winter, ebullition measurements with funnels were unfortunately not possible, however, ebullition is excepted to be very low in winter due to temperature dependence (Aben et al., 2017).

4.4.2 Seasonal methanogenic characterization with δ^{13}C source signatures of a subsaline reed wetland

The present study demonstrated that a subsaline reed wetland exhibits seasonal variability in the source signatures $\delta^{13}C\text{-}CH_4$ and $\delta^{13}C\text{-}CO_2$. The most ^{13}C-depleted $\delta^{13}C\text{-}CH_4$ source signature of -73.6 ‰ VPDB was observed in fall and may be attributed to the greater availability of substrates (acetate) at this time of year. In contrast, the most ^{13}C-enriched $\delta^{13}C\text{-}CH_4$ source signatures were observed in spring and winter (-59.2 ‰ VPDB) and are likely due to reduced substrate availability (Sriskantharajah et al., 2012). Fisher et al. (2017) previously assumed seasonal variability in the isotopic source signatures of diel measurements in a Finish fen, with the most ^{13}C-depleted $\delta^{13}C\text{-}CH_4$ in fall (October). However, their study did not cover all seasons.

Our summer δ^{13}C-CH_4 source signature of −62.6 ± 2.4 ‰ VPDB indicates a greater ^{13}C-enrichment compared to the summer source signature of boreal wetlands, which has been determined to be −70.9 ± 1.2 ‰ (Fisher et al., 2017). Whereas, the seasonal mean δ^{13}C-CH_4 source signature of our site (−63.6 ‰ VPDB) is slightly more ^{13}C-depleted than the ones from tropical reed wetlands with −62.7 ‰ (Hong Kong) or −59.6 ‰ (Zambia) (France et al., 2022). Fisher et al. (2017) elucidated the discrepancies observed in wetlands situated in more southern latitudes as a consequence of enhanced CH_4 oxidation in warmer wetlands, which exhibit thicker oxic layers, and due to variations in methanogenic communities. In our case, CH_4 oxidation was likely further facilitated by drought, resulting in a source signature comparable to that observed in tropical wetlands with reed.

This study corroborates the utility of Keeling plots derived from data of diel chamber measurements as a means of identifying source signatures of wetlands (Fisher et al., 2017). In summer, the δ^{13}C-CH_4 source signature shows a high correspondence with the δ^{13}C-CH_4 values of the collected ebullition gases. The source signatures illustrate, according to the methanogenic characterization plot of Whiticar et al. (1986), the predominance of acetoclastic methanogenesis across all seasons in the reed ecosystem under study. Until now, the dominance of acetoclastic methanogenesis at this site has only been confirmed during the April to July period by analyzing the ebullition gas (Baur et al., 2024a). However, the winter source signature indicates an influence of CH_4 oxidation due to the desiccation of the reed belt.

4.4.3 Sediment properties of a subsaline reed wetland

The reed wetland of Lake Neusiedl has two distinct sediment layers that differ in both appearance and properties. Despite the high TOC values in the upper sediment layer, the peaty layer is very shallow, with a mean thickness of 9.7 ± 3.8 cm. This is different from other reed wetlands, which are sometimes classified as minerotrophic peatlands due to their thicker peat deposits, such as the Federseemoor in van den Berg et al. (2020). In our studied reed ecosystem, most sediment properties, such as WC or sulfate, differ more between the two layers than between seasons. These properties show significantly higher average values in the upper, organic layer. However, the pH in the lower layer was significantly higher than in the upper organic layer. This difference may be due to the influence of organic or carbonic acids on the pH in the upper layer (Blume et al., 2016). A decrease in TOC and sulfate concentration was also observed with sediment depth in a *Phragmites* wetland in Australia (Jeffrey et al., 2019). The lower sediment layer most likely has (strongly) reducing conditions throughout the year since alternative electron acceptors, such as nitrate and sulfate, are present in very low concentration or are not detectable. In the upper sediment layer, sulfate, the energetically less favored electron acceptor, is noticeably increased, suggesting less reducing (and more oxidizing) conditions. The sediment sample results also indicate spatial variability of the sediment properties, especially in the upper layer, which is in contact with the atmosphere or the surface water and where most processes, such as the decomposition of organic matter and the transformation of nutrients, occur.

The upper layer exhibited the highest seasonal variability in sediment properties, such as TOC, CON, and nutrients, which could be partly attributed to the particular drying conditions during the study period. In contrast, Agoston-Szabo and Dinka (2006) observed no temporal change in TOC in the upper 4 cm of sediment in the Hungarian reed belt of Lake Neusiedl from April to September 2001. Despite the drying out of the surface water areas (= no water level above the sediment) in the reed belt from mid-July 2021 onward (after the summer campaign), the WC of the sediment in the upper (organic) layer remains relatively high due to saturation. However, since the sediment was no longer covered by water, and cracks had formed in it, the upper sediment layer (and perhaps deeper layer) had the opportunity for more direct contact with (atmospheric) oxygen. Additionally, sediment processes and properties may be influenced by the oxygen transport of *Phragmites australis* into the rhizosphere (Armstrong and Armstrong, 1988). The elevated ammonium concentration in the upper sediment layer in summer may result from freshly settled, easily degradable organic matter (van Luijn et al., 1999). The elevated nitrite concentration in the upper sediment layer in the following season (fall) could be explained by the oxidation of ammonium (1st step of nitrification), presumably influenced by dry conditions. In the subsequent season (winter), the elevated nitrate concentration in the upper sediment layer could be explained by the oxidation of nitrite (2nd step of nitrification).

4.4.4 Change of the sediment microbial community in a subsaline reed ecosystem within one year

The variations observed in the methanogenic community of Lake Neusiedl between the two sampling years include differences in both relative abundance and diversity. Despite their higher relative abundance of methanogens, the overall microbial biomass in the deeper layer was consistently low across both years, as evidenced by the little DNA yield from these samples (see Table S.8). *Methanomicrobiales*, an order detected in both 2021 and 2022, exhibited particularly high abundance in the latter year. Members of this group utilize H_2, CO_2, formate, and alcohols for methanogenesis (Garcia et al., 2006). *Methanococcales* and *Methanobacteriales*, also detected in 2021, encompass primarily hydrogenotrophic organisms (Bonin and Boone, 2006, Whitman and Jeanthon, 2006).

Notably, our campaign results indicate CH_4 production due to acetoclastic methanogenesis across all seasons. This process is exclusively carried out by representatives of *Methanosarcinales* (Stams et al., 2019), and while present in both years, these organisms were more prevalent in 2021 with lower levels detected in 2022. While it is worth pointing out that 16S rRNA gene relative abundance does not necessarily correlate to activity, these methanogens could be playing an important role in the CH_4 levels detected. Furthermore, syntrophic acetoclastic methanogenesis is known to occur, especially in environments less conducive to *Methanosarcinales* (Hattori, 2008). In this context, acetate is oxidized by organisms such as syntrophic acetate oxidizing bacteria, Woesearchaea, some sulfate-reducing bacteria, among others, and the resulting H_2 could be used for hydrogenotrophic methanogenesis (Castelle et al., 2021, Galushko and Kuever, 2019, Huang et al., 2021, Lee and Zinder, 1988, Spormann and Thauer, 1988). Interestingly, the co-occurrence network analysis (see Figure 4.6) of sediment samples from Lake Neusiedl shows possible syntrophic interactions between hydrogenotrophic methanogenic orders and examples of such groups (highlighted in pink), indicating that syntrophic acetoclastic methanogenesis might be further contributing to the observed results. Moreover, the consistent detection of methanotrophs across all layer in both years could have affected the CH_4 levels measured in the present study, as these organisms have been shown to potentially consume a substantial amount of upward CH_4 fluxes in sediments (Valentine and Reeburgh, 2000).

The different levels of O_2 tolerance and sensitivity of methanogens may explain the differences in occurrences between the two sediment layers. Furthermore, the change in methanogenic taxa between the two winters (2021 and 2022) can be attributed to the drying of the study site from mid-July 2021, which resulted in the formation of cracks where the sediments could come into increased contact with O_2. First, we observed a (near) absence of methanogens in the upper layer in winter 2022 after desiccation, which could indicate that oxic conditions were dominant in this layer. Secondly, only the O_2-tolerant methanogens, such as for example *Methanosarcina subterranea* and *Methanosarcina siciliae* belonging to *Methanosarcinales* group (Angel et al., 2011, Conrad, 2020b, Horne and Lessner, 2013, Lyu and Lu, 2018), were present in the upper layer in winter 2021, when the study site was flooded. This indicates that the O_2 delivery to the rhizosphere may have occurred through the aerenchyma of *P. australis* (Armstrong et al., 1992), thereby influencing the O_2 content in this sediment layer, as standing water was above the sediments in winter 2021. Third, after desiccation, a marked increase and dominance of *Methanomicrobiales*, which are O_2-tolerant methanogens (Conrad, 2020b, Lyu and Lu, 2018), was observed in the lower layer. Fourth, the lower layer prior to desiccation exhibited a high diversity of methanogens, including those belonging to the O_2 sensitive *Methanobacteriales* and *Methanococcales* (Conrad, 2020b, Lyu and Lu, 2018). However, these were absent after desiccation. These observed changes are inconsistent with the findings of Conrad (2020b), who was able to find methanogenic population dynamics after desiccation, but not with O_2 sensitivity as the exclusive criterion.

Considering that the sulfate reduction zone typically occurs closer to the surface compared to the methanogenesis zone (Jørgensen and Kasten, 2006), the observed higher relative abundance of sulfate-reducing bacteria in the upper layer and methanogens in the lower layer is not surprising. Furthermore, the increased detection of *Desulfovibrionales* with depth could be a consequence of a decrease in organic matter in the deeper layer (see Figure 4.4a), as members of this group have been shown to thrive in oligotrophic environments (Bade et al., 2000, Sass et al., 1998, Wörner and Pester, 2019). The detection of sulfate-reducing bacteria across both years draws attention due to their metabolic features in aquatic sediments. Acetate and H_2 serve as substrates for both sulfate reduction and methanogenesis (Conrad, 1999, Schink, 1997). Sulfate-reducing bacteria hold a thermodynamic advantage over methanogens, as they can utilize acetate and H_2 at lower concentrations, potentially outcompeting methanogens for substrate uptake. This process channels electron flow towards CO_2 production rather than CH_4 (King, 1984, Lovley et al., 1982, Lovley and Goodwin, 1988). However, it is worth noting that these organisms and processes can co-occur, as observed in environments such as the sulfate-methane transition zone, and could be coupled in ways that influence substrate production and consumption rates (Egger et al., 2016, Sela-Adler et al., 2017). Thus, it is possible that similar interactions occur in Lake Neusiedl. The higher relative abundance of sulfate reducers in the upper layer, followed by a decrease in their levels in the lower layer coinciding with an increase in methanogen relative abundance, suggests a putative competition scenario where methanogens may have been outcompeted for resources when sulfate reducers were more prevalent.

4.5 Conclusions

This study shows that in a wetland with reed, a distinct diel cycle of CH_4 fluxes occurs only in the emission pathway of plant-mediated transport and in the summer season. The plant-mediated transport pathway demonstrated the highest CH_4 emissions not only in summer, but also during other seasons. The distinct differences in the two sediment layers, namely in terms of carbon and water content, are also reflected in the variations observed in the microbial communities. The desiccation process resulted in a reduction in the methanogenic microbial diversity in the sediments over the course of a year. The findings of this study can be extended to other wetlands with reed vegetation, particularly those situated in similar subsaline or brackish conditions, or to other wetlands experiencing drought conditions. However, additional research is required to determine whether the methanogenic diversity will recover following an increase in water levels in reed wetlands.

Data availability

The sediment, isotope, and flux data generated by this study are available in the PHAIDRA repository of the University of Vienna under `https://doi.org/10.25365/phaidra.626`. All 16S rRNA raw sequences data are available at the NCBI database under the project identifier PRJNA1182700.

5 Study IV:
Spatial analysis of intra-annual reed ecosystem dynamics at Lake Neusiedl using RGB drone imagery and deep learning

Buchsteiner, C., **Baur, P.A.**, Glatzel, S.
Remote Sensing, 2023, 15 (16), 3961.
`https://doi.org/10.3390/rs15163961`

Graphical Abstract

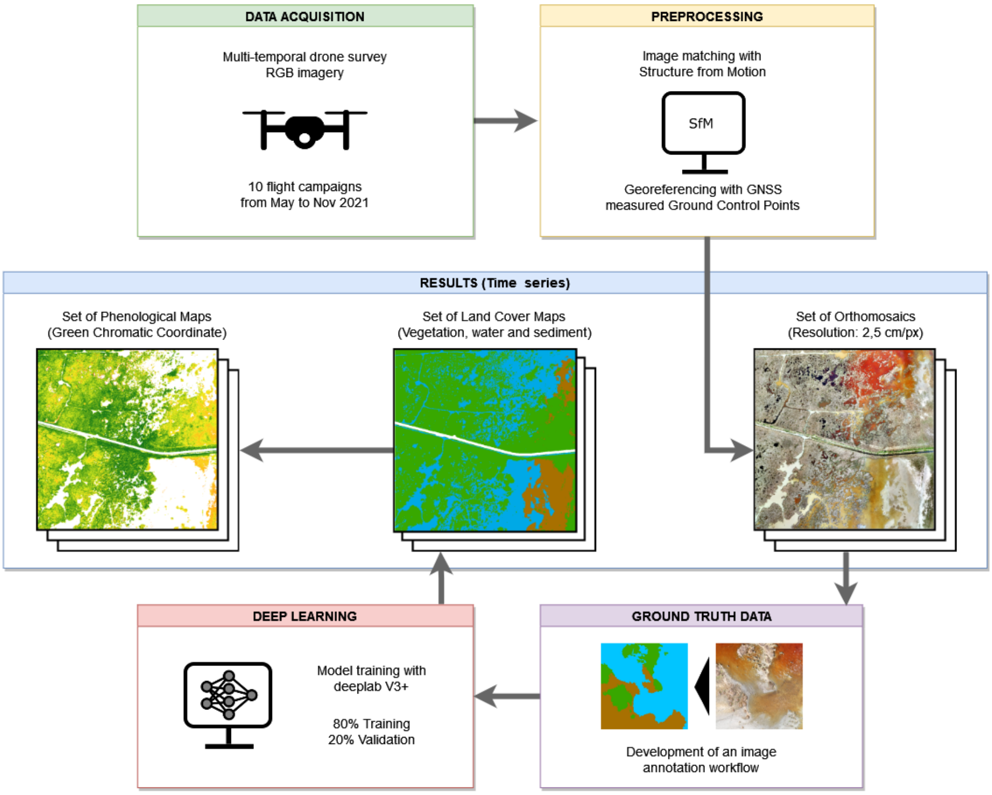

Abstract

The reed belt of Lake Neusiedl, covering half the size of the lake, is subject to massive changes due to the strong decline of the water level over the last several years, especially in 2021. In this study, we investigated the spatial and temporal variations within a long-term ecosystem research (LTER) site in a reed ecosystem at Lake Neusiedl in Austria under intense drought conditions. Spatio-temporal data sets from May to November 2021 were produced to analyze and detect changes in the wetland ecosystem over a single vegetation period. High-resolution orthomosaics processed from RGB imagery taken with an unmanned aerial vehicle (UAV) served as the basis for land cover classification and phenological analysis. An image annotation workflow was developed, and deep learning techniques using semantic image segmentation were applied to map land cover changes. The trained models delivered highly favorable results in terms of the assessed performance metrics. When considering the region between their minima and maxima, the water surface area decreased by 26.9%, the sediment area increased by 23.1%, and the vegetation area increased successively by 10.1% over the investigation period. Phenocam data for lateral phenological monitoring of the vegetation development of *Phragmites australis* was directly compared with phenological analysis from aerial imagery. This study reveals the enormous dynamics of the reed ecosystem of Lake Neusiedl, and additionally confirms the importance of remote sensing via drone and the strengths of deep learning for wetland classification.

5.1 Introduction

Wetlands are of immense importance as highly valuable ecosystems intertwined with human welfare. They fulfill an indispensable function in preserving biodiversity, purifying water, enhancing resilience against storm surges, sequestering carbon, regulating microclimates, and more (Mitsch et al., 2015). Reed belts in particular have ecological importance as habitats for highly specialized species and as a buffer zone for lakes and rivers. They provide an indispensable habitat for waterfowl (Čížková et al., 2023) and invertebrates. Reed shoots are a food source for herbivores, and in an aquatic setting reed stands provide a spawning ground and nursery for fish (Kallasvuo et al., 2011), prevent erosion, and stabilize the strength of the bank (Yu et al., 2020). The reed belt of Lake Neusiedl is the second largest coherent reed ecosystem in Europe after the Danube Delta, and for nature conservation reasons it is a very important habitat for many protected bird species (Nemeth and Dvorak, 2022). Lake Neusiedl is a long-term ecological research (LTER) site contributing to a pan-European research network seeking to better understand the structures and functions of ecosystems (Mirtl et al., 2015). Remote sensing imagery is required to spatially visualize and analyze such sites and understand the effects of global changes at the local scale (Díaz-Delgado et al., 2019). The following aerial image analysis studies of 1979, 2008, 2018/2019 addressed the extent of the reed belt of Lake Neusiedl. The Austrian reed belt of Lake Neusiedl was mapped as early as 1979 to study the vegetation damage and age classes of reeds through color infrared aerial photography (Csaplovics, 1982). The study of August 1979 was carried out on the basis of a three-feature classification utilizing the density, height, and vitality classes. In contrast, the reed mapping of August 2008 used a continuous stereoscopic (visual) interpretation of assigned pairs of aerial photographs (stereo pairs) (Csaplovics and Schmidt, 2011). Although the total reed belt area of Lake Neusiedl increased between 1979 and 2008, the reed stocks within the reed belt area decreased (Csaplovics and Schmidt, 2011). The authors showed that in the year 2008 around 12.5% of the total reed belt was covered by humic water. For the same aerial photographs from August 2008, the study of Nemeth et al. (2014) measured 19% water coverage in the reed belt; the authors included small water areas with a spatial resolution of 0.25 m^2 as water. In Csaplovics and Nemeth (2014), NDVI-inclusive airborne optical imaging was used in support of habitat ecological monitoring of the Austrian reed belt in a study investigating the different reed classes and habitat-specific dependencies of different bird species. The reed belt coverage is clearly higher in the Hungarian part of Lake Neusiedl (83.6% in 2007, which included grassland with reed coverage of around 5%) as compared to the Austrian part (around 50%). The Hungarian reed belt area decreased slightly, by 0.8% from 1979 to 2007, due to the increase in "feltöltés" (embankment/levee areas), though not in open-water areas (Márkus and Király, 2012). In 2007, only 1.2% of the Hungarian part of Lake Neusiedl was covered by humic water (Márkus and Király, 2012), which is a very small share compared to the Austrian reed belt (Nemeth et al., 2014). Márkus and Király (2012) recognized a strong degradation of the Hungarian reed belt due to damage caused by the harvesting machines, which were called die-back sites in Dinka et al. (2010); these were observed in the Austrian part, though to a lesser extent, in Csaplovics and Schmidt (2011). One study from 2018/2019 used Sentinel-2b data to monitor the age of reed stands, finding that the dominant age class (especially in the eastern reed belt) was areas older than 14 years (Nemeth and Dvorak, 2022).

Previous studies analyzing the spatial patterns of the reed belt have been based on either low-resolution satellite data or medium-resolution aerial imagery derived from costly single-flight surveys. To date, the spatial patterns of the reed belt have not been studied with high-resolution data. In addition, little is known about the temporal dynamics of the surface structure of the reed belt within a one-year time frame. To address this gap, in this study we used an unmanned aerial vehicle (UAV) to generate a time series of high-resolution aerial imagery data. A series of ten UAV-derived orthomosaics provided the basis for land cover classification and phenological analysis to track changes in intra-annual variability in the spatial dynamics of the reed ecosystem over the growing season of 2021, which is of particular interest due to the intense drought during the study period. The region of Lake Neusiedl has been facing drought conditions since the summer of 2015, causing the average water level of the lake to decrease, especially in recent years (Hackl and Ledolter, 2023).

The main objectives of this work are:

- To provide a detailed workflow for land cover classification of high-resolution orthoimagery using deep learning image segmentation.
- To reveal the spatial and temporal variability of a reed ecosystem under intensive drought conditions.
- To disclose the phenological stages of *Phragmites australis* in the reed stands of Lake Neusiedl over the 2021 vegetation period.

5.2 Materials and methods

5.2.1 Study area

The study area is located in the reed belt of Lake Neusiedl near Illmitz in Austria (47°46′09″N, 16°45′30″E). With a maximum area of 315 km^2, Lake Neusiedl is Austria's largest lake, stretching across the Austrian-Hungarian border. It is characterized by a remarkably shallow lake basin (Z_{mean} = 1.2 m, Z_{max}= 1.8 m) with no natural outflow (Wolfram and Herzig, 2013). The lake water has an alkaline and subsaline character (Hammer, 1986), with high electrical conductivity (1300–3200 µS cm^{-1}) and an average pH of 8.7. The mean annual precipitation sums between 1971 and 2020 measured from eight stations surrounding the lake were 556 mm, and ranged from 353 mm to 833 mm (Hackl and Ledolter, 2023). Due to the relatively small catchment area of the lake, rainfall contributes 79% to the total water supply via direct input through the lake surface. The lake's shallowness and expansive water surface area make it particularly sensitive to climatic variations (Soja et al., 2013).

More than half of the lake (about 181 km^2) is covered by a reed belt, which consists of a temporally changing mosaic of reeds (*Phragmites australis*), water, and sediment patches. The lake and its reed belt belong to various protected areas, including the Austrian-Hungarian national park 'Neusiedler See – Seewinkel / Fertő – Hanság', a Ramsar site, and Natura 2000 area.

This study focused on an area of approximately 53 ha in the eastern reed belt of Lake Neusiedl; the study area extends from sparsely vegetated shores (landwards) to densely vegetated areas near the open lake surface. The area surveyed in the UAV flights was about twice the size of the actual study area (as shown in Figure 5.1) in order to achieve proper rectification and georeferencing results for the aerial images within the study area. The research area is located in the nature zone of the national park, where no management is conducted and access restrictions apply. An eddy covariance (EC) tower for measuring greenhouse gas exchange is located in the center of the study area. Several channels lead through the research area and a constructed dam pathway runs through the middle of the study site, crossing the reed belt from the land shore to the open water area.

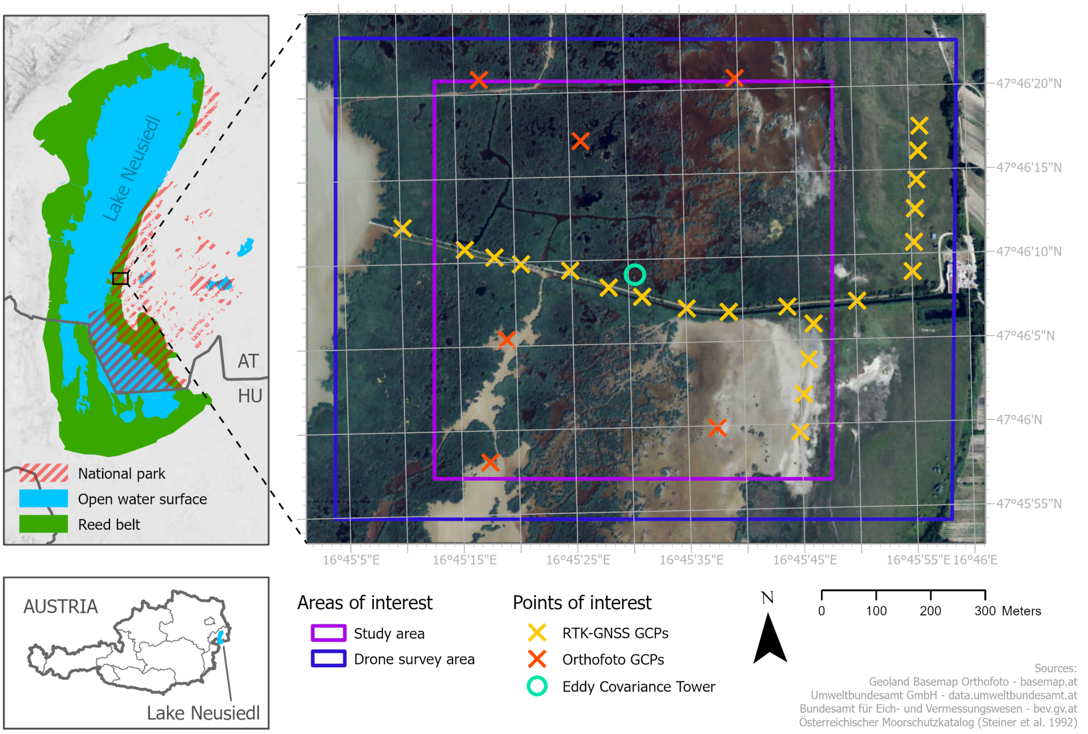

Figure 5.1: Overview maps and detailed map of the research area in the reed belt of Lake Neusiedl, eastern Austria (data source used in the overview map: Steiner et al. (1992)).

5.2.2 Data preparation

UAV data acquisition

High-resolution images were captured using a quadcopter drone (Mavic 2 Pro, DJI Technologies Co., Ltd., Shenzhen, China) equipped with a CMOS sensor that captures optical images in RGB with a resolution of 5472 × 3648 pixel (20 MP). The camera has a focal length of 10.3 mm and a sensor width of 12.8 mm (DJI, 2023). A total of ten flight campaigns were conducted at three-week intervals, starting on 5 May and ending on 6 November 2021 (dates listed in Table 5.1). Because very few land cover changes in the study area's surface were expected during winter to early spring, no flights were carried out from December to April. The capacity of the four drone batteries covered an average drone survey area of 96 ha during each flight campaign (Table 5.1), lasting about 2.5 h each. Because distortion can occur at the edges of a processed orthomosaic, we extended the drone survey area well beyond the actual study area used for analysis (see Figure 5.1). In order to have as little shade as possible in the captured images, all flights were carried out at midday when the sun was at its highest. Because alternating sunny and cloudy weather conditions were to be expected over the duration of a flight campaign, the camera settings (ISO values, shutter speed and aperture) were set to automatic mode during the flights to prevent blurring and/or overexposure in the images. More than 1000 aerial images were generated during each flight campaign, with a mean data volume of 15 GB. All flights were performed in automatic flight mode with predefined parallel flight lines at a constant height of 100 m above the ground and an image front and side overlap of 75%, with all images taken at 90° to the surface (nadir). Flight plans were created using the flight planning app PIX4Dcapture, version 4.10.0 (Pix4D S.A., Prilly, Switzerland).

Table 5.1: Results and uncertainty values from processing orthomosaics with structure from motion (SfM) techniques.[1] Ground sampling distance, [2] Root mean square error.

Flight campaign	**Average GSD[1]** [cm]	**Drone survey area** [km^2]	**RMSE[2] georeferencing** ($N = 21$) **X Error** [cm]	**Y Error** [cm]	**RMSE check points** ($N = 6$) **X Error** [cm]	**Y Error** [cm]
2021-05-05	2.43	0.84	4.6	2.9	2.0	5.9
2021-05-26	2.39	0.92	23.9	11.7	3.2	3.6
2021-06-18	2.50	1.02	11.6	4.9	1.9	4.4
2021-07-07	2.49	0.99	24.2	8.9	10.7	5.0
2021-07-27	2.45	0.99	14.3	3.0	1.7	4.9
2021-08-18	2.41	0.99	15.5	10.2	3.9	4.2
2021-09-10	2.45	0.95	6.8	3.1	4.5	5.8
2021-09-29	2.36	0.97	5.2	3.8	3.8	5.2
2021-10-20	2.36	0.94	8.3	28.7	2.7	6.0
2021-11-06	2.32	1.00	3.0	1.4	3.2	5.6
Average	2.42	0.96	11.7	7.9	3.8	5.1

Photogrammetric preprocessing

To georeference the drone imagery, 21 ground control points (GCPs) with a chessboard pattern in DIN-A3 format were produced and distributed in the study area (displayed with a yellow x in Figure 5.1). To ensure their durability over the duration of all flight campaigns, the GCPs were laminated with a strong and UV-resistant film and fixed to wooden boards before attaching them to driven wooden piles and existing fence posts. Fixing the GCPs on posts above ground guaranteed their visibility to the drone sensors throughout the vegetation period. A GNSS receiver (Trimble R10, Trimble Inc., Sunnyvale, USA) was used for precise location measurement of the GCPs (Trimble, 2023). In addition, RTK-based correction using the Austrian Positioning Service (APOS) was applied to improve the precision of the measurements.

To obtain distortion-free image processing results, the GCPs were distributed evenly over the study area (Villanueva and Blanco, 2019). Due to access restrictions in the national park covering the study area, our original idea of deploying GCPs along the water channels of the study site could not be implemented, as this was considered a potential disturbance factor for breeding birds. For this reason, GCPs were densified along the dam pathway and along the land shore line of the reed belt, where temporary entry was permitted. The area of the drone survey had to be extended in the easterly direction in order to capture the easternmost GCPs with the drone sensor. Furthermore, an additional set of control points (displayed with a red x in Figure 5.1) was derived from an orthophoto (2019-06-26, resolution 20 cm) obtained from the Austrian Federal Office of Metrology and Surveying (BEV, 2019) by manually locating the center of small, isolated, and uniquely identifiable reed patches.

The image data sets from each flight were processed to a rectified and georeferenced orthomosaic using the Structure-from-Motion (SfM) image matching technique, which is widely used in geoscience applications (Westoby et al., 2012) and described in detail by Deliry and Avdan (2021). This preprocessing workflow was carried out using the photogrammetry software PIX4Dmapper, version 4.6.4 (Pix4D S.A., Prilly, Switzerland) according to the instructions (Pix4D, 2023). Processing options such as the image scale at which key points were computed or the degree of camera optimization were adapted to the individual requirements of each flight data set. In SfM processing, GCPs must be manually marked in different images captured from different angles. Identifying the same geolocation in the small isolated reed patches of the six orthophoto-derived control points was more challenging than identifying the center of the RTK-GNSS measured chessboard-patterned wooden boards designed for accurate marking. Of the 27 available control points, 21 were used for rectifying and georeferencing, while the remaining six served as check points to verify the accuracy of the resulting orthomosaics (results shown in Table 5.1). The control points derived from the orthophoto were not used as check points, as check points were not included in the process used to rectify the orthomosaic and would have caused wide areas with distortion of unknown extent. The average ground sampling distance (GSD) across all flights was 2.42 cm/pixel. The RMSE (root mean square error) of the control points used for georeferencing was 11.7 cm in the X and 7.9 cm in the Y direction; while relatively high compared to the GSD, this is acceptable considering the size of the covered area. Both the lower resolution of the orthophoto and the inherently less accurate method of identifying the center of the reed patches resulted in significantly higher uncertainty values for georeferencing than we initially aimed for (see Table 5.1). Because only RTK-GNSS-measured GCPs were used as control points, their significantly lower uncertainty values apply only along the areas of their spatial distribution. The computationally intensive procedure of photogrammetric processing was performed on an Intel(R) Core(TM) i7-10700 CPU @ 2.90 GHz with 32 GB RAM (Intel Corporation, Santa Clara, USA) and a Radeon RX 550X GPU (AMD Inc., Santa Clara, USA).

5.2.3 Semantic segmentation

In this study, we used semantic image segmentation for classifying the different land cover types of the study area. Semantic segmentation is a machine learning technique that assigns a class label to each pixel in an image (Shen and Zeng, 2019). The whole workflow, from generating training data for deep learning to model training and pixel classification, was carried out in ArcGIS Pro 3.0.3 (ESRI, 2022b) with the Image Analyst license and Deep Learning Libraries for ArcGIS Pro 3.0.3 (ESRI, 2022c). Figure 5.2 illustrates the most important processing steps carried out for each orthomosaic, which are described in detail as follows. (**a**) Deriving ground truth data: from each orthomosaic, a subset of eight square areas (referred to henceforth as "ground truth areas") covering 2500 m^2 each was obtained. The ground truth areas were carefully selected to cover the various characteristics of the land cover classes, such as their structure and color expression. Care was taken to ensure that the transition zones between classes (water to sediment, water to vegetation, and sediment to vegetation) were represented within the ground truth imagery. (**b**) Image annotation: for each of the eight ground truth areas, a fully labeled layer was generated using a semi-automated workflow. A detailed description of the procedure can be found in Section 5.2.3. (**c**) Construction of a chip data set for deep learning: a data set consisting of image chips and analog labels was derived from the fully labeled ground truth data. All chips were exported in TIFF format with a size of 256 × 256 pixels and a 50% overlap both horizontally and vertically. The chip data set was cleaned to remove chips containing areas without any information. This processing step yielded an average of 1641 chips and the same number of corresponding labels per data set. (**d**) Training a deep learning model: the chip data set was used to train and validate a deep learning model. A detailed description of the procedure can be found in Section 5.2.3. (**e**) Semantic segmentation for classifying land cover types of the reed belt: the trained model was finally used to assign a semantic class label to each pixel of the respective orthomosaic using the "Classify Pixels Using Deep Learning" tool in ArcGIS Pro. The dam pathway and a boat pier were generously cut out of the classified data used for further analysis.

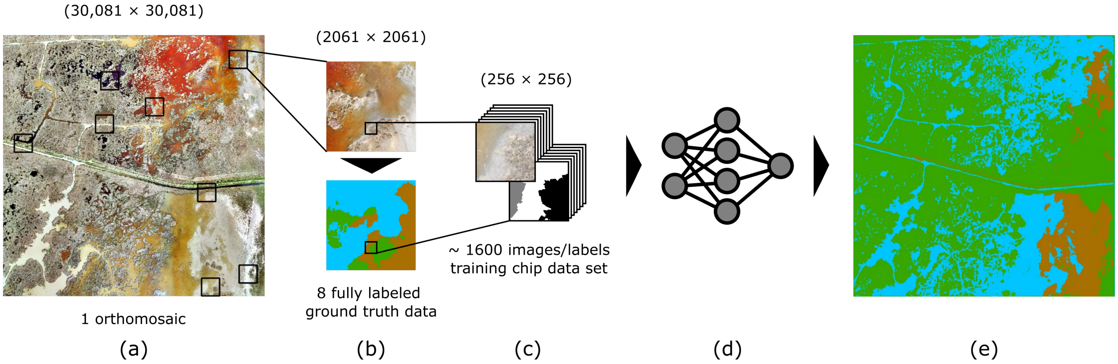

Figure 5.2: Full workflow for classifying different land cover types in the reed belt through semantic segmentation. The different stages of data processing are shown with the respective image size in pixels. (**a**) Orthomosaic of the study area (from flight 2021-05-05), with selected locations for ground truth areas. (**b**) Image annotation data, consisting of ground truth imagery and a fully labeled layer indicating the corresponding land cover classes (vegetation = green, water = blue, sediment = brown). (**c**) Chip data set containing small image chips and analog labels derived from ground truth data. (**d**) Training and validation of a deep learning model with the training chip data set. (**e**) Semantic segmentation performed on the orthomosaic using the trained model.

Image annotation

The process of generating ground truth data is known in the machine learning domain as image annotation. A number of image annotation programs have recently become available, although most of them are proprietary. With the aim of preparing ground truth data at no additional cost and with maximum control over the parameter settings, a standardized semi-automated workflow for image annotation was developed within the ArcGIS Pro environment using the segmentation tool for object based image analysis (OBIA). For each of the ten orthomosaics, a ground truth data set was prepared as follows (the individual steps are shown in Figure 5.3):

(a) The eight carefully selected ground truth areas were clipped from the orthomosaic and resampled to a resolution of 10 cm using the bilinear resampling technique. Resizing of the imagery was done to reduce processing time for the next step.

(b) The resampled imagery was segmented into groups of adjacent pixels with similar spectral characteristics. The segmentation tool within the software can be used to define the spectral and spatial detail. It was found that the best segmentation results for distinguishing between the classes in our data were obtained when the spectral detail was set between 15 and 17 and the spatial detail set to 1. Furthermore, the minimum segment size was set to 500 pixels. With these parameter settings, while the segmentation algorithm produced fragmented patches that were smaller then required, it provided proper delineation between land cover classes along certain segment boundaries.

(c) The raster output from the segmentation tool was vectorized for the next processing step.

(d) Segments from the same semantic classes were manually merged. Merging was performed by visual interpretation of the polygons while overlaying the ground truth imagery. To speed up this process, segments smaller than 1 m^2 were removed and the resulting gaps were filled by adding the geometry of the gap to the adjacent polygon with which it shared the longest edge. This step provided fully overlapping semantic class polygons, with each polygon covering the entire area of a class along with its various intra-class variations contained in the ground truth imagery.

(e) As a last step, the polygons were assigned to the corresponding land cover class in order to obtain a fully labeled polygon layer.

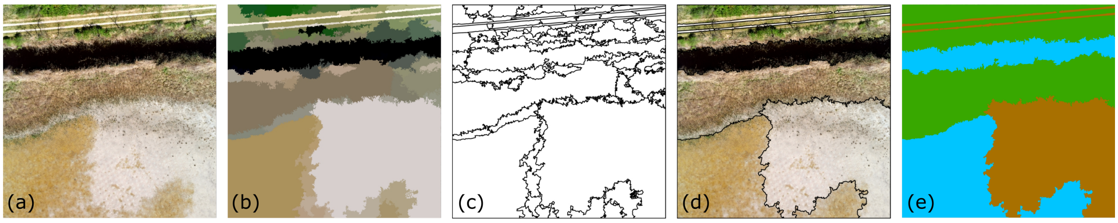

Figure 5.3: Workflow example of image annotation from one selected ground truth area. (**a**) Clipped and resampled ground truth imagery covering various characteristics of vegetation, water and sediment. (**b**) Segmentation output showing adjacent pixel groups with similar levels of spectral detail. (**c**) Segmentation raster converted into polygons. (**d**) Polygon segments merged by visual interpretation. (**e**) Fully labeled polygon layer for respective ground truth imagery, showing the land cover classes of vegetation (*green*), water (*blue*), and sediment (*brown*).

Steps (**a**) through (**e**) were repeated for the eight selected ground truth areas from each of the ten orthomosaics. The ground truth imagery in original resolution and the corresponding fully labeled polygon layer were used as input data for exporting the training chips data set.

Deep learning

A deep learning model was trained with each chip data set using a deep convolutional neural network (CNN) architecture for image segmentation. With the rise of deep learning, CNNs have been applied for various land cover classification applications on high-resolution remote sensing data (Tong et al., 2020, Volpi and Tuia, 2017, Zhang et al., 2020b). In this study, we used the state-of-the-art DeepLabv3+ model architecture, which uses an encoder–decoder framework with atrous convolution and a variant of the Xception network as its backbone (Chen et al., 2018). This model proved to be highly accurate in wetland classification on high-resolution RGB imagery (Pashaei et al., 2020, Zhao and Du, 2016).

The chip data sets were split into 80% training and 20% validation data and stratified in order to maintain the class proportions between the training and validation data. The optimum learning rate for the model training was determined for each chip data set (see Table S.9). Pre-testing revealed that the model's accuracy was saturated after 20 to 30 epochs. With the intent of making the results more comparable, we trained each model for 25 epochs. Several performance metrics were calculated at the land cover class level to evaluate the accuracy of the models. Precision (Equation 5.1), Recall (Equation 5.2), and F1-Score (Equation 5.3) were calculated as standard evaluation metrics for machine learning models. In addition, Intersection over Union (IoU), which is a standard measure for semantic image segmentation, was calculated using Equation 5.4 (Rahman and Wang, 2016). In contrast to the other metrics, IoU uses the entire ground truth map instead of labeled points to assess the similarity between the predicted and the ground truth map for a given class. This performance metric is progressively being applied in deep learning-based UAV remote sensing classification (Anagnostis et al., 2021, Pashaei et al., 2020, Zhang et al., 2020b, Zheng et al., 2022a).

Formulas for the above-mentioned metrics are provided in Equations 5.1–5.4, where true positive (TP) represents the count of correctly labeled pixels, false positive (FP) refers to the count of pixels misclassified as the target class while belonging to other classes, and false negative (FN) refers to the count of pixels that belong to the target class and are misclassified as belonging to other classes.

$$Precision = \frac{TP}{TP + FP} \tag{5.1}$$

$$Recall = \frac{TP}{TP + FN} \tag{5.2}$$

$$F1\text{-}Score = 2 * \frac{(Precision * Recall)}{(Precision + Recall)} \tag{5.3}$$

$$IoU = \frac{TP}{FP + TP + FN} \tag{5.4}$$

Model training was carried out on an ArcGIS Notebook (integrated Jupyter Notebook, version 5.7.10) with the *arcgis.learn* module included in ArcGIS API for Python 3.9.11 (ESRI, 2022a). The training took about one hour per model and was performed on an Intel(R) UHD Graphics 630 GPU (Intel Corporation, Santa Clara, USA) with NVIDIA Quadro T2000 (Nvidia Corporation, Santa Clara, USA).

5.2.4 Phenological analysis

A vegetation index was calculated with the aim of tracking phenological stages over the vegetation period within the study area. We extracted the vegetated areas of each orthomosaic using the results from the land cover classification. For these areas, the Green Chromatic Coordinates (GCC) vegetation index was calculated from the red–green–blue (RGB) color channel information using the formula in Equation 5.5. Of the various vegetation indices available for RGB data, we chose GCC due to its effectiveness in suppressing changes in scene illumination (Sonnentag et al., 2012), which occurred in several orthomosaics.

$$GCC = \frac{G}{R + G + B} \tag{5.5}$$

Phenocam data

In the center of the study area, a digital camera (Powershot SX620 HS, Canon Inc., Tokyo, Japan) was positioned at the EC tower (see Figure 5.1) in the main wind direction (north–west) to study the phenological changes of the reed plant *Phragmites australis* since September 2020. The Phenocam automatically takes an RGB image every 1 h from 6 am to 5 pm (time zone UTC+1), which was ensured by manipulation with the Canon Hack Development Kit (CHDK). The photos were analyzed with the R package *Phenopix* (Filippa et al., 2020). For this study, one polygon as region of interest (ROI) was drawn in the reference picture to study the temporal changes of *P. australis* in the entire year 2021 (see Figure 5.4). For the ROI, the GCC vegetation index was extracted using an ROI-averaging approach (Filippa et al., 2016). GCC values were filtered according to the *max* approach following (Sonnentag et al., 2012) after determination of the 90th percentile values in three-day moving windows, as this filter effectively minimized the impact of lighting changes in the environment.

Figure 5.4: The region of interest (ROI) is marked as a black polygon in the reference picture 2021-06-23 of the Phenocam, which is aligned at the Eddy Covariance tower in the reed belt of Lake Neusiedl in the main northwest wind direction.

Processing and statistical analysis of the Phenocam data were carried out using R (Version 4.1.2, R Core Team (2021)). For faster data processing, the R package *data.table* was used (Dowle and Srinivasan, 2023). The R package *ggplot2* was used to visualize the results (Wickham, 2016).

5.3 Results

5.3.1 Performance metrics

Performance evaluation of deep learning models was based on the accuracy metrics Precision, Recall, F1-Score, and IoU. The Precision, Recall, and F1-score achieved mean results above 90% over all class types, with a small deviation in the maximum SD of 2.7% (see Table 5.2). The vegetation class scored particularly highly on these metrics, with noticeably low deviation. The IoU reached mean results ranging from 68.5% to 89.9%, showing higher variance within the class types. The vegetation class again performed the best of all classes. The sediment class type achieved a mean IoU of 72.0% with an SD of 8.1%, and the water class type reached a mean value of 68.5% with a comparably high variance of 11.5% SD. Detailed information on the models' accuracy metrics can be found in Table S.9.

Table 5.2: Performance metrics of deep learning models ($N = 10$) trained for land cover classification of UAV imagery tracking the reed ecosystem from May–November 2021. Metrics are represented with mean values ± SD of trained models at the class level (UAV = Unmanned Aerial Vehicle, SD = Standard Deviation, IoU = Intersection over Union). The full table is provided in Supplement Table S.9.

Class	**Precision**	**Recall**	**F1-Score**	**IoU**
	Mean ± SD	**Mean ± SD**	**Mean ± SD**	**Mean ± SD**
Vegetation	0.958 ± 0.010	0.957 ± 0.007	0.958 ± 0.006	0.899 ± 0.020
Water	0.929 ± 0.026	0.923 ± 0.024	0.925 ± 0.020	0.685 ± 0.115
Sediment	0.918 ± 0.023	0.927 ± 0.027	0.922 ± 0.020	0.720 ± 0.081

5.3.2 Land cover classification

Area shares of the three land cover class were calculated from each orthomosaic ($N = 10$). Figure 5.5 shows the spatial and temporal variability of land cover in the study area within the study period of May to November 2021.

The majority of the study area is covered with vegetation (60.8% to 70.9%), and vegetation has the lowest variation of all the class types over the entire study period. The vegetated area showed a rapid increase from May to mid-June (+6.6%). After a sudden vegetation decline at the beginning of July (−2.7%), a steady increase began, peaking at the end of September (+6.2%). Thereafter, the vegetation class remained almost stable, with a slight decline until November (−0.3%). The area shares of water and sediment have an interdependent relationship, and show similar variations, although their area shares differ. Water had its maximum surface coverage in May (29.9% and 30.2%), when sediment showed its minimum extent (9.3% and 6.3%). Within two months, a strong decline in the water class (−25.2%) caused sediment to reach its maximum extent (29.4%) at the end of July. In August, the water area increased slightly before declining to its minimum extent at the beginning of September (3.3%). From the end of September to November, the respective shares of water and sediment areas fluctuated at a very low level, with maxima of ± 0.5% and ± 0.7%, respectively.

The changes in the spatial distribution of land cover classes during the study period are shown in the land cover classification maps in Figures S.27 and S.28. An increase in vegetation area was observed along the edges of existing reed stands. For this reason, the water channels became increasingly overgrown with *Phragmites australis* during the study period, as can be seen in the maps. In addition, densification of loosely vegetated areas was observed from early May to late September. The land cover development in the study area shows a constant and large increase in sediment area from the land shore side combined with a large decrease in water area from end of May to end of July 2021. Moreover, the maps show a rather stable spatial distribution with minimal changes in land cover from the end of September to the beginning of November.

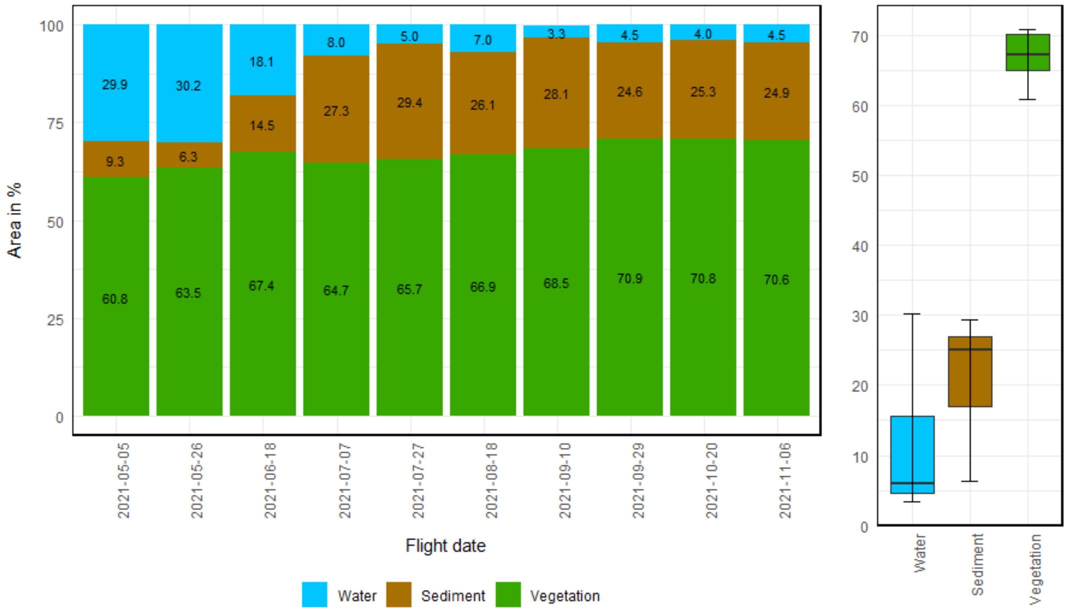

Figure 5.5: Spatio-temporal variability in the study area of Lake Neusiedl's reed belt from May–November 2021.

5.3.3 Vegetation index

The seasonal course of vegetation development during the study period could be observed based on the orthomosaics of our study area. For better understanding of phenological development, GCC values were calculated for each pixel of the vegetated areas. The seasonal course of vegetation phenology in the entire vegetated study area is presented as the mean ± SD of the GCC value pixel counts, and can be seen in green in Figure 5.6. In the study period, the mean values of GCC ranged between 0.33 to 0.40. The vegetation areas showed an increase in GCC values from early May until late July, when it peaked.

Thereafter, the mean GCC values decreased and remained stable at 0.37 until the end of September, continuing to decrease until again reaching the baseline value from early May (0.33) in November.

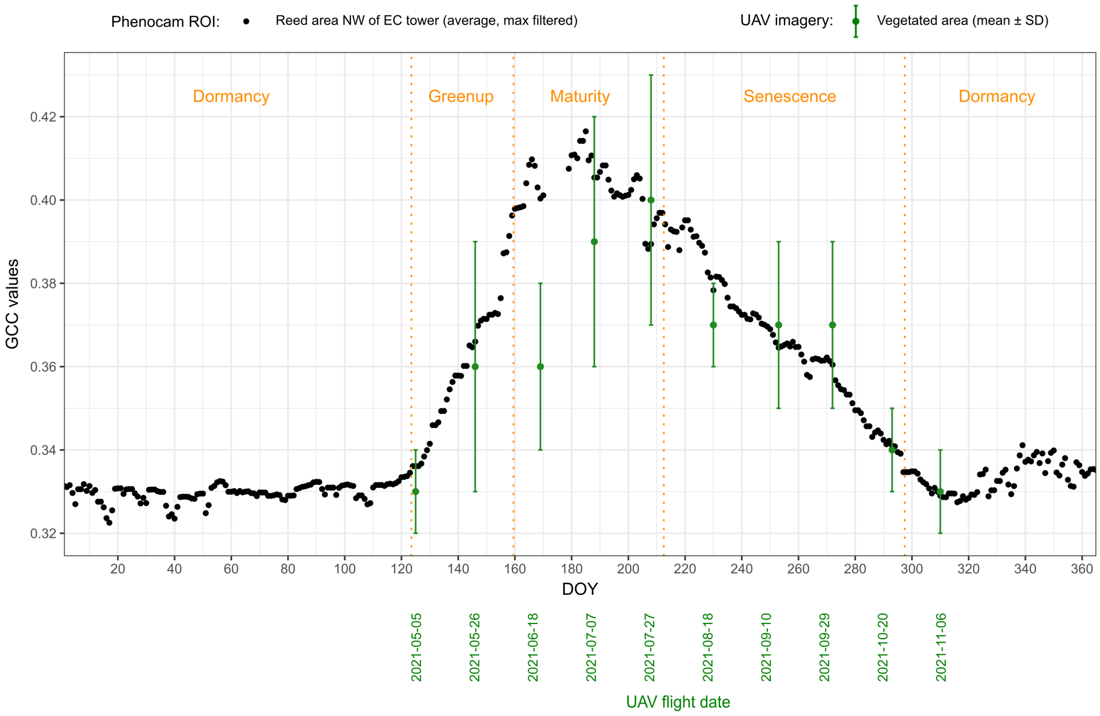

Figure 5.6: Comparison of the seasonal course of vegetation phenology (year 2021) between the ROI (region of interest) of the Phenocam data and the study area covered by the UAV imagery using the GCC vegetation index. The GCC values of the Phenocam ROI (black dots) show the average phenology of the reed stands at the Eddy Covariance tower in the NW direction (center of the study site) for almost every day of year (DOY) in 2021 as compared to the mean ± Standard Deviation (SD) of the GCC values calculated from the ten UAV flights (green dots with error bar) for the entire study site covering the land to the open water shore of the reed belt. The phenology stages of the Phenocam data are separated by the orange dotted lines.

The GCC maps in Supplement S.27 and S.28 reveal the spatial and temporal heterogeneity of the phenological development within the vegetated areas. At the beginning of the study period, the GCC values increased along the edges of existing reed stands and in loosely vegetated areas. In areas of dense vegetation, the GCC values gradually increased until the end of July, though they did not reach the maximum in the most densely vegetated areas. The GCC histograms in Supplement S.27 and S.28 differ in width and height. A narrow distribution of GCC values indicates more homogeneous status of the reed stands (e.g., 2021-05-05), while a wider distribution shows heterogeneity of reed shoot development within the reed stands (e.g., 2021-07-27).

The Phenocam provided us with the opportunity to study the phenological changes of the reed stands of *P. australis* to the northwest (the main wind direction) of the EC tower located in the center of the study area on a daily basis. The trend of the GCC values of the Phenocam in 2021 are shown together with the mean ± SD GCC values of the UAV flights in Figure 5.5. From January to the beginning of May, the GCC values of the Phenocam were stable at 0.33 (phenology stage *Dormancy*). The GCC values started to increase in the beginning of May 2021 (DOY 124). The phenology stage *Greenup* ranged until the beginning of June (DOY 159). The phenology stage *Maturity* started at DOY 160, with the highest peak at the beginning of July (DOY 177) with 0.42. The *Senescence* phenology stage started at the beginning of August (DOY 213). The GCC values decreased to 0.33 until the end of October (DOY 298), then slightly increased in the *Dormancy* phenology stage to 0.34 at the end of the year 2021. According to the GCC values of the Phenocam data, the vegetation period of the reed stands next to the EC tower in 2021 was around 173 days (4 May until 24 October).

5.4 Discussion

Changes in the land cover and phenological stages of the reed belt of Lake Neusiedl were investigated and identified using ten study dates in the period between 5 May 2021 and 6 November 2021. Land cover classification was performed using deep learning image segmentation, while phenological analysis were carried out using the GCC vegetation index. As a basis for these analyses, SfM-derived orthomosaics generated with high-resolution RGB drone imagery were used. Furthermore, we have provided the detailed workflow used in generating the fully labeled ground truth data for training and validation of our deep learning model.

Due to access restrictions, GCPs could not be evenly distributed within the study area as recommended (Villanueva and Blanco, 2019). In order to obtain comparable SfM results and derived subsequent land cover classifications, it was necessary to acquire additional control points from an orthophoto. This solution led to a higher RMSE than was initially targeted in terms the uncertainty values of the SfM processing; however, this was accepted due to the lack of alternatives and can be considered sufficient as compared to the existing literature (Deliry and Avdan, 2021). Considering the access restrictions imposed by the national park, the minimally invasive method of UAV surveying is currently the most feasible way to collect data covering large areas with this level of detail, despite the constraints around GCP distribution.

One of the biggest challenges anticipated in our study involved the different appearance of the surface of the study area throughout the investigation period due differences in the sunlight conditions between flights. As can be seen from Figure 5.3 and Table S.9, even within a single orthomosaic the study area showed strong variations within classes; e.g., water could range from crystal-clear to opaque turbid due to the sediment load, and had different color expressions, while certain inter-class expressions such as dry sediment and dead reeds hardly differed. Our attempt to use traditional machine learning techniques, namely, Support Vector Machine and Random Forest, delivered strong pixel misclassifications due to the above-mentioned challenges. The use of deep learning for image classification considerably reduced this kind of misclassifications error; however, our attempt to train a single deep learning model using the training chips from the flight campaigns during which the reeds were in the phenological maturity stage in order to classify the corresponding orthomosaics using the same generic model was unsuccessful. Not only were the performance metrics significantly lower for this model, the classification results were weak. Strong noise occurred in certain areas, described as "pepper effects" by (Zheng et al., 2022a). Large areas of changing light conditions were generally misclassified, and transition areas between land cover classes appeared in straight edges rather than smooth lines. As a consequence, we trained an individual model for each orthomosaic. This approach, described in Section 5.3.1, achieved satisfactory results in terms of performance metrics compared to related studies (Al-Najjar et al., 2019, Bhatnagar et al., 2020, Zheng et al., 2022a). The individual models were good at merging intra-class variation into one class as well as at distinguishing between classes. Even changes in the light intensity of the images due to changing sunlight conditions, which Bhatnagar et al. (2020) stated as a key challenge, did not influence the classification results of the affected orthomosaics.

While reed ecosystems such as the reed belt of Lake Neusiedl are very valuable wetlands for nature conservation, they are difficult to access and should generally not be entered; remote sensing is an excellent tool to circumvent these concerns. As such, UAV data were used to determine the height, status, and density of reed stands in the lake (Meneses et al., 2018a,b). Other studies have mostly used satellite data to separate reed beds from other vegetation in wetlands (see, e.g., Davranche et al. (2010), Villa et al. (2013)), while other studies have used airborne laser scanning to map the extent of reed wetlands (see, e.g., Csaplovics and Schmidt (2011), Dienst et al. (2004), Márkus and Király (2012), Zlinszky (2013)). These studies investigated the respective reed ecosystems only once in a growing season. In addition, airborne laser scanning is highly costly compared to using a UAV. There have been studies mapping salt marshes, including reed ecosystems, with satellite data along the coast and comparing the classification results between the years (see, e.g., Sun et al. (2023)). The evaluation of reed bed changes in Tiškus et al. (2023) showed that changes were induced by management, i.e., reed mowing. In general, satellite data offer lower resolution, and can involve difficulties with cloud cover compared to remote sensing via drone. The height and greenness of vegetation in a floodplain partly covered with reed was studied with several UAV flights per year in van Iersel et al. (2018). Higgisson et al. (2021) illustrated that the structure of the reeds was detectable by a CNN. Our study showed that drone (UAV) remote sensing combined with deep learning is a powerful tool for surveying and classifying reed beds of wetlands in high detail. High-resolution images were obtained several times within a single growing season, allowing the phenology of the reed plant *Phragmites australis* to be observed. We were able to determine the extent of the reed stands as well as the changes in the surrounding areas, such as water and sediment areas, which were induced by the decrease in the water level of the lake due to drought conditions.

5.4.1 Model prediction

As input for model training, we fully labeled a subset of eight square-shaped areas on each orthomosaic using the semi-automated image annotation workflow described in Section 5.2.3. These labeled ground truth areas summed to only 4% of the entire study area, and the model prediction yielded favorable results for land cover classification despite the expected challenges stated above. We assumed that it would be crucial to cover the various expressions of each class in the training data; thus, the selection of training areas was carried out with great care. To assess the quality of the model prediction, we manually labeled a representative test area and compared it with the classification results for the same area. The error map in Figure 5.7 shows that the differences between model prediction and the labeled test area occurred almost exclusively along the class boundaries, where different reasons for pixel misclassifications could be identified.

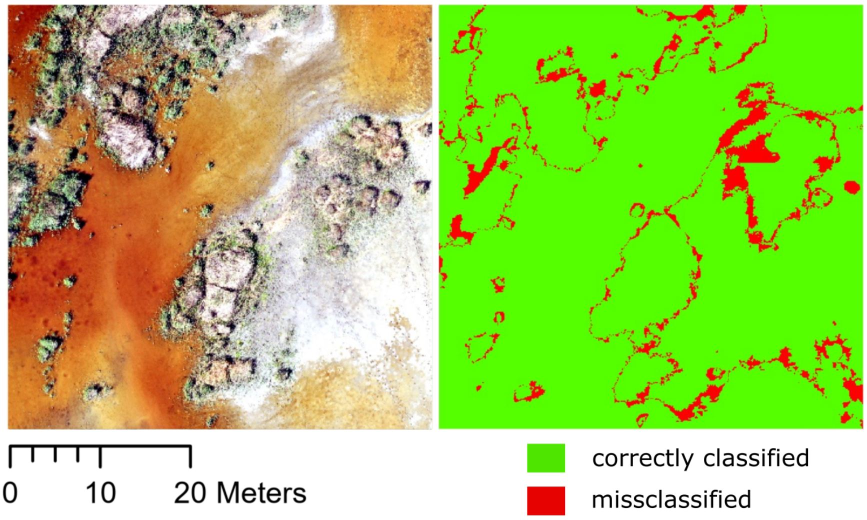

Figure 5.7: Classification performance of a deep learning model visualized in an error map, showing the difference between labeled test data and the model prediction in a reed ecosystem. Misclassifications occurred primarily along class boundaries, especially in transition zones with sparse reed vegetation or very shallow waters, as well as in heavily shaded areas.

First, class boundaries resulting from model prediction ran more smoothly than the class boundaries resulting from the image annotation workflow, which can be considered a negligible error. Second, class boundaries were difficult to predict in extensive transition areas, for example, where water level depths were in the centimeter to millimeter range or in areas with sparse reed vegetation. Third, shaded areas were often reported as misclassified even though they may have been more accurate than the ground truth when compared directly to the imagery. This error may contribute to the significantly lower IoU values for water and sediment in the model performance metrics (see Table 5.2 and S.9), and suggests that preparation of ground truth data must be done with utmost care.

Because misclassifications occurred primarily along class boundaries, we believe that adding more representative training data from transition zones could further improve model performance. On the other hand, transition zones are inherently difficult to delineate, which poses a challenge when generating training data. Both the OBIA segmentation tool used in this study and the visual interpretation when merging the segmented polygons had limitation in terms of the accuracy of separating classes in the transition zones.

5.4.2 Spatio-temporal variability

The results of the land cover classification show a clear dominance of reed vegetation in the study area. Previous studies showing a decline of aquatic reeds in central Europe during the last decades (Dienst et al., 2004, Nechwatal et al., 2008, Ostendorp, 1989) do not match our data within one year. The vegetation area recorded a continuous increase from May to September except for a short period from mid-June to the beginning of July 2021. This rebound of vegetation was likely due to the sudden and complete drying of former water pool areas along the northeastern shore (landward) side of the study area. These pools were sparsely overgrown with juvenile reed shoots in spring, and could be detected well as vegetation by the model. When the pools dried out, increased salinity may have contributed to the dying back of juvenile shoots (Lissner and Schierup, 1997), leading to leaf area loss until the plants could no longer be detected as vegetation by the model. It was clear that large water pool areas dried out and became sediment areas during the study period; when the sediment area reached its maximum extent at the end of June, it was more than four times the size of its minimum extent at the end of May. Water areas declined rapidly from the end of May to mid-September, with the exception of a slight increase on 18 August 2021 due to precipitation in the days immediately preceding the UAV flight (about 20 mm HD Bgld (2023c)). The distribution of area shares hardly changed from the end of September to the end of the study period. The minor decrease in vegetation area within this period suggests that biomass was no longer being built up, reed growth stopped, and reed leaf surfaces shrank slightly due to dehydration and the onset of wilting. Water and sediment areas were stable because water input (precipitation) and evaporation rates were in balance at this time of the year.

The seasonal temporal changes of the water level of Lake Neusiedl and of the reed belt usually occur annually, with a maximum in spring (March/April) and minimum in autumn (September/October) (Hackl and Ledolter, 2023). Therefore, the temporal change of the mosaic of the reed belt consisting of reed stands, water, and open sediment areas occurs annually due to the change in water level even in "normal" years, though of course with a lower extent compared to the results of our study. Because the reed belt has a gradient from land to open water, spatial changes occur at different rates within the reed belt even in "normal" years. Thus, temporal and spatial changes can be observed in "dry" years as well as in "normal" years. Of course, 2021 was an extreme year, with an especially dry autumn, and conditions actually intensified the following year. It may be suspected that a major consequence of the observed changes in "dry" years for the ecosystem of Lake Neusiedl would be a disconnection between reed belt and open water areas, which would alter food webs and have faunistic and biogeochemical consequences, among others. In "wet" years, on the other hand, there would naturally be rather less spreading of the reed stand areas, though water level changes would nevertheless continue over the year. In this context, however, it should be noted that the last "wet" year with high water levels was 2014 (Hackl and Ledolter, 2023).

None of the current studies of Lake Neusiedl (Csaplovics, 1982, Csaplovics and Nemeth, 2014, Csaplovics and Schmidt, 2011, Márkus and Király, 2012, Nemeth and Dvorak, 2022, Nemeth et al., 2014) have investigated the spatial and temporal pattern of the three wetland classes (reed, water, and sediment) within one year, though they have often compared the extent of the reed belt between two years, for example, 1979 and 2008. Our study is the first to identify open sediment areas as a separate land cover class in the reed belt. Comparing August 2008 (Csaplovics and Schmidt, 2011) with August 2021 of our study, the share of water areas in the reed belt decreased by 3.7% (from 10.7 to 7%), which would be an opposite development from that of 1979 to 2008, and the vegetation coverage decreased from 88 to 67%. However, Csaplovics and Schmidt (2011) surveyed the entire Austrian reed belt and reported only humic water; therefore, it is unclear whether the lake water of the channels is included in the water areas of the reed belt, as it is not shown as separate class. In contrast to Dinka et al. (2010), Márkus and Király (2012), Nemeth and Dvorak (2022), we observed no die-back sites in our study site for the period from May to November 2021.

The entire lake, including the reed belt, experienced a sharp drop in water level in 2021; thus, the decrease in water areas inside the reed belt could be observed in other parts of the reed belt of Lake Neusiedl as well. Therefore, the decline in water areas in our study can be generalized to an extent to the entire reed belt of Lake Neusiedl. However, because the reed stands vary in age and structure depending on usage/management (west side) or no usage (east side) (see e.g., Csaplovics and Schmidt (2011)), and some even include reed stands that have died back (see Dinka et al. (2010), Nemeth and Dvorak (2022)), the increase in reed area within the reed belt cannot be generalized to all areas. Nevertheless, this study shows exemplary temporal and spatial changes in the three wetland classes over the 2021 vegetation period, which was affected by drought conditions.

5.4.3 Vegetation phenology

Recently, an example of rapid change in wetland vegetation has been reported from the Rodewiese site, a formerly drained fen on the Baltic coast in NE Germany that was rewetted in 2010. Grassland species that are sensitive to a high water table, such as *Holcus lanatus*, *Potentilla anserina*, and *Trifolium repens*, died back very quickly and were replaced by hydrophytes such as *Lemna* spp. and, with some delay, *Bolboschoenus maritimus*, *Schoenoplectus tabermontanii*, and *Phragmites australis* (Koch et al., 2017). Then, in 2018, most of the site that had been covered by water experienced a drought and turned dry, and the fen canopy, with the exception of *Phragmites australis*, disappeared and was colonized by *Tephroseris palustris* and *Ranunculus sceleratus* (Beyer et al., 2021), pioneer species that rapidly spread along nutrient-rich shores of dried-up water bodies (Fukarek et al., 2006). Beyer et al. (2021) have pointed out that analogous climate effect feedback generally cannot be anticipated; moreover, van Diggelen et al. (2006) and Klimkowska et al. (2010) pointed out that in restored fens, water availability, soil, and trophic status were irreversibly altered, along with propagule availability. The conditions experienced in the reed belt of Lake Neusiedl favor *Phragmites australis* as long as the broad ecological amplitude of this reed is not surpassed.

The vegetation in the study area is dominated by reeds, and was tracked using the GCC vegetation index for phenological analysis. The Phenocam data suggest that the phenological time window of the reed stand was well covered in this UAV study. Nevertheless, there is an offset in the GCC data between the Phenocam and the UAV flights in the phenological *Greenup* phase, which is probably due to the different image perspective. Due to the Phenocam's lateral perspective of the reed plants, it naturally detects greening-up earlier than the UAV does from its nadir perspective. However, the UAV covers a much larger spatial area, which of course develops at different rates in the *Greenup* phase from land to open water areas; we have shown the mean and standard deviation of the GCC for the entire study area in Figure 5.6. The GCC maps in Supplement S.27 and S.28 show that new vigorous reed shoots grow first along the edges of reed stands and in loosely vegetated areas, leading to an expansion of the vegetation area. In the existing reed mats, shoots break through only gradually, especially in dense areas. When GCC levels peaked in late July, the densest areas of the reed mats were only sparsely overgrown with new reed sprouts; therefore, we do not consider these to be die-back sites.

Phenocam data have the advantages of a lateral perspective and high temporal resolution (hourly/daily basis); however, they are limited to the small area that a single photo is able to cover. On the other hand, while aerial surveys with hundreds of images acquired during a UAV flight campaign can provide detailed information on the spatial development of vegetation over a comparatively large area, they are limited to a lower temporal resolution. Therefore, a combination of both methods can provide complementary analysis.

5.5 Conclusions

This study aimed to investigate the spatial and temporal changes in the reed belt of Lake Neusiedl under intensive drought conditions. For this purpose, a set of 10 SfM-derived orthomosaics from UAV imagery collected over the 2021 growing season was created. The high-resolution orthomosaics served as a basis to detect changes in land cover and to reveal phenological development. We have demonstrated a semi-automated procedure for generating fully labeled ground truth data for deep learning image segmentation in the context of land cover classification of a wetland. The results of this study underline the strong ability of deep learning models to extract complex features from high-resolution imagery. However, our unsuccessful attempt to train a generic model using training data from multiple flight campaigns encountered limitations. The classification maps revealed an enormous decline in water areas within the reed belt, with a simultaneous increase in sediment areas during the investigation period. Reed vegetation, on the other hand, increased at a nearly constant rate throughout the growing season due to vigorous reed growth along existing reed stands and in loosely vegetated areas, as identified by the GCC maps. While the results of our study can be generalized to the entire reed belt of Lake Neusiedl to a certain extent, the findings may not be applicable to other ecosystems with different environmental factors. This study provides a detailed data set which can be used to assess the habitat diversity of the reed belt or its ecosystem productivity. In particular, the generated land cover maps may serve as ground truth data for upscaling to more coarsely grained sensor data such as satellite imagery.

Data availability

Data are available in the PHAIDRA Repository `https://doi.org/10.25365/phaidra.397`.

6 General conclusions

The main goal of this doctoral thesis was to improve our understanding of the influence of drought on the spatial and temporal dynamics of reed wetlands, with a particular focus on GHG fluxes, emission pathways, microbial communities in sediments, and land cover. Therefore, my research quantified, analyzed, and compared temporal (and spatial) variations in CO_2 and CH_4 fluxes, emission pathways (plant-mediated transport, diffusion, and ebullition), vegetation indices (GCC, LAI, NDVI, and EVI), land cover classes (vegetation/reed areas, open water areas, and open sediment areas), sediments, reed plants, and surface water at the reed wetland of the Lake Neusiedl in Austria.

6.1 Main findings

This thesis offers novel insights into the release of GHGs in a reed wetland, such as Lake Neusiedl, during periods of drought conditions. The following main findings are highlighted:

1. CH_4 ebullition rates showed a distinct heterogeneity over time (from March to July 2021) and space (locations) at Lake Neusiedl. By studying three subsystems of the lake ecosystem, we were able to observe the substantial influence of the different site characteristics on the CH_4 emission rates, particularly on the ebullition pathway. Although ebullition rates vary considerably within the lake, the dominant methanogenesis pathway remains consistent with acetoclastic throughout the lake. The predominance of the ebullition pathway over the diffusion pathway cannot be confirmed for Lake Neusiedl. (**study I**)
2. A reed wetland can release more CO_2 annually than it absorbs, challenging the assumption that reed ecosystems are exclusively CO_2 sinks. During droughts, a reed ecosystem can initially benefit from falling water levels by growing reeds in previously flooded areas. However, the water content of the sediment appears to be a good indicator of the point at which a reed ecosystem ceases to benefit and instead becomes a major source of C, despite the reduction in CH_4 emissions. (**study II**)
3. A reed wetland shows a pronounced diel cycle of CH_4 fluxes only via plant-mediated transport and in the summer season. The plant-mediated transport demonstrated the highest CH_4 emissions not only in summer, but also in the other seasons. The distinct differences between the two sediment layers, especially in carbon and water content, are also reflected in the observed variations in the microbial communities. The desiccation process led to a reduction in methanogenic microbial diversity in the sediments over the course of a year. (**study III**)

4. A semi-automated workflow was presented for generating fully labeled ground truth data for deep learning image segmentation in the context of land cover classification of a wetland. The results of this study highlight the strong ability of deep learning models to extract complex features from high-resolution images. However, limitations were encountered when attempting to train a generic model using training data from several flight campaigns. The classification maps demonstrated a substantial decrease in water areas within the reed belt, concurrent with an increase of sediment areas during the study period. In contrast, reed vegetation exhibited an almost constant rate of increase during the growing season, driven by vigorous reed growth along existing reed stands and in sparsely vegetated areas, as identified by the GCC maps. (**study IV**)

Collectively, these findings contribute to a comprehensive understanding of the land cover and GHG emission dynamics of reed wetlands under changing climate conditions, provide new GHG emission metrics for estimating GHG emissions from wetlands at regional, national, and global scales, and lay the foundation for future studies. Moreover, the findings of this thesis substantiate the following conclusion:

- The negative SPEI at Lake Neusiedl indicates drought, which has persisted almost contentiously since mid-2015 and lasted at least until 2022.
- It has been demonstrated that not all reed wetlands function as CO_2 sinks like it was postulated by Brix et al. (2001), a finding that has been observed in the context of drought and under the specific water characteristics (e.g., subsaline) of Lake Neusiedl.
- When combining CO_2 and CH_4 fluxes into annual GHG balances, the median GHG emission factor for reed ecosystems is 8.1 t CO_2 eq. ha^{-1} a^{-1}, with a 95% CI ranging from 3.1 to 13.7 t CO_2 eq. ha^{-1} a^{-1}. This calculation considers the 100-year GWP (global warming potential) of CH_4, which is 27 according to IPCC (2023).
- The reed belt of Lake Neusiedl has not only inter-annual dynamics in reed and water areas (Csaplovics, 1982, 2019, Csaplovics and Schmidt, 2011), but also intra-annual dynamics and the occurrence of open sediment areas.
- It is imperative to emphasize the significance of long-term research in a variety of disciplines. This is particular true in the context of EC measurements, as well as in the domains of phenology (Phenocam) and land cover dynamics (remote sensing). For example, if we had terminated the research in 2021, it would not have been possible to observe the reed wetland's carbon emission reduction development being suddenly reversed into a substantial increase in carbon emission due to the decline in SWC. In connection with this, the spread of reeds within the reed belt, caused by the decrease in water level, was also stopped.
- In the context of reed wetlands, the plant-mediated transport is the dominant emission pathway of CH_4 not only in summer (van den Berg et al., 2020), but also in winter, which is the season that is often neglected or not so often studied.

- Ebullition is not the most dominant CH_4 emission pathway in all (shallow) lakes as it was implied by Aben et al. (2017), Bastviken et al. (2011).

- The top sediment layer of Lake Neusiedl's reed belt cannot be defined as peat soil after the definition of Joosten and Clarke (2002) or the Austrian soil classification system (Nestroy et al., 2011). This is due the fact that both definitions require a minimum thickness of 30 cm, which is not met by the top sediment layer, which measures a mean thickness of 9.7 ± 3.8 cm. However, the other requirement of at least 30% (Joosten and Clarke, 2002) or 35% organic matter (Nestroy et al., 2011) is partially met in the top layer (31.3 ± 16.5%), assuming that 58% of organic matter is organic carbon (Austrian Standards International, 2021).

In addition, this work provides valuable insights into the meteorological, limnological, and biogeochemical characteristics of this wetland of international importance. The characteristics of the current Lake Neusiedl and its reed belt under the influence of drought, including water, sediment, and reed properties, as determined by the work of this thesis, are summarized in Table 6.1.

From 2018 to 2022, the mean water level of Lake Neusiedl was 1.3 ± 0.2 m, with annual minimums ranging from 0.87 to 1.27 m, while the maximum water level of 1.8 m mentioned by Wolfram and Herzig (2013) was not reached during this period.

During the 4.5 years under study (mid-2018 to 2022), the annual precipitation in the reed belt of Lake Neusiedl was lower than the 30-year mean (1993–2022) in three years (2019, 2021, 2022). In addition, the annual mean air temperature was higher than the 30-year mean in all years studied. This work records further evidence of climate change at Lake Neusiedl: The annual mean air temperature of the current 30-year mean (1993–2022) has increased by 1.2°C compared to the climate description of Lake Neusiedl (1971–2000) by Eitzinger et al. (2009), while the current 30-year mean annual precipitation has decreased by 74 mm.

Most of the physical and chemical parameters in the surface water of Lake Neusiedl have higher values within the reed belt than in the open lake area, with the exceptions of pH and dissolved oxygen (see Table 6.1). For example, in 2021, the electrical conductivity values of the surface water within the reed belt was nearly twice that of the open lake area. The mean pH of the water pools of the reed belt is 8.5, which is slightly lower than the mean pH of 8.9 in the open lake areas. All of these differences in water parameters between the open lake and the reed belt can be explained by the lost connectivity between the two subsystems and by site-specific differences in processes such as evapotranspiration, biological activity, and sedimentation (Zoboli et al., 2023).

Currently, the reed ecosystem of Lake Neusiedl loses more carbon than it takes up annually. However, the reed belt still contains temporary carbon stocks found in fine sediments, water (dissolved and particulate matter, organic and inorganic components), and living and dead reed components above and below the sediment surface (see Table 6.1). In order to determine exactly where the system is losing carbon, more frequent carbon stock measurements are needed, especially in the sediments.

Table 6.1: Characteristics of the present Lake Neusiedl and its reed belt in numbers, mainly measured near Illmitz and its Biological Station. Unless otherwise stated, the values are the mean ± standard deviation (CON = electrical conductivity; DO = dissolved oxygen; ORP = oxidation–reduction potential; NPOC = dissolved non-purgeable organic carbon; DIC = dissolved inorganic carbon; TDN = total dissolved nitrogen; C = carbon; DW = dry weight).

Parameter	Value	Unit	Time period	Reference
Lake Neusiedl				
water level	1.3 ± 0.2	m	2018–2022	Baur et al. (2024b)
annual maximum water level	1.33–1.66	m	2018–2022	Baur et al. (2024b)
annual minimum water level	0.87–1.27	m	2018–2022	Baur et al. (2024b)
mean annual precipitation	500.2	mm	1993–2022	Baur et al. (2024b)
annual mean air temperature	11.3	°C	1993–2022	Baur et al. (2024b)
surface water of the open lake area				
CON	2.9 ± 0.2	mS cm^{-1}	2021	Baur et al. (2024a)
pH	8.9 ± 0.1		2021	Baur et al. (2024a)
mean (max–min) water temperature	12.9 (−0.3–31.5)	°C	2018–2022	Baur et al. (2024b)
DO	96 ± 8	%	2021	Baur et al. (2024a)
ORP	144 ± 58	mV	2021	Baur et al. (2024a)
NPOC	28 ± 5	mg L^{-1}	2021	Baur et al. (2024a)
DIC	160 ± 36	mg L^{-1}	2021	Baur et al. (2024a)
TDN	1.4 ± 0.7	mg L^{-1}	2021	Baur et al. (2024a)
sulfate	454 ± 76	mg L^{-1}	2021	Baur et al. (2024a)
surface water of the reed belt				
CON	4.4 ± 1.3	mS cm^{-1}	2021	Baur et al. (2024a)
pH	8.5 ± 0.2		2021	Baur et al. (2024a)
water temperature	20.6 ± 8.2	°C	2021	Baur et al. (2024a)
DO	77 ± 52	%	2021	Baur et al. (2024a)
ORP	118 ± 65	mV	2021	Baur et al. (2024a)
NPOC	83 ± 34	mg L^{-1}	2021	Baur et al. (2024a)
DIC	265 ± 95	mg L^{-1}	2021	Baur et al. (2024a)
TDN	4.0 ± 1.4	mg L^{-1}	2021	Baur et al. (2024a)
sulfate	627 ± 235	mg L^{-1}	2021	Baur et al. (2024a)
sediment of the reed belt				
depth of top (organic) layer	9.7 ± 3.8	cm	2021/2022	Baur et al. (2025)
CON of top layer	3.3 ± 1.2	mS cm^{-1}	2021/2022	Baur et al. (2025)
CON of lower layer	0.7 ± 0.5	mS cm^{-1}	2021/2022	Baur et al. (2025)
pH of top layer	8.3 ± 0.5		2021/2022	Baur et al. (2025)
pH of lower layer	9.1 ± 0.5		2021/2022	Baur et al. (2025)
water content of top layer	82.3 ± 6.7	mass-%	2021/2022	Baur et al. (2025)
water content of lower layer	29.4 ± 8.4	mass-%	2021/2022	Baur et al. (2025)
C content of top (organic) layer	20.4 ± 8.6	mass-%	2021/2022	Baur et al. (2025)
C content of lower (sandy) layer	2.9 ± 0.9	mass-%	2021/2022	Baur et al. (2025)
sulfate content of top layer	6.9 ± 2.6	mg g^{-1} DW	2021/2022	Baur et al. (2025)
sulfate content of lower layer	0.8 ± 0.7	mg g^{-1} DW	2021/2022	Baur et al. (2025)
reed (*Phragmites australis*)				
shoot height (with inflorescence)	1.99 ± 0.50	m	fall 2022	Holzer (2024)
shoot density	159 ± 85	shoots m^{-2}	fall 2022	Holzer (2024)
share litter on aboveground biomass	52 ± 19	%	fall 2022	Holzer (2024)
C storage in aboveground biomass	1.44 ± 0.66	kg C m^{-2}	fall 2022	Baur et al. (2024b)
C storage in belowground biomass	2.33 ± 1.28	kg C m^{-2}	fall 2022	Baur et al. (2024b)

6.2 Outlook and challenges

The decreasing water levels and the almost dry reed belt since fall 2021 challenged our study of the emission pathways of diffusion and ebullition. However, this partly reflects the (natural) dynamics of wetlands and their interfaces with the atmosphere, but also in the context of anthropogenic climate change and increasing droughts (IPCC, 2023).

Due to the desiccation, we observed strong changes in the microbial community in the sediment within one year. It would be interesting to study the intra-annual changes in the future.

Since the study area of this thesis is located in the core zone of the national park, we were able to study the reed ecosystem without direct human use or influence. On the other hand, due to the strict conservation rules and to avoid disturbing the breeding birds, we were somewhat more restricted in the selection of sites for GCPs or chamber measurements. Nevertheless, we were able to survey the area in the best possible way and obtain satisfactory results.

In cooperation and under the leadership of Pia Gottschalk (GFZ Potsdam, Germany), the analysis of extreme weather events of wetlands and their influence on carbon and water fluxes, including the reed belt of Lake Neusiedl, is currently in progress.

As the study site is also a LTER site and part of the LTWER (long-term wetland ecosystem research) core facility of the University of Vienna, the EC and biometeorological measurements in the reed belt will be continued. It will be interesting to observe and to study, how the reed wetland develops and recovers, and how rising water levels (hopefully) affect the carbon cycle of the ecosystem.

With hopefully higher water levels in Lake Neusiedl, it would be interesting to study and quantify the lateral dynamics of water and carbon between the reed belt and the open lake. In the REBEN project, a first initiative on this topic was started with two measurement days (Wolfram et al., 2020). However, the focus of the project was more on the hydrology, nutrients, and trace elements, while the lateral transport of carbon (organic and inorganic, dissolved and particulate) was not investigated.

It also remains to be seen how the older or degraded reed stands or reed mats (Dinka et al., 2010, Nemeth and Dvorak, 2022) in the reed belt affect carbon processes such as decomposition, plant respiration, or photosynthesis in detail. This should be further investigated in the future.

In the future, the N_2O fluxes of the reed belt of Lake Neusiedl shall be investigated, especially in the context of decreasing water levels or droughts, which allow more oxygen to reach the sediments and thus influence the N_2O fluxes.

All data generated in this thesis are openly published in the PHAIDRA repository of the University of Vienna (Baur, 2024, 2025, Baur and Henry Pinilla, 2023, Buchsteiner and Baur, 2023) and can be used for further and comparable studies. In addition, the study site and the EC measurements are part of the international networks LTER and FLUXNET, and will soon be part of global comparative studies and data sets.

References

Aben, R.C.H., Barros, N., van Donk, E., Frenken, T., Hilt, S., Kazanjian, G., Lamers, L.P.M., Peeters, E.T.H.M., Roelofs, J.G.M., de Senerpont Domis, L.N., Stephan, S., Velthuis, M., van de Waal, D.B., Wik, M., Thornton, B.F., Wilkinson, J., DelSontro, T., Kosten, S., 2017. Cross continental increase in methane ebullition under climate change. Nature communications 8, 1682. doi:`10.1038/s41467-017-01535-y`.

Acosta, M., Dušek, J., Chamizo, S., Serrano-Ortiz, P., Pavelka, M., 2019. Autumnal fluxes of CH_4 and CO_2 from Mediterranean reed wetland based on eddy covariance and chamber methods. CATENA 183, 104191. doi:`10.1016/j.catena.2019.104191`.

Afreen, F., Zobayed, S.M.A., Armstrong, J., Armstrong, W., 2007. Pressure gradients along whole culms and leaf sheaths, and other aspects of humidity-induced gas transport in *Phragmites australis*. Journal of experimental botany 58, 1651–1662. doi:`10.1093/jxb/erm017`.

Agoston-Szabo, E., Dinka, M., 2006. Changes in sediment and sediment interstitial water characteristics in Lake Fertő/Neusiedler See. Opuscula Zoologica 35, 3–17.

Aguirrezabala-Campano, T., Gerardo-Nieto, O., Gonzalez-Valencia, R., Souza, V., Thalasso, F., 2019. Methane dynamics in the subsaline ponds of the Chihuahuan Desert: A first assessment. Science of the Total Environment 666, 1255–1264. doi:`10.1016/j.scitotenv.2019.02.163`.

Al-Najjar, H.A.H., Kalantar, B., Pradhan, B., Saeidi, V., Halin, A.A., Ueda, N., Mansor, S., 2019. Land cover classification from fused DSM and UAV images using convolutional neural networks. Remote Sensing 11, 1461. doi:`10.3390/rs11121461`.

Alexandridis, T.K., Ovakoglou, G., Clevers, J.G.P.W., 2020. Relationship between MODIS EVI and LAI across time and space. Geocarto International 35, 1385–1399. doi:`10.1080/10106049.2019.1573928`.

Alin, S.R., Johnson, T.C., 2007. Carbon cycling in large lakes of the world: A synthesis of production, burial, and lake-atmosphere exchange estimates. Global Biogeochemical Cycles 21, GB3002. doi:`10.1029/2006GB002881`.

Anagnostis, A., Tagarakis, A.C., Kateris, D., Moysiadis, V., Sørensen, C.G., Pearson, S., Bochtis, D., 2021. Orchard mapping with deep learning semantic segmentation. Sensors 21, 3813. doi:`10.3390/s21113813`.

Angel, R., Matthies, D., Conrad, R., 2011. Activation of methanogenesis in arid biological soil crusts despite the presence of oxygen. PloS one 6, e20453. doi:`10.1371/journal.pone.0020453`.

Anonymous, 1958. The Venice system for the classification of marine waters according to salinity: Symposium on the classification of brackish waters, Venice, 8-14 April 1958. Limnology and Oceanography 3, 346–347. doi:`10.4319/lo.1958.3.3.0346`.

Antonielli, M., Pasqualini, S., Batini, P., Ederli, L., Massacci, A., Loreto, F., 2002. Physiological and anatomical characterisation of *Phragmites australis* leaves. Aquatic botany 72, 55–66. doi:`10.1016/S0304-3770(01)00220-0`.

Armstrong, J., Armstrong, W., 1988. *Phragmites australis* - A preliminary study of soil-oxidizing sites and internal gas transport pathways. New Phytologist 108, 373–382. doi:`10.1111/j.1469-8137.1988.tb04177.x`.

Armstrong, J., Armstrong, W., 1990. Light-enhanced convective throughflow increases oxygenation in rhizomes and rhizosphere of *Phragmites australis* (Cav.) Trin. ex Steud. New Phytologist 114, 121–128. doi:`10.1111/j.1469-8137.1990.tb00382.x`.

Armstrong, J., Armstrong, W., 1991. A convective through-flow of gases in *Phragmites australis* (Cav.) Trin. ex Steud. Aquatic botany 39, 75–88. doi:`10.1016/0304-3770(91)90023-X`.

Armstrong, J., Armstrong, W., Beckett, P.M., 1992. *Phragmites australis*: venturi- and humidity-induced pressure flows enhance rhizome aeration and rhizosphere oxidation. New Phytologist 120, 197–207. doi:`10.1111/j.1469-8137.1992.tb05655.x`.

Armstrong, J., Armstrong, W., Beckett, P.M., Halder, J.E., Lythe, S., Holt, R., Sinclair, A., 1996. Pathways of aeration and the mechanisms and beneficial effects of humidity- and venturi-induced convections in *Phragmites australis* (Cav.) Trin. ex Steud. Aquatic botany 54, 177–197. doi:`10.1016/0304-3770(96)01044-3`.

Aubinet, M., Vesala, T., Papale, D. (Eds.), 2012. Eddy covariance: A practical guide to measurement and data analysis. Springer Atmospheric Sciences. 1. ed., Springer, Dordrecht. doi:`10.1007/978-94-007-2351-1`.

Auguie, B., 2017. gridExtra: miscellaneous functions for "grid" graphics. R package version 2.3. doi:`10.32614/CRAN.package.gridExtra`.

Austrian Standards International, 2021. ÖNORM L 1080:2021-12-15. Soil and waste properties – Determination of organic carbon and humus content by dry combustion taking into account carbonates and elemental carbon. Austrian Standards International, Vienna. URL: `https://www.austrian-standards.at/en/shop/onorm-l-1080-2021-12-15~p2608300`.

Bade, K., Manz, W., Szewzyk, U., 2000. Behavior of sulfate reducing bacteria under oligotrophic conditions and oxygen stress in particle-free systems related to drinking water. FEMS Microbiology Ecology 32, 215–223. doi:`10.1111/j.1574-6941.2000.tb00714.x`.

Bai, Y.N., Wang, X.N., Wu, J., Lu, Y.Z., Fu, L., Zhang, F., Lau, T.C., Zeng, R.J., 2019. Humic substances as electron acceptors for anaerobic oxidation of methane driven by ANME-2d. Water research 164, 114935. doi:`10.1016/j.watres.2019.114935`.

Bakker, E.S., Wood, K.A., Pagès, J.F., Veen, G.F., Christianen, M.J., Santamaría, L., Nolet, B.A., Hilt, S., 2016. Herbivory on freshwater and marine macrophytes: A review and perspective. Aquatic botany 135, 18–36. doi:`10.1016/j.aquabot.2016.04.008`.

Baldocchi, D., Falge, E., Gu, L., Olson, R., Hollinger, D., Running, S., Anthoni, P., Bernhofer, C., Davis, K., Evans, R., Fuentes, J., Goldstein, A., Katul, G., Law, B., Lee, X., Malhi, Y., Meyers, T., Munger, W., Oechel, W., Paw, K.T., Pilegaard, K., Schmid, H.P., Valentini, R., Verma, S., Vesala, T., Wilson, K., Wofsy, S., 2001. FLUXNET: A new tool to study the temporal and spatial variability of ecosystem–scale carbon dioxide, water vapor, and energy flux densities. Bulletin of the American Meteorological Society 82, 2415–2434. doi:`10.1175/1520-0477(2001)082<2415:FANTTS>2.3.CO;2`.

Baldocchi, D.D., 2003. Assessing the eddy covariance technique for evaluating carbon dioxide exchange rates of ecosystems: past, present and future. Global Change Biology 9, 479–492. doi:`10.1046/j.1365-2486.2003.00629.x`.

Barrett, T., Dowle, M., Srinivasan, A., Gorecki, J., Chirico, M., Hocking, T., 2024. data.table: Extension of ‘data.frame‘. R package version 1.15.4. doi:`10.32614/CRAN.package.data.table`.

Bartosiewicz, M., Laurion, I., MacIntyre, S., 2015. Greenhouse gas emission and storage in a small shallow lake. Hydrobiologia 757, 101–115. doi:`10.1007/s10750-015-2240-2`.

Bastviken, D., Cole, J.J., Pace, M.L., van de Bogert, M.C., 2008. Fates of methane from different lake habitats: connecting whole-lake budgets and CH_4 emissions. Journal of Geophysical Research: Biogeosciences 113, G02024. doi:`10.1029/2007JG000608`.

Bastviken, D., Ejlertsson, J., Tranvik, L., 2002. Measurement of methane oxidation in lakes: a comparison of methods. Environmental Science & Technology 36, 3354–3361. doi:`10.1021/es010311p`.

Bastviken, D., Tranvik, L.J., Downing, J.A., Crill, P.M., Enrich-Prast, A., 2011. Freshwater methane emissions offset the continental carbon sink. Science 331, 50. doi:`10.1126/science.1196808`.

Baty, F., Ritz, C., Charles, S., Brutsche, M., Flandrois, J.P., Delignette-Muller, M.L., 2015. A toolbox for nonlinear regression in R: the package nlstools. Journal of statistical software 66, 1–21. doi:`10.18637/jss.v066.i05`.

Baur, P.A., 2024. Multi-year data set of CO_2 fluxes, CH_4 fluxes and environmental parameters of the wetland with reeds at Lake Neusiedl from mid-2018 to 2022 [Data set]. V1. PHAIDRA Repositorium (University of Vienna). doi:`10.25365/phaidra.490`.

Baur, P.A., 2025. Data sets of seasonal sediment properties, stable carbon isotope ratios and diel CH_4 fluxes for each emission pathway of the reed belt at Lake Neusiedl [Data set]. V1. PHAIDRA Repositorium (University of Vienna). doi:`10.25365/phaidra.626`.

Baur, P.A., Henry Pinilla, D., 2023. Measurements of methane ebullition and diffusion fluxes, and water parameters at Lake Neusiedl: March–July 2021 [Data set]. V1. PHAIDRA Repositorium (University of Vienna). doi:`10.25365/phaidra.424`.

Baur, P.A., Henry Pinilla, D., Glatzel, S., 2024a. Is ebullition or diffusion more important as methane emission pathway in a shallow subsaline lake? Science of the Total Environment 912, 169112. doi:`10.1016/j.scitotenv.2023.169112`.

Baur, P.A., Maier, A., Buchsteiner, C., Zechmeister, T., Glatzel, S., 2024b. Consequences of intense drought on CO_2 and CH_4 fluxes of the reed ecosystem at Lake Neusiedl. Environmental research 262, 119907. doi:`10.1016/j.envres.2024.119907`.

Baur, P.A., Rodrigues-Oliveira, T., Hager, K., Luo, Z.H., Schleper, C., Glatzel, S., 2025. Pathways of CH_4 formation and emission in the subsaline reed wetland of Lake Neusiedl. EGUsphere [preprint] doi:`10.5194/egusphere-2025-443`.

Beguería, S., Vicente-Serrano, S.M., 2023. SPEI: calculation of the Standardized Precipitation-Evapotranspiration Index. R package version 1.8.1. doi:`10.32614/CRAN.package.SPEI`.

Bergström, I., Mäkelä, S., Kankaala, P., Kortelainen, P., 2007. Methane efflux from littoral vegetation stands of southern boreal lakes: An upscaled regional estimate. Atmospheric Environment 41, 339–351. doi:`10.1016/j.atmosenv.2006.08.014`.

BEV, 2019. Orthophoto 7930-58 from flight date 2019-06-26 [Data set]. Bundesamt für Eich- und Vermessungswesen, Vienna. URL: `https://www.bev.gv.at`.

Beyer, F., Jansen, F., Jurasinski, G., Koch, M., Schröder, B., Koebsch, F., 2021. Drought years in peatland rewetting: rapid vegetation succession can maintain the net CO_2 sink function. Biogeosciences 18, 917–935. doi:`10.5194/bg-18-917-2021`.

Bhatnagar, S., Gill, L., Ghosh, B., 2020. Drone image segmentation using machine and deep learning for mapping raised bog vegetation communities. Remote Sensing 12, 2602. doi:`10.3390/rs12162602`.

Blume, H.P., Brümmer, G.W., Fleige, H., Horn, R., Kandeler, E., Kögel-Knabner, I., Kretzschmar, R., Stahr, K., Wilke, B.M. (Eds.), 2016. Scheffer/Schachtschabel Soil Science. Springer, Berlin, Heidelberg. doi:`10.1007/978-3-642-30942-7`.

Bogard, M.J., Bergamaschi, B.A., Butman, D.E., Anderson, F., Knox, S.H., Windham-Myers, L., 2020. Hydrologic export is a major component of coastal wetland carbon budgets. Global Biogeochemical Cycles 34, e2019GB006430. doi:`10.1029/2019GB006430`.

Bogard, M.J., del Giorgio, P.A., Boutet, L., Chaves, M.C.G., Prairie, Y.T., Merante, A., Derry, A.M., 2014. Oxic water column methanogenesis as a major component of aquatic CH_4 fluxes. Nature communications 5, 5350. doi:`10.1038/ncomms6350`.

Boguski, T.K., 2006. Understanding units of measurement. Environmental science and technology briefs for citizens, 2 p. URL: `https://engg.k-state.edu/chsr/outreach/resources/docs/measure.pdf`.

Bokulich, N.A., Kaehler, B.D., Rideout, J.R., Dillon, M., Bolyen, E., Knight, R., Huttley, G.A., Gregory Caporaso, J., 2018. Optimizing taxonomic classification of marker-gene amplicon sequences with QIIME 2's q2-feature-classifier plugin. Microbiome 6, 1–17. doi:`10.1186/s40168-018-0470-z`.

Bolyen, E., Rideout, J.R., Dillon, M.R., Bokulich, N.A., Abnet, C.C., Al-Ghalith, G.A., Alexander, H., Alm, E.J., Arumugam, M., Asnicar, F., Bai, Y., Bisanz, J.E., Bittinger, K., Brejnrod, A., Brislawn, C.J., Brown, C.T., Callahan, B.J., Caraballo-Rodríguez, A.M., Chase, J., Cope, E.K., Da Silva, R., Diener, C., Dorrestein, P.C., Douglas, G.M., Durall, D.M., Duvallet, C., Edwardson, C.F., Ernst, M., Estaki, M., Fouquier, J., Gauglitz, J.M., Gibbons, S.M., Gibson, D.L., Gonzalez, A., Gorlick, K., Guo, J., Hillmann, B., Holmes, S., Holste, H., Huttenhower, C., Huttley, G.A., Janssen, S., Jarmusch, A.K., Jiang, L., Kaehler, B.D., Kang, K.B., Keefe, C.R., Keim, P., Kelley, S.T., Knights, D., Koester, I., Kosciolek, T., Kreps, J., Langille, M.G.I., Lee, J., Ley, R., Liu, Y.X., Loftfield, E., Lozupone, C., Maher, M., Marotz, C., Martin, B.D., McDonald, D., McIver, L.J., Melnik, A.V., Metcalf, J.L., Morgan, S.C., Morton, J.T., Naimey, A.T., Navas-Molina, J.A., Nothias, L.F., Orchanian, S.B., Pearson, T., Peoples, S.L., Petras, D., Preuss, M.L., Pruesse, E., Rasmussen, L.B., Rivers, A., Robeson, M.S., Rosenthal, P., Segata, N., Shaffer, M., Shiffer, A., Sinha, R., Song, S.J., Spear, J.R., Swafford, A.D., Thompson, L.R., Torres, P.J., Trinh, P., Tripathi, A., Turnbaugh, P.J., Ul-Hasan, S., van der Hooft, J.J.J., Vargas, F., Vázquez-Baeza, Y., Vogtmann, E., von Hippel, M., Walters, W., Wan, Y., Wang, M., Warren, J., Weber, K.C., Williamson, C.H.D., Willis, A.D., Xu, Z.Z., Zaneveld, J.R., Zhang, Y., Zhu, Q., Knight, R., Caporaso, J.G., 2019. Reproducible, interactive, scalable and extensible microbiome data science using QIIME 2. Nature Biotechnology 37, 852–857. doi:`10.1038/s41587-019-0209-9`.

Bonin, A.S., Boone, D.R., 2006. The Order Methanobacteriales, in: Dworkin, M., Falkow, S., Rosenberg, E., Schleifer, K., Stackebrandt, E. (Eds.), The Prokaryotes. Springer, New York, pp. 231–243. doi:`10.1007/0-387-30743-5_11`.

Boros, E., Horváth, Z., Wolfram, G., Vörös, L., 2014. Salinity and ionic composition of the shallow astatic soda pans in the Carpathian Basin. Annales de Limnologie - International Journal of Limnology 50, 59–69. doi:`10.1051/limn/2013068`.

Brix, H., 1989. Gas exchange through dead culms of reed, *Phragmites australis* (Cav.) Trin. ex Steudel. Aquatic botany 35, 81–98. doi:`10.1016/0304-3770(89)90069-7`.

Brix, H., Sorrell, B.K., Lorenzen, B., 2001. Are *Phragmites*–dominated wetlands a net source or net sink of greenhouse gases? Aquatic botany 69, 313–324. doi:`10.1016/S0304-3770(01)00145-0`.

Brix, H., Sorrell, B.K., Orr, P.T., 1992. Internal pressurization and convective gas flow in some emergent freshwater macrophytes. Limnology and Oceanography 37, 1420–1433. doi:`10.4319/lo.1992.37.7.1420`.

Brix, H., Sorrell, B.K., Schierup, H.H., 1996. Gas fluxes achieved by in situ convective flow in *Phragmites australis*. Aquatic botany 54, 151–163. doi:`10.1016/0304-3770(96)01042-X`.

Brouns, K., Verhoeven, J.T.A., Hefting, M.M., 2014. The effects of salinization on aerobic and anaerobic decomposition and mineralization in peat meadows: the roles of peat type and land use. Journal of environmental management 143, 44–53. doi:`10.1016/j.jenvman.2014.04.009`.

Buchsteiner, C., Baur, P.A., 2023. Spatial and intra-annual datasets on reed ecosystem dynamics at Lake Neusiedl of 2021 using RGB drone imagery, phenocam and deep learning [Data set]. V1. PHAIDRA Repositorium (University of Vienna). doi:`10.25365/phaidra.397`.

Buchsteiner, C., Baur, P.A., Glatzel, S., 2023. Spatial analysis of intra-annual reed ecosystem dynamics at Lake Neusiedl using RGB drone imagery and deep learning. Remote sensing 15, 3961. doi:`10.3390/rs15163961`.

Burba, G., 2013. Eddy Covariance Method for Scientific, Industrial, Agricultural and Regulatory Applications: A Field Book on Measuring Ecosystem Gas Exchange and Areal Emission Rates. LI-COR Biosciences. doi:`10.13140/RG.2.1.4247.8561`.

Burba, G., Schmidt, A., Scott, R.L., Nakai, T., Kathilankal, J., Fratini, G., Hanson, C., Law, B., McDermitt, D.K., Eckles, R., Furtaw, M., Velgersdyk, M., 2012. Calculating CO_2 and H_2O eddy covariance fluxes from an enclosed gas analyzer using an instantaneous mixing ratio. Global Change Biology 18, 385–399. doi:`10.1111/j.1365-2486.2011.02536.x`.

Butterbach-Bahl, K., Kiese, R., Liu, C., 2011. Measurements of biosphere-atmosphere exchange of CH_4 in terrestrial ecosystems. Methods in enzymology 495, 271–287. doi:`10.1016/B978-0-12-386905-0.00018-8`.

Camacho, A., Picazo, A., Rochera, C., Santamans, A., Morant, D., Miralles-Lorenzo, J., Castillo-Escrivà, A., 2017. Methane emissions in spanish saline lakes: Current rates, temperature and salinity responses, and evolution under different climate change scenarios. Water 9, 659. doi:`10.3390/w9090659`.

Canty, A., Ripley, B., 2021. boot: bootstrap R (S-plus) functions. R package version 1.3-28. doi:`10.32614/CRAN.package.boot`.

Caporaso, J.G., Lauber, C.L., Walters, W.A., Berg-Lyons, D., Lozupone, C.A., Turnbaugh, P.J., Fierer, N., Knight, R., 2011. Global patterns of 16S rRNA diversity at a depth of millions of sequences per sample. Proceedings of the National Academy of Sciences of the United States of America 108, 4516–4522. doi:`10.1073/pnas.1000080107`.

Castelle, C.J., Méheust, R., Jaffe, A.L., Seitz, K., Gong, X., Baker, B.J., Banfield, J.F., 2021. Protein family content uncovers lineage relationships and bacterial pathway maintenance mechanisms in DPANN archaea. Frontiers in Microbiology 12, 1–13. doi:`10.3389/fmicb.2021.660052`.

Chamberlain, S.D., Hemes, K.S., Eichelmann, E., Szutu, D.J., Verfaillie, J.G., Baldocchi, D.D., 2020. Effect of drought-induced salinization on wetland methane emissions, gross ecosystem productivity, and their interactions. Ecosystems 23, 675–688. doi:`10.1007/s10021-019-00430-5`.

Chanton, J.P., 2005. The effect of gas transport on the isotope signature of methane in wetlands. Organic geochemistry 36, 753–768. doi:`10.1016/j.orggeochem.2004.10.007`.

Chanton, J.P., Arkebauer, T.J., Harden, H.S., Verma, S.B., 2002. Diel variation in lacunal CH_4 and CO_2 concentration and $\delta^{13}C$ in *Phragmites australis*. Biogeochemistry 59, 287–301. doi:`10.1023/A:1016067610783`.

Chen, L.C., Zhu, Y., Papandreou, G., Schroff, F., Adam, H., 2018. Encoder-decoder with atrous separable convolution for semantic image segmentation. arXiv doi:`10.48550/arXiv.1802.02611`.

Chu, H., Gottgens, J.F., Chen, J., Sun, G., Desai, A.R., Ouyang, Z., Shao, C., Czajkowski, K., 2015. Climatic variability, hydrologic anomaly, and methane emission can turn productive freshwater marshes into net carbon sources. Global Change Biology 21, 1165–1181. doi:`10.1111/gcb.12760`.

Čížková, H., Kučera, T., Poulin, B., Květ, J., 2023. Ecological basis of ecosystem services and management of wetlands dominated by common reed (*Phragmites australis*): European perspective. Diversity 15, 629. doi:`10.3390/d15050629`.

Čížková, H., Květ, J., Comín, F.A., Laiho, R., Pokorný, J., Pithart, D., 2013. Actual state of European wetlands and their possible future in the context of global climate change. Aquatic Sciences 75, 3–26. doi:`10.1007/s00027-011-0233-4`.

Cohen, J., 1988. Statistical Power Analysis for the Behavioral Sciences. 2nd ed., Routledge, New York. doi:`10.4324/9780203771587`.

Conrad, R., 1996. Soil microorganisms as controllers of atmospheric trace gases (H_2, CO, CH_4, OCS, N_2O, and NO). Microbiological reviews 60, 609–640. doi:`10.1128/mr.60.4.609-640.1996`.

Conrad, R., 1999. Contribution of hydrogen to methane production and control of hydrogen concentrations in methanogenic soils and sediments. FEMS Microbiology Ecology 28, 193–202. doi:`10.1111/j.1574-6941.1999.tb00575.x`.

Conrad, R., 2005. Quantification of methanogenic pathways using stable carbon isotopic signatures: a review and a proposal. Organic geochemistry 36, 739–752. doi:`10.1016/j.orggeochem.2004.09.006`.

Conrad, R., 2007. Microbial ecology of methanogens and methanotrophs. Advances in Agronomy 96, 1–63. doi:`10.1016/S0065-2113(07)96005-8`.

Conrad, R., 2009. The global methane cycle: recent advances in understanding the microbial processes involved. Environmental microbiology reports 1, 285–292. doi:`10.1111/j.1758-2229.2009.00038.x`.

Conrad, R., 2020a. Importance of hydrogenotrophic, aceticlastic and methylotrophic methanogenesis for methane production in terrestrial, aquatic and other anoxic environments: A mini review. Pedosphere 30, 25–39. doi:`10.1016/S1002-0160(18)60052-9`.

Conrad, R., 2020b. Methane production in soil environments-anaerobic biogeochemistry and microbial life between flooding and desiccation. Microorganisms 8. doi:`10.3390/microorganisms8060881`.

Conrad, R., 2023. Complexity of temperature dependence in methanogenic microbial environments. Frontiers in microbiology 14, 1232946. doi:`10.3389/fmicb.2023.1232946`.

Cowardin, L.M., Carter, V., Golet, F.C., LaRoe, E.T., 1979. Classification of wetlands and deepwater habitats of the United States. U.S. Department of the Interior, Fish and Wildlife Service, Washington, D.C.

Csaplovics, E., 1982. Interpretation von Farbinfrarotbildern: Kartierung von Vegetationsschäden in Brixlegg; Schilfkartierung Neusiedler See. Geowissenschaftliche Mitteilungen 23, VIII, 178. URL: `http://hdl.handle.net/20.500.12708/533`.

Csaplovics, E., 2019. Der Schilfgürtel des Neusiedler Sees. Österreichische Wasser- und Abfallwirtschaft 71, 494–507. doi:`10.1007/s00506-019-00622-2`.

Csaplovics, E., Nemeth, E., 2014. Airborne optical imaging in support of habitat ecological monitoring of the Austrian reed belt of Lake Neusiedl. Proceedings of the GISScience RSGIS4HQ, 163–167. URL: `https://www.ub.tuwien.ac.at/pub/2014/AC12058060_Proceedings.pdf`.

Csaplovics, E., Schmidt, J., 2011. Schilfkartierung Neusiedler See: Ausdehnung und Struktur der Schilfbestände des Neusiedler Sees – Projektmanagement, Erfassung und Kartierung des österreichischen Anteiles durch Luftbildklassifikation. Endbericht an den Naturschutzbund Österreich – Landesgruppe Burgenland. Technische Universität Wien - Institut für Photogrammetrie und Fernerkundung, Dresden, 34 p. URL: `https:`

//naturschutzbund.at/files/bgl_homepage/projekte/lebensraeume/anlagen/AbschlussberichtSchilfkartierung.pdf.

Dang, C.C., Xie, G.J., Liu, B.F., Xing, D.F., Ding, J., Ren, N.Q., 2021. Heavy metal reduction coupled to methane oxidation: Mechanisms, recent advances and future perspectives. Journal of hazardous materials 405, 124076. doi:10.1016/j.jhazmat.2020.124076.

Davidson, N.C., Fluet-Chouinard, E., Finlayson, C.M., 2018a. Global extent and distribution of wetlands: trends and issues. Marine and Freshwater Research 69, 620. doi:10.1071/MF17019.

Davidson, T.A., Audet, J., Jeppesen, E., Landkildehus, F., Lauridsen, T.L., Søndergaard, M., Syväranta, J., 2018b. Synergy between nutrients and warming enhances methane ebullition from experimental lakes. Nature Climate Change 8, 156–160. doi:10.1038/s41558-017-0063-z.

Davison, A.C., Hinkley, D.V., 1997. Bootstrap Methods and Their Applications. Cambridge University Press, Cambridge. doi:10.1017/CBO9780511802843.

Davranche, A., Poulin, B., Lefebvre, G., 2010. Reedbed monitoring using classification trees and SPOT-5 seasonal time series, in: International Symposium on Advanced Methods of Monitoring Reed Habitats in Europe, Nov 2010, Illmitz, Austria, pp. 15–29. URL: https://hal.science/hal-00692542.

Deliry, S.I., Avdan, U., 2021. Accuracy of unmanned aerial systems photogrammetry and structure from motion in surveying and mapping: A review. Journal of the Indian Society of Remote Sensing 49, 1997–2017. doi:10.1007/s12524-021-01366-x.

DelSontro, T., Beaulieu, J.J., Downing, J.A., 2018. Greenhouse gas emissions from lakes and impoundments: upscaling in the face of global change. Limnology and Oceanography Letters 3, 64–75. doi:10.1002/lol2.10073.

DelSontro, T., Boutet, L., St-Pierre, A., del Giorgio, P.A., Prairie, Y.T., 2016. Methane ebullition and diffusion from northern ponds and lakes regulated by the interaction between temperature and system productivity. Limnology and Oceanography 61, S62–S77. doi:10.1002/lno.10335.

Delwiche, K.B., Knox, S.H., Malhotra, A., Fluet-Chouinard, E., McNicol, G., Feron, S., Ouyang, Z., Papale, D., Trotta, C., Canfora, E., Cheah, Y.W., Christianson, D., Alberto, M.C.R., Alekseychik, P., Aurela, M., Baldocchi, D., Bansal, S., Billesbach, D.P., Bohrer, G., Bracho, R., Buchmann, N., Campbell, D.I., Celis, G., Chen, J., Chen, W., Chu, H., Dalmagro, H.J., Dengel, S., Desai, A.R., Detto, M., Dolman, H., Eichelmann, E., Euskirchen, E., Famulari, D., Fuchs, K., Goeckede, M., Gogo, S., Gondwe, M.J., Goodrich, J.P., Gottschalk, P., Graham, S.L., Heimann, M., Helbig, M., Helfter, C., Hemes, K.S., hirano, t., Hollinger, D., Hörtnagl, L., Iwata, H., Jacotot, A., Jurasinski, G., Kang, M., Kasak, K., King, J., Klatt, J., Koebsch, F., Krauss, K.W., Lai, D.Y.F., Lohila, A., Mammarella, I., Belelli Marchesini, L., Manca, G., Matthes, J.H., Maximov, T., Merbold, L., Mitra, B., Morin, T.H., Nemitz, E., Nilsson, M.B., Niu, S., Oechel, W.C., Oikawa, P.Y., Ono, K., Peichl, M., Peltola, O., Reba, M.L., Richardson, A.D., Riley, W., Runkle, B.R.K., Ryu, Y., Sachs, T., Sakabe, A., Sanchez, C.R., Schuur, E.A., Schäfer, K.V.R., Sonnentag, O., Sparks, J.P., Stuart-Haëntjens, E., Sturtevant, C., Sullivan, R.C., Szutu, D.J., Thom, J.E., Torn, M.S., Tuittila, E.S., Turner, J., Ueyama, M., Valach, A.C., Vargas, R., Varlagin, A., Vazquez-Lule, A., Verfaillie, J.G., Vesala, T., Vourlitis, G.L., Ward, E.J., Wille, C., Wohlfahrt, G., Wong, G.X., Zhang, Z., Zona, D., Windham-Myers, L., Poulter, B., Jackson, R.B., 2021. FLUXNET-CH_4: a global, multi-ecosystem dataset and analysis of methane seasonality from freshwater wetlands. Earth System Science Data 13, 3607–3689. doi:`10.5194/essd-13-3607-2021`.

Dienst, M., Schmieder, K., Ostendorp, W., 2004. Dynamik der Schilfröhrichte am Bodensee unter dem Einfluss von Wasserstandsvariationen (Effects of water level variations on the dynamics of the reed belts of Lake Constance). Limnologica 34, 29–36. doi:`10.1016/S0075-9511(04)80019-7`.

van Diggelen, R., Middleton, B., Bakker, J., Grootjans, A., Wassen, M., 2006. Fens and floodplains of the temperate zone: Present status, threats, conservation and restoration. Applied Vegetation Science 9, 157–162. doi:`10.1111/j.1654-109X.2006.tb00664.x`.

DIN, 2009. DIN EN ISO 10304-1:2009-07. Water quality - Determination of dissolved anions by liquid chromatography of ions - Part 1: Determination of bromide, chloride, fluoride, nitrate, nitrite, phosphate and sulfate (ISO 10304-1:2007); German version EN ISO 10304-1:2009. doi:`10.31030/1518948`.

DIN, 2019. DIN EN 1484:2019-04. Water analysis - Guidelines for the determination of total organic carbon (TOC) and dissolved organic carbon (DOC); German version EN 1484:1997. doi:`10.31030/3042067`.

Dinka, M., Ágoston-Szabó, E., Szeglet, P., 2010. Comparison between biomass and C, N, P, S contents of vigorous and die-back reed stands of Lake Fertő/Neusiedler See. Biologia 65. doi:`10.2478/s11756-010-0006-x`.

DJI, 2023. Mavic 2 Technische Daten. URL: `https://www.dji.com/at/mavic-2/info`.

Dowle, M., Srinivasan, A., 2023. data.table: Extension of ‘data.frame‘. R package version 1.14.8. doi:`10.32614/CRAN.package.data.table`.

Draganits, E., Weißl, M., Zámolyi, A., Doneus, M., 2022. Lake Neusiedl Area: A Particular Lakescape at the Boundary Between Alps and Pannonian Basin, in: Embleton-Hamann, C. (Ed.), Landscapes and Landforms of Austria. Springer, Cham. World Geomorphological Landscapes, pp. 207–222. doi:`10.1007/978-3-030-92815-5_13`.

Duan, X., Wang, X., Ouyang, Z., 2006. Plant-mediated CH_4 emission from a Phragmites-dominated wetland in an arid region, China. Journal of Freshwater Ecology 21, 139–145. doi:`10.1080/02705060.2006.9664106`.

Dvorak, M., Grüll, A., Ranner, A., Laber, J., Berg, H.M., Pellinger, A., Hadarics, T., Kohler, B., 2024. Die Vogelwelt des Neusiedler See-Gebietes. 1st ed., Verlag Naturhistorisches Museum Wien, Vienna.

Díaz-Delgado, R., Cazacu, C., Adamescu, M., 2019. Rapid assessment of ecological integrity for LTER wetland sites by using UAV multispectral mapping. Drones 3, 3. doi:`10.3390/drones3010003`.

Egger, M., Lenstra, W., Jong, D., Meysman, F.J., Sapart, C.J., Van Der Veen, C., Röckmann, T., Gonzalez, S., Slomp, C.P., 2016. Rapid sediment accumulation results in high methane effluxes from coastal sediments. PLoS ONE 11, 1–22. doi:`10.1371/journal.pone.0161609`.

Eitzinger, J., Kubu, G., Formayer, H., Haas, P., Gerersdorfer, T., Kromp-Kolb, H., 2009. Auswirkungen einer Klimaänderung auf den Wasserhaushalt des Neusiedlersees. Endbericht im Auftrag der Burgenländischen Landesregierung vom 15. Juli 2005. BOKU-Met Report, 1. URL: `https://meteo.boku.ac.at/report`.

Eller, F., Brix, H., 2012. Different genotypes of *Phragmites australis* show distinct phenotypic plasticity in response to nutrient availability and temperature. Aquatic botany 103, 89–97. doi:`10.1016/j.aquabot.2012.07.001`.

Eller, F., Lambertini, C., Nguyen, L.X., Brix, H., 2014. Increased invasive potential of non-native *Phragmites australis*: elevated CO_2 and temperature alleviate salinity effects on photosynthesis and growth. Global Change Biology 20, 531–543. doi:`10.1111/gcb.12346`.

Eller, F., Skálová, H., Caplan, J.S., Bhattarai, G.P., Burger, M.K., Cronin, J.T., Guo, W.Y., Guo, X., Hazelton, E.L.G., Kettenring, K.M., Lambertini, C., McCormick, M.K., Meyerson, L.A., Mozdzer, T.J., Pyšek, P., Sorrell, B.K., Whigham, D.F., Brix, H., 2017. Cosmopolitan species as models for ecophysiological responses to global change: The common reed *Phragmites australis*. Frontiers in Plant Science 8, 1833. doi:`10.3389/fpls.2017.01833`.

Encinas Fernández, J., Peeters, F., Hofmann, H., 2016. On the methane paradox: Transport from shallow water zones rather than in situ methanogenesis is the major source of CH_4 in the open surface water of lakes. Journal of Geophysical Research: Biogeosciences 121, 2717–2726. doi:`10.1002/2016JG003586`.

ESRI, 2022a. ArcGIS API for Python - arcgis.learn module. URL: `https://developers.arcgis.com/python/api-reference/arcgis.learn.toc.html#deeplab`.

ESRI, 2022b. ArcGIS Pro. Version 3.0.3. Redlands.

ESRI, 2022c. Deep Learning Libraries for ArcGIS Pro 3.0.3. URL: `https://github.com/Esri/deep-learning-frameworks.git`.

Filippa, G., Cremonese, E., Migliavacca, M., Galvagno, M., Folker, M., Richardson, A.D., Tomelleri, E., 2020. Package 'phenopix': process digital images of a vegetation cover. R package version 2.4.2. doi:`10.32614/CRAN.package.phenopix`.

Filippa, G., Cremonese, E., Migliavacca, M., Galvagno, M., Forkel, M., Wingate, L., Tomelleri, E., Di Morra Cella, U., Richardson, A.D., 2016. Phenopix: a R package for image-based vegetation phenology. Agricultural and Forest Meteorology 220, 141–150. doi:`10.1016/j.agrformet.2016.01.006`.

Finkelstein, P.L., Sims, P.F., 2001. Sampling error in eddy correlation flux measurements. Journal of Geophysical Research: Biogeosciences 106, 3503–3509. doi:`10.1029/2000JD900731`.

Fisher, R.E., France, J.L., Lowry, D., Lanoisellé, M., Brownlow, R., Pyle, J.A., Cain, M., Warwick, N., Skiba, U.M., Drewer, J., Dinsmore, K.J., Leeson, S.R., Bauguitte, S.J.B., Wellpott, A., O'Shea, S.J., Allen, G., Gallagher, M.W., Pitt, J., Percival, C.J., Bower, K., George, C., Hayman, G.D., Aalto, T., Lohila, A., Aurela, M., Laurila, T., Crill, P.M., McCalley, C.K., Nisbet, E.G., 2017. Measurement of the ^{13}C isotopic signature of methane emissions from northern European wetlands. Global Biogeochemical Cycles 31, 605–623. doi:`10.1002/2016GB005504`.

Fluet-Chouinard, E., Lehner, B., Rebelo, L.M., Papa, F., Hamilton, S.K., 2015. Development of a global inundation map at high spatial resolution from topographic downscaling of coarse-scale remote sensing data. Remote Sensing of Environment 158, 348–361. doi:`10.1016/j.rse.2014.10.015`.

Fluet-Chouinard, E., Stocker, B.D., Zhang, Z., Malhotra, A., Melton, J.R., Poulter, B., Kaplan, J.O., Goldewijk, K.K., Siebert, S., Minayeva, T., Hugelius, G., Joosten, H., Barthelmes, A., Prigent, C., Aires, F., Hoyt, A.M., Davidson, N., Finlayson, C.M., Lehner, B., Jackson, R.B., McIntyre, P.B., 2023. Extensive global wetland loss over the past three centuries. Nature 614, 281–286. doi:`10.1038/s41586-022-05572-6`.

Flury, S., McGinnis, D.F., Gessner, M.O., 2010. Methane emissions from a freshwater marsh in response to experimentally simulated global warming and nitrogen enrichment. Journal of Geophysical Research 115. doi:`10.1029/2009JG001079`.

Foken, T., Göockede, M., Mauder, M., Mahrt, L., Amiro, B., Munger, W., 2004. Post-field data quality control, in: Lee, X., Massman, W., Law, B. (Eds.), Handbook of micrometeorology. Kluwer Academic Publishers, Dordrecht. Atmospheric and Oceanographic Sciences Library, pp. 181–208. doi:`10.1007/1-4020-2265-4_9`.

Foken, T., Leuning, R., Oncley, S.R., Mauder, M., Aubinet, M., 2012. Corrections and data quality control, in: Aubinet, M., Vesala, T., Papale, D. (Eds.), Eddy covariance. Springer, Dordrecht and Heidelberg. Springer Atmospheric Sciences, pp. 85–131. doi:`10.1007/978-94-007-2351-1_4`.

France, J.L., Fisher, R.E., Lowry, D., Allen, G., Andrade, M.F., Bauguitte, S.J.B., Bower, K., Broderick, T.J., Daly, M.C., Forster, G., Gondwe, M., Helfter, C., Hoyt, A.M., Jones, A.E., Lanoisellé, M., Moreno, I., Nisbet-Jones, P.B.R., Oram, D., Pasternak, D., Pitt, J.R., Skiba, U., Stephens, M., Wilde, S.E., Nisbet, E.G., 2022. δ^{13}C methane source signatures from tropical wetland and rice field emissions. Philosophical transactions. Series A, Mathematical, physical, and engineering sciences 380, 20200449. doi:`10.1098/rsta.2020.0449`.

Fratini, G., Ibrom, A., Arriga, N., Burba, G., Papale, D., 2012. Relative humidity effects on water vapour fluxes measured with closed-path eddy-covariance systems with short sampling lines. Agricultural and Forest Meteorology 165, 53–63. doi:`10.1016/j.agrformet.2012.05.018`.

Friedman, J., Alm, E.J., 2012. Inferring correlation networks from genomic survey data. PLoS Computational Biology 8, 1–11. doi:`10.1371/journal.pcbi.1002687`.

Fukarek, F., Henker, H., Berg, C., 2006. Flora von Mecklenburg-Vorpommern: Farn-und Blütenpflanzen. Weissdorn, Jena.

Gagolewski, M., 2022. stringi: fast and portable character string processing in R. Journal of statistical software 103. doi:`10.18637/jss.v103.i02`.

Galushko, A., Kuever, J., 2019. Desulfatiglans, in: Trujillo, M.E., Dedysh, S., DeVos, P., Hedlund, B., Kämpfer, P., Rainey, F.A., Whitman, W.B. (Eds.), Bergey's Manual of Systematics of Archaea and Bacteria. Wiley, pp. 1–4. doi:`10.1002/9781118960608.gbm01679`.

Gao, Y., Chen, J., Zhang, T., Zhao, B., McNulty, S., Guo, H., Zhao, F., Zhuang, P., 2021. Lateral detrital C transfer across a *Spartina alterniflora* invaded estuarine wetland. Ecological Processes 10, 70. doi:`10.1186/s13717-021-00340-2`.

Garcia, J.L., Ollivier, B., Whitman, W.B., 2006. The Order Methanomicrobiales, in: Dworkin, M., Falkow, S., Rosenberg, E., Schleifer, K.H., Stackebrandt, E. (Eds.), The Prokaryotes. Springer, New York, pp. 208–230. doi:`10.1007/0-387-30743-5_10`.

Gardener, W.H., 1986. Chapter 21: Water content, in: Klute, A. (Ed.), Methods of soil analysis. Part 1, Physical and mineralogical methods. American Society of Agronomy, Inc. Soil Science Society of America, Inc., Madison. SSSA Book Series, pp. 493–544. doi:`10.2136/sssabookser5.1.2ed.c21`.

Gardolinski, P.C., Hanrahan, G., Achterberg, E.P., Gledhill, M., Tappin, A.D., House, W.A., Worsfold, P.J., 2001. Comparison of sample storage protocols for the determination of nutrients in natural waters. Water Research 35, 3670–3678. doi:`10.1016/S0043-1354(01)00088-4`.

GBIF.org, 2025. GIBF Occurrence Download (12 March 2025), *Phragmites australis* (Cav.) Trin. ex Steud. [Data set]. doi:`10.15468/dl.422tn3`.

GeoData Bgld, 2024. Orthophoto 7930-58 from flight date 2022-07-03 [Data set]. Amt der Burgenländischen Landesregierung, Abt.2/Referat GIS Koordination, Eisenstadt. URL: `https://geodaten.bgld.gv.at/de/downloads/hoehenmodelle-orthofotos.html`.

Goltermann, H.L. (Ed.), 1969. Methods for Chemical Analysis of Fresh Waters. volume 8 of *IBP-Handbook*. Blackwell Scientific Publications, Oxford, Edinburgh.

Golub, M., Koupaei-Abyazani, N., Vesala, T., Mammarella, I., Ojala, A., Bohrer, G., Weyhenmeyer, G., Blanken, P.D., Eugster, W., Koebsch, F., Chen, J., Czajkowski, K., Deshmukh, C., Guérin, F., Heiskanen, J., Humphreys, E.R., Jonsson, A., Karlsson, J., Kling, G., Lee, X., Liu, H., Lohila, A., Lundin, E., Morin, T., Podgrajsek, E., Provenzale, M., Rutgersson, A., Sachs, T., Sahlée, E., Serça, D., Shao, C., Spence, C., Strachan, I.B., Xiao, W., Desai, A.R., 2023. Diel, seasonal, and inter-annual variation in carbon dioxide effluxes from lakes and reservoirs. Environmental Research Letters 18, 034046. doi:`10.1088/1748-9326/acb834`.

de Groot, D., Brander, L., Finlayson, C.M., 2018. Wetland ecosystem services, in: Finlayson, C.M., Milton, G.R., Prentice, R.C., Davidson, N.C. (Eds.), The Wetland Book. Springer, Dordrecht, pp. 323–333. doi:`10.1007/978-90-481-9659-3_66`.

Gunatilaka, A., 1986. Nährstoffkreisläufe im Schilfgürtel des Neusiedler Sees: Auswirkungen des Grünschnittes. Wasserwirtschaftliche Arbeiten aus dem Burgenland 72, 223–310. URL: `https://www.zobodat.at/pdf/Wiss-Arbeiten-Burgenland_072_0223-0310.pdf`.

Gupta, H.V., Kling, H., Yilmaz, K.K., Martinez, G.F., 2009. Decomposition of the mean squared error and NSE performance criteria: Implications for improving hydrological modelling. Journal of hydrology 377, 80–91. doi:`10.1016/j.jhydrol.2009.08.003`.

Hackl, P., Ledolter, J., 2023. A statistical analysis of the water levels at Lake Neusiedl. Austrian Journal of Statistics 52, 87–100. doi:`10.17713/ajs.v52i1.1444`.

Hammer, U.T., 1986. Saline lake ecosystems of the world. volume 59 of *Monographiae Biologicae*. Junk, Dordrecht [et al.].

Han, G., Yang, L., Yu, J., Wang, G., Mao, P., Gao, Y., 2013. Environmental controls on net ecosystem CO_2 exchange over a reed (*Phragmites australis*) wetland in the Yellow River delta, China. Estuaries and Coasts 36, 401–413. doi:`10.1007/s12237-012-9572-1`.

Hansen, D.L., Lambertini, C., Jampeetong, A., Brix, H., 2007. Clone-specific differences in *Phragmites australis*: Effects of ploidy level and geographic origin. Aquatic Botany 86, 269–279. doi:`10.1016/j.aquabot.2006.11.005`.

Happell, J.D., Chanton, J.P., Showers, W.S., 1994. The influence of methane oxidation on the stable isotopic composition of methane emitted from florida swamp forests. Geochimica et cosmochimica acta 58, 4377–4388. doi:`10.1016/0016-7037(94)90341-7`.

Haroon, M.F., Hu, S., Shi, Y., Imelfort, M., Keller, J., Hugenholtz, P., Yuan, Z., Tyson, G.W., 2013. Anaerobic oxidation of methane coupled to nitrate reduction in a novel archaeal lineage. Nature 500, 567–570. doi:`10.1038/nature12375`.

Haslam, S.M., 2010. A book of reed (*Phragmites australis* (Cav.) Trin. ex Steudel, Phragmites communis Trin.). Forrest Text, Cardigan.

Hattori, S., 2008. Syntrophic Acetate-Oxidizing Microbes in Methanogenic Environments. Microbes and Environments 23, 118–127. doi:`10.1264/jsme2.23.118`.

Hayal, D., Brook, L., Aramde, F., 2012. Aspects of climate change and its associated impacts on wetland ecosystem functions - a review. Journal of American Science 8, 582–596. doi:`10.7537/marsjas081012.81`.

HD Bgld, 2023a. Data from measurement station 122010 and 210179 (Biologische Station Illmitz / Neusiedler See) [Data set]. Amt der Burgenländischen Landesregierung, Abt.5/Baudirektion, Eisenstadt.

HD Bgld, 2023b. Ground water data from measurement station 305854 (Illmitz, Br 16) [Data set]. Amt der Burgenländischen Landesregierung, Abt.5/Baudirektion, Eisenstadt.

HD Bgld, 2023c. Wasserportal Burgenland: Niederschlag: Illmitz - Biologische Station. Amt der Burgenländischen Landesregierung, Abt.5/Baudirektion, Eisenstadt. URL: `https://wasser.bgld.gv.at/hydrographie/der-niederschlag/illmitz-biologische-station`.

HD Bgld, 2023d. Wasserportal Burgenland: The weir in Mexikopußta - discharge data. Amt der Burgenländischen Landesregierung, Abt.5/Baudirektion, Eisenstadt. URL: `https://wasser.bgld.gv.at/hydrographie/der-neusiedler-see/webcam-wehr`.

Heiskanen, L., Tuovinen, J.P., Vekuri, H., Räsänen, A., Virtanen, T., Juutinen, S., Lohila, A., Mikola, J., Aurela, M., 2023. Meteorological responses of carbon dioxide and methane fluxes in the terrestrial and aquatic ecosystems of a subarctic landscape. Biogeosciences 20, 545–572. doi:`10.5194/bg-20-545-2023`.

Helfter, C., Gondwe, M., Murray-Hudson, M., Makati, A., Skiba, U., 2022. From sink to source: high inter-annual variability in the carbon budget of a Southern African wetland. Philosophical transactions. Series A, Mathematical, physical, and engineering sciences 380, 20210148. doi:`10.1098/rsta.2021.0148`.

Henneberg, A., Sorrell, B.K., Brix, H., 2012. Internal methane transport through juncus effusus: experimental manipulation of morphological barriers to test above- and below-ground diffusion limitation. New Phytologist 196, 799–806. doi:`10.1111/j.1469-8137.2012.04303.x`.

Hepp, G., 2022. DTSg: A Class for Working with Time Series Based on 'data.table' and 'R6' with Largely Optional Reference Semantics. R package version 1.1.1. doi:`10.32614/CRAN.package.DTSg`.

Higgisson, W., Cobb, A., Tschierschke, A., Dyer, F., 2021. Estimating the cover of *phragmites australis* using unmanned aerial vehicles and neural networks in a semi–arid wetland. River Research and Applications 37, 1312–1322. doi:`10.1002/rra.3832`.

Hilderbrand, R.H., Keller, S.R., Laperriere, S.M., Santoro, A.E., Cessna, J., Trott, R., 2020. Microbial communities can predict the ecological condition of headwater streams. PloS one 15, e0236932. doi:`10.1371/journal.pone.0236932`.

Hoehler, T.M., Alperin, M.J., Albert, D.B., Martens, C.S., 1994. Field and laboratory studies of methane oxidation in an anoxic marine sediment: Evidence for a methanogen–sulfate reducer consortium. Global Biogeochemical Cycles 8, 451–463. doi:`10.1029/94GB01800`.

Hoffmann, M., Schulz-Hanke, M., Garcia Alba, J., Jurisch, N., Hagemann, U., Sachs, T., Sommer, M., Augustin, J., 2017. A simple calculation algorithm to separate high-resolution CH_4 flux measurements into ebullition- and diffusion-derived components. Atmospheric Measurement Techniques 10, 109–118. doi:`10.5194/amt-10-109-2017`.

Holzer, P., 2024. Ökologische und biometrische Untersuchungen zu *Phragmites australis* am Neusiedler See. Master thesis. University of Vienna. Vienna. doi:`10.25365/thesis.75750`.

Hope, R.M., 2022. Rmisc: Ryan Miscellaneous. R package version 1.5.1. URL: `https://CRAN.R-project.org/package=Rmisc`.

Horne, A.J., Lessner, D.J., 2013. Assessment of the oxidant tolerance of *Methanosarcina acetivorans*. FEMS microbiology letters 343, 13–19. doi:`10.1111/1574-6968.12115`.

Horst, T.W., Lenschow, D.H., 2009. Attenuation of scalar fluxes measured with spatially-displaced sensors. Boundary-layer meteorology 130, 275–300. doi:`10.1007/s10546-008-9348-0`.

Huang, W.C., Liu, Y., Zhang, X., Zhang, C.J., Zou, D., Zheng, S., Xu, W., Luo, Z., Liu, F., Li, M., 2021. Comparative genomic analysis reveals metabolic flexibility of Woesearchaeota. Nature Communications 12, 1–14. doi:`10.1038/s41467-021-25565-9`.

Huang, Y., Chen, Z., Tian, B., Zhou, C., Wang, J., Ge, Z., Tang, J., 2020. Tidal effects on ecosystem CO_2 exchange in a *Phragmites* salt marsh of an intertidal shoal. Agricultural and Forest Meteorology 292-293, 108108. doi:`10.1016/j.agrformet.2020.108108`.

Hufkens, K., 2022. The MODISTools package: an interface to the MODIS Land Products Subsets Web Services. R package version 1.1.4. doi:`10.5281/zenodo.7551164`.

Hutchinson, G.L., Livingston, G.P., 1993. Use of chamber systems to measure trace gas fluxes, in: Harper, Lowry, A., Mosier, A.R., Duxbury, J.M., Rolston, D.E. (Eds.), Agricultural Ecosystem Effects on Trace Gases and Global Climate Change. American Society of Agronomy, Crop Science Society of America, Soil Science Society of America, Madison. volume 55, pp. 63–78. doi:`10.2134/asaspecpub55.c4`.

Hutchinson, G.L., Livingston, G.P., 2001. Vents and seals in non–steady–state chambers used for measuring gas exchange between soil and the atmosphere. European Journal of Soil Science 52, 675–682. doi:`10.1046/j.1365-2389.2001.00415.x`.

Ibrom, A., Dellwik, E., Larsen, S.E., Pilegaard, K., 2007. On the use of the Webb–Pearman–Leuning theory for closed-path eddy correlation measurements. Tellus B 59, 937–946. doi:`10.1111/j.1600-0889.2007.00311.x`.

IPCC, 2023. Climate Change 2021: The Physical Science Basis. Contribution of Working Group I to the Sixth Assessment Report of the Intergovernmental Panel on Climate Change. Cambridge University Press, Cambridge. doi:`10.1017/9781009157896`.

Irvin, J., Zhou, S., McNicol, G., Lu, F., Liu, V., Fluet-Chouinard, E., Ouyang, Z., Knox, S.H., Lucas-Moffat, A., Trotta, C., Papale, D., Vitale, D., Mammarella, I., Alekseychik, P., Aurela, M., Avati, A., Baldocchi, D., Bansal, S., Bohrer, G., Campbell, D.I., Chen, J., Chu, H., Dalmagro, H.J., Delwiche, K.B., Desai, A.R., Euskirchen, E., Feron, S., Goeckede, M., Heimann, M., Helbig, M., Helfter, C., Hemes, K.S., hirano, t., Iwata, H., Jurasinski, G., Kalhori, A., Kondrich, A., Lai, D.Y.F., Lohila, A., Malhotra, A., Merbold, L., Mitra, B., Ng, A., Nilsson, M.B., Noormets, A., Peichl, M., Rey-Sanchez, A.C., Richardson, A.D., Runkle, B.R.K., Schäfer, K.V.R., Sonnentag, O., Stuart-Haëntjens, E., Sturtevant, C., Ueyama, M., Valach, A.C., Vargas, R., Vourlitis, G.L., Ward, E.J., Wong, G.X., Zona, D., Alberto, M.C.R., Billesbach, D.P., Celis, G., Dolman, H., Friborg, T., Fuchs, K., Gogo, S., Gondwe, M.J., Goodrich, J.P., Gottschalk, P., Hörtnagl, L., Jacotot, A., Koebsch, F., Kasak, K., Maier, R., Morin, T.H., Nemitz, E., Oechel, W.C., Oikawa, P.Y., Ono, K., Sachs, T., Sakabe, A., Schuur, E.A., Shortt, R., Sullivan, R.C., Szutu, D.J., Tuittila, E.S., Varlagin, A., Verfaillie, J.G., Wille, C., Windham-Myers, L., Poulter, B., Jackson, R.B., 2021a. Gap-filling eddy covariance methane fluxes: Comparison of machine learning model predictions and uncertainties at FLUXNET-CH_4 wetlands. Agricultural and Forest Meteorology 308-309, 108528. doi:`10.1016/j.agrformet.2021.108528`.

Irvin, J., Zhou, Y., Lu, F., Liu, V., Zhou, S., McNicol, G., Liu, J., 2021b. FluxGapfill: A Python Interface for Machine-learning Driven Methane Gap-filling. Version 0.2.1. doi:`10.5281/zenodo.5515761`.

Jeffrey, L.C., Maher, D.T., Johnston, S.G., Maguire, K., Steven, A.D.L., Tait, D.R., 2019. Rhizosphere to the atmosphere: contrasting methane pathways, fluxes, and geochemical drivers across the terrestrial–aquatic wetland boundary. Biogeosciences 16, 1799–1815. doi:`10.5194/bg-16-1799-2019`.

Johnson, M.S., Matthews, E., Du, J., Genovese, V., Bastviken, D., 2022. Methane emission from global lakes: New spatiotemporal data and observation-driven modeling of methane dynamics indicates lower emissions. Journal of geophysical research. Biogeosciences 127, e2022JG006793. doi:`10.1029/2022JG006793`.

Jones, J., 1985. Microbes and microbial processes in sediments. Philosophical Transactions of the Royal Society of London. Series A, Mathematical and Physical Sciences 315, 3–17. doi:`10.1098/rsta.1985.0025`.

Joosten, H., Clarke, D., 2002. Wise use of mires and peatlands: Background and principles including a framework for decision-making. International Peat Society and International Mire Conservation Group, Jyväskylä and Greifswald.

Jørgensen, B.B., Kasten, S., 2006. Sulfur cycling and methane oxidation, in: Schulz, H.D., Zabel, M. (Eds.), Marine Geochemistry. Springer, Berlin, Heidelberg, pp. 271–309. doi:`10.1007/3-540-32144-6_8`.

Käki, T., Ojala, A., Kankaala, P., 2001. Diel variation in methane emissions from stands of *Phragmites australis* (Cav.) Trin. ex Steud. and Typha latifolia L. in a boreal lake. Aquatic botany 71, 259–271. doi:`10.1016/S0304-3770(01)00186-3`.

Kallasvuo, M., Lappalainen, A., Urho, L., 2011. Coastal reed belts as fish reproduction habitats. Boreal Environment Research 16, 1–14. URL: `https://jukuri.luke.fi/handle/10024/530546`.

Kallingal, J.T., Lindström, J., Miller, P.A., Rinne, J., Raivonen, M., Scholze, M., 2024. Optimising CH_4 simulations from the LPJ-GUESS model v4.1 using an adaptive Markov chain Monte Carlo algorithm. Geoscientific Model Development 17, 2299–2324. doi:`10.5194/gmd-17-2299-2024`.

Kandeler, E., Gerber, H., 1988. Short-term assay of soil urease activity using colorimetric determination of ammonium. Biology and fertility of Soils 6, 68–72. doi:`10.1007/BF00257924`.

Kankaala, P., Kaki, T., Makela, S., Ojala, A., Pajunen, H., Arvola, L., 2005. Methane efflux in relation to plant biomass and sediment characteristics in stands of three common emergent macrophytes in boreal mesoeutrophic lakes. Global Change Biology 11, 145–153. doi:`10.1111/j.1365-2486.2004.00888.x`.

Kankaala, P., Ojala, A., Käki, T., 2004. Temporal and spatial variation in methane emissions from a flooded transgression shore of a boreal lake. Biogeochemistry 68, 297–311. doi:`10.1023/B:BIOG.0000031030.77498.1f`.

Kassambara, A., 2023a. ggpubr: 'ggplot2' Based Publication Ready Plots. R package version 0.6.0. doi:`10.32614/CRAN.package.ggpubr`.

Kassambara, A., 2023b. rstatix: Pipe-Friendly Framework for Basic Statistical Tests. R package version 0.7.2. doi:`10.32614/CRAN.package.rstatix`.

Keddy, P.A., 2024. Wetland Ecology: Principles and Conservation. 3rd ed., Cambridge University Press, Cambridge, UK. doi:`10.1017/9781009288675`.

Keeling, C.D., 1958. The concentration and isotopic abundances of atmospheric carbon dioxide in rural areas. Geochimica et cosmochimica acta 13, 322–334. doi:`10.1016/0016-7037(58)90033-4`.

Kim, J., Verma, S.B., Billesbach, D.P., 1998a. Seasonal variation in methane emission from a temperate *Phragmites*–dominated marsh: effect of growth stage and plant–mediated transport. Global Change Biology 5, 433–440. doi:`10.1046/j.1365-2486.1999.00237.x`.

Kim, J., Verma, S.B., Billesbach, D.P., Clement, R.J., 1998b. Diel variation in methane emission from a midlatitude prairie wetland: significance of convective throughflow in *Phragmites australis*. Journal of Geophysical Research 103, 28029–28039. doi:`10.1029/98JD02441`.

King, G.M., 1984. Utilization of hydrogen, acetate, and "noncompetitive"; substrates by methanogenic bacteria in marine sediments. Geomicrobiology Journal 3, 275–306. doi:`10.1080/01490458409377807`.

King, G.M., 1992. Ecological aspects of methane oxidation, a key determinant of global methane dynamics, in: Marshall, K.C. (Ed.), Advances in Microbial Ecology. Springer, New York. volume 12 of *Advances in Microbial Ecology Series*, pp. 431–468. doi:`10.1007/978-1-4684-7609-5_9`.

Kiss, M., Torma, P., 2014. Flux-gradient based estimation of the turbulent energy flux of shallow lakes from eddy-covariance measurements: Sekély tavi energiaáramok fluxus gradiens eljárás alapú becslése örvény-kovariancia mérésekből. Hidrológiai Közlöny , 48–56URL: `https://www.researchgate.net/publication/303959666_Sekely_tavi_energiaaramok_fluxus_gradiens_eljaras_alapu_becslese_orveny-kovariancia_meresekbol`.

Kleint, J.F., Wellach, Y., Schroll, M., Keppler, F., Isenbeck-Schröter, M., 2021. The impact of seasonal sulfate–methane transition zones on methane cycling in a sulfate–enriched freshwater environment. Limnology and Oceanography 66, 2290–2308. doi:`10.1002/lno.11754`.

Klimkowska, A., Van Diggelen, R., Grootjans, A.P., Kotowski, W., 2010. Prospects for fen meadow restoration on severely degraded fens. Perspectives in Plant Ecology, Evolution and Systematics 12, 245–255. doi:`10.1016/j.ppees.2010.02.004`.

Kljun, N., Calanca, P., Rotach, M.W., Schmid, H.P., 2015. A simple two-dimensional parameterisation for flux footprint prediction (FFP). Geoscientific Model Development 8, 3695–3713. doi:`10.5194/gmd-8-3695-2015`.

Knox, S.H., Jackson, R.B., Poulter, B., McNicol, G., Fluet-Chouinard, E., Zhang, Z., Hugelius, G., Bousquet, P., Canadell, J.G., Saunois, M., Papale, D., Chu, H., Keenan, T.F., Baldocchi, D., Torn, M.S., Mammarella, I., Trotta, C., Aurela, M., Bohrer, G., Campbell, D.I., Cescatti, A., Chamberlain, S., Chen, J., Chen, W., Dengel, S., Desai, A.R., Euskirchen, E., Friborg, T., Gasbarra, D., Goded, I., Goeckede, M., Heimann, M., Helbig, M., hirano, t., Hollinger, D.Y., Iwata, H., Kang, M., Klatt, J., Krauss, K.W., Kutzbach, L., Lohila, A., Mitra, B., Morin, T.H., Nilsson, M.B., Niu, S., Noormets, A., Oechel, W.C., Peichl, M., Peltola, O., Reba, M.L., Richardson, A.D., Runkle, B.R.K., Ryu, Y., Sachs, T., Schäfer, K.V.R., Schmid, H.P., Shurpali, N., Sonnentag, O., Tang, A.C.I., Ueyama, M., Vargas, R., Vesala, T., Ward, E.J., Windham-Myers, L., Wohlfahrt, G., Zona, D., 2019. FLUXNET-CH_4 Synthesis Activity: Objectives, Observations, and Future Directions. Bulletin of the American Meteorological Society 100, 2607–2632. doi:`10.1175/BAMS-D-18-0268.1`.

Köbbing, J.F., Thevs, N., Zerbe, S., 2013. The utilisation of reed (*Phragmites australis*): a review. Mires and Peat 13, 1–14.

Koch, M., Koebsch, F., Hahn, J., Jurasinski, G., 2017. From meadow to shallow lake: Monitoring secondary succession in a coastal fen after rewetting by flooding based on aerial imagery and plot data. Mires and Peat 19, 1. doi:`10.19189/MaP.2015.OMB.188`.

Koebsch, F., Gottschalk, P., Beyer, F., Wille, C., Jurasinski, G., Sachs, T., 2020. The impact of occasional drought periods on vegetation spread and greenhouse gas exchange in rewetted fens. Philosophical transactions of the Royal Society of London. Series B, Biological sciences 375, 20190685. doi:`10.1098/rstb.2019.0685`.

Kowalska, N., Chojnicki, B.H., Rinne, J., Haapanala, S., Siedlecki, P., Urbaniak, M., Juszczak, R., Olejnik, J., 2013. Measurements of methane emission from a temperate wetland by the eddy covariance method. International Agrophysics 27, 283–290. doi:`10.2478/v10247-012-0096-5`.

Kroon, P.S., Hensen, A., van den Bulk, W.C.M., Jongejan, P.A.C., Vermeulen, A.T., 2008. The importance of reducing the systematic error due to non-linearity in N_2O flux measurements by static chambers. Nutrient Cycling in Agroecosystems 82, 175–186. doi:`10.1007/s10705-008-9179-x`.

Kubu, G., Krámer, T., Szilágyi, J., 2014. Kapitel 2.2. Hydrologie und Wasserwirtschaft, in: Wolfram, G., Déri, L., Zech, S. (Eds.), Strategiestudie Neusiedler See – Phase 1. Studie im Auftrag der Österreichisch-Ungarischen Gewässerkommission. Wien – Szombathely, pp. 10–24. URL: `https://wasser.bgld.gv.at/fileadmin/user_upload/Studien/Neusiedler_See/STRATEGY_STUDY_14-06-16_DE_-_final_END.pdf`.

Lal, R., 2008. Carbon sequestration. Philosophical transactions of the Royal Society of London. Series B, Biological sciences 363, 815–830. doi:`10.1098/rstb.2007.2185`.

Land Burgenland, 2017. UNESCO Welterbe Burgenland: Abgrenzung der Kern und Pufferzone zum Welterbegebiet Neusiedler See [Data set]. Amt der Burgenländischen Landesregierung, Abt.2/Hauptreferat Landesplanung, Eisenstadt. URL: `https://www.data.gv.at/katalog/de/dataset/unesco-welterbe-burgenland`.

Land Burgenland, 2022a. N2000 - Habitatrichtlinie Burgenland [Data set]. Amt der Burgenländischen Landesregierung, Abt.2/Referat GIS-Koordination, Eisenstadt. URL: `https://www.data.gv.at/katalog/de/dataset/n2000-habitatrichtlinie-burgenland`.

Land Burgenland, 2022b. N2000 - Vogelschutzrichtlinie Burgenland [Data set]. Abt.2/Referat GIS-Koordination, Eisenstadt. URL: `https://www.data.gv.at/katalog/de/dataset/n2000-vogelschutzrichtlinie-burgenland`.

Land Burgenland, 2022c. Ramsargebiet Burgenland [Data set]. Amt der Burgenländischen Landesregierung, Abt.2/Referat GIS-Koordination, Eisenstadt. URL: `https://www.data.gv.at/katalog/de/dataset/ramsargebiet-burgenland`.

Langenegger, T., Vachon, D., Donis, D., McGinnis, D.F., 2019. What the bubble knows: Lake methane dynamics revealed by sediment gas bubble composition. Limnology and Oceanography 64, 1526–1544. doi:`10.1002/lno.11133`.

Lee, M.J., Zinder, S.H., 1988. Isolation and characterization of a thermophilic bacterium which oxidizes acetate in syntrophic association with a methanogen and which grows acetogenically on H_2-CO_2. Applied and Environmental Microbiology 54, 124–129. doi:`10.1128/aem.54.1.124-129.1988`.

Lee, X., Massman, W., Law, B. (Eds.), 2004. Handbook of micrometeorology: A guide for surface flux measurement and analysis. volume 29 of *Atmospheric and Oceanographic Sciences Library*. Kluwer Academic Publishers, Dordrecht.

Legendre, P., 2018. lmodel2: model II regression. R package version 1.7-3. doi:`10.32614/CRAN.package.lmodel2`.

Lehner, B., Anand, M., Fluet-Chouinard, E., Tan, F., Aires, F., Allen, G.H., Bousquet, P., Canadell, J.G., Davidson, N., Ding, M., Finlayson, C.M., Gumbricht, T., Hilarides, L., Hugelius, G., Jackson, R.B., Korver, M.C., Liu, L., McIntyre, P.B., Nagy, S., Olefeldt, D., Pavelsky, T.M., Pekel, J.F., Poulter, B., Prigent, C., Wang, J., Worthington, T.A., Yamazaki, D., Zhang, X., Thieme, M., 2025. Mapping the world's inland surface waters: an upgrade to the Global Lakes and Wetlands Database (GLWD v2). Earth System Science Data 17, 2277–2329. doi:`10.5194/essd-17-2277-2025`.

Leisler, B., 1981. Die ökologische Einnischung der mitteleuropäischen Rohrsänger (*Acrocephalus*, Sylviinae). 1. Habitattrennung. Vogelwarte 31, 45–74. URL: `https://www.zobodat.at/pdf/Vogelwarte_31_1981_0045-0074.pdf`.

Leisler, B., Schulze-Hagen, K., 2011. The Reed Warblers. KNNV Publishing, Zeist. doi:`10.1163/9789004278028`.

Li, J., Jiang, M., Pei, J., Fang, C., Li, B., Nie, M., 2023. Convergence of carbon sink magnitude and water table depth in global wetlands. Ecology letters 26, 797–804. doi:`10.1111/ele.14199`.

Li, M., Peng, C., Zhu, Q., Zhou, X., Yang, G., Song, X., Zhang, K., 2020. The significant contribution of lake depth in regulating global lake diffusive methane emissions. Water research 172, 115465. doi:`10.1016/j.watres.2020.115465`.

Li, Y., Yang, J., Yu, M., Zhao, W., Xiao, Y., Di Zhou, Zhan, C., Yu, Y., Zhang, J., Lv, Z., Yu, J., 2019. Different effects of NaCl and Na_2SO_4 on the carbon mineralization of an estuarine wetland soil. Geoderma 344, 179–183. doi:`10.1016/j.geoderma.2019.02.035`.

Linkhorst, A., Hiller, C., DelSontro, T., M. Azevedo, G., Barros, N., Mendonça, R., Sobek, S., 2020. Comparing methane ebullition variability across space and time in a brazilian reservoir. Limnology and Oceanography 65, 1623–1634. doi:`10.1002/lno.11410`.

Lissner, J., Schierup, H.H., 1997. Effects of salinity on the growth of *Phragmites australis*. Aquatic Botany 55, 247–260. doi:`10.1016/S0304-3770(96)01085-6`.

Löffler, H., 1974. Der Neusiedlersee: Naturgeschichte eines Steppensees. 1st ed., Molden, Vienna.

Löffler, H. (Ed.), 1979. Neusiedlersee: the limnology of a shallow lake in Central Europe. volume 37 of *Monographiae Biologicae*. Springer, Dordrecht. doi:`10.1007/978-94-009-9168-2`.

Lovley, D.R., Dwyer, D.F., Klug, M.J., 1982. Kinetic analysiis of competition between sulfate reducers and methanogens for hydrogen in sediments. Applied and Environmental Microbiology 43, 1373–1379. doi:`10.1128/aem.43.6.1373-1379.1982`.

Lovley, D.R., Goodwin, S., 1988. Hydrogen concentrations as an indicator of the predominant terminal electron-accepting reactions in aquatic sediments. Geochimica et Cosmochimica Acta 52, 2993–3003. doi:`10.1016/0016-7037(88)90163-9`.

Lovley, D.R., Klug, M.J., 1983. Sulfate reducers can outcompete methanogens at freshwater sulfate concentrations. Applied and environmental microbiology 45, 187–192. doi:`10.1128/aem.45.1.187-192.1983`.

Lu, W., Xiao, J., Liu, F., Zhang, Y., Liu, C., Lin, G., 2017. Contrasting ecosystem CO_2 fluxes of inland and coastal wetlands: a meta-analysis of eddy covariance data. Global Change Biology 23, 1180–1198. doi:`10.1111/gcb.13424`.

Luo, M., Huang, J.F., Zhu, W.F., Tong, C., 2019. Impacts of increasing salinity and inundation on rates and pathways of organic carbon mineralization in tidal wetlands: a review. Hydrobiologia 827, 31–49. doi:`10.1007/s10750-017-3416-8`.

Lyu, Z., Lu, Y., 2018. Metabolic shift at the class level sheds light on adaptation of methanogens to oxidative environments. The ISME Journal 12, 411–423. doi:`10.1038/ismej.2017.173`.

Maes, S.L., Dietrich, J., Midolo, G., Schwieger, S., Kummu, M., Vandvik, V., Aerts, R., Althuizen, I.H.J., Biasi, C., Björk, R.G., Böhner, H., Carbognani, M., Chiari, G., Christiansen, C.T., Clemmensen, K.E., Cooper, E.J., Cornelissen, J.H.C., Elberling, B., Faubert, P., Fetcher, N., Forte, T.G.W., Gaudard, J., Gavazov, K., Guan, Z., Gudmundsson, J., Gya, R., Hallin, S., Hansen, B.B., Haugum, S.V., He, J.S., Hicks Pries, C., Hovenden, M.J., Jalava, M., Jónsdóttir, I.S., Juhanson, J., Jung, J.Y., Kaarlejärvi, E., Kwon, M.J., Lamprecht, R.E., Le Moullec, M., Lee, H., Marushchak, M.E., Michelsen, A., Munir, T.M., Myrsky, E.M., Nielsen, C.S., Nyberg, M., Olofsson, J., Óskarsson, H., Parker, T.C., Pedersen, E.P., Petit Bon, M., Petraglia, A., Raundrup, K., Ravn, N.M.R., Rinnan, R., Rodenhizer, H., Ryde, I., Schmidt, N.M., Schuur, E.A.G., Sjögersten, S., Stark, S., Strack, M., Tang, J., Tolvanen, A., Töpper, J.P., Väisänen, M.K., van Logtestijn, R.S.P., Voigt, C., Walz, J., Weedon, J.T., Yang, Y., Ylänne, H., Björkman, M.P., Sarneel, J.M., Dorrepaal, E., 2024. Environmental drivers of increased ecosystem respiration in a warming tundra. Nature 629, 105–113. doi:`10.1038/s41586-024-07274-7`.

Maier, M., Weber, T.K.D., Fiedler, J., Fuß, R., Glatzel, S., Huth, V., Jordan, S., Jurasinski, G., Kutzbach, L., Schäfer, K., Weymann, D., Hagemann, U., 2022. Introduction of a guideline for measurements of greenhouse gas fluxes from soils using non–steady–state chambers. Journal of Plant Nutrition and Soil Science 185, 447–461. doi:`10.1002/jpln.202200199`.

Malone, S.L., Staudhammer, C.L., Loescher, H.W., Olivas, P., Oberbauer, S.F., Ryan, M.G., Schedlbauer, J., Starr, G., 2014. Seasonal patterns in energy partitioning of two freshwater marsh ecosystems in the Florida Everglades. Journal of Geophysical Research: Biogeosciences 119, 1487–1505. doi:`10.1002/2014JG002700`.

Männistö, E., Korrensalo, A., Alekseychik, P., Mammarella, I., Peltola, O., Vesala, T., Tuittila, E.S., 2019. Multi-year methane ebullition measurements from water and bare peat surfaces of a patterned boreal bog. Biogeosciences 16, 2409–2421. doi:`10.5194/bg-16-2409-2019`.

Márkus, I., Király, G., 2012. A Fertő magyarországi nádasainak minősítése, osztályozása és térképezése (Qualification, classification and mapping of the reed stands of the Hungarian part of Lake Fertő), in: Monografikus tanulmányok a Fertő és a Hanság vidékéről (Monographic studies of Lake Fertő and Hanság area). Budapest, pp. 73–81. URL: `https://docplayer.hu/8473926-A-ferto-to-magyarorszagi-nadasainak-minositese-es-osztalyozasa-the-qualification-and-classification-of-the-reed-stands-at-lake-ferto.html`.

Martin, M., 2011. Cutadapt removes adapter sequences from high-throughput sequencing reads. EMBnet.journal 17, 10–12. doi:`10.14806/ej.17.1.200`.

Martin, R.M., Moseman-Valtierra, S., 2015. Greenhouse gas fluxes vary between *Phragmites australis* and native vegetation zones in coastal wetlands along a salinity gradient. Wetlands 35, 1021–1031. doi:`10.1007/s13157-015-0690-y`.

Mauder, M., Cuntz, M., Drüe, C., Graf, A., Rebmann, C., Schmid, H.P., Schmidt, M., Steinbrecher, R., 2013. A strategy for quality and uncertainty assessment of long-term eddy-covariance measurements. Agricultural and Forest Meteorology 169, 122–135. doi:`10.1016/j.agrformet.2012.09.006`.

Mauder, M., Foken, T., 2015. Documentation and instruction manual of the eddy-covariance software package TK3 (update). Universität Bayreuth, Abt. Mikrometeorologie, Arbeitsergebnisse Nr. 62, Bayreuth. URL: `https://epub.uni-bayreuth.de/id/eprint/2130/1/ARBERG062.pdf`.

Mauder, M., Foken, T., Cuxart, J., 2020. Surface-energy-balance closure over land: A review. Boundary-Layer Meteorology 177, 395–426. doi:`10.1007/s10546-020-00529-6`.

McClure, R.P., Lofton, M.E., Chen, S., Krueger, K.M., Little, J.C., Carey, C.C., 2020. The magnitude and drivers of methane ebullition and diffusion vary on a longitudinal gradient in a small freshwater reservoir. Journal of Geophysical Research: Biogeosciences 125, e2019JG005205. doi:`10.1029/2019JG005205`.

Megonigal, J.P., Hines, M.E., Visscher, P.T., 2003. Anaerobic metabolism: Linkages to trace gases and aerobic processes, in: Holland, H.D., Turekian, K.K. (Eds.), Treatise on Geochemistry. Elsevier Pergamon, Oxford. volume 8 of *Biogeochemistry (edited by Schlesinger, W. H.)*, pp. 317–424. doi:`10.1016/B0-08-043751-6/08132-9`.

Meneses, N.C., Baier, S., Reidelstürz, P., Geist, J., Schneider, T., 2018a. Modelling heights of sparse aquatic reed (*Phragmites australis*) using structure from motion point clouds derived from rotary- and fixed-wing unmanned aerial vehicle (UAV) data. Limnologica 72, 10–21. doi:`10.1016/j.limno.2018.07.001`.

Meneses, N.C., Brunner, F., Baier, S., Geist, J., Schneider, T., 2018b. Quantification of extent, density, and status of aquatic reed beds using point clouds derived from UAV–RGB imagery. Remote Sensing 10, 1869. doi:`10.3390/rs10121869`.

Messager, M.L., Lehner, B., Grill, G., Nedeva, I., Schmitt, O., 2016. Estimating the volume and age of water stored in global lakes using a geo-statistical approach. Nature communications 7, 13603. doi:`10.1038/ncomms13603`.

Middleton, B.A., Kleinebecker, T., 2012. The effects of climate-change-induced drought and freshwater wetlands, in: Middleton, B. (Ed.), Global change and the function and distribution of wetlands. Springer, Dordrecht. volume 1 of *Global change ecology and wetlands*, pp. 117–147. doi:`10.1007/978-94-007-4494-3_4`.

Millennium Ecosystem Assessment, 2005. Ecosystems and human well-being: Synthesis. Island Press, Washington, DC. URL: `https://www.millenniumassessment.org/documents/document.356.aspx.pdf`.

Miller, B.L., Holtgrieve, G.W., Arias, M.E., Uy, S., Chheng, P., 2022. Coupled CH_4 production and oxidation support CO_2 supersaturation in a tropical flood pulse lake

(Tonle Sap Lake, Cambodia). Proceedings of the National Academy of Sciences of the United States of America 119. doi:`10.1073/pnas.2107667119`.

Minke, M., Augustin, J., Burlo, A., Yarmashuk, T., Chuvashova, H., Thiele, A., Freibauer, A., Tikhonov, V., Hoffmann, M., 2016. Water level, vegetation composition, and plant productivity explain greenhouse gas fluxes in temperate cutover fens after inundation. Biogeosciences 13, 3945–3970. doi:`10.5194/bg-13-3945-2016`.

Miranda, K.M., Espey, M.G., Wink, D.A., 2001. A rapid, simple spectrophotometric method for simultaneous detection of nitrate and nitrite. Nitric oxide 5, 62–71. doi:`10.1006/niox.2000.0319`.

Mirtl, M., Bahn, M., Battin, T., Borsdorf, A., Dirnböck, T., Englisch, M., Erschbamer, B., Fuchsberger, J., Gaube, V., Grabherr, G., Gratzer, G., Haberl, H., Klug, H., Kreiner, D., Mayer, R., Peterseil, J., Richter, A., Schindler, S., Stocker-Kiss, A., Tappeiner, U., Weisse, T., Winiwarter, V., Wohlfahrt, G., Zink, R., 2015. Research for the Future – LTER-Austria White Paper 2015 – On the status and orientation of process oriented ecosystem research, biodiversity and conservation research and socio-ecological research in Austria. LTER-Austria Series, Vol.2, Vienna. URL: `https://www.lter-austria.at/wp_lter/wp-content/uploads/2015/03/LTER_Austria_WhitePaper_2015_en.pdf`.

Mitsch, W.J., Bernal, B., Hernandez, M.E., 2015. Ecosystem services of wetlands. International Journal of Biodiversity Science, Ecosystem Services & Management 11, 1–4. doi:`10.1080/21513732.2015.1006250`.

Mitsch, W.J., Bernal, B., Nahlik, A.M., Mander, Ü., Zhang, L., Anderson, C.J., Jørgensen, S.E., Brix, H., 2013. Wetlands, carbon, and climate change. Landscape Ecology 28, 583–597. doi:`10.1007/s10980-012-9758-8`.

Mitsch, W.J., Gosselink, J.G., 2015. Wetlands. 5th ed., John Wiley and Sons Inc, Hoboken NJ.

Moncrieff, J., Clement, R., Finnigan, J., Meyers, T., 2005. Averaging, detrending, and filtering of eddy covariance time series, in: Lee, X., Law, B., Massman, W. (Eds.), Handbook of Micrometeorology. Springer, Dordrecht. volume 29 of *Atmospheric and Oceanographic Sciences Library*, pp. 7–31. doi:`10.1007/1-4020-2265-4_2`.

Morin, T.H., Riley, W.J., Grant, R.F., Mekonnen, Z., Stefanik, K.C., Sanchez, A.C.R., Mulhare, M.A., Villa, J., Wrighton, K., Bohrer, G., 2022. Water level changes in Lake Erie drive 21st century CO_2 and CH_4 fluxes from a coastal temperate wetland. Science of the Total Environment 821, 153087. doi:`10.1016/j.scitotenv.2022.153087`.

Moshiri, G.A., 1993. Constructed Wetlands for Water Quality Improvement. 1st ed., CRC Press, Boca Raton. doi:`10.1201/9781003069997`.

Müller, K., 2023. hms: pretty time of day. R package version 1.1.3. doi:`10.32614/CRAN.package.hms`.

Murphy, J., Riley, J.P., 1962. A modified single solution method for the determination of phosphate in natural waters. Analytica chimica acta 27, 31–36. doi:`10.1016/S0003-2670(00)88444-5`.

Muyzer, G., Stams, A.J., 2008. The ecology and biotechnology of sulphate-reducing bacteria. Nature Reviews Microbiology 6, 441–454. doi:`10.1038/nrmicro1892`.

Nakai, T., Shimoyama, K., 2012. Ultrasonic anemometer angle of attack errors under turbulent conditions. Agricultural and Forest Meteorology 162-163, 14–26. doi:`10.1016/j.agrformet.2012.04.004`.

Nationalparks Austria, 2017. Grenzlayer Nationalpark Neusiedler See - Seewinkel [Data set]. NP Neusiedler See - Seewinkel. URL: `https://www.data.gv.at/katalog/de/dataset/nationalparks-austria_grenzlayer-nationalpark-neusiedler-see-seewinkel`.

Nechwatal, J., Wielgoss, A., Mendgen, K., 2008. Flooding events and rising water temperatures increase the significance of the reed pathogen *Pythium phragmitis* as a contributing factor in the decline of *Phragmites australis*. Hydrobiologia 613, 109–115. doi:`10.1007/s10750-008-9476-z`.

Nemeth, E., Dvorak, M., 2022. Reed die-back and conservation of small reed birds at Lake Neusiedl, Austria. Journal of Ornithology 163, 683–693. doi:`10.1007/s10336-022-01961-w`.

Nemeth, E., Dvorak, M., Glaser, F., Kohler, B., Schwienbacher, M., 2022. Entwicklung nachhaltiger Schilfernttetechniken und Monitoring Schilfgürtel Neusiedler See. Projektendbericht an das Amt der Burgenländischen Landesregierung Abt. 4, Hauptreferat Naturschutz und Landschaftspflege, Eisenstadt. URL: `https://www.parcs.at/npns/pdf_public/2023/50627_20230626_144215_2022_Nemeth_etal_Schilfmanagement_NeusiedlerSee_Final.pdf`.

Nemeth, E., Dvorak, M., Knoll, T., Kohler, B., Mühlbacher, S., Werba, F., 2014. Managementplan für den Neusiedler See als Teil des Europaschutzgebiets Neusiedler See - Nordöstliches Leithagebirge. Studie im Auftrag des Vereins BERTA. BirdLife Österreich, Vienna, 245 p. URL: `https://www.burgenland.at/fileadmin/user_upload/Natura2000_MP__NeusiedlerSee_web.pdf`.

Nestroy, O., Aust, G., Blum, W., Englisch, M., Hager, H., Herzberger, E., Kilian, W., Nelhiebel, P., Ortner, G., Pecina, E., Pehamberger, A., Schneider, W., Wagner, J., 2011. Systematische Gliederung der Böden Österreichs: Österreichische Bodensystematik 2000 in der revidierten Fassung von 2011. Mitteilungen der Österreichischen Bodenkundlichen Gesellschaft, Wien. URL: `https://www.bodensystematik.de/OEBG-Systematik.pdf`.

Neubauer, S.C., Megonigal, J.P., 2015. Moving beyond global warming potentials to quantify the climatic role of ecosystems. Ecosystems 18, 1000–1013. doi:`10.1007/s10021-015-9879-4`.

Ostendorp, W., 1989. ‘Die-back’ of reeds in Europe — a critical review of literature. Aquatic Botany 35, 5–26. doi:`10.1016/0304-3770(89)90063-6`.

Pangala, S.R., Hornibrook, E.R.C., Gowing, D.J., Gauci, V., 2015. The contribution of trees to ecosystem methane emissions in a temperate forested wetland. Global Change Biology 21, 2642–2654. doi:`10.1111/gcb.12891`.

Papale, D., Reichstein, M., Aubinet, M., Canfora, E., Bernhofer, C., Kutsch, W., Longdoz, B., Rambal, S., Valentini, R., Vesala, T., Yakir, D., 2006. Towards a standardized processing of net ecosystem exchange measured with eddy covariance technique: algorithms and uncertainty estimation. Biogeosciences 3, 571–583. doi:`10.5194/bg-3-571-2006`.

Pashaei, M., Kamangir, H., Starek, M.J., Tissot, P., 2020. Review and Evaluation of Deep Learning Architectures for Efficient Land Cover Mapping with UAS Hyper-Spatial Imagery: A Case Study Over a Wetland. Remote Sensing 12, 959. doi:`10.3390/rs12060959`.

Pataki, D.E., Ehleringer, J.R., Flanagan, L.B., Yakir, D., Bowling, D.R., Still, C.J., Buchmann, N., Kaplan, J.O., Berry, J.A., 2003. The application and interpretation of keeling plots in terrestrial carbon cycle research. Global Biogeochemical Cycles 17, 1022. doi:`10.1029/2001GB001850`.

Patil, I., 2021. Visualizations with statistical details: The ’ggstatsplot’ approach. Journal of Open Source Software 6, 3167. doi:`10.21105/joss.03167`.

Peeters, F., Encinas Fernandez, J., Hofmann, H., 2019. Sediment fluxes rather than oxic methanogenesis explain diffusive CH_4 emissions from lakes and reservoirs. Scientific reports 9, 243. doi:`10.1038/s41598-018-36530-w`.

Philipp, K., Juang, J.Y., Deventer, M.J., Klemm, O., 2017. Methane emissions from a subtropical grass marshland, northern Taiwan. Wetlands 37, 1145–1157. doi:`10.1007/s13157-017-0947-8`.

Pi, X., Luo, Q., Feng, L., Xu, Y., Tang, J., Liang, X., Ma, E., Cheng, R., Fensholt, R., Brandt, M., Cai, X., Gibson, L., Liu, J., Zheng, C., Li, W., Bryan, B.A., 2022. Mapping global lake dynamics reveals the emerging roles of small lakes. Nature communications 13, 5777. doi:`10.1038/s41467-022-33239-3`.

Pix4D, 2023. Documentation. URL: `https://support.pix4d.com/hc/general#main-content`.

Poffenbarger, H.J., Needelman, B.A., Megonigal, J.P., 2011. Salinity influence on methane emissions from tidal marshes. Wetlands 31, 831–842. doi:`10.1007/s13157-011-0197-0`.

R Core Team, 2021. R: A Language and Environment for Statistical Computing. Version 4.1.2. R Foundation for Statistical Computing. Vienna. URL: `https://www.R-project.org`.

R Core Team, 2022. R: A Language and Environment for Statistical Computing. Version 4.2.2. R Foundation for Statistical Computing. Vienna. URL: `https://www.R-project.org`.

Rahman, M.A., Wang, Y., 2016. Optimizing intersection-over-union in deep neural networks for image segmentation, in: Bebis, G., Boyle, R., Parvin, B., Koracin, D., Porikli, F., Skaff, S., Entezari, A., Min, J., Iwai, D., Sadagic, A., Scheidegger, C., Isenberg, T. (Eds.), Advances in Visual Computing. Springer, Cham. volume 10072, pp. 234–244. doi:`10.1007/978-3-319-50835-1_22`. series Title: Lecture Notes in Computer Science.

Ramsar, 1971. Convention of Wetlands of International Importance especially as Waterfowl Habitat. Ramsar, Iran, 20 February 1971.

Reichstein, M., Falge, E., Baldocchi, D., Papale, D., Aubinet, M., Berbigier, P., Bernhofer, C., Buchmann, N., Gilmanov, T., Granier, A., Grunwald, T., Havrankova, K., Ilvesniemi, H., Janous, D., Knohl, A., Laurila, T., Lohila, A., Loustau, D., Matteucci, G., Meyers, T., Miglietta, F., Ourcival, J.M., Pumpanen, J., Rambal, S., Rotenberg, E., Sanz, M., Tenhunen, J., Seufert, G., Vaccari, F., Vesala, T., Yakir, D., Valentini, R., 2005. On the separation of net ecosystem exchange into assimilation and ecosystem respiration: review and improved algorithm. Global Change Biology 11, 1424–1439. doi:`10.1111/j.1365-2486.2005.001002.x`.

Reif, D., Zoboli, O., Wolfram, G., Amann, A., Saracevic, E., Riedler, P., Hainz, R., Hintermaier, S., Krampe, J., Zessner, M., 2022. Pollutant source or sink? Adsorption and mobilization of PFOS and PFOA from sediments in a large shallow lake with extended reed belt. Journal of environmental management 320, 115871. doi:`10.1016/j.jenvman.2022.115871`.

Rezania, S., Park, J., Rupani, P.F., Darajeh, N., Xu, X., Shahrokhishahraki, R., 2019. Phytoremediation potential and control of *Phragmites australis* as a green phytomass: an overview. Environmental science and pollution research international 26, 7428–7441. doi:`10.1007/s11356-019-04300-4`.

Richardson, A.D., Hollinger, D.Y., 2007. A method to estimate the additional uncertainty in gap-filled NEE resulting from long gaps in the CO_2 flux record. Agricultural and Forest Meteorology 147, 199–208. doi:`10.1016/j.agrformet.2007.06.004`.

Riley, W.J., Subin, Z.M., Lawrence, D.M., Swenson, S.C., Torn, M.S., Meng, L., Mahowald, N.M., Hess, P., 2011. Barriers to predicting changes in global terrestrial methane fluxes: analyses using CLM4Me, a methane biogeochemistry model integrated in CESM. Biogeosciences 8, 1925–1953. doi:`10.5194/bg-8-1925-2011`.

Rochette, P., Ellert, B., Gregorich, E.G., Desjardins, R.L., Pattey, E., Lessard, R., Johnson, B.G., 1997. Description of a dynamic closed chamber for measuring soil respiration and its comparison with other techniques. Canadian Journal of Soil Sciences 77, 195–203. doi:`10.4141/S96-110`.

Rochette, P., Eriksen-Hamel, N.S., 2008. Chamber measurements of soil nitrous oxide flux: Are absolute values reliable? Soil Science Society of America Journal 72, 331–342. doi:`10.2136/sssaj2007.0215`.

Rõõm, E.I., Nõges, P., Feldmann, T., Tuvikene, L., Kisand, A., Teearu, H., Nõges, T., 2014. Years are not brothers: Two-year comparison of greenhouse gas fluxes in large shallow lake võrtsjärv, estonia. Journal of Hydrology 519, 1594–1606. doi:`10.1016/j.jhydrol.2014.09.011`.

Rosentreter, J.A., Borges, A.V., Deemer, B.R., Holgerson, M.A., Liu, S., Song, C., Melack, J., Raymond, P.A., Duarte, C.M., Allen, G.H., Olefeldt, D., Poulter, B., Battin, T.I., Eyre, B.D., 2021. Half of global methane emissions come from highly variable aquatic ecosystem sources. Nature Geoscience 14, 225–230. doi:`10.1038/s41561-021-00715-2`.

Sanders-DeMott, R., Eagle, M.J., Kroeger, K.D., Wang, F., Brooks, T.W., O'Keefe Suttles, J.A., Nick, S.K., Mann, A.G., Tang, J., 2022. Impoundment increases methane emissions in *Phragmites*–invaded coastal wetlands. Global Change Biology 28, 4539–4557. doi:`10.1111/gcb.16217`.

Sass, H., Wieringa, E., Cypionka, H., Babenzien, H.D., Overmann, J., 1998. High genetic and physiological diversity of sulfate-reducing bacteria isolated from an oligotrophic lake sediment. Archives of Microbiology 170, 243–251. doi:`10.1007/s002030050639`.

Sauerzopf, F. (Ed.), 1959. Landschaft Neusiedlersee: Grundriss der Naturgeschichte des Großraumes Neusiedlersee. Anläßlich des XIV. Internationalen Limnologen-Kongresses in Österreich 1959. volume 23 of *Wissenschaftliche Arbeiten aus dem Burgenland*. Burgenländisches Landesmuseum, Eisenstadt.

Saunois, M., Stavert, A.R., Poulter, B., Bousquet, P., Canadell, J.G., Jackson, R.B., Raymond, P.A., Dlugokencky, E.J., Houweling, S., Patra, P.K., Ciais, P., Arora, V.K., Bastviken, D., Bergamaschi, P., Blake, D.R., Brailsford, G., Bruhwiler, L., Carlson, K.M., Carrol, M., Castaldi, S., Chandra, N., Crevoisier, C., Crill, P.M., Covey, K., Curry, C.L., Etiope, G., Frankenberg, C., Gedney, N., Hegglin, M.I., Höglund-Isaksson, L., Hugelius, G., Ishizawa, M., Ito, A., Janssens-Maenhout, G., Jensen, K.M., Joos, F., Kleinen, T., Krummel, P.B., Langenfelds, R.L., Laruelle, G.G., Liu, L., Machida, T., Maksyutov, S., McDonald, K.C., McNorton, J., Miller, P.A., Melton, J.R., Morino, I., Müller, J., Murguia-Flores, F., Naik, V., Niwa, Y., Noce, S., O'Doherty, S., Parker, R.J., Peng, C., Peng, S., Peters, G.P., Prigent, C., Prinn, R., Ramonet, M., Regnier, P., Riley, W.J., Rosentreter, J.A., Segers, A., Simpson, I.J., Shi, H., Smith, S.J., Steele, L.P., Thornton, B.F., Tian, H., Tohjima, Y., Tubiello, F.N., Tsuruta, A., Viovy, N., Voulgarakis, A., Weber, T.S., van Weele, M., van der Werf, G.R., Weiss, R.F., Worthy, D., Wunch, D., Yin, Y., Yoshida, Y., Zhang, W., Zhang, Z., Zhao, Y., Zheng, B., Zhu, Q., Zhu, Q., Zhuang, Q., 2020. The global methane budget 2000–2017. Earth System Science Data 12, 1561–1623. doi:`10.5194/essd-12-1561-2020`.

Scheller, S., Yu, H., Chadwick, G.L., McGlynn, S.E., Orphan, V.J., 2016. Artificial electron acceptors decouple archaeal methane oxidation from sulfate reduction. Science 351, 703–707. doi:`10.1126/science.aad7154`.

Schenk, J., Sawakuchi, H.O., Sieczko, A.K., Pajala, G., Rudberg, D., Hagberg, E., Fors, K., Laudon, H., Karlsson, J., Bastviken, D., 2021. Methane in lakes: Variability in stable carbon isotopic composition and the potential importance of groundwater input. Frontiers in Earth Science 9, 722215. doi:`10.3389/feart.2021.722215`.

Schink, B., 1997. Energetics of syntrophic cooperation in methanogenic degradation. Microbiology and Molecular Biology Reviews 61, 262–280. doi:`10.1128/mmbr.61.2.262-280.1997`.

Schlesinger, W.H., Bernhardt, E.S., 2013. Chapter 7 - wetland ecosystems, in: Schlesinger, W.H., Bernhardt, E.S. (Eds.), Biogeochemistry. 3rd ed.. Academic Press, pp. 233–274. doi:`10.1016/B978-0-12-385874-0.00007-8`.

Schmid, H.P., Oke, T.R., 1990. A model to estimate the source area contributing to turbulent exchange in the surface layer over patchy terrain. Quarterly Journal of the Royal Meteorological Society 116, 965–988. doi:`10.1002/qj.49711649409`.

Schmiedeskamp, M., Praetzel, L.S.E., Bastviken, D., Knorr, K.H., 2021. Whole–lake methane emissions from two temperate shallow lakes with fluctuating water levels: Relevance of spatiotemporal patterns. Limnology and Oceanography 66, 2455–2469. doi:`10.1002/lno.11764`.

Sebacher, D.I., Harriss, R.C., Bartlett, K.B., 1985. Methane emissions to the atmosphere through aquatic plants. Journal of Environmental Quality 14, 40–46. doi:`10.2134/jeq1985.00472425001400010008x`.

Sela-Adler, M., Ronen, Z., Herut, B., Antler, G., Vigderovich, H., Eckert, W., Sivan, O., 2017. Co-existence of methanogenesis and sulfate reduction with common substrates in sulfate-rich estuarine sediments. Frontiers in Microbiology 8, 1–11. doi:`10.3389/fmicb.2017.00766`.

Serrano-Ortiz, P., Aranda-Barranco, S., López-Ballesteros, A., Lopez-Canfin, C., Sánchez-Cañete, E.P., Meijide, A., Kowalski, A.S., 2020. Transition Period Between Vegetation Growth and Senescence Controlling Interannual Variability of C Fluxes in a Mediterranean Reed Wetland. Journal of Geophysical Research: Biogeosciences 125, 307. doi:`10.1029/2019JG005169`.

Shannon, P., Markiel, A., Ozier, O., Baliga, N.S., Wang, J.T., Ramage, D., Amin, N., Schwikowski, B., Ideker, T., 2003. Cytoscape: A Software Environment for Integrated Models of Biomolecular Interaction Networks. Genome Research 13, 2498–2504. doi:`10.1101/gr.1239303`.

Shen, F., Zeng, G., 2019. Semantic image segmentation via guidance of image classification. Neurocomputing 330, 259–266. doi:`10.1016/j.neucom.2018.11.027`.

Sø, J.S., Sand-Jensen, K., Martinsen, K.T., Polauke, E., Kjær, J.E., Reitzel, K., Kragh, T., 2023. Methane and carbon dioxide fluxes at high spatiotemporal resolution from a small temperate lake. Science of the Total Environment 878, 162895. doi:`10.1016/j.scitotenv.2023.162895`.

Soja, A.M., Kutics, K., Maracek, K., Molnár, G., Soja, G., 2014a. Changes in ice phenology characteristics of two Central European steppe lakes from 1926 to 2012 - influences of local weather and large scale oscillation patterns. Climatic Change 126, 119–133. doi:`10.1007/s10584-014-1199-8`.

Soja, G., Kitzler, B., Soja, A.M., 2014b. Emissions of greenhouse gases from Lake Neusiedl, a shallow steppe lake in Eastern Austria. Hydrobiologia 731, 125–138. doi:`10.1007/s10750-013-1681-8`.

Soja, G., Züger, J., Knoflacher, M., Kinner, P., Soja, A.M., 2013. Climate impacts on water balance of a shallow steppe lake in Eastern Austria (Lake Neusiedl). Journal of Hydrology 480, 115–124. doi:`10.1016/j.jhydrol.2012.12.013`.

Soman, V., Suresh, A., Krishnankutty Remani, A., Kalladathvalappil Venugopalan, V., Keedakkadan, H.R., 2024. A holistic review on diverse lipid biomarkers as environmental indicators: Extraction and analysis from sediments to microbial communities. Geomicrobiology Journal 41, 891–909. doi:`10.1080/01490451.2024.2397685`.

Sonnentag, O., Hufkens, K., Teshera-Sterne, C., Young, A.M., Friedl, M., Braswell, B.H., Milliman, T., O'Keefe, J., Richardson, A.D., 2012. Digital repeat photography for phenological research in forest ecosystems. Agricultural and Forest Meteorology 152, 159–177. doi:`10.1016/j.agrformet.2011.09.009`.

Spormann, A.M., Thauer, R.K., 1988. Anaerobic acetate oxidation to CO_2 by $Desulfotomaculum$ *acetoxidans* — demonstration of enzymes required for the operation of an oxidative acetyl-CoA/carbon monoxide dehydrogenase pathway. Archives of Microbiology 150, 374–380. doi:`10.1007/BF00408310`.

Sriskantharajah, S., Fisher, R.E., Lowry, D., Aalto, T., Hatakka, J., Aurela, M., LAURILA, T., Lohila, A., Kuitunen, E., Nisbet, E.G., 2012. Stable carbon isotope signatures of methane from a Finnish subarctic wetland. Tellus B: Chemical and Physical Meteorology 64, 18818. doi:`10.3402/tellusb.v64i0.18818`.

Stagg, C.L., Baustian, M.M., Perry, C.L., Carruthers, T.J.B., Hall, C.T., 2018. Direct and indirect controls on organic matter decomposition in four coastal wetland communities along a landscape salinity gradient. Journal of Ecology 106, 655–670. doi:`10.1111/1365-2745.12901`.

Stagg, C.L., Schoolmaster, D.R., Krauss, K.W., Cormier, N., Conner, W.H., 2017. Causal mechanisms of soil organic matter decomposition: deconstructing salinity and flooding impacts in coastal wetlands. Ecology 98, 2003–2018. doi:`10.1002/ecy.1890`.

Stalzer, W., Spatzierer, G., 1987. Zusammenhang zwischen Feststoff- und Nährstoffbelastung des Neusiedler Sees: b) durch Sedimentverfrachtung. Wissenschaftliche Arbeiten aus dem Burgenland 077, 93–226. URL: `https://www.zobodat.at/pdf/Wiss-Arbeiten-Burgenland_077_0093-0226.pdf`.

Stams, A.J.M., Teusink, B., Sousa, D.Z., 2019. Ecophysiology of Acetoclastic Methanogens, in: Stams, A.J.M., Sousa, D.Z. (Eds.), Biogenesis of Hydrocarbons. Handbook of Hydrocarbon and Lipid Microbiology. Springer, Cham, pp. 1–14. doi:`10.1007/978-3-319-53114-4_21-1`.

Steiner, G.M., Englmaier, P., Fink, M., Grünweis, F., Höfner, I., Korner, I., Ströhle, A., Wolf, W., 1992. Mittelpunkte der Moorflächen aus dem Moorschutzkatalog (Steiner et al. 1992). URL: `https://www.data.gv.at/katalog/de/dataset/moorschutzkatalog_1992_points`.

Stirling, E., Fitzpatrick, R.W., Mosley, L.M., 2020. Drought effects on wet soils in inland wetlands and peatlands. Earth-Science Reviews 210, 103387. doi:`10.1016/j.earscirev.2020.103387`.

Stoy, P.C., Mauder, M., Foken, T., Marcolla, B., Boegh, E., Ibrom, A., Arain, M.A., Arneth, A., Aurela, M., Bernhofer, C., Cescatti, A., Dellwik, E., Duce, P., Gianelle, D., van Gorsel, E., Kiely, G., Knohl, A., Margolis, H., McCaughey, H., Merbold, L., Montagnani, L., Papale, D., Reichstein, M., Saunders, M., Serrano-Ortiz, P., Sottocornola, M., SPANO, D., Vaccari, F., Varlagin, A., 2013. A data-driven analysis of energy balance closure across fluxnet research sites: The role of landscape scale heterogeneity. Agricultural and Forest Meteorology 171-172, 137–152. doi:`10.1016/j.agrformet.2012.11.004`.

Ström, L., Ekberg, A., Mastepanov, M., Røjle Christensen, T., 2003. The effect of vascular plants on carbon turnover and methane emissions from a tundra wetland. Global Change Biology 9, 1185–1192. doi:`10.1046/j.1365-2486.2003.00655.x`.

Ström, L., Mastepanov, M., Christensen, T.R., 2005. Species-specific effects of vascular plants on carbon turnover and methane emissions from wetlands. Biogeochemistry 75, 65–82. doi:`10.1007/s10533-004-6124-1`.

Sun, C., Li, J., Liu, Y., Zhao, S., Zheng, J., Zhang, S., 2023. Tracking annual changes in the distribution and composition of saltmarsh vegetation on the Jiangsu coast of China using Landsat time series–based phenological parameters. Remote sensing of environment 284, 113370. doi:`10.1016/j.rse.2022.113370`.

Thornthwaite, C.W., 1948. An approach toward a rational classification of climate. Geographical Review 38, 55. doi:`10.2307/210739`.

Thottathil, S.D., Prairie, Y.T., 2021. Coupling of stable carbon isotopic signature of methane and ebullitive fluxes in northern temperate lakes. Science of the Total Environment 777, 146117. doi:`10.1016/j.scitotenv.2021.146117`.

Tiškus, E., Vaičiūtė, D., Bučas, M., Gintauskas, J., 2023. Evaluation of common reed (*Phragmites australis*) bed changes in the context of management using earth observation and automatic threshold. European Journal of Remote Sensing 56, 2161070. doi:`10.1080/22797254.2022.2161070`.

Tolotti, M., Guella, G., Herzig, A., Rodeghiero, M., Rose, N.L., Soja, G., Zechmeister, T., Yang, H., Teubner, K., 2021. Assessing the ecological vulnerability of the shallow steppe Lake Neusiedl (Austria-Hungary) to climate-driven hydrological changes using a palaeolimnological approach. Journal of Great Lakes research 47, 1327–1344. doi:`10.1016/j.jglr.2021.06.004`.

Tong, X.Y., Xia, G.S., Lu, Q., Shen, H., Li, S., You, S., Zhang, L., 2020. Land-cover classification with high-resolution remote sensing images using transferable deep models. Remote Sensing of Environment 237, 111322. doi:`10.1016/j.rse.2019.111322`.

Trimble, 2023. Trimble R10 - Datasheet, Model 2 GNSS SYSTEMS. URL: `https://geomaticslandsurveying.com/wp-content/uploads/2018/11/Trimble-R10-Model-2-BROCHURE.pdf`.

Tuck, S.L., Phillips, H.R., Hintzen, R.E., Scharlemann, J.P., Purvis, A., Hudson, L.N., 2014. MODISTools - downloading and processing MODIS remotely sensed data in R. Ecology and Evolution 4, 4658–4668. doi:`10.1002/ece3.1273`.

UBA, 2023. Meteorological data set from station AT0ILL1 (Illmitz, Lake Neusiedl) [Data set]. Umweltbundesamt GmbH, Vienna. URL: `https://www.umweltbundesamt.at`.

U.S.EPA, 1999. Test methods for evaluating solid waste physical/chemical methods. Method 9038: sulfate (turbidimetric). U.S. Environmental Protection Agency (SW-846). URL: `https://www.epa.gov/sites/default/files/2015-12/documents/9038.pdf`.

Valentine, D.L., 2002. Biogeochemistry and microbial ecology of methane oxidation in anoxic environments: a review. Antonie van Leeuwenhoek 81, 271–282. doi:`10.1023/A:1020587206351`.

Valentine, D.L., Reeburgh, W.S., 2000. New perspectives on anaerobic methane oxidation. Environmental Microbiology 2, 477–484. doi:`10.1046/j.1462-2920.2000.00135.x`.

van den Berg, M., Ingwersen, J., Lamers, M., Streck, T., 2016. The role of *Phragmites* in the CH_4 and CO_2 fluxes in a minerotrophic peatland in southwest Germany. Biogeosciences 13, 6107–6119. doi:`10.5194/bg-13-6107-2016`.

van den Berg, M., van den Elzen, E., Ingwersen, J., Kosten, S., Lamers, L.P.M., Streck, T., 2020. Contribution of plant-induced pressurized flow to CH_4 emission from a *Phragmites* fen. Scientific reports 10, 12304. doi:`10.1038/s41598-020-69034-7`.

van den Brand, T., 2023. ggh4x: hacks for 'ggplot2'. R package version 0.2.4. doi:`10.32614/CRAN.package.ggh4x`.

van der Nat, F.J.W., Middelburg, J.J., 1998. Seasonal variation in methane oxidation by the rhizosphere of *Phragmites australis* and *Scirpus lacustris*. Aquatic botany 61, 95–110. doi:`10.1016/S0304-3770(98)00072-2`.

van Dijk, A., Moene, A.F., de Bruin, H., 2004. The principles of surface flux physics: theory, practice and description of the ECPACK library: Internal Report 2004/1, Updated version 1.3, September 14, 2006. Meteorology and Air Quality Group, Wageningen University, Wageningen, Netherlands.

van Iersel, W., Straatsma, M., Addink, E., Middelkoop, H., 2018. Monitoring height and greenness of non-woody floodplain vegetation with UAV time series. ISPRS Journal of Photogrammetry and Remote Sensing 141, 112–123. doi:`10.1016/j.isprsjprs.2018.04.011`.

van Luijn, F., Boers, P., Lijklema, L., Sweerts, J.P., 1999. Nitrogen fluxes and processes in sandy and muddy sediments from a shallow eutrophic lake. Water research 33, 33–42. doi:`10.1016/S0043-1354(98)00201-2`.

Van Rossum, G., Drake, F.L., 2009. Python 3 Reference Manual. CreateSpace, Scotts Valley.

Vicente-Serrano, S.M., Beguería, S., López-Moreno, J.I., 2010. A multiscalar drought index sensitive to global warming: The standardized precipitation evapotranspiration index. Journal of Climate 23, 1696–1718. doi:`10.1175/2009JCLI2909.1`.

Vickers, D., Mahrt, L., 1997. Quality control and flux sampling problems for tower and aircraft data. Journal of Atmospheric and Oceanic Technology 14, 512–526. doi:`10.1175/1520-0426(1997)014<0512:QCAFSP>2.0.CO;2`.

Villa, P., Laini, A., Bresciani, M., Bolpagni, R., 2013. A remote sensing approach to monitor the conservation status of lacustrine *Phragmites australis* beds. Wetlands Ecology and Management 21, 399–416. doi:`10.1007/s11273-013-9311-9`.

Villanueva, J.K.S., Blanco, A.C., 2019. Optimization of ground control point (GCP) configuration for unmanned aerial vehicle (UAV) survey using structure from motion (SfM). The International Archives of the Photogrammetry, Remote Sensing and Spatial Information Sciences XLII-4/W12, 167–174. doi:`10.5194/isprs-archives-XLII-4-W12-167-2019`.

Volpi, M., Tuia, D., 2017. Dense semantic labeling of subdecimeter resolution images with convolutional neural networks. IEEE Transactions on Geoscience and Remote Sensing 55, 881–893. doi:`10.1109/TGRS.2016.2616585`.

Vroom, R., van den Berg, M., Pangala, S.R., van der Scheer, O.E., Sorrell, B.K., 2022. Physiological processes affecting methane transport by wetland vegetation – A review. Aquatic Botany 182, 103547. doi:`10.1016/j.aquabot.2022.103547`.

Wang, C., Tong, C., Chambers, L.G., Liu, X., 2017. Identifying the salinity thresholds that impact greenhouse gas production in subtropical tidal freshwater marsh soils. Wetlands 37, 559–571. doi:`10.1007/s13157-017-0890-8`.

Wang, G., Xia, X., Liu, S., Zhang, L., Zhang, S., Wang, J., Xi, N., Zhang, Q., 2021a. Intense methane ebullition from urban inland waters and its significant contribution to greenhouse gas emissions. Water research 189, 116654. doi:`10.1016/j.watres.2020.116654`.

Wang, L., Du, Z., Wei, Z., Xu, Q., Feng, Y., Lin, P., Lin, J., Chen, S., Qiao, Y., Shi, J., Xiao, C., 2021b. High methane emissions from thermokarst lakes on the Tibetan Plateau are largely attributed to ebullition fluxes. Science of the Total Environment 801, 149692. doi:`10.1016/j.scitotenv.2021.149692`.

Wang, Z., Zeng, D., Patrick, W.H., 1996. Methane emissions from natural wetlands. Environmental Monitoring and Assessment 42, 143–161. doi:`10.1007/BF00394047`.

Wang, Z.A., Kroeger, K.D., Ganju, N.K., Gonneea, M.E., Chu, S.N., 2016. Intertidal salt marshes as an important source of inorganic carbon to the coastal ocean. Limnology and Oceanography 61, 1916–1931. doi:`10.1002/lno.10347`.

Wantzen, K.M., Beer, F., Jungkunst, H.F., Glatzel, S., 2022. Carbon dynamics in wetlands, in: Tockner, K., Mehner, T. (Eds.), Encyclopedia of Inland Waters. Elsevier, San Diego. volume Volume 3, pp. 169–181. doi:`10.1016/B978-0-12-819166-8.00051-7`.

Webb, E.K., Pearman, G.I., Leuning, R., 1980. Correction of flux measurements for density effects due to heat and water vapour transfer. Quarterly Journal of the Royal Meteorological Society 106, 85–100. doi:`10.1002/qj.49710644707`.

Westoby, M.J., Brasington, J., Glasser, N.F., Hambrey, M.J., Reynolds, J.M., 2012. 'Structure-from-Motion' photogrammetry: A low-cost, effective tool for geoscience applications. Geomorphology 179, 300–314. doi:`10.1016/j.geomorph.2012.08.021`.

Weyhenmeyer, G.A., Kosten, S., Wallin, M.B., Tranvik, L.J., Jeppesen, E., Roland, F., 2015. Significant fraction of CO_2 emissions from boreal lakes derived from hydrologic inorganic carbon inputs. Nature Geoscience 8, 933–936. doi:`10.1038/ngeo2582`.

Whiticar, M., Faber, E., Schoell, M., 1986. Biogenic methane formation in marine and freshwater environments: CO_2 reduction vs. acetate fermentation—Isotope evidence. Geochimica et Cosmochimica Acta 50, 693–709. doi:`10.1016/0016-7037(86)90346-7`.

Whiticar, M.J., 1999. Carbon and hydrogen isotope systematics of bacterial formation and oxidation of methane. Chemical Geology 161, 291–314. doi:`10.1016/S0009-2541(99)00092-3`.

Whiticar, M.J., Faber, E., 1986. Methane oxidation in sediment and water column environments—isotope evidence. Organic Geochemistry 10, 759–768. doi:`10.1016/S0146-6380(86)80013-4`.

Whitman, W.B., Jeanthon, C., 2006. Methanococcales, in: Dworkin, M., Falkow, S., Rosenberg, E., Schleifer, K.H., Stackebrandt, E. (Eds.), The Prokaryotes. Springer, New York, pp. 257–273. doi:`10.1007/0-387-30743-5_13`.

Wickham, H., 2016. ggplot2: Elegant Graphics for Data Analysis. Springer, New York. URL: `https://ggplot2.tidyverse.org`.

Wickham, H., Averick, M., Bryan, J., Chang, W., McGowan, L., François, R., Grolemund, G., Hayes, A., Henry, L., Hester, J., Kuhn, M., Pedersen, T., Miller, E., Bache, S., Müller, K., Ooms, J., Robinson, D., Seidel, D., Spinu, V., Takahashi, K., Vaughan, D., Wilke, C., Woo, K., Yutani, H., 2019. Welcome to the tidyverse. Journal of Open Source Software 4, 1686. doi:`10.21105/joss.01686`.

Wickham, H., Pedersen, T.L., Seidel, D., 2023. scales: scale functions for visualization. R package version 1.3.0. doi:`10.32614/CRAN.package.scales`.

Wik, M., Crill, P.M., Varner, R.K., Bastviken, D., 2013. Multiyear measurements of ebullitive methane flux from three subarctic lakes. Journal of Geophysical Research: Biogeosciences 118, 1307–1321. doi:`10.1002/jgrg.20103`.

Wik, M., Thornton, B.F., Bastviken, D., Macintyre, S., Varner, R.K., Crill, P.M., 2014. Energy input is primary controller of methane bubbling in subarctic lakes. Geophysical Research Letters 41, 555–560. doi:`10.1002/2013GL058510`.

Wik, M., Thornton, B.F., Bastviken, D., Uhlbäck, J., Crill, P.M., 2016. Biased sampling of methane release from northern lakes: A problem for extrapolation. Geophysical Research Letters 43, 1256–1262. doi:`10.1002/2015GL066501`.

Wik, M., Thornton, B.F., Varner, R.K., McCalley, C., Crill, P.M., 2020. Stable methane isotopologues from northern lakes suggest that ebullition is dominated by sub–lake scale processes. Journal of Geophysical Research: Biogeosciences 125, e2019JG005601. doi:`10.1029/2019JG005601`.

Wilkinson, G.M., Buelo, C.D., Cole, J.J., Pace, M.L., 2016. Exogenously produced CO_2 doubles the CO_2 efflux from three north temperate lakes. Geophysical Research Letters 43, 1996–2003. doi:`10.1002/2016GL067732`.

Wilkinson, J., Bodmer, P., Lorke, A., 2019. Methane dynamics and thermal response in impoundments of the Rhine River, Germany. Science of the Total Environment 659, 1045–1057. doi:`10.1016/j.scitotenv.2018.12.424`.

Winter, T.C., 2000. The vulnerability of wetlands to climate change: A hydrologic landscape perspective 1. JAWRA Journal of the American Water Resources Association 36, 305–311. doi:`10.1111/j.1752-1688.2000.tb04269.x`.

Wolfram, G., Blaschke, A.P., Hainz, R., Riedler, P., Zessner, M., Zoboli, O., Csaplovics, E., 2020. Austrian-Hungarian Synthesis. Report on applied hydrological and basic limnological investigations of the project REBEN – Reed Belt Neusiedler See/Fertő

(Interreg-Projekt AT-HU 2014-20): Technical report for the Amt der Burgenländischen Landesregierung, Abt. 5 - Baudirektion. Vienna. URL: `https://wasser.bgld.gv.at/fileadmin/user_upload/Studien/Neusiedler_See/REBEN_Bericht_7a_nationale_Synthese_EN.pdf`.

Wolfram, G., Hainz, R., Hintermaier, S., Kum, G., Riedler, P., Zessner, M., Zoboli, O., Herzig, A., 2019. Eintragspfade, Umsetzungsprozesse und Langzeitveränderungen von Nährstoffen im Neusiedler See. Österreichische Wasser- und Abfallwirtschaft 71, 508–521. doi:`10.1007/s00506-019-00620-4`.

Wolfram, G., Herzig, A., 2013. Nährstoffbilanz Neusiedler See. Wiener Mitteilungen 228, 317–338. URL: `https://www.dws-hydro-oekologie.at/wp-content/uploads/wolfram_herzig_2013.pdf`.

Wörner, S., Pester, M., 2019. The active sulfate-reducing microbial community in littoral sediment of oligotrophic lake constance. Frontiers in Microbiology 10, 247. doi:`10.3389/fmicb.2019.00247`.

Worsfold, P.J., Gimbert, L.J., Mankasingh, U., Omaka, O.N., Hanrahan, G., Gardolinski, P.C., Haygarthd, P.M., Turnere, B.L., Keith-Roach, M.J., McKelvie, I.D., 2005. Sampling, sample treatment and quality assurance issues for the determination of phosphorus species in natural waters and soils. Talanta 66, 273–293. doi:`10.1016/j.talanta.2004.09.006`.

Wurtsbaugh, W.A., Miller, C., Null, S.E., DeRose, R.J., Wilcock, P., Hahnenberger, M., Howe, F., Moore, J., 2017. Decline of the world's saline lakes. Nature Geoscience 10, 816–821. doi:`10.1038/ngeo3052`.

Wutzler, T., Lucas-Moffat, A., Migliavacca, M., Knauer, J., Sickel, K., Šigut, L., Menzer, O., Reichstein, M., 2018. Basic and extensible post-processing of eddy covariance flux data with REddyProc. Biogeosciences 15, 5015–5030. doi:`10.5194/bg-15-5015-2018`.

Yamamoto, S., Alcauskas, J.B., Crozier, T.E., 1976. Solubility of methane in distilled water and seawater. Journal of Chemical & Engineering Data 21, 78–80. doi:`10.1021/je60068a029`.

Yao, F., Livneh, B., Rajagopalan, B., Wang, J., Crétaux, J.F., Wada, Y., Berge-Nguyen, M., 2023. Satellites reveal widespread decline in global lake water storage. Science 380, 743–749. doi:`10.1126/science.abo2812`.

Yu, G.A., Li, Z., Yang, H., Lu, J., Huang, H.Q., Yi, Y., 2020. Effects of riparian plant roots on the unconsolidated bank stability of meandering channels in the tarim river, china. Geomorphology 351, 106958. doi:`10.1016/j.geomorph.2019.106958`.

Yvon-Durocher, G., Allen, A.P., Bastviken, D., Conrad, R., Gudasz, C., St-Pierre, A., Thanh-Duc, N., del Giorgio, P.A., 2014. Methane fluxes show consistent temperature dependence across microbial to ecosystem scales. Nature 507, 488–491. doi:`10.1038/nature13164`.

Zambrano-Bigiarini, Mauricio, 2020. hydroGOF: Goodness-of-fit functions for comparison of simulated and observed hydrological time series. R package version 0.4-0. doi:`10.5281/zenodo.839854`.

Zhang, B., Li, Y., Xiang, S.Z., Yan, Y., Yang, R., Lin, M.P., Wang, X.M., Xue, Y.L., Guan, X.Y., 2020a. Sediment microbial communities and their potential role as environmental pollution indicators in xuande atoll, south china sea. Frontiers in Microbiology 11, 1011. doi:`10.3389/fmicb.2020.01011`.

Zhang, Q., Sun, R., Jiang, G., Xu, Z., Liu, S., 2016. Carbon and energy flux from a *Phragmites australis* wetland in Zhangye oasis-desert area, China. Agricultural and Forest Meteorology 230-231, 45–57. doi:`10.1016/j.agrformet.2016.02.019`.

Zhang, X., Han, L., Han, L., Zhu, L., 2020b. How well do deep learning-based methods for land cover classification and object detection perform on high resolution remote sensing imagery? Remote Sensing 12, 417. doi:`10.3390/rs12030417`.

Zhang, Z., Poulter, B., Melton, J.R., Riley, W.J., Allen, G.H., Beerling, D.J., Bousquet, P., Canadell, J.G., Fluet-Chouinard, E., Ciais, P., Gedney, N., Hopcroft, P.O., Ito, A., Jackson, R.B., Jain, A.K., Jensen, K., Joos, F., Kleinen, T., Knox, S.H., Li, T., Li, X., Liu, X., McDonald, K., McNicol, G., Miller, P.A., Müller, J., Patra, P.K., Peng, C., Peng, S., Qin, Z., Riggs, R.M., Saunois, M., Sun, Q., Tian, H., Xu, X., Yao, Y., Xi, Y., Zhang, W., Zhu, Q., Zhu, Q., Zhuang, Q., 2025. Ensemble estimates of global wetland methane emissions over 2000–2020. Biogeoscience 22, 305–321. doi:`10.5194/bg-22-305-2025`.

Zhao, W., Du, S., 2016. Learning multiscale and deep representations for classifying remotely sensed imagery. ISPRS Journal of Photogrammetry and Remote Sensing 113, 155–165. doi:`10.1016/j.isprsjprs.2016.01.004`.

Zheng, J.Y., Hao, Y.Y., Wang, Y.C., Zhou, S.Q., Wu, W.B., Yuan, Q., Gao, Y., Guo, H.Q., Cai, X.X., Zhao, B., 2022a. Coastal wetland vegetation classification using pixel-based, object-based and deep learning methods based on RGB-UAV. Land 11, 2039. doi:`10.3390/land11112039`.

Zheng, Y., Wu, S., Xiao, S., Yu, K., Fang, X., Xia, L., Wang, J., Liu, S., Freeman, C., Zou, J., 2022b. Global methane and nitrous oxide emissions from inland waters and estuaries. Global Change Biology 28, 4713–4725. doi:`10.1111/gcb.16233`.

Zhong, Q., Wang, K., Lai, Q., Zhang, C., Zheng, L., Wang, J., 2016. Carbon dioxide fluxes and their environmental control in a reclaimed coastal wetland in the Yangtze estuary. Estuaries and Coasts 39, 344–362. doi:`10.1007/s12237-015-9997-4`.

Zhou, L., Zhou, G., Jia, Q., 2009. Annual cycle of CO_2 exchange over a reed (*Phragmites australis*) wetland in Northeast China. Aquatic Botany 91, 91–98. doi:`10.1016/j.aquabot.2009.03.002`.

Zlinszky, A., 2013. Mapping and conservation of the reed wetlands on Lake Balaton. PhD thesis. Eötvös Loránd University. Budapest. URL: `https://core.ac.uk/download/pdf/162468405.pdf`.

Zoboli, O., Hainz, R., Riedler, P., Kum, G., Sigmund, E., Hintermaier, S., Saracevic, E., Krampe, J., Zessner, M., Wolfram, G., 2023. Fate of nutrients and trace contaminants in a large shallow soda lake. Spatial gradients and underlying processes from the tributary river to the reed belt. Environmental Science: Processes & Impacts 25, 1505–1518. doi:`10.1039/d3em00152k`.

List of Figures

1.1 The global coverage of wetlands (including lakes) per grid cell (map source: Lehner et al. (2025)). 3
1.2 The predominant wetland class per grid cell of the global wetland cover (map source: Lehner et al. (2025)). 3
1.3 The processes, parameters, and management options that favor carbon (C) sequestration or C release in wetlands (figure source: Wantzen et al. (2022)). 5
1.4 The methane emission pathways of a wetland with reed (*Phragmites australis*) under wet and dry conditions (dry means no water level above the surface). 7
1.5 Various types of chambers such as vegetation, floating, or soil/sediment chambers for measuring greenhouse gas fluxes, but also bubble traps for collecting bubbles (from ebullition), all of which are used in this thesis. . . 10
1.6 The principle of the eddy covariance (EC) technique including the flux tower and source area (drawing partly based on Schmid and Oke (1990)), the annual mean 80% footprint, and the cross-wind integrated (CWI) footprint (according to Kljun et al. (2015)), shown here for the EC tower at the reed belt of Lake Neusiedl. 11
1.7 The global distribution map of *Phragmites australis* (Cav.) Trin. ex Steud. (data source: GBIF.org (2025)). 13
1.8 Lake Neusiedl and its reed belt are located on the Austrian-Hungarian border and demonstrate their international importance through various cross-border protected areas such as Ramsar, UNESCO Wold Heritage Site, national park, SAC, and SPA (data sources: ESRI World Imagery sources Land Burgenland, Land NÖ, Maxar, Microsoft, Earthstar Geographics; orthophoto from BEV (2019); boundaries of Austrian protected areas from Land Burgenland (2017, 2022a,b,c), Nationalparks Austria (2017); boundaries of Hungarian protected areas based on the database of the Fertő-Hanság National Park Directorate). 16

2.1 The contribution and dominance of CH_4 emissions from the ebullition and the diffusion pathway of a shallow subsaline lake was investigated at three representative locations (*Channel*, *Reed belt*, *Open water/Lake*) at Lake Neusiedl. 23
2.2 Geographic location of the study site and monitoring locations of ebullition traps and floating chambers at the reed belt of Lake Neusiedl, near Illmitz, Austria (map data source: Buchsteiner et al. (2023)). 28

2.3 Methane ebullition rates and their spatial (**A**) and temporal (**B**) variability at Lake Neusiedl during the measurement period from March to July 2021 (locations: *Channel* (CH, gray), *Reed belt* (RB, brown), and *Open water/Lake* (OW, blue); black dots (•) showing mean value per location; number under boxplot per location in the left graph is mean ± standard deviation; Dunn's post-hoc test with non-significant (ns, $p > 0.05$) or very significant (****, $p < 0.0001$) differences (Holm's adjustment); the fitted lines show the local polynomial regressions (loess)). 36

2.4 Stable carbon isotopes δ^{13}C-CH_4 (**A**) and δ^{13}C-CO_2 (**B**) and their fractionation factor α_C (**C**) measured from the ebullition gas samples in the different locations: *Channel* (CH, gray), *Reed belt* (RB, brown), and *Open water/Lake* (OW, blue) at Lake Neusiedl (black dots (•) showing mean value per location; number under boxplot indicating the mean ± standard deviation per location; Dunn's post-hoc test with non-significant (ns, $p > 0.05$), significant (**, $p < 0.01$), or very significant (****, $p < 0.0001$) differences (Holm's adjustment)). **D**: Methanogenic characterization after Whiticar and Faber (1986) using the measured δ^{13}C-CH_4 - and δ^{13}C-CO_2 -pairs. 37

2.5 Methane diffusion rates and their spatial (**A**) and temporal (**B**) variability at Lake Neusiedl during the measurement period from March to July 2021 (locations: *Channel* (CH, gray), *Reed belt* (RB, brown), and *Open water/Lake* (OW, blue); black dots (•) showing mean value per location; number under boxplot per location in the left graph is mean ± standard deviation; Dunn's post-hoc test with non-significant (ns, $p > 0.05$) or significant (**, $p < 0.01$) differences (Holm's adjustment); the fitted lines show the local polynomial regressions (loess)). 40

2.6 Methane ebullition and diffusion rates and their spatial variability at Lake Neusiedl during the measurement period from March to July 2021 (locations: *Channel* (CH, gray), *Reed belt* (RB, brown), and *Open water/Lake* (OW, blue); black dots (•) showing mean value per location; Dunn's post-hoc test with significant (**, $p < 0.01$) or very significant (****, $p < 0.0001$) differences (Holm's adjustment)). 41

2.7 Cumulative sums of CH_4 ebullition and diffusion rates (**A**), total CH_4 emission rates (**B**), and bubble fluxes (**C**) for the entire measurement period of 107 days, separated by the three locations: *Channel* (CH, gray), *Reed belt* (RB, brown), and *Open water/Lake* (OW, blue). Black dots (•) showing the replicated measurements per location; colored bar indicates the mean value of the replicates per location; error bar presents the 95% confidence interval of the replicates per location; Wilcoxon signed-rank test with non-significant (ns, $p > 0.05$), significant (*, $p < 0.05$), (**, $p < 0.01$), or very significant (***, $p < 0.001$) differences (Holm's adjustment). . . . 42

3.1 The study site is located in the eastern reed belt of Lake Neusiedl near Illmitz in Austria, showing the position of the eddy covariance (EC) tower, the 80% annual mean footprint of the EC tower from 2019, and a wind rose with the two main wind directions at this site. 57
3.2 **A)** Temporal change of the drought index SPEI (standardized precipitation evapotranspiration index) with a 12-month time scale for the reed belt of Lake Neusiedl from 1992 to 2022 (data source for the calculation: UBA (2023); dry periods in red and as negative values). **B)** Temporal variation of groundwater depth (GW) at the landward edge of the reed belt, cumulative sum of precipitation (P), sediment water content (SWC) in 5 cm depth at the reed belt, and the daily mean water level (WL) of the open water of Lake Neusiedl (Biological Station Illmitz) per day of year (DOY) from 2018 to 2022 (Data source of WL and GW: HD Bgld (2023a,b)). Our estimated WL threshold for a (mostly) dry reed belt at 1.25 m WL of the open lake (orange dotted line) and a completely dry reed belt at 1 m WL of the open lake according to Wolfram et al. (2020) (red dashed line) without considering the water channel (with dredging) that runs across the reed belt from the Biological Station to the open lake area along the dam pathway. The brown dashed vertical line shows the date (9 October 2020) when the sediment sensors were replaced. 62
3.3 The change in the share of land cover classes (reed, water, and open sediment) in the 80% annual mean footprints of the eddy covariance (EC) tower in the reed belt of Lake Neusiedl from June 2019, 2021 to July 2022. 64
3.4 Temporal variability of vegetation and green indices of the reed belt of Lake Neusiedl per day of the year (DOY) from 2018 to 2022: **A)** the enhanced vegetation index (EVI) and the normalized difference vegetation index (NDVI) from MODIS, **B)** the leaf area index (LAI) from MODIS, and **C)** the *max*-filtered green chromatic coordinates (GCC) of the Phenocam at the eddy covariance tower. The GCC data set of 2021 has already been published in Buchsteiner et al. (2023). 64
3.5 Monthly CO_2 fluxes ± uncertainty estimate (random error) of the reed belt of Lake Neusiedl from mid-2018 to 2022: net ecosystem exchange (NEE, gray), gross primary production (GPP, green) and ecosystem respiration (R_{eco}, orange). 66
3.6 Inter-annual variability of the carbon fluxes of the reed belt of Lake Neusiedl from 2019 to 2022: **A)** cumulative sums of net ecosystem exchange (NEE) and **B)** CH_4 flux over the day of the year (DOY), **C)** annual NEE and **D)** CH_4 flux ± uncertainty estimation (random error) and **E)** carbon balance. 67
3.7 Monthly CH_4 emissions ± uncertainty estimate (random error) of the reed belt of Lake Neusiedl from mid-2018 to 2022. 68
3.8 Diurnal variations of CH_4 flux of the reed belt of Lake Neusiedl for each month from mid-2018 until 2022 using the smoothing gam-function (gray area indicates 95% confidence interval). The displayed time is in UTC+1 (local time zone without daylight saving time). 69

3.9 Relationships between environmental variables and carbon fluxes: Monthly **A)** mean sediment temperature (T_{sed}) at 5 cm depth vs. mean methane (CH_4) flux, **B)** mean absolute water vapor pressure (e_a) vs. mean CH_4 flux, **C)** mean enhanced vegetation index (EVI) of the reed belt vs. mean ecosystem respiration (R_{eco}), and **D)** mean EVI vs. gross primary production (GPP); Significant Spearman correlation coefficient (ρ) with $p < 0.0001$ (****, Adjustment Holm); The fitted lines (blue) show the local polynomial regressions (loess) with the 95% confidence interval (gray area). 71

4.1 The study site is **(a)** located in the eastern reed belt of Lake Neusiedl in Austria (maps data: ©2020 austria-navigator.at, ©2020 Google Earth Image Landsat/Copernicus, Buchsteiner and Baur (2023)) and was used for **(b)** intensive 24 h measurement campaigns in each season. The different emission pathways of the CH_4 fluxes in the reed belt were measured with four chamber types illustrated in **(c)**. The setup of the measurement campaigns is shown in a schematic representation in **(d)**. 86

4.2 Diel variability of the CH_4 fluxes for each season and emission pathway (plant-mediated, water–air interface, sediment–air interface, ebullition); each point represents an individual measured flux rate; the fitted lines show the 3^{rd} order polynomial regressions with the 95% confidence interval; due to the water level or dryness of the reed belt, not every pathway was present or could be measured in each season; nighttime when incoming shortwave radiation was < 10 W m^{-2} (gray shading). 96

4.3 Keeling plots to determine the seasonal source signatures **(a)** $\delta^{13}C\text{-}CH_4$ and **(b)** $\delta^{13}C\text{-}CO_2$ of the reed belt as the y axis intercepts (shown as number in ‰ VPDB) of the fitted ordinary least square linear regression lines (black) with 95% confidence interval (shaded light gray) and their centroids (red cross) using the mean chamber air values during the chamber closure, and **(c)** the methanogenic characterization according to Whiticar et al. (1986) using the calculated source signature pairs of $\delta^{13}C\text{-}CH_4$ and $\delta^{13}C\text{-}CO_2$ and their standard errors from the plots **(a)** and **(b)**. 97

4.4 Seasonal and layer specific differences of **(a)** total organic carbon content (TOC), **(b)** gravimetric water content (WC), and **(c)** sulfate (SO_4^{2-}) concentration in the upper (L1) and lower layer (L2) of sediments in the reed belt of Lake Neusiedl. Very significant differences (****, $p < 0.0001$ with Holm's adjustment, Dunn's test) in the parameters between the two layers in the sediments independent of the season. 98

4.5 Relative abundance of **(a)** methanogens, **(b)** sulfate-reducing bacteria, and **(c)** methanotrophs in four depth sections of the two sediment cores (I and II) in winter 2021 and 2022. The two sediment sections, 0–2 cm and 4–6 cm, are part of the top organic layer (L1) of the sediment, while the sections 20–22 cm and 24–26 cm are located in the lower sandy layer (L2). Due to the insufficient amplicon sequencing quality of core II at the depth of 4–6 cm from the 2022 sampling, the sample was not used for further analyses. 99

4.6 Co-occurrence network ($p < 0.05$) of hydrogenotrophic methanogens (yellow) with other microbes, with groups containing organisms with potential for acetate oxidation highlighted (pink). Only the top 10 microbes (blue) with links to methanogens were included. The size of each node is proportional to the relative abundance of the group and the thickness of each line is proportional to the number of links between the nodes. 101

5.1 Overview maps and detailed map of the research area in the reed belt of Lake Neusiedl, eastern Austria (data source used in the overview map: Steiner et al. (1992)). 113

5.2 Full workflow for classifying different land cover types in the reed belt through semantic segmentation. The different stages of data processing are shown with the respective image size in pixels. (**a**) Orthomosaic of the study area (from flight 2021-05-05), with selected locations for ground truth areas. (**b**) Image annotation data, consisting of ground truth imagery and a fully labeled layer indicating the corresponding land cover classes (vegetation = green, water = blue, sediment = brown). (**c**) Chip data set containing small image chips and analog labels derived from ground truth data. (**d**) Training and validation of a deep learning model with the training chip data set. (**e**) Semantic segmentation performed on the orthomosaic using the trained model. 116

5.3 Workflow example of image annotation from one selected ground truth area. (**a**) Clipped and resampled ground truth imagery covering various characteristics of vegetation, water and sediment. (**b**) Segmentation output showing adjacent pixel groups with similar levels of spectral detail. (**c**) Segmentation raster converted into polygons. (**d**) Polygon segments merged by visual interpretation. (**e**) Fully labeled polygon layer for respective ground truth imagery, showing the land cover classes of vegetation (*green*), water (*blue*), and sediment (*brown*). 118

5.4 The region of interest (ROI) is marked as a black polygon in the reference picture 2021-06-23 of the Phenocam, which is aligned at the Eddy Covariance tower in the reed belt of Lake Neusiedl in the main northwest wind direction. 120

5.5 Spatio-temporal variability in the study area of Lake Neusiedl's reed belt from May–November 2021. 122

5.6 Comparison of the seasonal course of vegetation phenology (year 2021) between the ROI (region of interest) of the Phenocam data and the study area covered by the UAV imagery using the GCC vegetation index. The GCC values of the Phenocam ROI (black dots) show the average phenology of the reed stands at the Eddy Covariance tower in the NW direction (center of the study site) for almost every day of year (DOY) in 2021 as compared to the mean ± Standard Deviation (SD) of the GCC values calculated from the ten UAV flights (green dots with error bar) for the entire study site covering the land to the open water shore of the reed belt. The phenology stages of the Phenocam data are separated by the orange dotted lines. . . 123

5.7 Classification performance of a deep learning model visualized in an error map, showing the difference between labeled test data and the model prediction in a reed ecosystem. Misclassifications occurred primarily along class boundaries, especially in transition zones with sparse reed vegetation or very shallow waters, as well as in heavily shaded areas. 126

S.1 Bubble fluxes and their (**A**) spatial and (**B**) temporal variability at Lake Neusiedl during the measurement period from March to July 2021 (locations: *Channel* (CH, gray), *Reed belt* (RB, brown), and *Open water/Lake* (OW, blue); black dots (●) showing mean value per location; number under boxplot per location in the left graph is mean ± standard deviation (SD); Dunn's post-hoc test with non-significant (ns, p-values > 0.05) differences (Holm's adjustment); the fitted lines show the local polynomial regressions (loess)). 201

S.2 Spatial and temporal variability of the stable carbon isotope ratios of (**A**) CH_4, (**B**) CO_2, and (**C**) the carbon isotope fractionation factor α_C at Lake Neusiedl during the measurement period from March to July 2021 (locations: *Channel* (CH, gray), *Reed belt* (RB, brown), *Open water/Lake* (OW, blue); the fitted lines show the local polynomial regressions (loess)). 202

S.3 (**A – B**) Water, (**C**) air, and (**D**) sediment temperature dependency of CH_4 ebullition rates at the three locations *Channel* (CH, gray), *Reed belt* (RB, brown), *Open water/Lake* (OW, blue) (fitted regression line with modified Arrhenius equation according to Aben et al. (2017); E_{20} = ebullition rate at 20°C (95% confidence interval); θ_s = overall system temperature coefficient (95% confidence interval); N = number of data points). 203

S.4 Spearman correlation analysis between CH_4 ebullition rates and significant correlated environmental parameters of all three locations *Channel*, *Reed belt*, and *Open water/Lake* (DIC = dissolved inorganic carbon; NPOC = dissolved non-purgeable organic carbon; TDN = total dissolved nitrogen; CON = electrical conductivity; Twater = water temperature; WL = water level; Tair = air temperature; PA = air pressure; LWin = incoming longwave radiation; SD = standard deviation; max = maximum; Biomet = biometeorological measurements; EC-tower = eddy covariance tower; HOBO = HOBO sensors; HD Bgld = Hydrographischer Dienst Burgenland. 205

S.5 Spearman correlation analysis between CH_4 ebullition rates and significant correlated environmental parameters of the *Channel* location) (DIC = dissolved inorganic carbon; TDN = total dissolved nitrogen; CON = electrical conductivity; Twater = water temperature; WL = water level; VPD = water vapor pressure deficit; Tair = air temperature; PPFD = photosynthetically active photon flux density; max = maximum; Biomet = biometeorological measurements; EC-tower = eddy covariance tower; HOBO = HOBO sensors; HD Bgld = Hydrographischer Dienst Burgenland). 206

S.6 Spearman correlation analysis between CH_4 ebullition rates and significant correlated environmental parameters of the *Reed belt* location (DIC = dissolved inorganic carbon; NPOC = dissolved non-purgeable organic carbon; CON = electrical conductivity; ORP = oxygen–reduction potential; Twater = water temperature; WL = water level; VPD = water vapor pressure deficit; Tair = air temperature; PA = air pressure; LWout = outgoing longwave radiation; SHF = sediment heat flux; SWC = sediment water content; Tsed = sediment temperature; max = maximum; Biomet = biometeorological measurements; EC-tower = eddy covariance tower; HOBO = HOBO sensors; HD Bgld = Hydrographischer Dienst Burgenland. 207

S.7 Spearman correlation analysis between CH_4 ebullition rates and significant correlated environmental parameters of the *Open water/Lake* location (DIC = dissolved inorganic carbon; WL = water level; WS = wind speed; MaxWS = maximum wind speed; WD = wind direction; PA = air pressure; max = maximum; δ^{13}C-CH_4 = stable carbon isotope ratio of methane; EC-tower = eddy covariance tower; HD Bgld = Hydrographischer Dienst Burgenland. 208

S.8 (**A**) Nitrate (NO_3^-), (**B**) ammonium (NH_4^+), and (**C**) orthophosphate (PO_4^{3-}) concentrations of the surface water during the measurement period from March to July 2021 in the three locations *Channel* (gray), *Reed belt* (brown), and *Open water/Lake* (blue). 209

S.9 (**A**) Sulfate (SO_4^{2-}), (**B**) total dissolved nitrogen (TDN), and (**C**) dissolved inorganic carbon (DIC) concentrations of the surface water during the measurement period from March to July 2021 in the three locations *Channel* (gray), *Reed belt* (brown), and *Open water/Lake* (blue). 210

S.10 (**A**) Dissolved non-purgeable organic carbon (NPOC) concentration, (**B**) electrical conductivity (CON), and (**C**) water temperature (T_{water}) of the surface water during the measurement period from March to July 2021 in the three locations *Channel* (gray), *Reed belt* (brown), and *Open water/Lake* (blue). 211

S.11 (**A**) pH and (**B**) dissolved oxygen (DO) of the surface water during the measurement period from March to July 2021 in the three locations *Channel* (gray), *Reed belt* (brown), and *Open water/Lake* (blue). 212

S.12 (**A**) Oxidation–reduction potential (ORP) and (**B**) water level of the surface water during the measurement period from March to July 2021 in the three locations *Channel* (gray), *Reed belt* (brown), and *Open water/Lake* (blue). 213

S.13 Linear regression between the available energy (net radiation (R_n) minus ground heat flux at the surface (G_0)) and the turbulence energy fluxes (latent heat flux (LE) plus sensible heat flux (H)) of the reed belt of Lake Neusiedl: with daily mean data **A)** for all 4.5 years together (mid-2018 until 2022), **B)** for every year separated and **C)** for every season separated. 217

S.14 Diurnal variations of carbon fluxes of the reed belt of Lake Neusiedl for each month from mid-2018 until 2022 using the smoothing gam-function (gray area indicates 95% confidence interval): **A)** ecosystem respiration (R_{eco}), **B)** gross primary production (GPP), and **C)** net ecosystem exchange (NEE). The displayed time is in UTC+1 (local time zone without daylight saving time). 218

S.15 Diurnal variations of energy fluxes of the reed belt of Lake Neusiedl for each month from mid-2018 until 2022 using the smoothing gam-function (gray area indicates 95% confidence interval): **A)** sensible heat flux (H), **B)** latent heat flux (LE), **C)** net radiation (R_n), and **D)** ground heat flux (G_0). The displayed time is in UTC+1 (local time zone without daylight saving time). 219

S.16 Wind speed thresholds from which the current water level (WL) differs from the **A)** daily mean WL or **B)** weekly mean WL of Lake Neusiedl (Biological Station Illmitz), independent of the prevailing two main wind direction categories northwest (NW, blue) and southeast (SE, green). These thresholds could indicate times at which a potential lateral flow between the open lake water and the reed belt may be possible, regardless of other necessary conditions. 222

S.17 Results of the Spearman correlation analysis of the data set with all years studied (mid-2018 to 2022; NEE = net ecosystem exchange, Reco = ecosystem respiration, GPP = gross primary production, ET = evapotranspiration rate, ea = absolute water vapor pressure, es = saturated water vapor pressure, LAI = leaf area index, EVI = enhanced vegetation index, NDVI = normalized difference vegetation index, SWout = outgoing shortwave radiation, LWout = outgoing longwave radiation, LWin = incoming longwave radiation, SWin = incoming shortwave radiation, Rn = net radiation, PPFD = photosynthetically active photon flux density, WS = wind speed, WL = water level of Lake Neusiedl, SWC = sediment water content, rH = relative humidity, VPD = water vapor pressure deficit, Twater = water temperature of Lake Neusiedl, Tsed = sediment temperature, Tair = air temperature, SHF = sediment heat flux, LE = latent heat flux, H = sensible heat flux). 223

S.18 Temporal variation of photosynthetically active photon flux density (PPFD), relative humidity (rH), air temperature (T_{air}), sediment temperature (T_{sed}) at 5 cm depth, and water vapor pressure deficit (VPD) in the reed belt of Lake Neusiedl per day of the year (DOY) from 2018 to 2022. The brown dashed vertical line shows the date (9 October 2020) when the sediment sensors were replaced. 224

S.19 Temporal variation of mean and maximum wind speed (WS), friction velocity (u*), shortwave incoming (SW_{in}), shortwave outgoing (SW_{out}), longwave incoming (LW_{in}), and longwave outgoing (LW_{out}) radiation in the reed belt of Lake Neusiedl per day of the year (DOY) from 2018 to 2022. 225

S.20 Temporal variation of sediment temperature (T_{sed}) at 10 cm and 15 cm depth in the reed belt of Lake Neusiedl per day of the year (DOY) from 2018 to 2022. The brown dashed vertical line shows the date (9 October 2020) when the sediment sensors were replaced. 226

S.21 Temporal variation of sediment water content (SWC) at 10 cm and 15 cm depth in the reed belt of Lake Neusiedl per day of the year (DOY) from 2018 to 2022. The brown dashed vertical line shows the date (9 October 2020) when the sediment sensors were replaced. 227

S.22 Temporal variation of sediment heat flux (SHF) at 5 cm, 10 cm and 15 cm depth in the reed belt of Lake Neusiedl per day of the year (DOY) from 2018 to 2022. The brown dashed vertical line shows the date (9 October 2020) when the sediment sensors were replaced. 228

S.23 Temporal variation of the observed (black points) or gap-filled (red points) half-hourly values of **A)** ecosystem respiration (R_{eco}), **B)** gross primary production (GPP), **C)** net ecosystem exchange (NEE), **D)** CH_4 flux, **E)** sensible heat flux (H), and **F)** latent heat flux (LE) of the reed belt of Lake Neusiedl per day of the year (DOY) from 2018 to 2022. 229

S.24 Diel and seasonal differences in **(a)** ambient air and sediment temperature, **(b)** incoming shortwave radiation (SW_{in}), and **(c)** water vapor pressure deficit (VPD) in the reed belt of Lake Neusiedl (data source: Baur (2024)); the fitted lines showing the decic polynomial regressions with the 95% confidence interval; nighttime when SW_{in} was < 10 W m^{-2} (gray shading). 230

S.25 Diel and seasonal variability in surface water properties of the reed belt during 24 h campaigns: **(a)** water temperature (T_{water}), **(b)** dissolved oxygen (DO), **(c)** chlorophyll-a concentration (Chl-a), **(d)** oxygen–reduction potential (ORP), **(e)** total organic carbon concentration (TOC), **(f)** sulfate concentration, **(g)** electrical conductivity (CON), and **(h)** pH. Nighttime when incoming shortwave radiation was < 10 W m^{-2} (gray shading). In fall 2021 no water above the sediment surface was present. 231

S.26 Seasonal and layer specific differences of **(a)** total inorganic carbon content (TIC), **(b)** total carbon content (TC), **(c)** phosphate (PO_4^{3-}), **(d)** ammonium (NH_4^+), **(e)** nitrate (NO_3^-), **(f)** nitrite (NO_2^-) concentration, **(g)** pH, and **(h)** electrical conductivity (CON) in the upper (L1) and lower layer (L2) of sediments in the reed belt of Lake Neusiedl. Non-significant (ns, $p > 0.05$ with Holm's adjustment, Dunn's test), significant (**, $p < 0.01$), or very significant differences (****, $p < 0.0001$) in the parameters between the two layers in the sediments independent of the season. 232

S.27 Spatio-temporal development of the study area in the reed ecosystem of Lake Neusiedl from May to July 2021. The mean green chromatic coordinates (GCC) (red solid line) and the standard deviation (blue dotted lines) of each flight date are shown in the GCC histogram. 235
S.28 Spatio-temporal development of the study area in the reed ecosystem of Lake Neusiedl from August to November 2021. The mean green chromatic coordinates (GCC) (red solid line) and the standard deviation (blue dotted lines) of each flight date are shown in the GCC histogram. 236

List of Tables

1.1 The characteristics of the Lake Neusiedl and its reed belt in numbers, mainly measured near Illmitz and its Biological Station (SD = standard deviation; CON = electrical conductivity; DOC = dissolved organic carbon; POC = particulate organic carbon; Pt = total phosphorus; NO_3-N = nitrate-nitrogen; NH_4-N = ammonium-nitrogen; SO_4-S = sulfate-sulfur). . 18

2.1 Spatial variability of water characteristics at Lake Neusiedl, illustrated using selected water parameters of three representative locations (CH = *Channel*; RB = *Reed belt*; OW = *Open water/Lake*) prior to the start of the measurement campaign in mid-March 2021 (WL = water level; T_{water} = water temperature; DO = dissolved oxygen; CON = electrical conductivity; TDN = total dissolved nitrogen; NPOC = dissolved non-purgeable organic carbon). 29

4.1 The mean ± standard deviation of meteorological, water, and reed properties of the reed belt at our study site during the seasonal 24 h measurement campaigns (T_{air} = air temperature, rH = relative humidity, LAI = leaf area index, T_{water} = water temperature, WL = water level, CON = electrical conductivity, DO = dissolved oxygen, ORP = oxygen–reduction potential, Chl-a = chlorophyll-a, SO_4^{2-} = sulfate, and TOC = total organic carbon concentration of the surface water, if water was present). For LAI and WL, pure spatial mean values per campaign were used. For the other water parameters, three spatial replicates were used (location see Figure 4.1d), which were sampled several times per campaign. For T_{air} and rH, pure temporal mean values of the 24 h campaigns were used. The number of data points per parameter is given in parentheses. 88

4.2 Differences in CH_4 fluxes for each emission pathway (plant-mediated, water–air interface, sediment–air interface, ebullition) and season are represented by their median ± standard deviation; significant differences ($p < 0.05$ with Holm's adjustment, Dunn's test) between the pathways in each season are indicated by different superscript letters, between the seasons in each pathway by different superscript symbols or between daytime and nighttime in each pathway and season by different superscript numbers; the number of quality checked measurement data is provided in brackets; due to the water level or dryness of the reed belt, not every pathway could be measured in each season; nighttime when incoming shortwave radiation was < 10 W m^{-2}. 95

5.1 Results and uncertainty values from processing orthomosaics with structure from motion (SfM) techniques.[1] Ground sampling distance, [2] Root mean square error. 114

5.2 Performance metrics of deep learning models ($N = 10$) trained for land cover classification of UAV imagery tracking the reed ecosystem from May–November 2021. Metrics are represented with mean values ± SD of trained models at the class level (UAV = Unmanned Aerial Vehicle, SD = Standard Deviation, IoU = Intersection over Union). The full table is provided in Supplement Table S.9. 121

6.1 Characteristics of the present Lake Neusiedl and its reed belt in numbers, mainly measured near Illmitz and its Biological Station. Unless otherwise stated, the values are the mean ± standard deviation (CON = electrical conductivity; DO = dissolved oxygen; ORP = oxidation–reduction potential; NPOC = dissolved non-purgeable organic carbon; DIC = dissolved inorganic carbon; TDN = total dissolved nitrogen; C = carbon; DW = dry weight). 134

S.1 Summary of temperature dependencies of CH_4 ebullition rates at the three locations *Channel* (CH), *Reed belt* (RB), *Open water/Lake* (OW): E_{20} = ebullition rate at 20°C and θ_s = overall system temperature coefficient of the fitted non-linear modified Arrhenius models according to Aben et al. (2017); KGE (Kling–Gupta Efficiency) metric of the fitted models; EA = activation energy in electron Volt (eV) converted from θ_s according to Wilkinson et al. (2019); CI = confidence interval; T_{water} = water temperature; T_{air} = air temperature; T_{sed} = sediment temperature; HOBO = HOBO sensors; Biomet = biometeorological measurements. 204

S.2 Statistics of CH_4 ebullition and diffusion rates at Lake Neusiedl, separated by the three locations *Channel*, *Reed belt*, and *Open water/Lake* (N = Number of available quality-checked data points; SD = standard deviation). 214

S.3 The seasonal u* (friction velocity) threshold estimation for the reed belt of Lake Neusiedl from 2018 to 2022 was performed using the moving-point test of Papale et al. (2006) in the REddyProc tool of Wutzler et al. (2018) and with continuous seasons to avoid breaks at annual boundaries (Papale et al., 2006). For the seasons with too few records, the maximum winter, spring, summer or fall u* threshold of the entire data set was used and marked in the season column with $^+$ (SD = standard deviation). 215

S.4 Coordinates of the 10 randomly selected plots within the 80% annual mean footprint of the eddy covariance tower for harvesting the aboveground and belowground reed biomass in October/November 2022 (Holzer, 2024). . . 216

S.5 Carbon fluxes (± uncertainty) of the reed belt of Lake Neusiedl in the non-growing (November–April) and growing season (May–October) and annually from mid-2018 to 2022: NEE (net ecosystem exchange), GPP (gross primary production), R_{eco} (ecosystem respiration), CH_4 flux and P (precipitation sum). 220
S.6 Days of the growing season of the reed belt at Lake Neusiedl from 2018 to 2022 with three definitions: with mean air temperature (T_{air}) > 10°C over 14 days, with negative mean daytime NEE (net ecosystem exchange) over 14 days or with negative daily mean NEE over 14 days. Start and end of the growing season are given as day of the year (DOY). Daytime is defined as shortwave incoming radiation $\geq$ 10 W m^{-2} as in Reichstein et al. (2005). 221
S.7 The change in the share of reed, water and open sediment area in the 80% annual mean footprints (2019, 2021, and 2022) based on the land cover classification of June/July, as well as the share of the unmodified gravel pathway along the channel. 221
S.8 DNA yield, total number of microbial classes, gravimetric water content (WC), pH, electrical conductivity (CON), and total organic carbon content (TOC) in four depth section of the sediment cores I and II from the reed belt of Lake Neusiedl in winter 2021 and 2022. The two sediment sections, 0–2 cm and 4–6 cm, are part of the upper layer (L1) of the sediment, while the sections 20–22 cm and 24–26 cm are located in the lower layer (L2). . 233
S.9 Detailed table of deep learning parameters and performance metrics (IoU = intersection over union). 10 CNN (convolutional neural network) models were trained for land cover classification of UAV (unmanned aerial vehicle) imagery for tracking a reed ecosystem over a vegetation period (SD = standard deviation). 237

List of Abbreviations

α_C	carbon isotope fractionation factor
Δt	the elapsed time
$\delta^{13}C$	stable carbon isotope ratio
$\delta^{13}C$-CH_4	stable carbon isotope ratio of CH_4
$\delta^{13}C$-CO_2	stable carbon isotope ratio of CO_2
ρ	Spearman rank correlation coefficient
ρ_a	air density
θ_s	overall system temperature coefficient
16S rRNA	16S ribosomal ribonucleic acid
^{12}C	stable carbon isotope with isotopic mass 12
A_c	chamber area where the gas exchange between air and water occurs
A_{fun}	funnel area
AM	Andreas Maier
APOS	Austrian positioning service
ASVs	amplicon sequence variants
Biomet	biometeorological
C	carbon
c	dry mole fraction of the gas
c_{CH_4}	CH_4 concentration
$CaCl_2$	calcium chloride
CB	Claudia Buchsteiner
CH	study location *Channel*
CH_3COOH	acetic acid

CH_3OH	methanol
CH_4	methane
CHDK	Canon hack development kit
Chl-a	chlorophyll-a
CI	confidence interval
CNN	convolutional neural network
CO_2	carbon dioxide
CON	electrical conductivity
CRDS	cavity ring-down spectroscopy
CWI	cross-wind integrated
DHP	Daniela Henry Pinilla
DIC	dissolved inorganic carbon
diel	24 h
DNA	deoxyribonucleic acid
DO	dissolved oxygen
DOC	dissolved organic carbon
DOY	day of year
DW	dry weight
E_{20}	modeled CH_4 ebullition rate at 20°C
e_a	absolute water vapor pressure
e_s	saturated water vapor pressure
EA	activation energy
EB	ebullition trap
EC	eddy covariance
ET	evapotranspiration
eV	electron volts
EVI	enhanced vegetation index

F_{Bubble}	bubble flux
F_{chamber}	chamber flux
$F_{\text{Diff-CH}_4}$	diffusion flux of CH_4
$F_{\text{Eb-CH}_4}$	ebullition flux of CH_4
F_{eddy}	eddy (turbulent) flux
FC	floating chamber
FLUXNET	a global network of micrometeorological tower sites
FN	false negative
FP	false positive
G	ground heat flux
G_0	ground heat flux at the surface
GCC	green chromatic coordinates
GCP	ground control point
GHG	greenhouse gas
GPP	gross primary production
GSD	ground sampling distance
GW	groundwater depth
GWP	global warming potential
H	sensible heat flux
H_2	hydrogen
H_2O	water
H_2S	hydrogen sulfide
H^+	hydron
HD Bgld	Hydrographischer Dienst Burgenland
IoU	intersection over union
KGE	Kling–Gupta efficiency
KH	Karin Hager

L1	upper sediment layer
L2	lower sediment layer
LAI	leaf area index
LE	latent heat flux
LTER	long-term ecosystem research
LTWER	long-term wetland ecosystem research
LW_{in}	incoming longwave radiation
LW_{out}	outgoing longwave radiation
M_m	the molar mass of CH_4
MDS	marginal distribution sampling
MODIS	moderate-resolution imaging spectroradiometer
N	sample size
N_2	nitrogen
N_2O	nitrous oxide
NDVI	normalized difference vegetation index
NEE	net ecosystem exchange
NH_4-N	ammonium-nitrogen
$NH_4{}^+$	ammonium
NMAE	normalized mean absolute error
$NO_2{}^-$	nitrite
NO_3-N	nitrate-nitrogen
$NO_3{}^-$	nitrate
NPOC	dissolved non-purgeable organic carbon
ns	non-significant
NW	northwest
O_2	oxygen
OBIA	object based image analysis

ORP	oxidation–reduction potential
OW	study location *Open water/Lake*
P	precipitation
p	significance value
p_a	atmospheric pressure
PA	air pressure
PCA	polymerase chain reaction
PET	potential evapotranspiration
PO_4^{3-}	orthophosphate
POC	particulate organic carbon
PPFD	photosynthetically active photon flux density
Pt	total phosphorus
QC	quality control
R	ideal gas constant
r	effect size of the Dunn's test
R_{eco}	ecosystem respiration
R_n	net radiation
R^2	coefficient of determination
RB	study location *Reed belt*
RGB	red–green–blue
rH	relative humidity
RMSE	root mean square error
ROI	region of interest
S	calculated slope of the linear regression of CH_4 concentration change inside the chamber over closure time
SAC	special area of conservation
SC	sediment chamber

SD	standard deviation
SE	southeast
SfM	structure from motion
SG	Stephan Glatzel
SGWP	sustained-flux global warming potential
SHF	sediment heat flux
SO_4-S	sulfate-sulfur
$SO_4{}^{2-}$	sulfate
SPA	special protection area for birds
SparCC	sparse correlations for composition data
SPEI	standardized precipitation evapotranspiration index
SSIM	small sample isotope module
SW_{in}	incoming shortwave radiation
SW_{out}	outgoing shortwave radiation
SWC	sediment water content
T_{air}	air temperature
T_c	mean air temperature inside the chamber during closure time
T_{sed}	sediment temperature
T_{water}	water temperature
TC	total carbon
TDN	total dissolved nitrogen
TIC	total inorganic carbon
TOC	total organic carbon
TP	true positive
TRO	Thiago Rodrigues-Oliveira
u*	friction velocity
UAV	unmanned aerial vehicle

UBA	Umweltbundesamt
UTC	coordinated universal time
V_c	volume of the floating chamber
V_{occ}	total volume of occurred gas in the respective syringe from where the gas was collected
VBCF	Vienna BioCenter core facilities
VC	vegetation chamber
VCl_3	vanadium(III) chloride
VPD	water vapor pressure deficit
VPDB	Vienna pee dee belemnite
w	vertical wind speed
WC	gravimetric water content
WD	wind direction
WL	water level
WS	wind speed
xgb	extreme gradient boosting
Z_{max}	maximum water level
Z_{mean}	mean water level
ZHL	Zhen-Hao Luo

Acknowledgments

I would like to thank Stephan Glatzel for supervising my doctoral thesis and providing the resources for research, business trips, and employment.

Special thanks go to Claudia and Daniela, who supported me extensively in the field and in the lab, were dedicated co-authors, and whose master's thesis I was privileged to supervise. Thanks to Andreas for the technical and field support and for the discussions about eddy covariance. Thanks to all other I have not yet mentioned who supported me during the intensive 24 h campaigns, such as Raphael, Sebastian, Katharina, and Yujing. Thanks to Camila and Beatrix for their advice and support in the lab. Thanks to Robert for welding the large metal frames for the vegetation chambers. Thanks to all my other co-authors for their collaborations.

I would also like to thank Thomas Zechmeister and his team at the Biological Station Illmitz for their support during the construction of the boardwalk in the reed belt, for providing accommodations during the campaigns, and for analyzing some water samples in their laboratory. I would also like to thank the Neusiedler See – Seewinkel National Park and the provincial government of Burgenland for granting me an exceptional permit (Naturschutzbehördliche Ausnahmebewilligung), which allowed me to conduct this research in the core zone of the national park.

I am very grateful for the love, patience, and unconditional support — both emotional and mental — of my parents Rita and Jürgen, my sister Michaela, and my partner Steffen. I would like to emphasize that Steffen is not only my daily support, but also one of the most critical and helpful researchers, and he has significantly improved my research! Many thanks to my family and friends for their support over the past five years.

Supplementary material

S.1 Supplementary material to Study I

S.1.1 Bubble fluxes

The highest mean bubble flux (281 ± 787 mL m^{-2} d^{-1}; ± SD) was found at OW, where also the highest variability was observed (ranging from 0 to 5026 mL m^{-2} d^{-1}, see Figure S.1A). The median bubble flux at RB was slightly higher but not significantly different to the median bubble fluxes at CH and OW (Dunn's post-hoc test, $p > 0.05$ (Holm's adjustment), effect size $r = 0.1$). The lowest variance of the bubble fluxes per location was observed at the RB location. Mean bubble fluxes were 66 ± 113 and 88 ± 96 mL m^{-2} d^{-1} at CH and RB, respectively. The mean bubble flux at the OW location was more than 12-fold higher than the median.

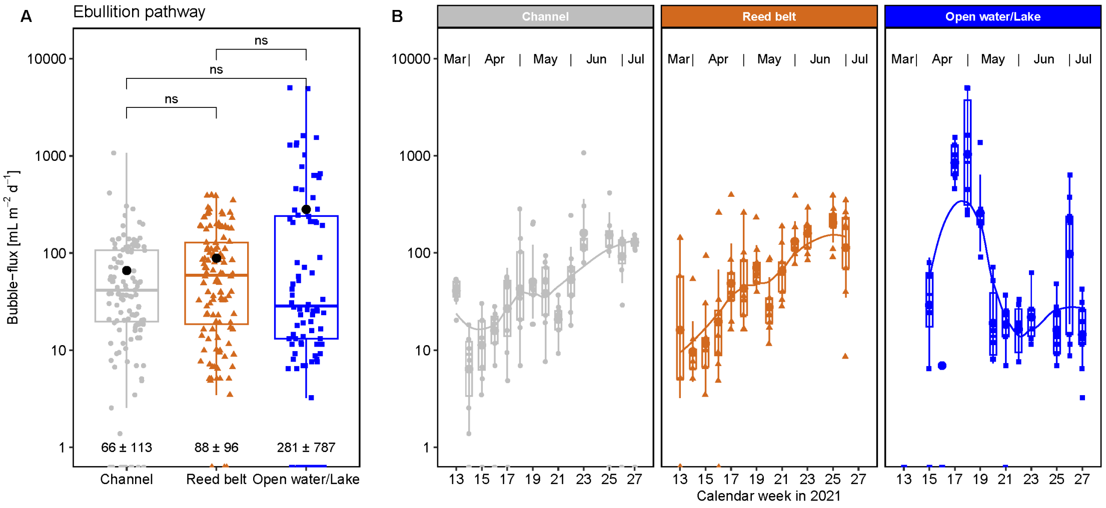

Figure S.1: Bubble fluxes and their (**A**) spatial and (**B**) temporal variability at Lake Neusiedl during the measurement period from March to July 2021 (locations: *Channel* (CH, gray), *Reed belt* (RB, brown), and *Open water/Lake* (OW, blue); black dots (●) showing mean value per location; number under boxplot per location in the left graph is mean ± standard deviation (SD); Dunn's post-hoc test with non-significant (ns, p-values > 0.05) differences (Holm's adjustment); the fitted lines show the local polynomial regressions (loess)).

S.1.2 Isotope ratios and fractionation factors

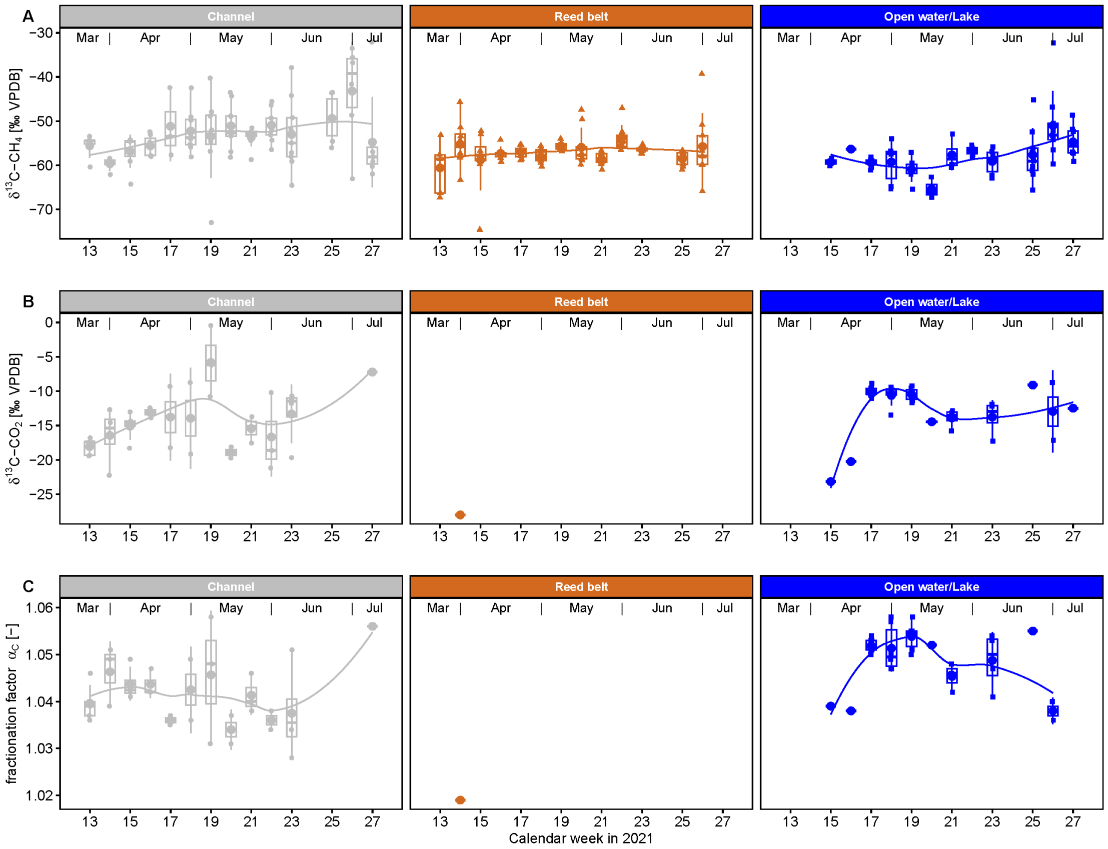

Figure S.2: Spatial and temporal variability of the stable carbon isotope ratios of (**A**) CH$_4$, (**B**) CO$_2$, and (**C**) the carbon isotope fractionation factor α_C at Lake Neusiedl during the measurement period from March to July 2021 (locations: *Channel* (CH, gray), *Reed belt* (RB, brown), *Open water/Lake* (OW, blue); the fitted lines show the local polynomial regressions (loess)).

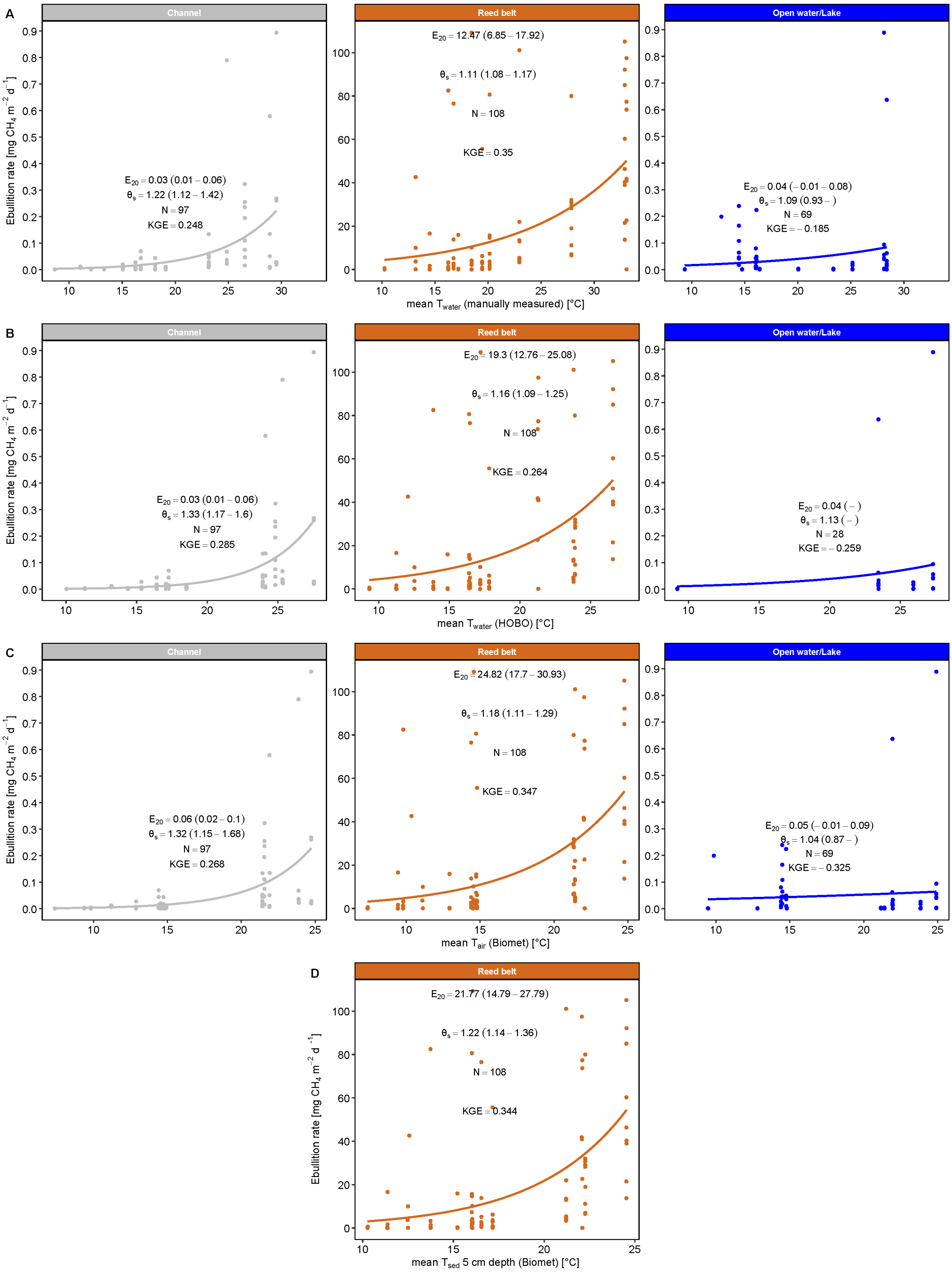

Figure S.3: (**A** – **B**) Water, (**C**) air, and (**D**) sediment temperature dependency of CH_4 ebullition rates at the three locations *Channel* (CH, gray), *Reed belt* (RB, brown), *Open water/Lake* (OW, blue) (fitted regression line with modified Arrhenius equation according to Aben et al. (2017); E_{20} = ebullition rate at 20°C (95% confidence interval); θ_s = overall system temperature coefficient (95% confidence interval); N = number of data points).

S.1.3 Temperature dependency of ebullition rates

Table S.1: Summary of temperature dependencies of CH_4 ebullition rates at the three locations *Channel* (CH), *Reed belt* (RB), *Open water/Lake* (OW): E_{20} = ebullition rate at 20°C and θ_s = overall system temperature coefficient of the fitted non-linear modified Arrhenius models according to Aben et al. (2017); KGE (Kling–Gupta Efficiency) metric of the fitted models; EA = activation energy in electron Volt (eV) converted from θ_s according to Wilkinson et al. (2019); CI = confidence interval; T_{water} = water temperature; T_{air} = air temperature; T_{sed} = sediment temperature; HOBO = HOBO sensors; Biomet = biometeorological measurements.

Location	**Temperature parameter**	**E_{20} (95% CI)**	**θ_s (95% CI)**	**KGE**	**EA** [eV]
CH	mean T_{water} (manually measured)	0.03 (0.01 - 0.06)	1.22 (1.12 - 1.42)	0.248	1.47
CH	mean T_{water} (HOBO)	0.03 (0.01 - 0.06)	1.33 (1.17 - 1.6)	0.285	2.21
CH	mean T_{air} (Biomet)	0.06 (0.02 - 0.1)	1.32 (1.15 - 1.68)	0.268	2.14
RB	mean T_{water} (manually measured)	12.47 (6.85 - 17.92)	1.11 (1.08 - 1.17)	0.35	0.74
RB	mean T_{water} (HOBO)	19.30 (12.76 - 25.08)	1.16 (1.09 - 1.25)	0.264	1.07
RB	mean T_{sed} 5 cm depth (Biomet)	21.77 (14.79 - 27.79)	1.22 (1.14 - 1.36)	0.344	1.47
RB	mean T_{air} (Biomet)	24.82 (17.7 - 30.93)	1.18 (1.11 - 1.29)	0.347	1.20
OW	mean T_{water} (manually measured)	0.04 (-0.01 - 0.08)	1.09 (0.93 -)	-0.185	0.60
OW	mean T_{water} (HOBO)	0.04 ( )	1.13 ( )	-0.259	0.87
OW	mean T_{air} (Biomet)	0.05 (-0.01 - 0.09)	1.04 (0.87 -)	-0.325	0.27

S.1.4 Correlation analysis of all locations together

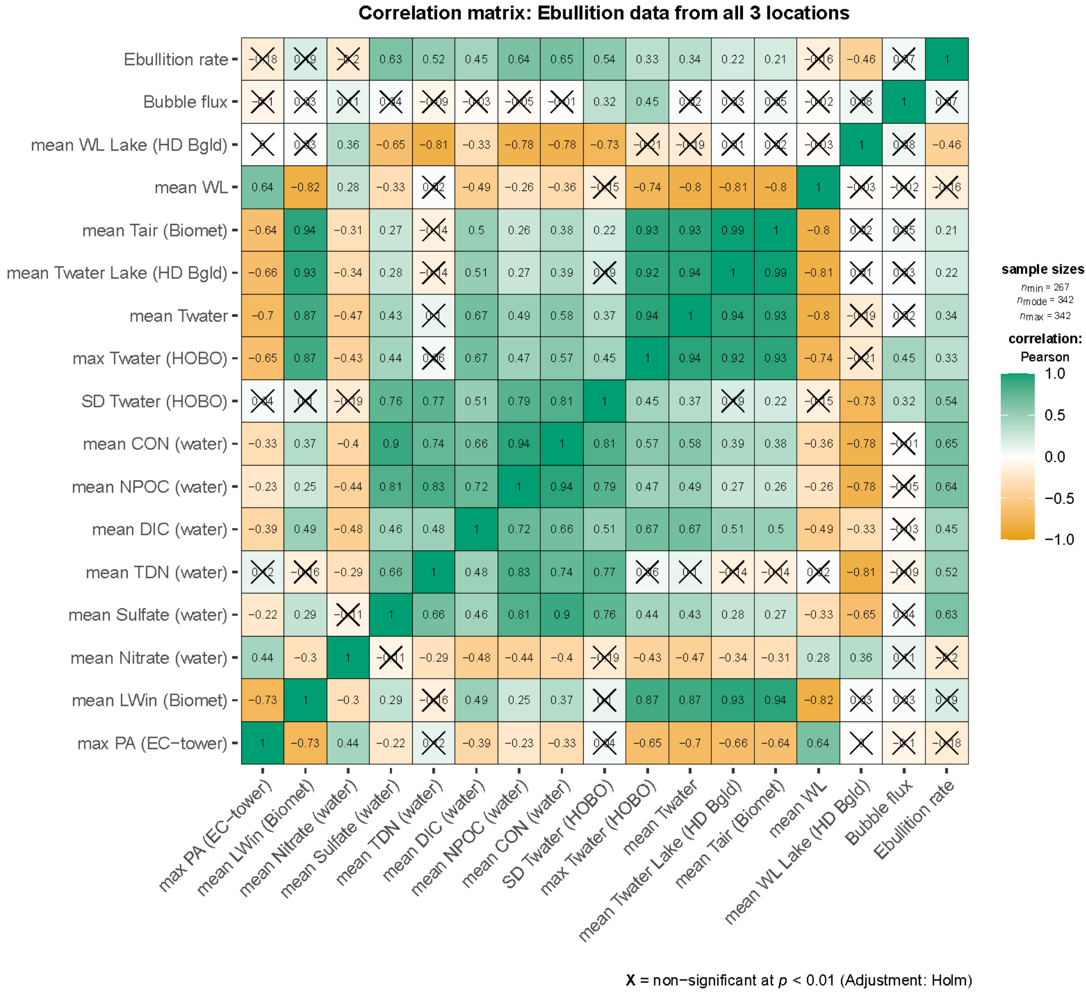

Figure S.4: Spearman correlation analysis between CH_4 ebullition rates and significant correlated environmental parameters of all three locations *Channel*, *Reed belt*, and *Open water/Lake* (DIC = dissolved inorganic carbon; NPOC = dissolved non-purgeable organic carbon; TDN = total dissolved nitrogen; CON = electrical conductivity; Twater = water temperature; WL = water level; Tair = air temperature; PA = air pressure; LWin = incoming longwave radiation; SD = standard deviation; max = maximum; Biomet = biometeorological measurements; EC-tower = eddy covariance tower; HOBO = HOBO sensors; HD Bgld = Hydrographischer Dienst Burgenland.

S.1.5 Correlation analysis per location

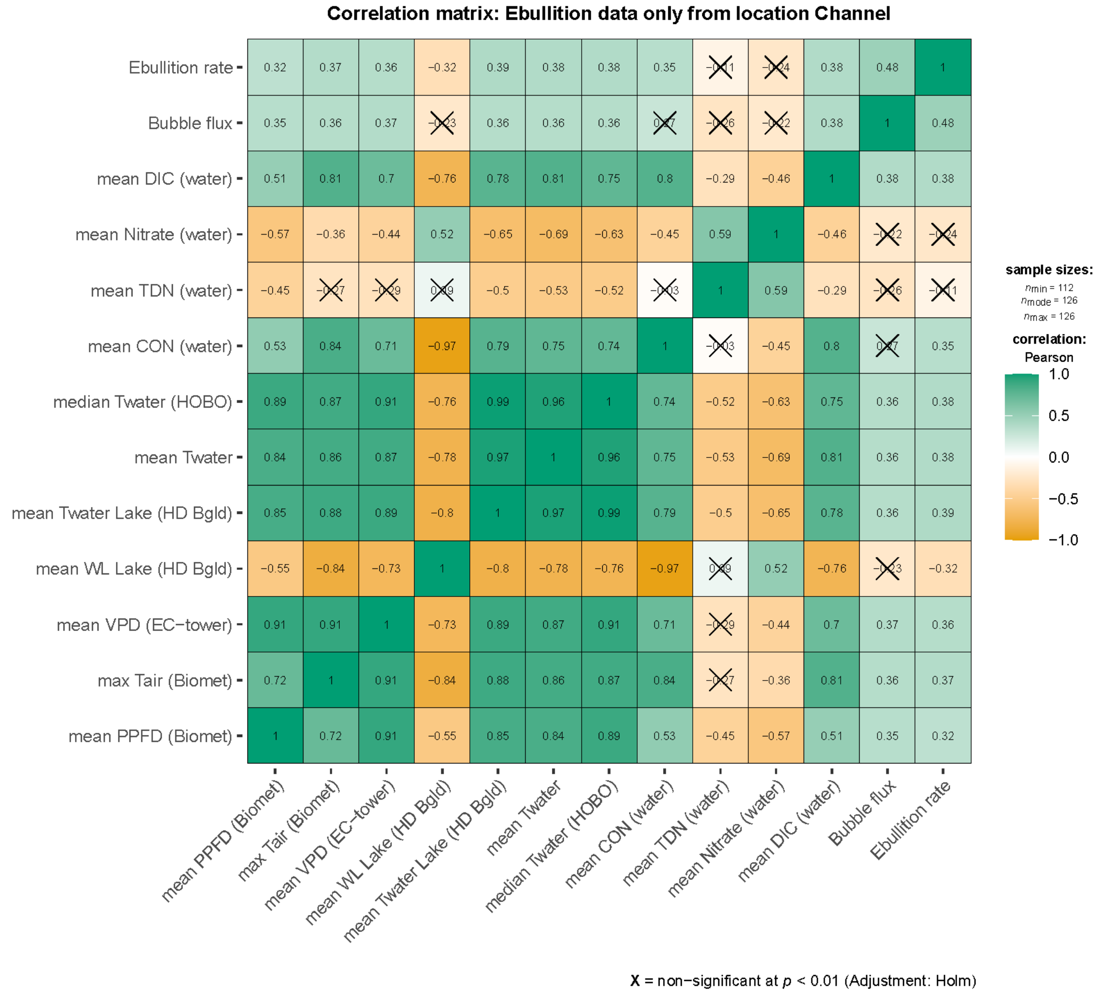

Correlation matrix: Ebullition data only from location Channel

	mean PPFD (Biomet)	max Tair (Biomet)	mean VPD (EC−tower)	mean WL Lake (HD Bgld)	mean Twater Lake (HD Bgld)	mean Twater	median Twater (HOBO)	mean CON (water)	mean TDN (water)	mean Nitrate (water)	mean DIC (water)	Bubble flux	Ebullition rate
Ebullition rate	0.32	0.37	0.36	−0.32	0.39	0.38	0.38	0.35	−0.11 X	−0.24 X	0.38	0.48	1
Bubble flux	0.35	0.36	0.37	−0.23 X	0.36	0.36	0.36	0.27 X	−0.26 X	−0.22 X	0.38	1	0.48
mean DIC (water)	0.51	0.81	0.7	−0.76	0.78	0.81	0.75	0.8	−0.29	−0.46	1	0.38	0.38
mean Nitrate (water)	−0.57	−0.36	−0.44	0.52	−0.65	−0.69	−0.63	−0.45	0.59	1	−0.46	−0.22 X	−0.24 X
mean TDN (water)	−0.45	−0.27 X	−0.29 X	0.09 X	−0.5	−0.53	−0.52	−0.03 X	1	0.59	−0.29	−0.26 X	−0.11 X
mean CON (water)	0.53	0.84	0.71	−0.97	0.79	0.75	0.74	1	−0.03 X	−0.45	0.8	0.27 X	0.35
median Twater (HOBO)	0.89	0.87	0.91	−0.76	0.99	0.96	1	0.74	−0.52	−0.63	0.75	0.36	0.38
mean Twater	0.84	0.86	0.87	−0.78	0.97	1	0.96	0.75	−0.53	−0.69	0.81	0.36	0.38
mean Twater Lake (HD Bgld)	0.85	0.88	0.89	−0.8	1	0.97	0.99	0.79	−0.5	−0.65	0.78	0.36	0.39
mean WL Lake (HD Bgld)	−0.55	−0.84	−0.73	1	−0.8	−0.78	−0.76	−0.97	0.09 X	0.52	−0.76	−0.23 X	−0.32
mean VPD (EC−tower)	0.91	0.91	1	−0.73	0.89	0.87	0.91	0.71	−0.29 X	−0.44	0.7	0.37	0.36
max Tair (Biomet)	0.72	1	0.91	−0.84	0.88	0.86	0.87	0.84	−0.27 X	−0.36	0.81	0.36	0.37
mean PPFD (Biomet)	1	0.72	0.91	−0.55	0.85	0.84	0.89	0.53	−0.45	−0.57	0.51	0.35	0.32

X = non−significant at $p < 0.01$ (Adjustment: Holm)

Figure S.5: Spearman correlation analysis between CH_4 ebullition rates and significant correlated environmental parameters of the *Channel* location) (DIC = dissolved inorganic carbon; TDN = total dissolved nitrogen; CON = electrical conductivity; Twater = water temperature; WL = water level; VPD = water vapor pressure deficit; Tair = air temperature; PPFD = photosynthetically active photon flux density; max = maximum; Biomet = biometeorological measurements; EC-tower = eddy covariance tower; HOBO = HOBO sensors; HD Bgld = Hydrographischer Dienst Burgenland).

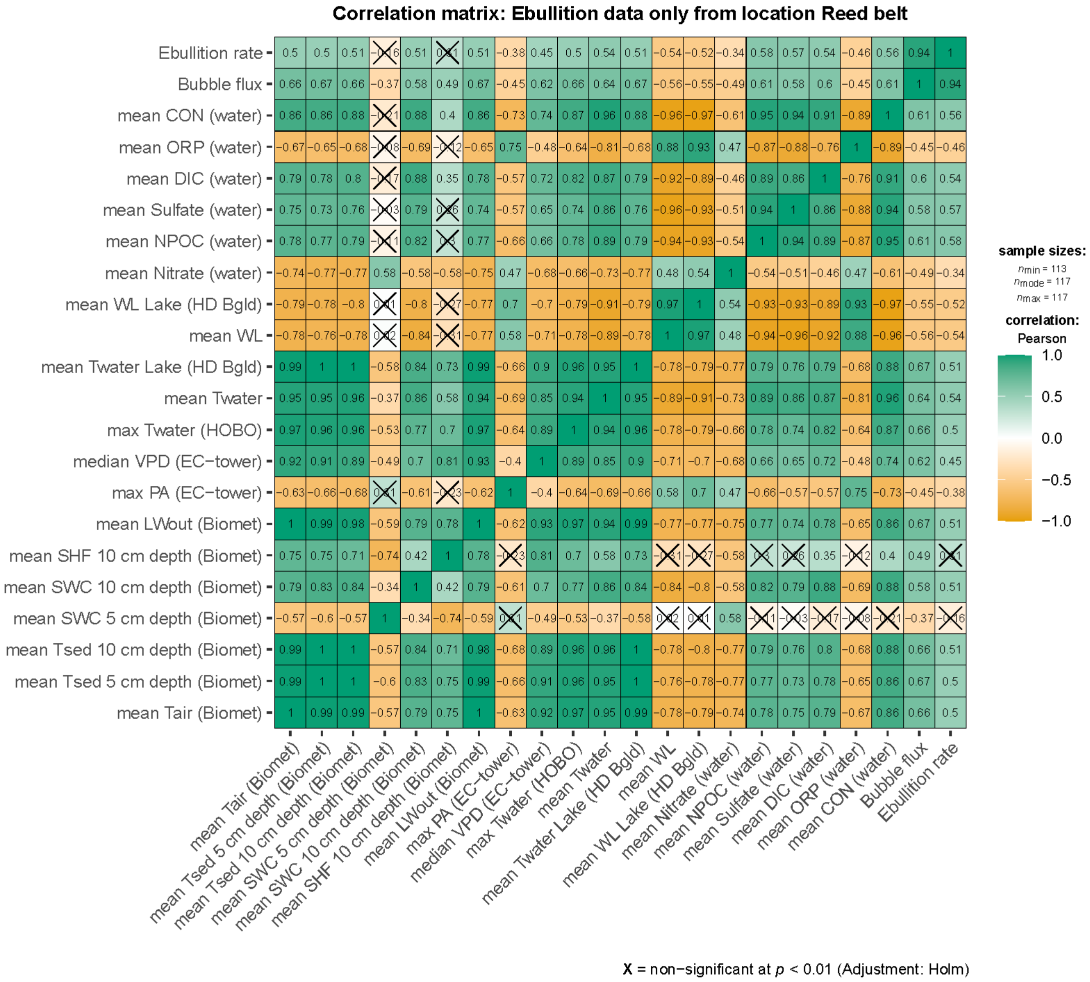

Figure S.6: Spearman correlation analysis between CH_4 ebullition rates and significant correlated environmental parameters of the *Reed belt* location (DIC = dissolved inorganic carbon; NPOC = dissolved non-purgeable organic carbon; CON = electrical conductivity; ORP = oxygen–reduction potential; Twater = water temperature; WL = water level; VPD = water vapor pressure deficit; Tair = air temperature; PA = air pressure; LWout = outgoing longwave radiation; SHF = sediment heat flux; SWC = sediment water content; Tsed = sediment temperature; max = maximum; Biomet = biometeorological measurements; EC-tower = eddy covariance tower; HOBO = HOBO sensors; HD Bgld = Hydrographischer Dienst Burgenland.

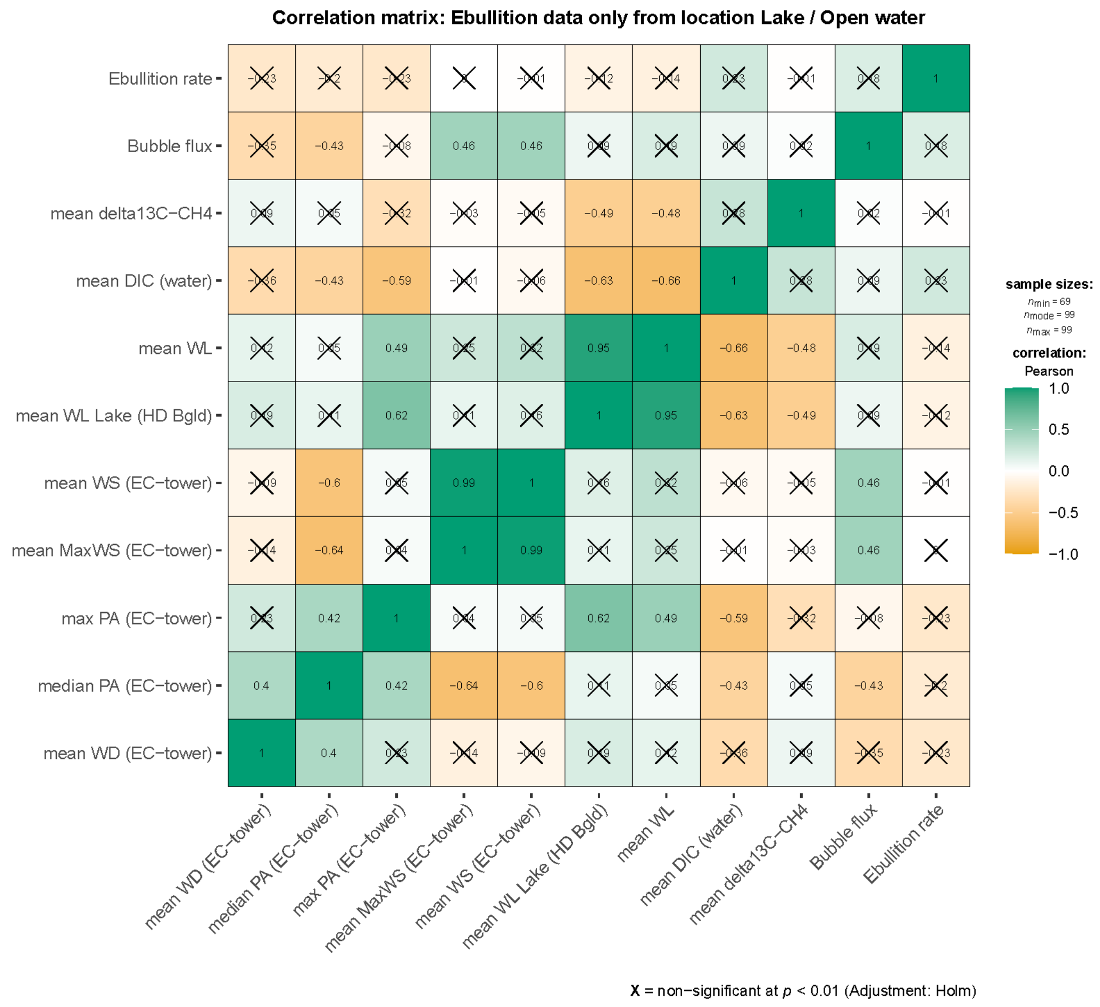

Figure S.7: Spearman correlation analysis between CH_4 ebullition rates and significant correlated environmental parameters of the *Open water/Lake* location (DIC = dissolved inorganic carbon; WL = water level; WS = wind speed; MaxWS = maximum wind speed; WD = wind direction; PA = air pressure; max = maximum; δ^{13}C-CH_4 = stable carbon isotope ratio of methane; EC-tower = eddy covariance tower; HD Bgld = Hydrographischer Dienst Burgenland.

S.1.6 Surface water analysis

The following section described and illustrated in detail the temporal variations of the water parameters, observed at the CH, RB and OW location, from late March to mid-July 2021.

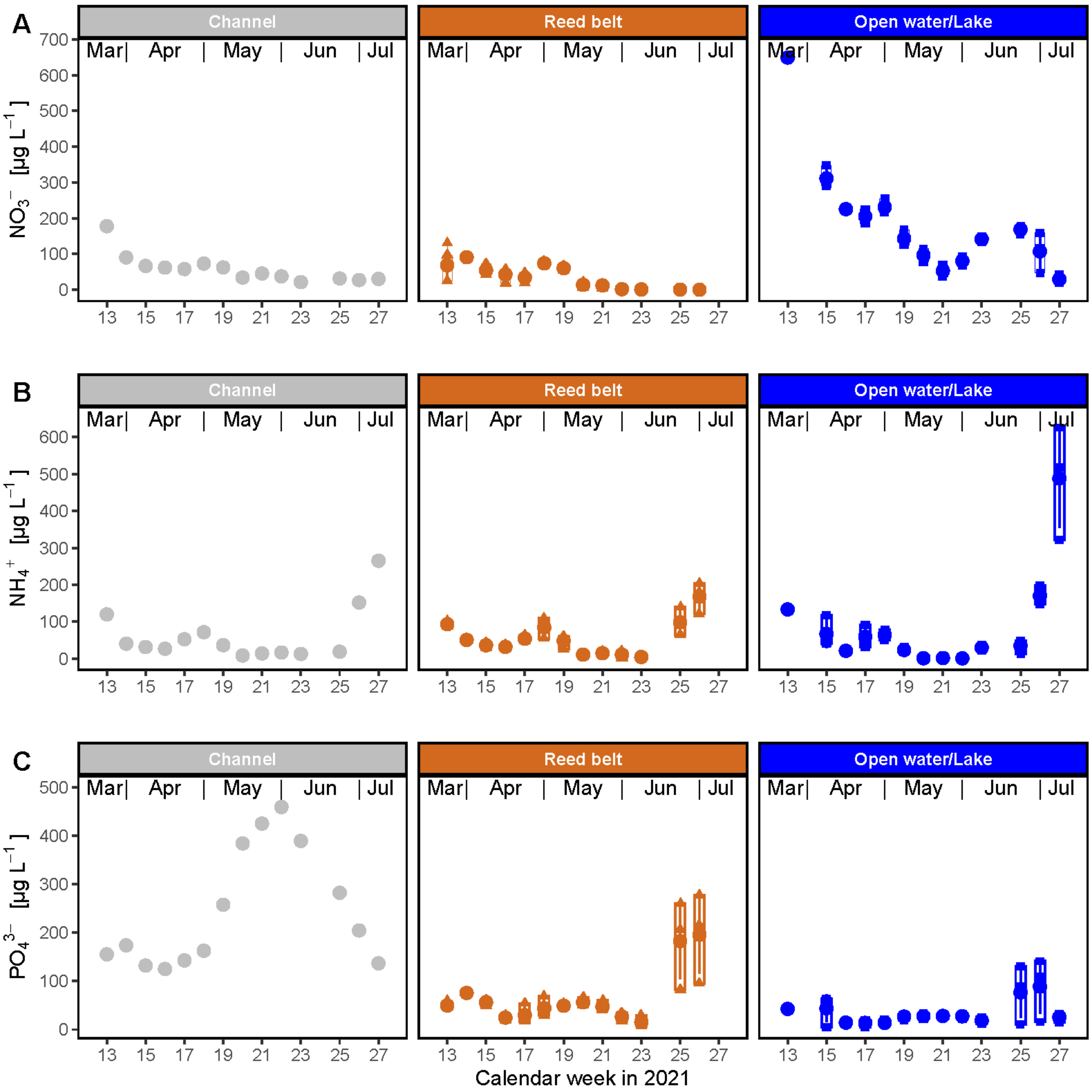

Figure S.8: (**A**) Nitrate (NO_3^-), (**B**) ammonium (NH_4^+), and (**C**) orthophosphate (PO_4^{3-}) concentrations of the surface water during the measurement period from March to July 2021 in the three locations *Channel* (gray), *Reed belt* (brown), and *Open water/Lake* (blue).

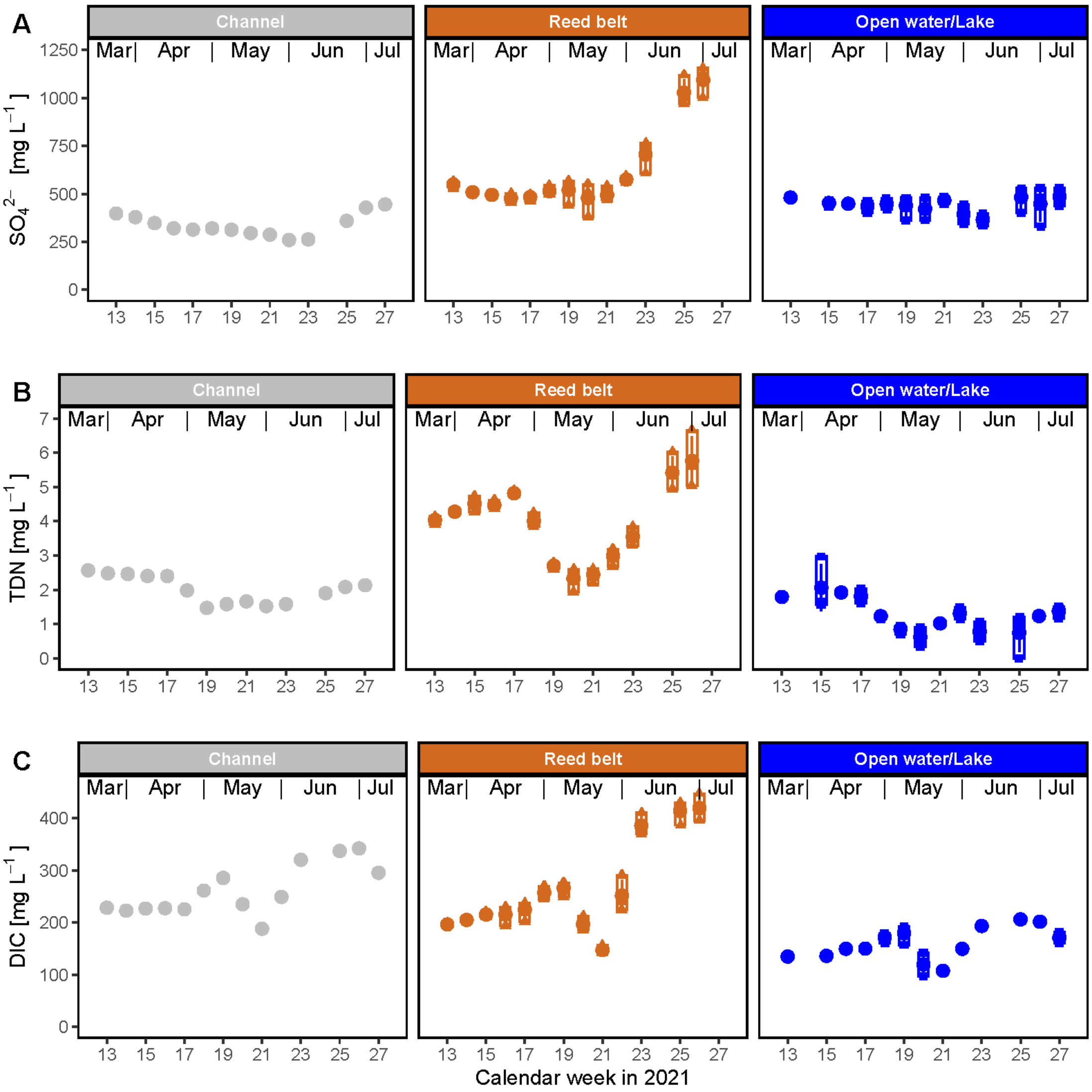

Figure S.9: (**A**) Sulfate (SO_4^{2-}), (**B**) total dissolved nitrogen (TDN), and (**C**) dissolved inorganic carbon (DIC) concentrations of the surface water during the measurement period from March to July 2021 in the three locations *Channel* (gray), *Reed belt* (brown), and *Open water/Lake* (blue).

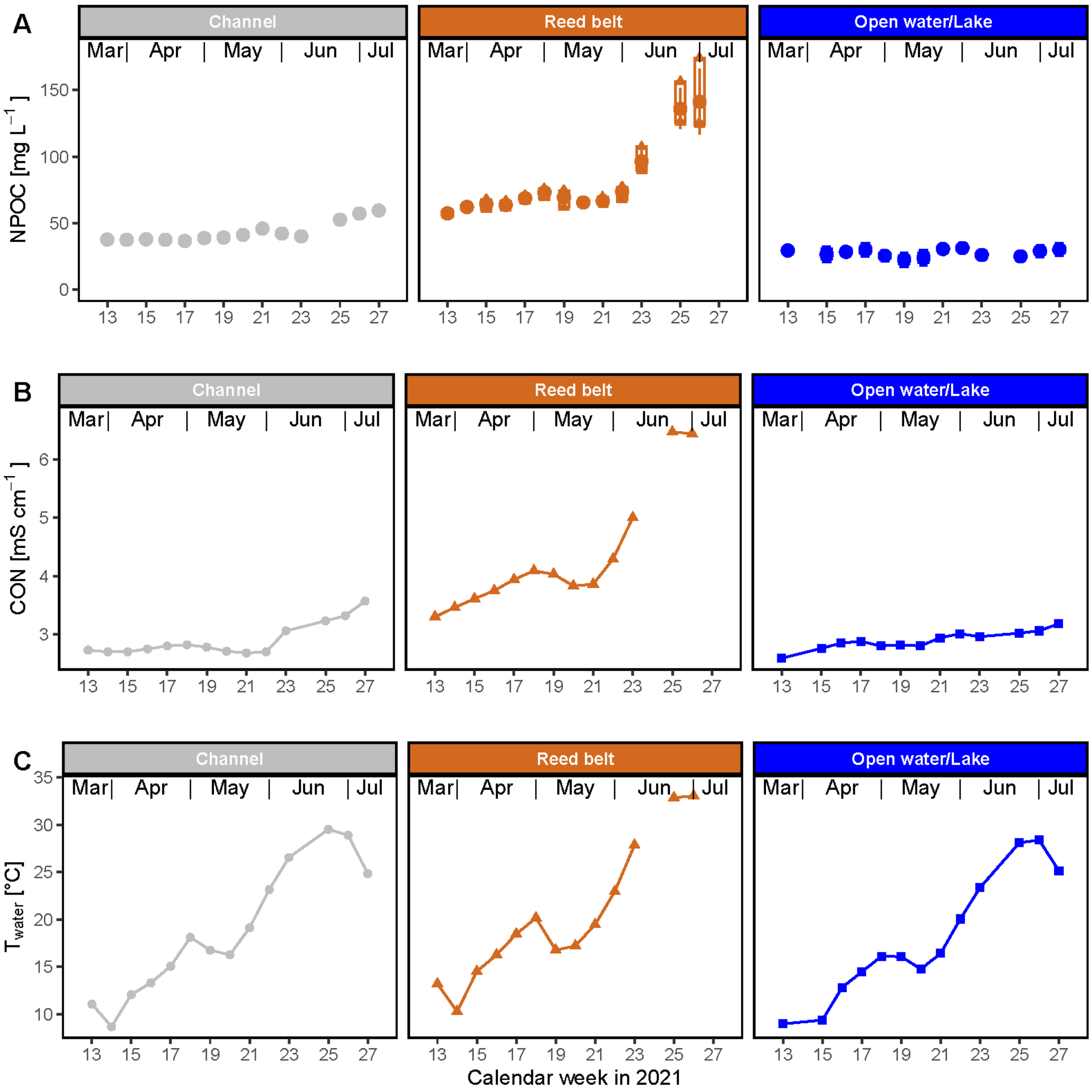

Figure S.10: (**A**) Dissolved non-purgeable organic carbon (NPOC) concentration, (**B**) electrical conductivity (CON), and (**C**) water temperature (T_{water}) of the surface water during the measurement period from March to July 2021 in the three locations *Channel* (gray), *Reed belt* (brown), and *Open water/Lake* (blue).

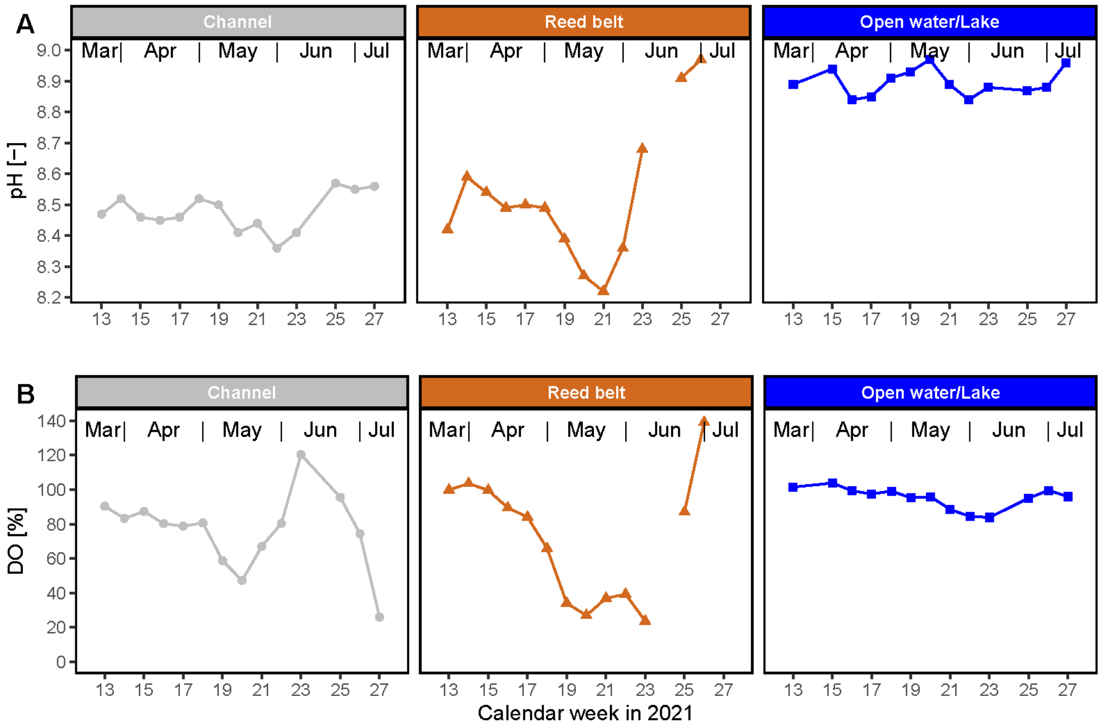

Figure S.11: (**A**) pH and (**B**) dissolved oxygen (DO) of the surface water during the measurement period from March to July 2021 in the three locations *Channel* (gray), *Reed belt* (brown), and *Open water/Lake* (blue).

In all three locations, surface water ORP started at approx. 180 mV in late March 2021 and dropped to about 50 mV (see Figure S.12A). Only at RB, ORP dropped further to about –50 mV in July 2021. The highest variability and concentration of PO_4^{3-} (460 µg L^{-1}) in the surface water were found at CH (see Figure S.8C). SO_4^{2-} and NPOC concentrations of the surface water showed little variability at CH and OW (see Figures S.9A and S.10A). In contrast, they increased sharply in RB from June 2021, when the water level dropped strongly. NO_3^- concentrations of the surface water decreased in all three locations from March to July 2021, with the strongest decrease at OW due to a high starting point of approx. 600 µg L^{-1} (see Figure S.8A). The NH_4^+ concentrations of the surface water showed some small variability in all three locations and increased at the end of June 2021 (see Figure S.8B).

In all three locations, the DIC concentration of the surface water dropped sharply after calendar week 19 (mid-May) but also increased again after calendar week 21 (end-May; see Figure S.9C). This trend can also be observed for the TDN concentration and the pH of the surface water, but only at RB (see Figures S.9B and S.11A). One reason for this could have been the dilution of concentrations due to precipitation during this period (mid to end of May 2021), whereas the periods before and after were very dry (low precipitation). As the RB location has the lowest water level, the dilution is naturally more significant. At CH, surface water pH fluctuated around 8.5, while at OW it was around 8.9.

The CON of the surface water increased slightly at CH and OW from 2.7 to 3.3 mS cm^{-1} from March to July 2021 (see Figure S.10B). At RB, CON showed the highest CON increase from 3.5 to > 6 mS cm^{-1}. The smallest variability of the DO of the surface water (with a mean of around 96%) was found at OW (see Figure S.11B). In contrast, at RB and CH, DO variability in surface water was high, with the lowest values of 25% in May/June and July 2021, respectively.

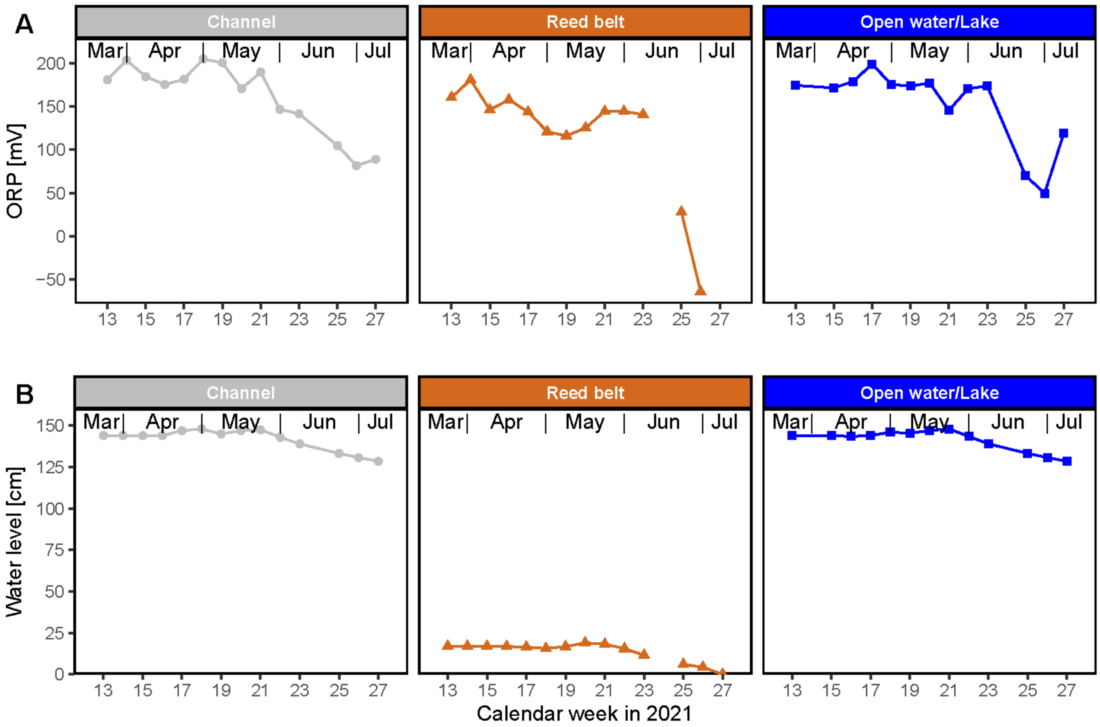

Figure S.12: (**A**) Oxidation–reduction potential (ORP) and (**B**) water level of the surface water during the measurement period from March to July 2021 in the three locations *Channel* (gray), *Reed belt* (brown), and *Open water/Lake* (blue).

S.1.7 Statistics of CH_4 ebullition and diffusion rates at Lake Neusiedl

Table S.2: Statistics of CH_4 ebullition and diffusion rates at Lake Neusiedl, separated by the three locations *Channel*, *Reed belt*, and *Open water/Lake* (N = Number of available quality-checked data points; SD = standard deviation).

Location	**Pathway**	**CH_4 emission rates** [mg m^{-2} d^{-1}]					***N***
		Mean	**SD**	**Median**	**Min**	**Max**	
Channel	Ebullition	0.05	0.13	0.01	0.00	0.89	112
Reed belt	Ebullition	17.18	28.18	3.21	0.00	109.20	113
Open water/Lake	Ebullition	0.04	0.12	0.00	0.00	0.89	86
Channel	Diffusion	7.43	4.91	6.17	2.32	22.06	24
Reed belt	Diffusion	15.84	11.42	14.51	4.20	60.17	27
Open water/Lake	Diffusion	12.69	11.51	9.05	1.87	34.91	11

S.2 Supplementary material to Study II

S.2.1 U* threshold estimation

Table S.3: The seasonal u* (friction velocity) threshold estimation for the reed belt of Lake Neusiedl from 2018 to 2022 was performed using the moving-point test of Papale et al. (2006) in the REddyProc tool of Wutzler et al. (2018) and with continuous seasons to avoid breaks at annual boundaries (Papale et al., 2006). For the seasons with too few records, the maximum winter, spring, summer or fall u* threshold of the entire data set was used and marked in the season column with $^+$ (SD = standard deviation).

Season start	**Season**	**U* threshold** [m s^{-1}]
2017-12$^+$	winter	0.211
2018-03$^+$	spring	0.183
2018-06	summer	0.171
2018-09$^+$	fall	0.381
2018-12	winter	0.211
2019-03	spring	0.095
2019-06	summer	0.158
2019-09	fall	0.195
2019-12	winter	0.165
2020-03	spring	0.142
2020-06$^+$	summer	0.404
2020-09	fall	0.381
2020-12	winter	0.122
2021-03	spring	0.105
2021-06	summer	0.378
2021-09	fall	0.229
2021-12	winter	0.171
2022-03	spring	0.183
2022-06	summer	0.404
2022-09	fall	0.234
2022-12$^+$	winter	0.211
mean ± SD		*0.225 ± 0.101*

S.2.2 Coordinates of the reed biomass harvesting

Table S.4: Coordinates of the 10 randomly selected plots within the 80% annual mean footprint of the eddy covariance tower for harvesting the aboveground and belowground reed biomass in October/November 2022 (Holzer, 2024).

Plot number	**Coordinates**
1	47.76906° N, 16.75928° E
2	47.76931° N, 16.75874° E
3	47.76963° N, 16.75769° E
4	47.76990° N, 16.75653° E
5	47.77053° N, 16.75821° E
6	47.77056° N, 16.75752° E
7	47.77058° N, 16.75615° E
8	47.76871° N, 16.75868° E
9	47.76866° N, 16.75812° E
10	47.76810° N, 16.75896° E

S.2.3 Energy balance closure of the reed belt of Lake Neusiedl

It is worth noting that the energy balance closure problem is a well-known issue in this field (Mauder et al., 2020). To some extent, the energy balance closure residuals in this study can be attributed to various environmental conditions, such as WL differences, spatial heterogeneity of albedo at the study site and thus affect the potential energy storage in the water above the surface and in the aboveground biomass. The energy balance closure improved from 76.7% (2019) to 86.1% (2021) as the WL in the reed belt decreased or even dried out. This is consistent with the findings of Malone et al. (2014), who also demonstrated a greater closure in dry versus inundated conditions in marshes. However, the closure of the energy balance decreased again to 77.9% in 2022, possibly due to changes in sediment heat capacity and in albedo (increase of open sediment areas and decrease of water areas). The latter is indicated by the higher $\mathrm{SW_{out}}$ in 2022 compared to previous years (see Figure S.19). Perhaps the current measurements do not accurately reflect the increased spatial heterogeneity of the albedo at the study site. The land cover heterogeneity of the site represents fresh and old reed cover, bare brown sediment and salt blooms in 2022. The energy balance closure of this study is higher than that of the half-hourly data (64.9%) in Kiss and Torma (2014), who measured several months in 2013 on the same lake, but at a higher WL and at the edge between reed belt and open water on the Hungarian side of the lake.

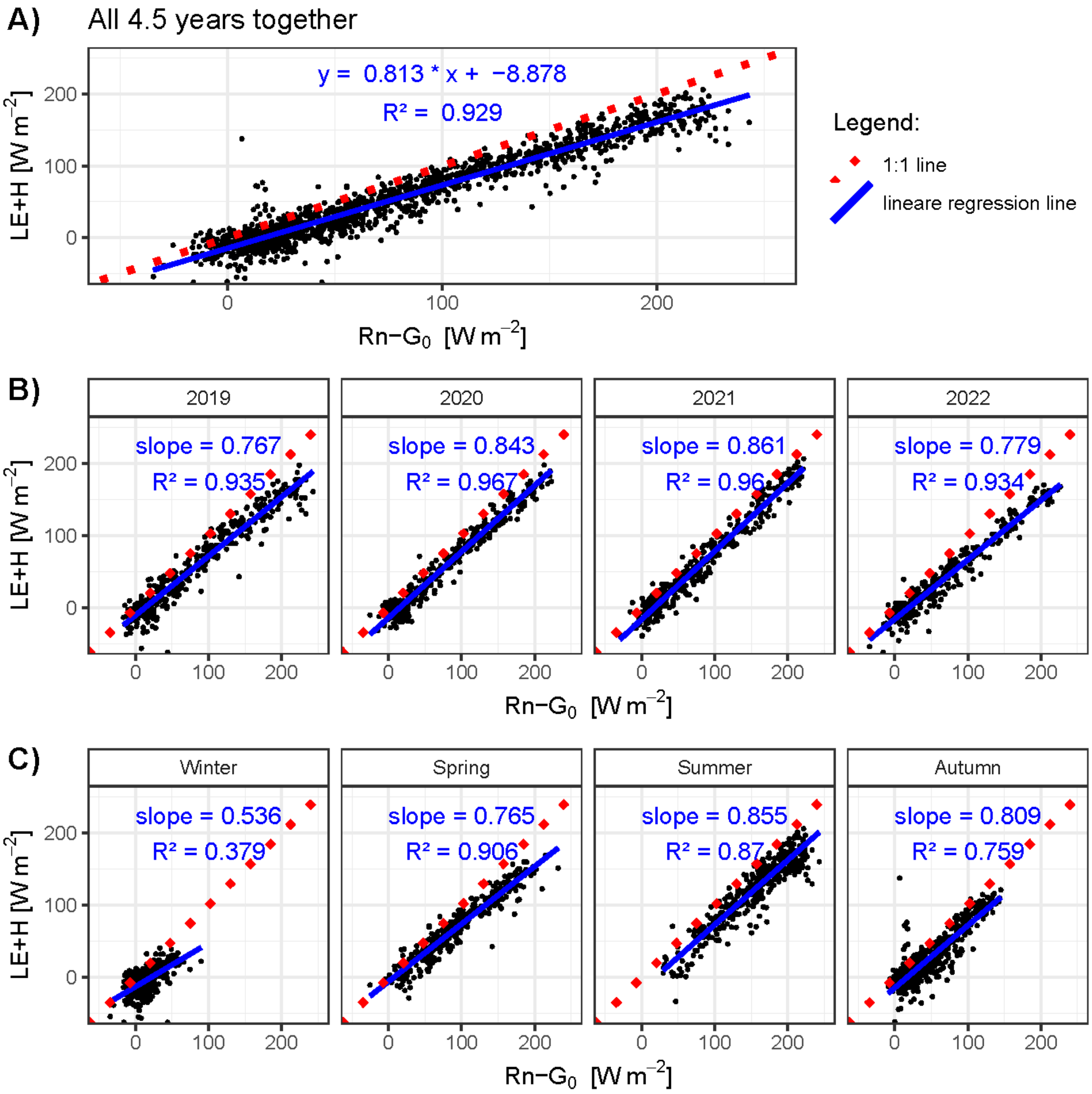

Figure S.13: Linear regression between the available energy (net radiation (R_n) minus ground heat flux at the surface (G_0)) and the turbulence energy fluxes (latent heat flux (LE) plus sensible heat flux (H)) of the reed belt of Lake Neusiedl: with daily mean data **A)** for all 4.5 years together (mid-2018 until 2022), **B)** for every year separated and **C)** for every season separated.

S.2.4 Diurnal variations of carbon and energy fluxes of the reed belt of Lake Neusiedl

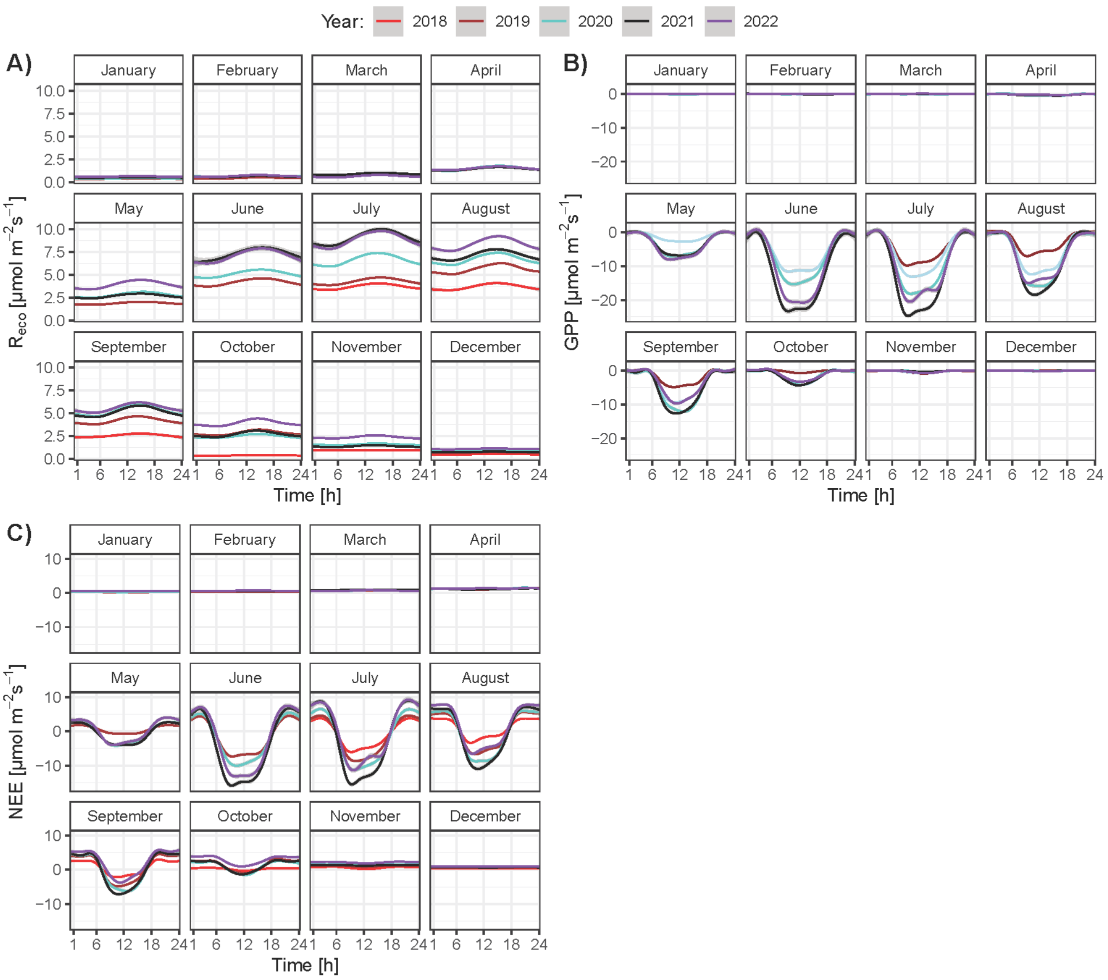

Figure S.14: Diurnal variations of carbon fluxes of the reed belt of Lake Neusiedl for each month from mid-2018 until 2022 using the smoothing gam-function (gray area indicates 95% confidence interval): **A)** ecosystem respiration (R_{eco}), **B)** gross primary production (GPP), and **C)** net ecosystem exchange (NEE). The displayed time is in UTC+1 (local time zone without daylight saving time).

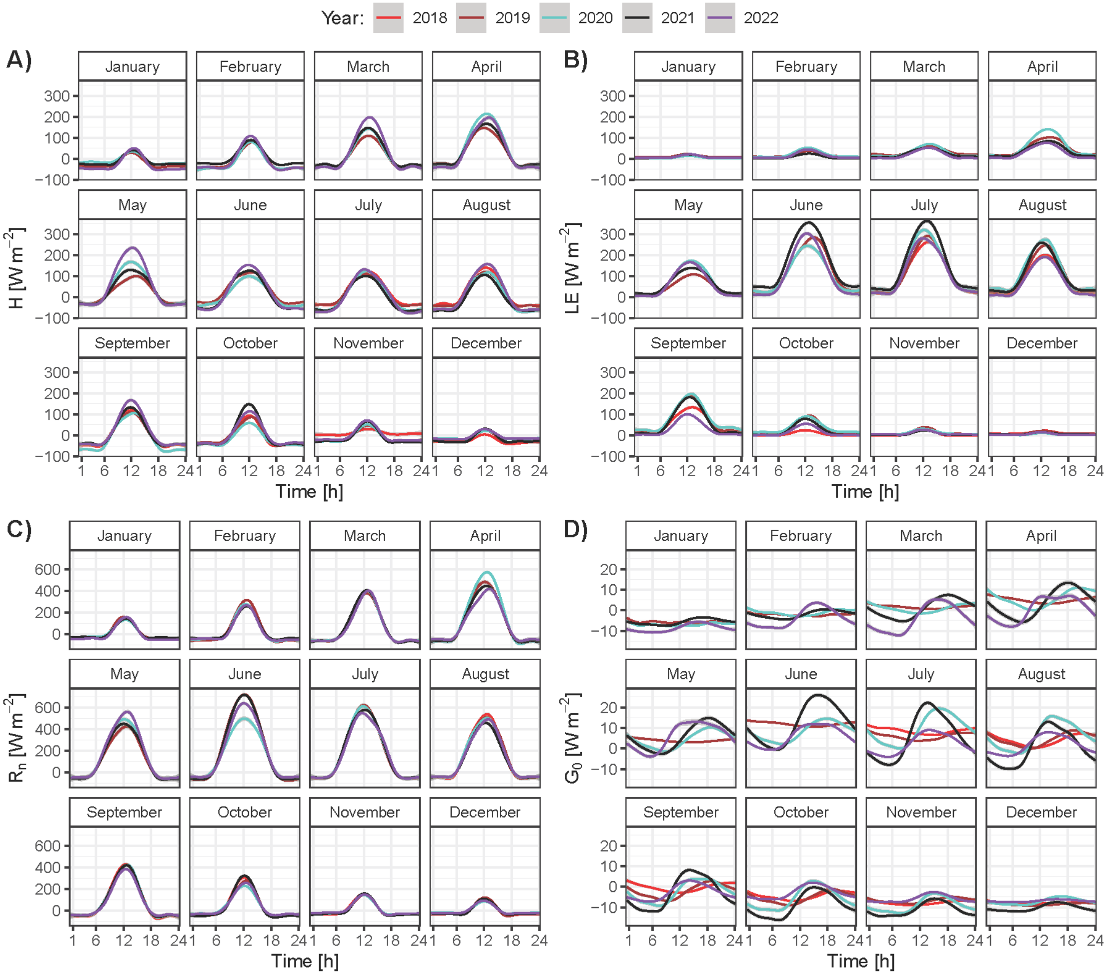

Figure S.15: Diurnal variations of energy fluxes of the reed belt of Lake Neusiedl for each month from mid-2018 until 2022 using the smoothing gam-function (gray area indicates 95% confidence interval): **A)** sensible heat flux (H), **B)** latent heat flux (LE), **C)** net radiation (R_n), and **D)** ground heat flux (G_0). The displayed time is in UTC+1 (local time zone without daylight saving time).

S.2.5 Seasonal and annual variability of the carbon fluxes of the reed belt of Lake Neusiedl

Table S.5: Carbon fluxes (± uncertainty) of the reed belt of Lake Neusiedl in the non-growing (November–April) and growing season (May–October) and annually from mid-2018 to 2022: NEE (net ecosystem exchange), GPP (gross primary production), R_{eco} (ecosystem respiration), CH_4 flux and P (precipitation sum).

Year	**Season**	**NEE** [g C m^{-2}]	**GPP** [g C m^{-2}]	**R_{eco}** [g C m^{-2}]	**CH_4 flux** [g C m^{-2}]	**P** [mm]
2019	*non-growing*	148.7 ± 16.2	-18.6 ± 10.8	167.3 ± 5.0	0.8 ± 0.2	161
2020	*non-growing*	174.1 ± 16.9	-10.7 ± 14.7	184.7 ± 6.6	0.5 ± 0.1	100
2021	*non-growing*	167.7 ± 19.6	-8.9 ± 18.8	176.6 ± 8.8	0.3 ± 0.2	158
2022	*non-growing*	209.3 ± 16.7	-8.3 ± 16.5	217.5 ± 8.6	0.2 ± 0.2	143
2018	*growing*	-4.8 ± 31.0	-523.0 ± 11.6	518.2 ± 4.0	9.6 ± 0.1	304
2019	*growing*	32.0 ± 44.8	-700.9 ± 11.0	732.9 ± 5.1	8.4 ± 0.4	306
2020	*growing*	-54.7 ± 24.9	-979.2 ± 14.9	924.5 ± 6.6	4.6 ± 0.1	404
2021	*growing*	-140.6 ± 48.9	-1224.7 ± 19.1	1084.1 ± 9.0	3.6 ± 0.1	286
2022	*growing*	181.6 ± 48.9	-1022.1 ± 16.8	1203.8 ± 8.8	2.1 ± 0.2	267
2019	*annual*	180.7 ± 9.2	-719.5 ± 21.9	900.2 ± 10.1	9.2 ± 0.6	467
2020	*annual*	119.4 ± 19.5	-989.8 ± 29.6	1109.2 ± 13.2	5.1 ± 0.3	504
2021	*annual*	27.2 ± 19.9	-1233.6 ± 37.9	1260.7 ± 17.8	3.9 ± 0.4	445
2022	*annual*	390.9 ± 19.5	-1030.4 ± 33.2	1421.3 ± 17.4	2.3 ± 0.4	410

S.2.6 Inter-annual variability of the growing season length

So far in this study it has been assumed, mainly for reasons of comparison, that the growing season lasts from May to October. However, the duration, start and end dates of the reed belt's growing season varied between years (2018–2022), depending on the definition used (see Table S.6): When considering the consecutive days with a daily mean $T_{air} > 10$°C over 14 days, the growing season lasted on median 183 days (from mid-April to mid-October). Two years (2020, 2021) had significantly fewer days than the average. When considering the days with a negative daily mean NEE over 14 days, the growing season lasted on median 82 days (mid-May to early August). The longest growing season was observed in 2021 (118 days), while the shortest was in 2022 (57 days). When considering days with a negative daytime mean NEE (daytime: $SW_{in} \geq 10$ W m^{-2}), the growing season lasted on median 165 days (early May to mid-October) and ended earlier than the average in 2022 (on DOY 255).

However, the duration of the growing season, defined as the period with a daily mean $T_{air} > 10$°C over 14 days, cannot explain the inter-annual variability of CO_2 fluxes. The years 2020 and 2021, which showed the shortest growing season duration with this definition (see Table S.6), had the lowest CO_2 emissions. However, the duration of the growing season, defined as the period with negative daily mean NEE over 14 days, increased from 2019 to 2021 due to the later end. In 2022, the growing season was the shortest recorded according to this definition, as already by mid-August, the daily mean NEE was no longer negative.

Table S.6: Days of the growing season of the reed belt at Lake Neusiedl from 2018 to 2022 with three definitions: with mean air temperature (T_{air}) $>$ 10°C over 14 days, with negative mean daytime NEE (net ecosystem exchange) over 14 days or with negative daily mean NEE over 14 days. Start and end of the growing season are given as day of the year (DOY). Daytime is defined as shortwave incoming radiation $\geq$ 10 W m^{-2} as in Reichstein et al. (2005).

Year	**mean $T_{air} > 10$°C**			**neg. mean daytime NEE**			**neg. mean NEE**		
	Start	**End**	**Duration** [days]	**Start**	**End**	**Duration** [days]	**Start**	**End**	**Duration** [days]
2018	98	286	188	111	282	171	127	198	71
2019	105	288	183	125	283	158	147	216	69
2020	107	272	165	118	283	165	127	223	96
2021	118	268	150	121	286	165	128	246	118
2022	113	296	183	125	255	130	135	192	57
median	107	286	183	121	283	165	128	216	71

S.2.7 Change of reed, water and open sediment areas in the reed belt of Lake Neusiedl

Table S.7: The change in the share of reed, water and open sediment area in the 80% annual mean footprints (2019, 2021, and 2022) based on the land cover classification of June/July, as well as the share of the unmodified gravel pathway along the channel.

Year	**Date of orthophoto**	**Reed** [%]	**Water** [%]	**Sediment** [%]	**Pathway** [%]
2019	2019-06-26	67.1	29.1	0.0	3.7
2021	2021-06-18	85.0	9.2	1.9	3.9
2022	2022-07-03	85.0	2.9	8.1	3.9

S.2.8 Water level differences depending on wind speeds

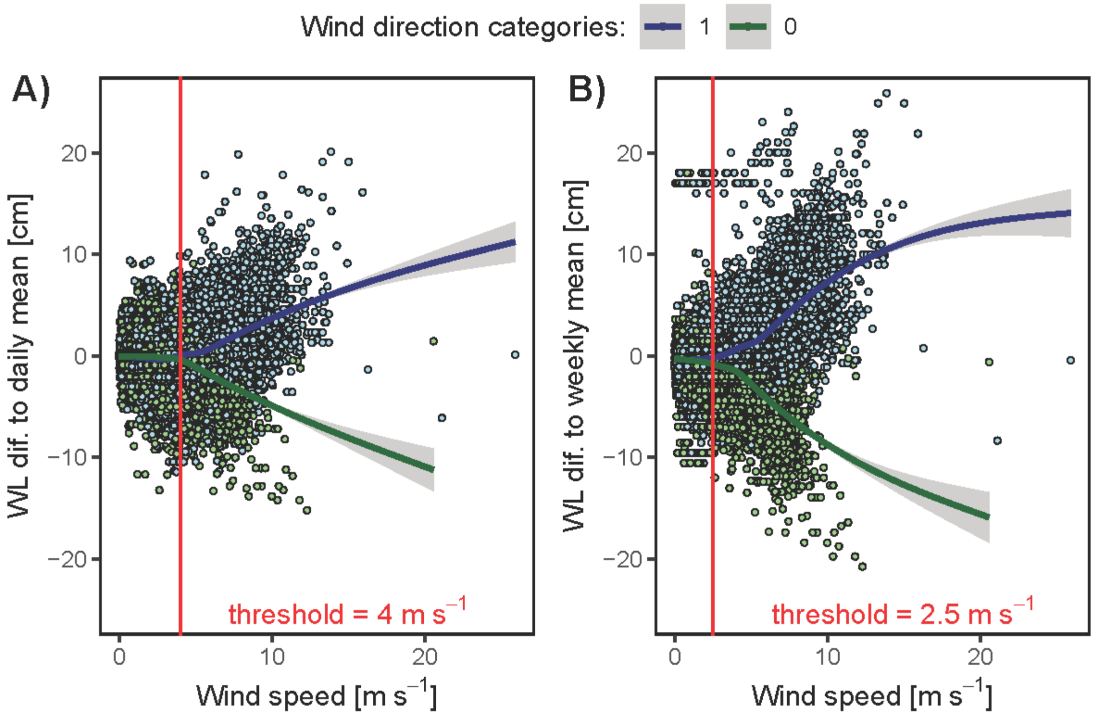

Figure S.16: Wind speed thresholds from which the current water level (WL) differs from the **A)** daily mean WL or **B)** weekly mean WL of Lake Neusiedl (Biological Station Illmitz), independent of the prevailing two main wind direction categories northwest (NW, blue) and southeast (SE, green). These thresholds could indicate times at which a potential lateral flow between the open lake water and the reed belt may be possible, regardless of other necessary conditions.

S.2.9 Drivers of carbon fluxes

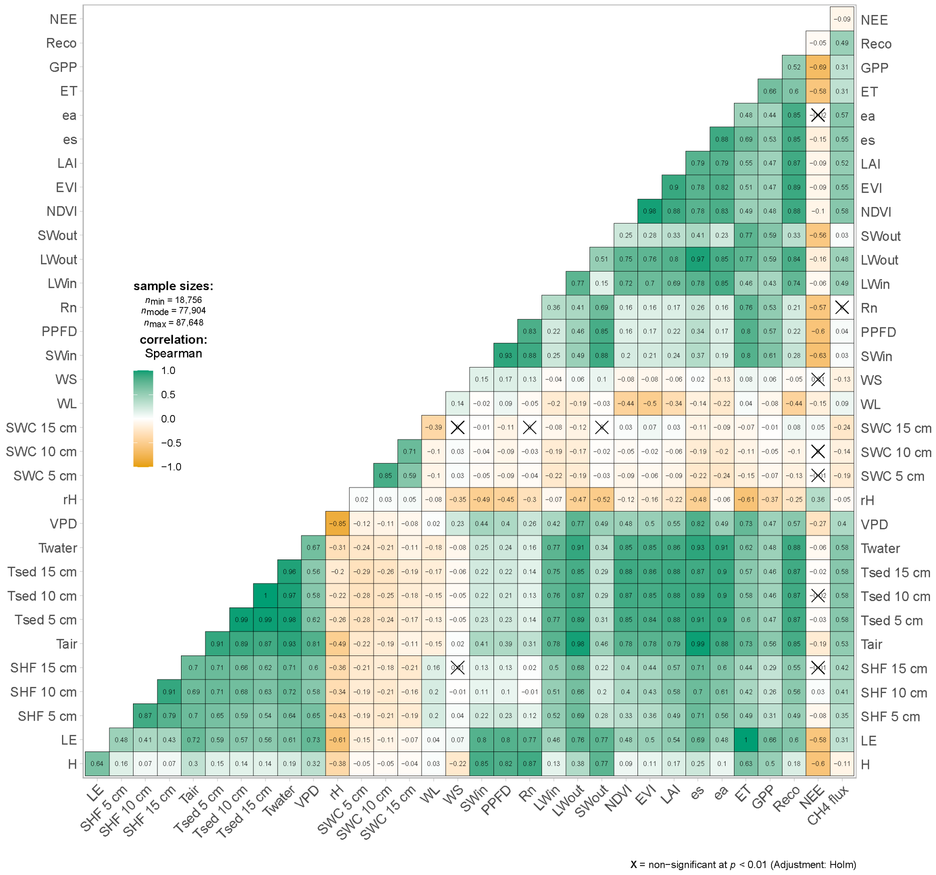

X = non−significant at p < 0.01 (Adjustment: Holm)

Figure S.17: Results of the Spearman correlation analysis of the data set with all years studied (mid-2018 to 2022; NEE = net ecosystem exchange, Reco = ecosystem respiration, GPP = gross primary production, ET = evapotranspiration rate, ea = absolute water vapor pressure, es = saturated water vapor pressure, LAI = leaf area index, EVI = enhanced vegetation index, NDVI = normalized difference vegetation index, SWout = outgoing shortwave radiation, LWout = outgoing longwave radiation, LWin = incoming longwave radiation, SWin = incoming shortwave radiation, Rn = net radiation, PPFD = photosynthetically active photon flux density, WS = wind speed, WL = water level of Lake Neusiedl, SWC = sediment water content, rH = relative humidity, VPD = water vapor pressure deficit, Twater = water temperature of Lake Neusiedl, Tsed = sediment temperature, Tair = air temperature, SHF = sediment heat flux, LE = latent heat flux, H = sensible heat flux).

S.2.10 Temporal variability of environmental parameters and fluxes

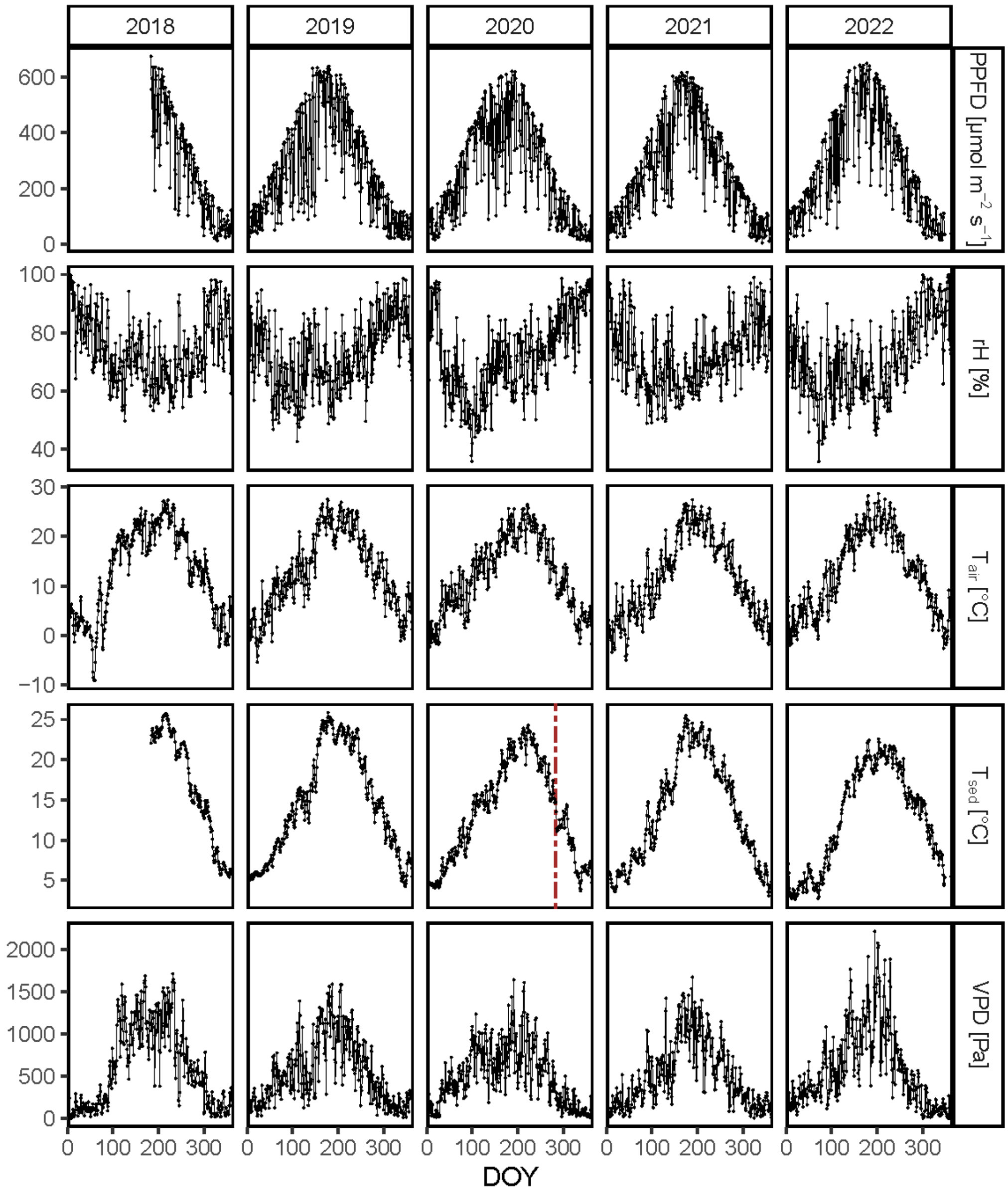

Figure S.18: Temporal variation of photosynthetically active photon flux density (PPFD), relative humidity (rH), air temperature (T_{air}), sediment temperature (T_{sed}) at 5 cm depth, and water vapor pressure deficit (VPD) in the reed belt of Lake Neusiedl per day of the year (DOY) from 2018 to 2022. The brown dashed vertical line shows the date (9 October 2020) when the sediment sensors were replaced.

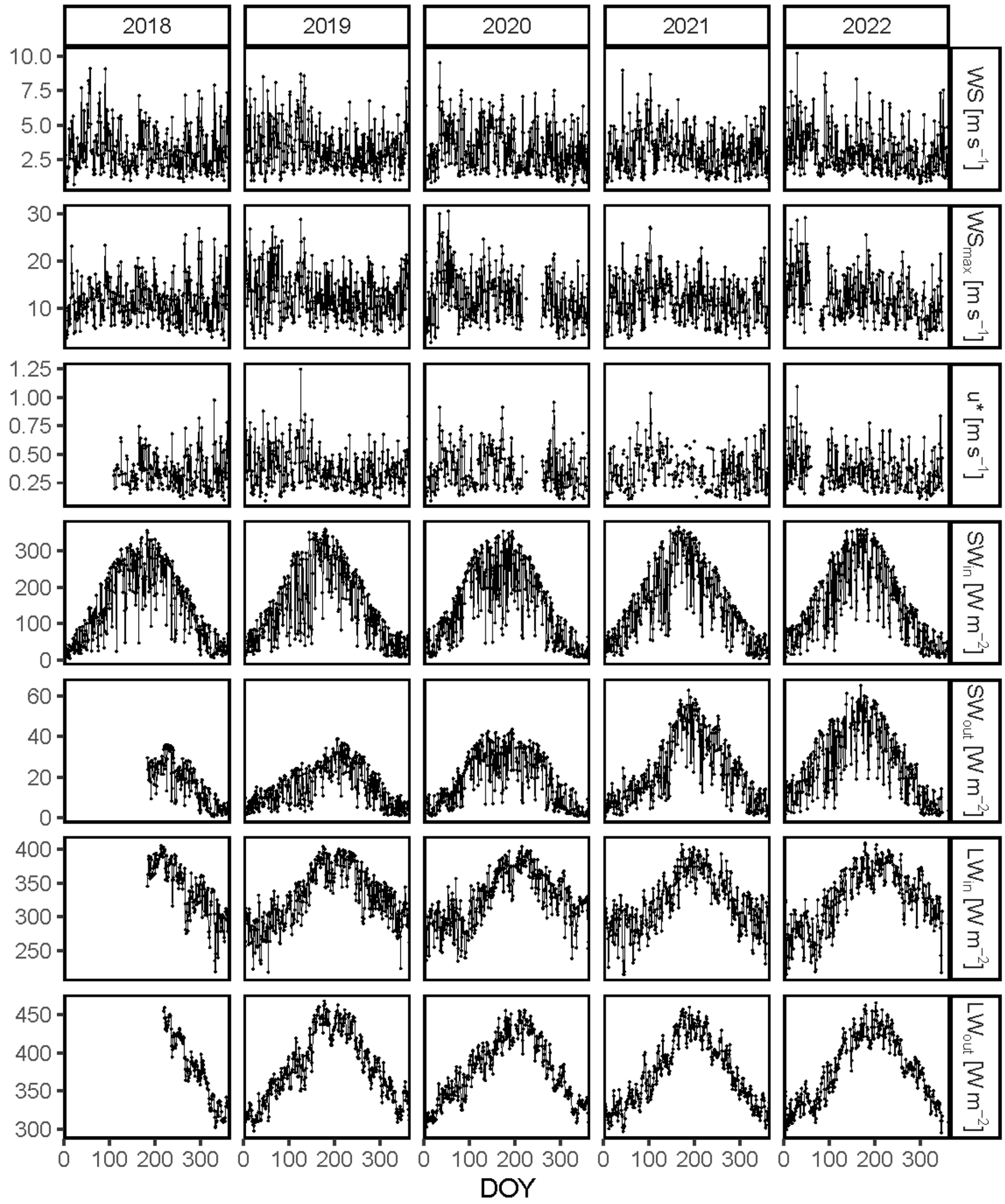

Figure S.19: Temporal variation of mean and maximum wind speed (WS), friction velocity (u*), shortwave incoming (SW$_{\text{in}}$), shortwave outgoing (SW$_{\text{out}}$), longwave incoming (LW$_{\text{in}}$), and longwave outgoing (LW$_{\text{out}}$) radiation in the reed belt of Lake Neusiedl per day of the year (DOY) from 2018 to 2022.

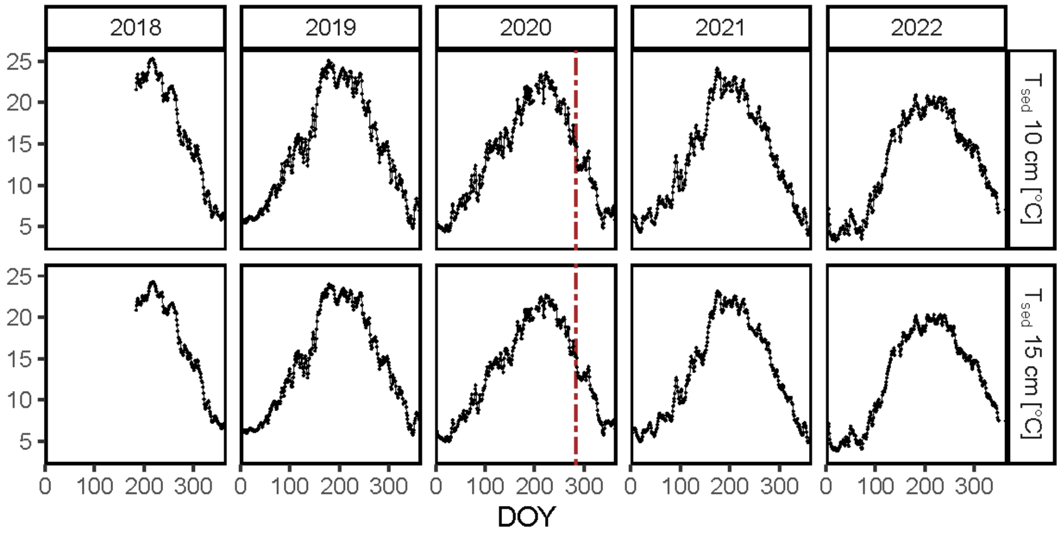

Figure S.20: Temporal variation of sediment temperature (T_{sed}) at 10 cm and 15 cm depth in the reed belt of Lake Neusiedl per day of the year (DOY) from 2018 to 2022. The brown dashed vertical line shows the date (9 October 2020) when the sediment sensors were replaced.

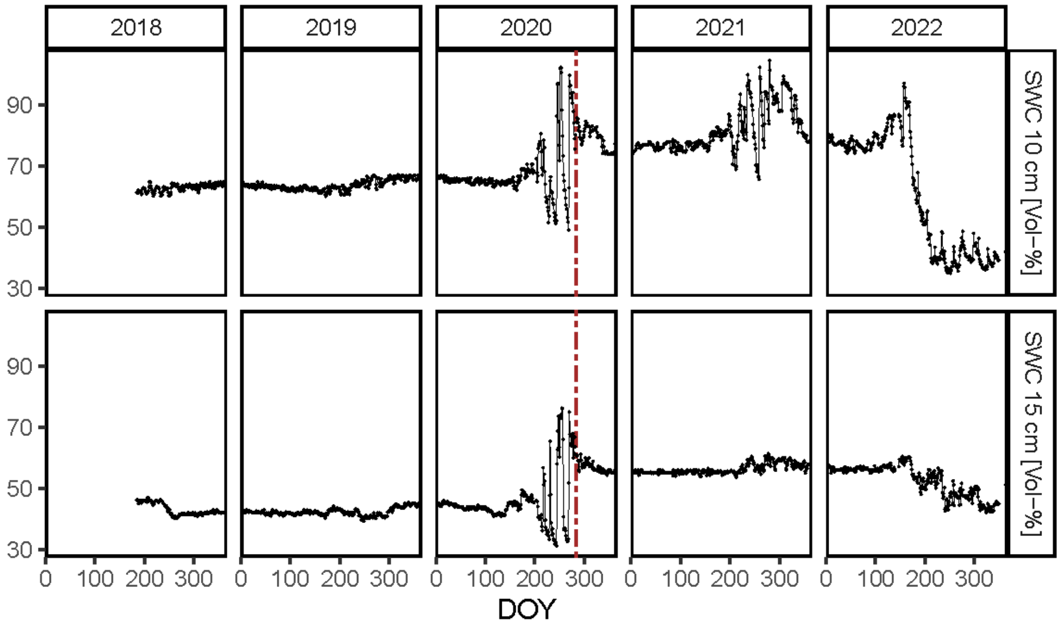

Figure S.21: Temporal variation of sediment water content (SWC) at 10 cm and 15 cm depth in the reed belt of Lake Neusiedl per day of the year (DOY) from 2018 to 2022. The brown dashed vertical line shows the date (9 October 2020) when the sediment sensors were replaced.

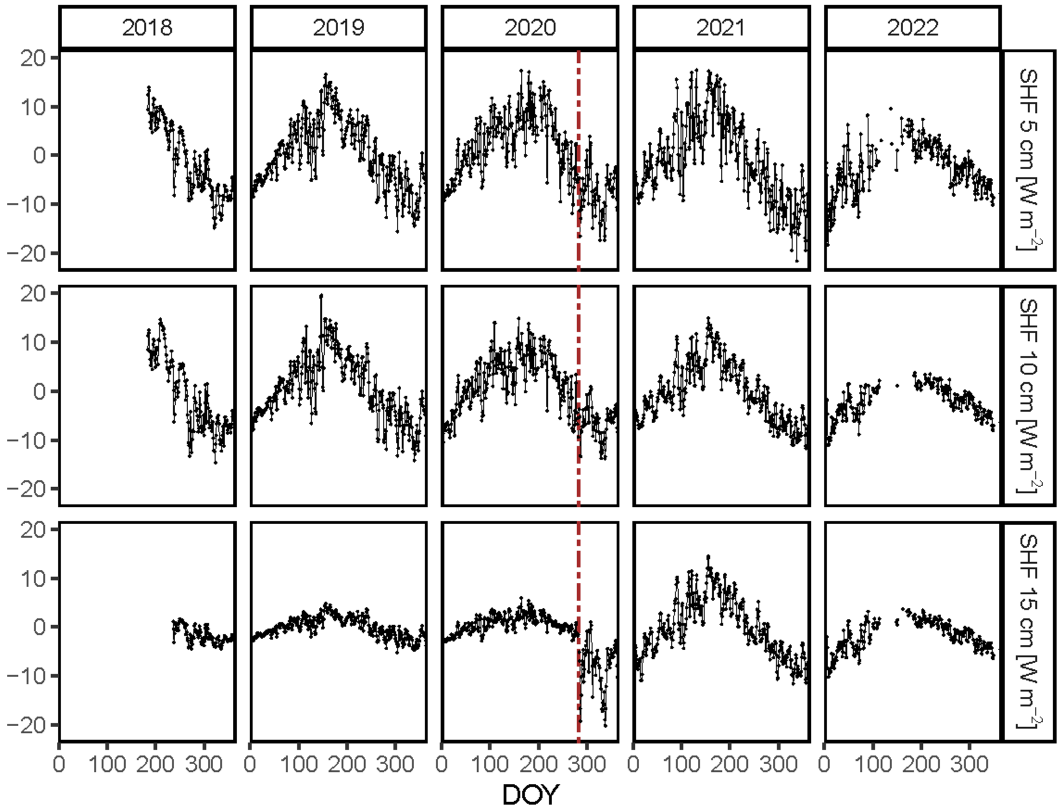

Figure S.22: Temporal variation of sediment heat flux (SHF) at 5 cm, 10 cm and 15 cm depth in the reed belt of Lake Neusiedl per day of the year (DOY) from 2018 to 2022. The brown dashed vertical line shows the date (9 October 2020) when the sediment sensors were replaced.

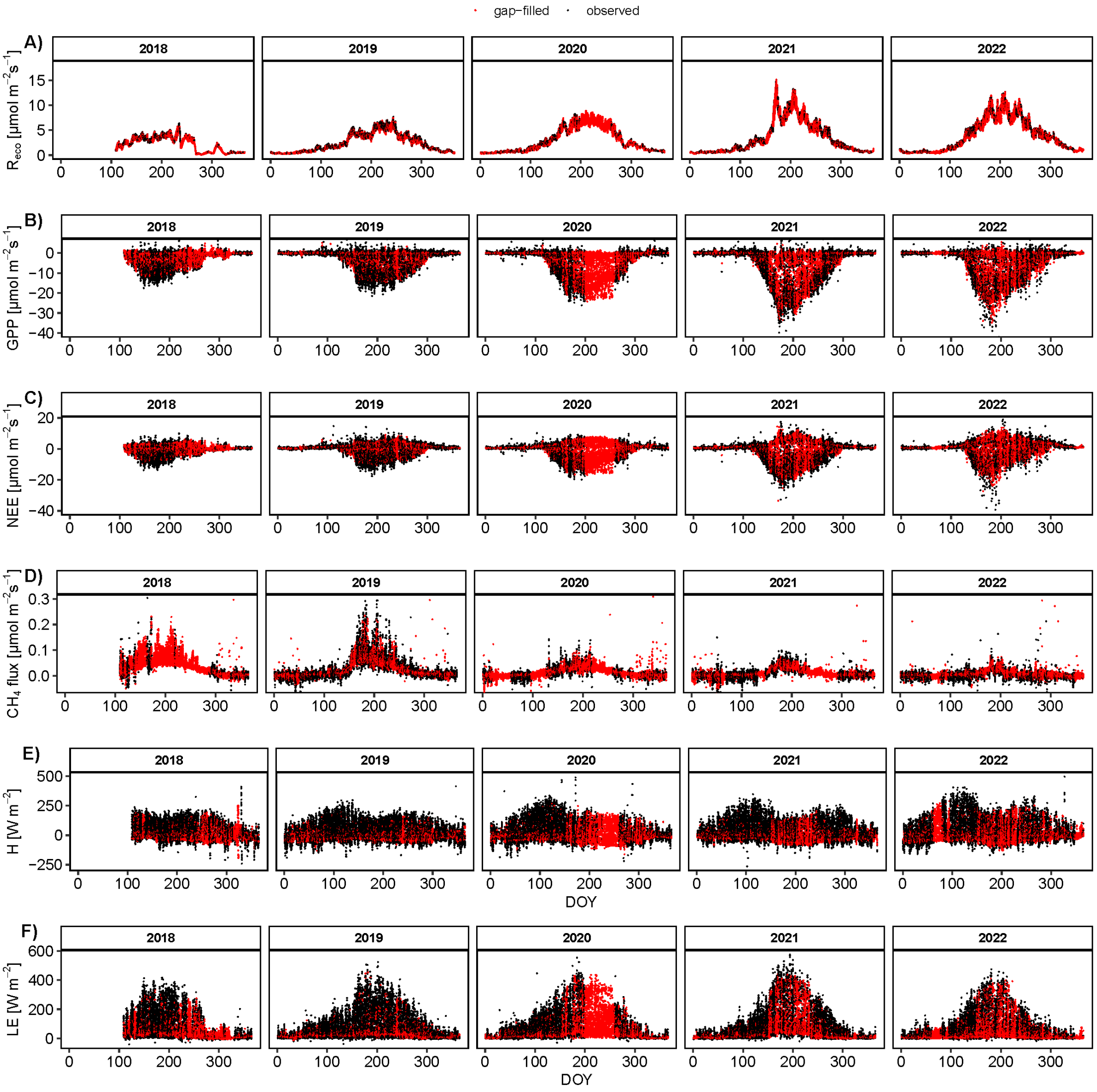

Figure S.23: Temporal variation of the observed (black points) or gap-filled (red points) half-hourly values of **A)** ecosystem respiration (R_{eco}), **B)** gross primary production (GPP), **C)** net ecosystem exchange (NEE), **D)** CH_4 flux, **E)** sensible heat flux (H), and **F)** latent heat flux (LE) of the reed belt of Lake Neusiedl per day of the year (DOY) from 2018 to 2022.

S.3 Supplementary material to Study III

S.3.1 Diel and seasonal differences in biometeorological and water parameters of the reed belt of Lake Neusiedl

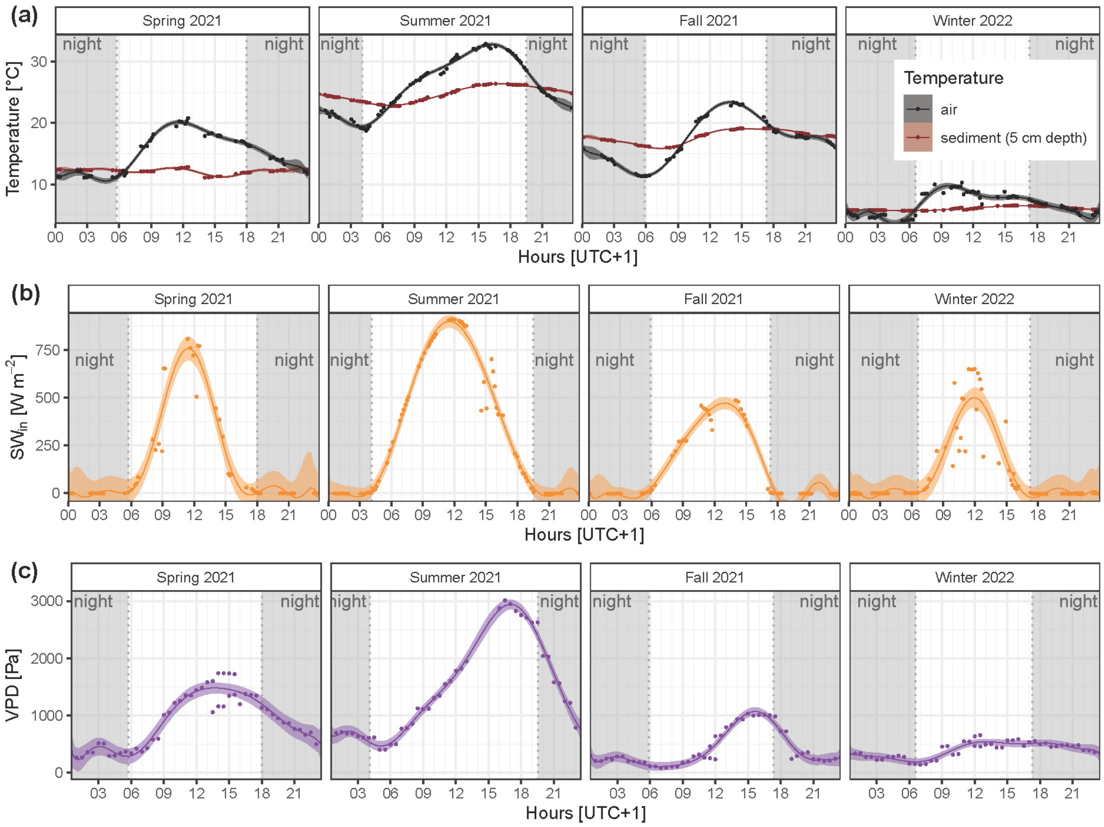

Figure S.24: Diel and seasonal differences in **(a)** ambient air and sediment temperature, **(b)** incoming shortwave radiation (SW_{in}), and **(c)** water vapor pressure deficit (VPD) in the reed belt of Lake Neusiedl (data source: Baur (2024)); the fitted lines showing the decic polynomial regressions with the 95% confidence interval; nighttime when SW_{in} was < 10 W m^{-2} (gray shading).

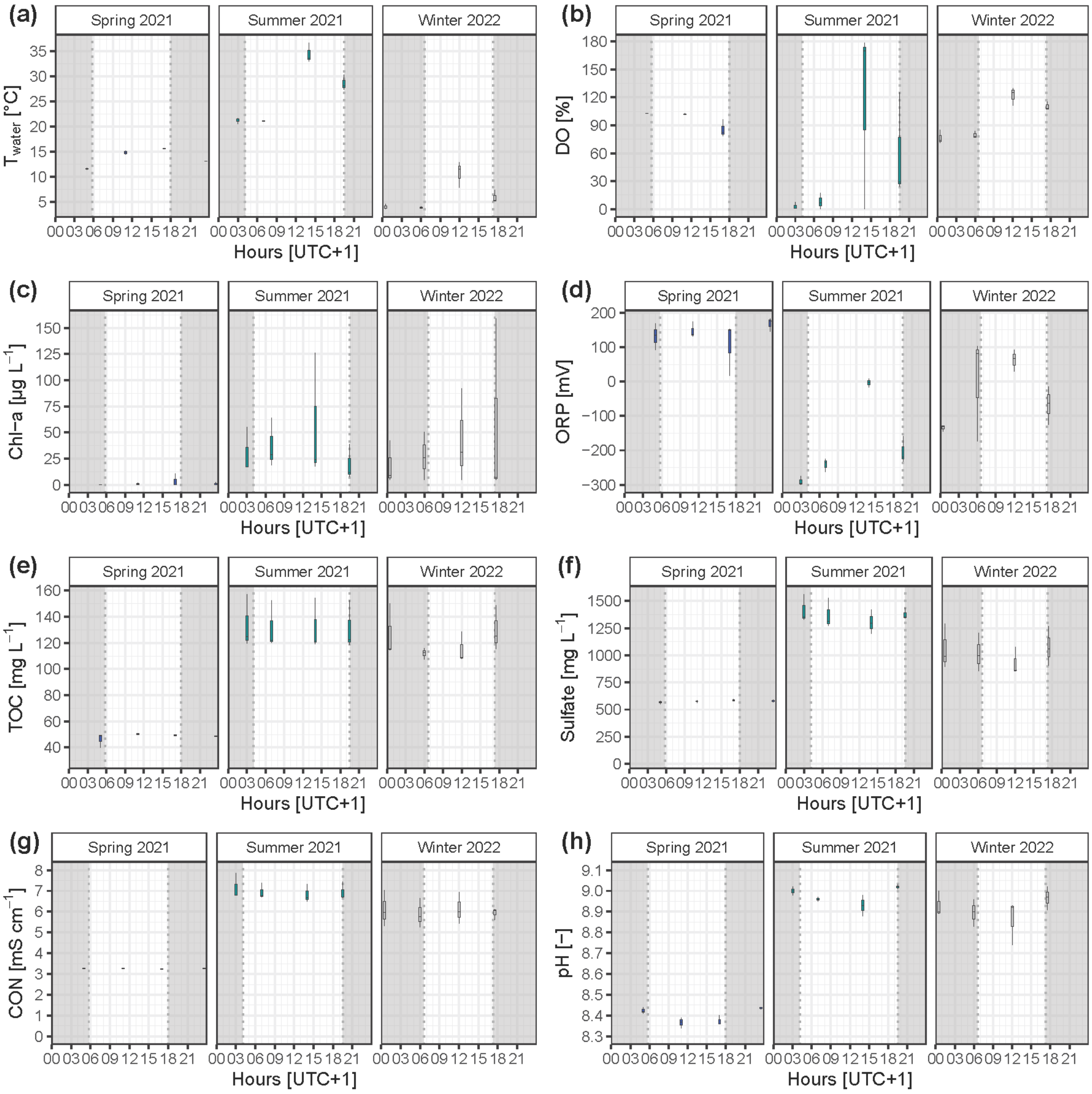

Figure S.25: Diel and seasonal variability in surface water properties of the reed belt during 24 h campaigns: **(a)** water temperature (T_{water}), **(b)** dissolved oxygen (DO), **(c)** chlorophyll-a concentration (Chl-a), **(d)** oxygen–reduction potential (ORP), **(e)** total organic carbon concentration (TOC), **(f)** sulfate concentration, **(g)** electrical conductivity (CON), and **(h)** pH. Nighttime when incoming shortwave radiation was < 10 W m^{-2} (gray shading). In fall 2021 no water above the sediment surface was present.

S.3.2 Seasonal and layer specific differences in sediment properties of the reed belt of Lake Neusiedl

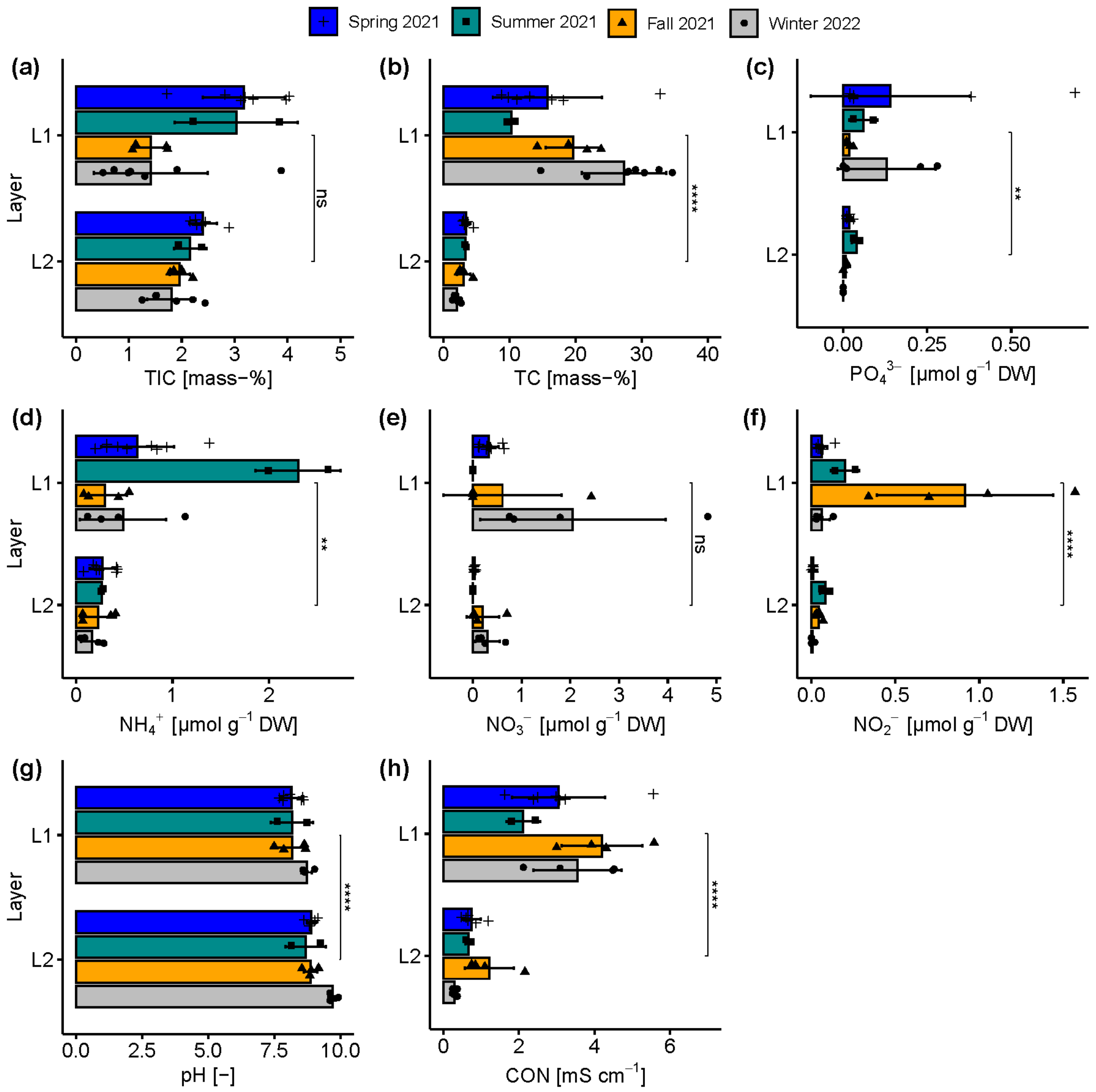

Figure S.26: Seasonal and layer specific differences of **(a)** total inorganic carbon content (TIC), **(b)** total carbon content (TC), **(c)** phosphate (PO_4^{3-}), **(d)** ammonium (NH_4^+), **(e)** nitrate (NO_3^-), **(f)** nitrite (NO_2^-) concentration, **(g)** pH, and **(h)** electrical conductivity (CON) in the upper (L1) and lower layer (L2) of sediments in the reed belt of Lake Neusiedl. Non-significant (ns, $p > 0.05$ with Holm's adjustment, Dunn's test), significant (**, $p < 0.01$), or very significant differences (****, $p < 0.0001$) in the parameters between the two layers in the sediments independent of the season.

S.3.3 Inter-annual differences in properties and microbial characteristics of sediments of the reed belt of Lake Neusiedl

Table S.8: DNA yield, total number of microbial classes, gravimetric water content (WC), pH, electrical conductivity (CON), and total organic carbon content (TOC) in four depth section of the sediment cores I and II from the reed belt of Lake Neusiedl in winter 2021 and 2022. The two sediment sections, 0–2 cm and 4–6 cm, are part of the upper layer (L1) of the sediment, while the sections 20–22 cm and 24–26 cm are located in the lower layer (L2).

Season	**Core**	**Depth section** [cm]	**DNA yield** [µg g^{-1} DW]	**Number of classes**	**TOC** [mass-%]	**WC** [mass-%]	**pH**	**CON** [mS cm^{-1}]
Winter 2021	**I**	0–2	41.172	143	33.2	89.1	8.36	3.35
		4–6	39.549	146	35.1	89.6		
		20–22	0.033	112	0.5	24.8	9.13	0.34
		24–26	0.042	124	0.8	31.0	8.76	0.88
	II	0–2	43.571	162	31.5	90.8	8.12	2.25
		4–6	42.747	166	30.9	89.6	8.33	2.56
		20–22	0.037	127	0.3	26.3	9.10	0.35
		24–26	0.001	84	0.2	21.4	9.34	0.35
Winter 2022	**I**	0–2	8.058	141	29.4	87.8	8.65	4.49
		4–6	9.889	134	31.9	87.8		
		20–22	0.628	108	0.4	24.0	9.60	0.37
		24–26	0.300	117	0.3	21.4	9.59	0.32
	II	0–2	7.899	127	26.8	88.0	8.65	4.52
		4–6	7.844		26.7	89.1		
		20–22	0.558	158	0.1	19.4	9.62	0.25
		24–26	0.282	106	0.3	22.6	9.53	0.33

S.4 Supplementary material to Study IV

S.4.1 GCC maps and histograms

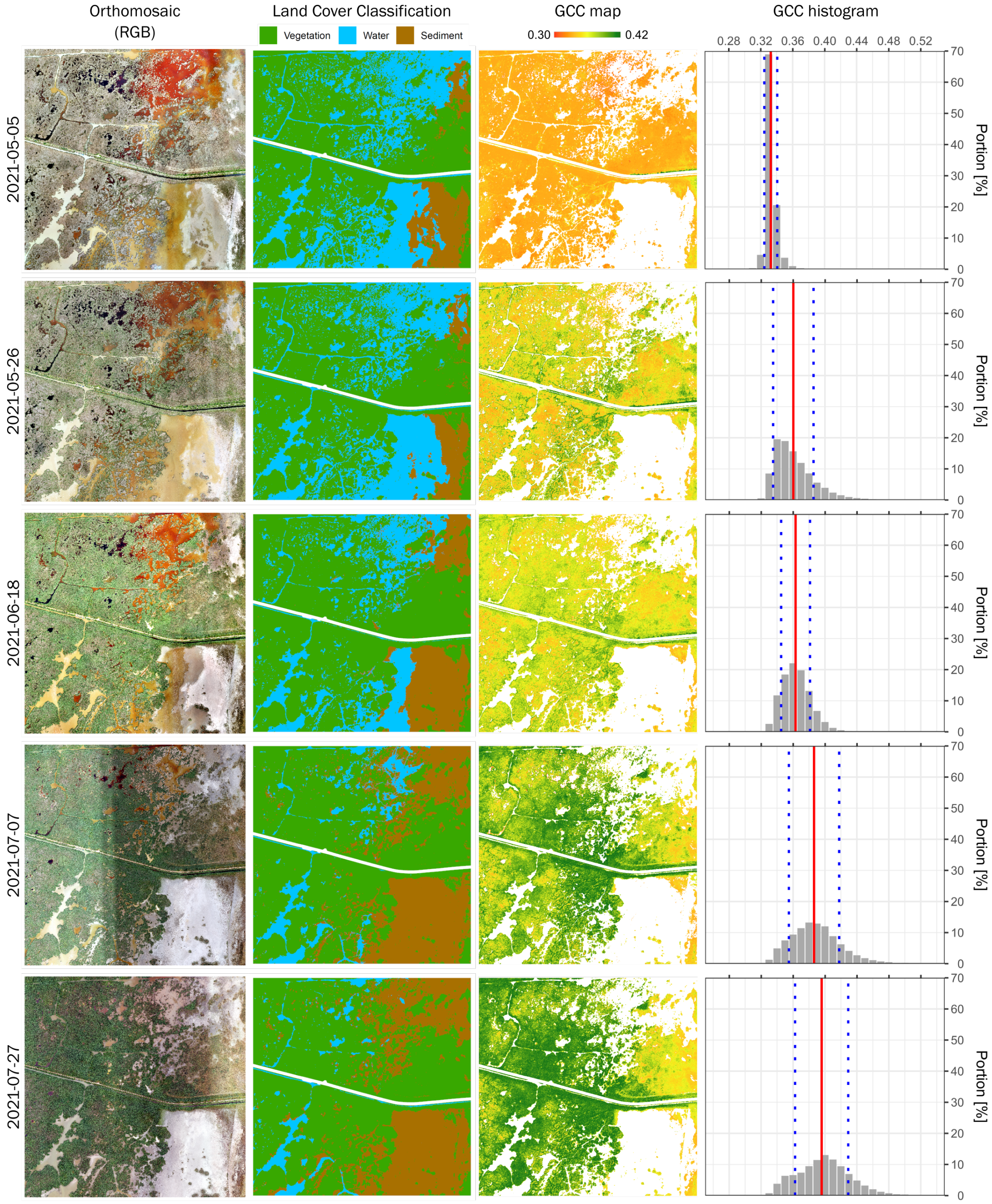

Figure S.27: Spatio-temporal development of the study area in the reed ecosystem of Lake Neusiedl from May to July 2021. The mean green chromatic coordinates (GCC) (red solid line) and the standard deviation (blue dotted lines) of each flight date are shown in the GCC histogram.

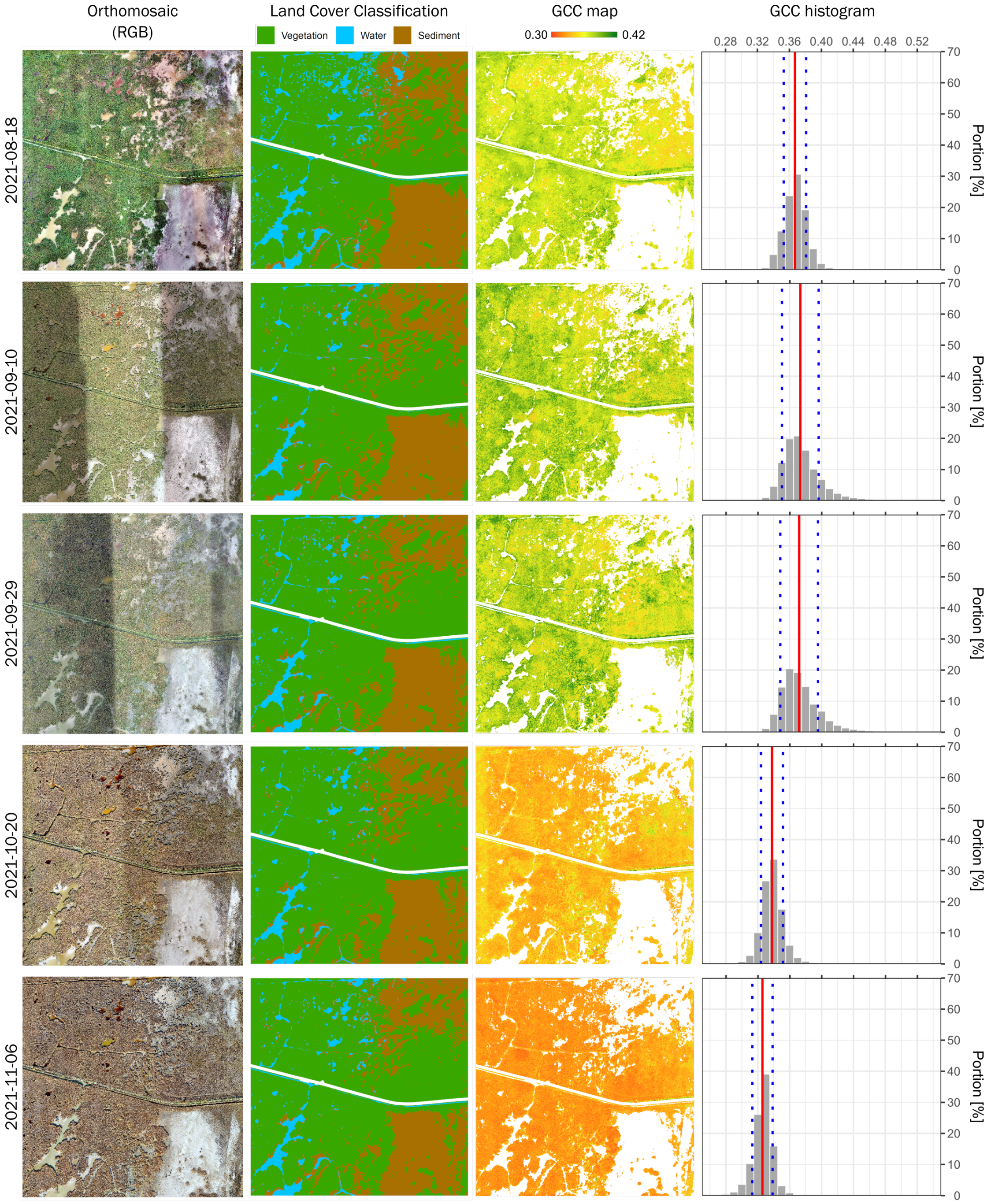

Figure S.28: Spatio-temporal development of the study area in the reed ecosystem of Lake Neusiedl from August to November 2021. The mean green chromatic coordinates (GCC) (red solid line) and the standard deviation (blue dotted lines) of each flight date are shown in the GCC histogram.

S.4.2 Deep learning parameters and performance metrics of the CNN models

Table S.9: Detailed table of deep learning parameters and performance metrics (IoU = intersection over union). 10 CNN (convolutional neural network) models were trained for land cover classification of UAV (unmanned aerial vehicle) imagery for tracking a reed ecosystem over a vegetation period (SD = standard deviation).

				Precision			**Recall**			**F1-Score**			**IoU**		
Orthomosaic date	**Image chips used for training**	**Learning rate**	**Accuracy of last epoch**	**Vegetation**	**Water**	**Sediment**	**Vegetation**	**Water**	**Sediment**	**Vegetation**	**Water**	**Sediment**	**Vegetation**	**Water**	**Sediment**
2021-05-05	1621	0.0004	0.945	0.958	0.967	0.892	0.941	0.946	0.952	0.950	0.956	0.921	0.851	0.837	0.629
2021-05-26	1642	0.0010	0.948	0.972	0.918	0.927	0.964	0.945	0.908	0.968	0.931	0.918	0.920	0.847	0.575
2021-06-18	1537	0.0010	0.958	0.977	0.959	0.931	0.965	0.917	0.975	0.971	0.938	0.953	0.924	0.731	0.784
2021-07-07	1574	0.0005	0.935	0.960	0.936	0.868	0.955	0.939	0.899	0.958	0.938	0.883	0.910	0.766	0.662
2021-07-27	1696	0.0008	0.939	0.948	0.878	0.944	0.957	0.912	0.924	0.952	0.895	0.934	0.887	0.476	0.801
2021-08-18	1642	0.0008	0.936	0.964	0.908	0.909	0.951	0.867	0.955	0.958	0.887	0.932	0.905	0.639	0.797
2021-09-10	1533	0.0005	0.950	0.951	0.952	0.947	0.964	0.906	0.951	0.958	0.928	0.949	0.890	0.603	0.835
2021-09-29	1706	0.0005	0.937	0.952	0.904	0.931	0.962	0.915	0.906	0.957	0.909	0.918	0.906	0.543	0.747
2021-10-20	1720	0.0005	0.939	0.958	0.923	0.906	0.953	0.953	0.899	0.955	0.938	0.903	0.904	0.689	0.680
2021-11-06	1741	0.0002	0.939	0.945	0.940	0.922	0.961	0.927	0.899	0.953	0.933	0.910	0.892	0.723	0.693
Mean	1641	0.0006	0.943	0.958	0.929	0.918	0.957	0.923	0.927	0.958	0.925	0.922	0.899	0.685	0.720
SD	71	0.0003	0.007	0.010	0.026	0.023	0.007	0.024	0.027	0.006	0.020	0.020	0.020	0.115	0.081